Process and Design Techniques for Low Loss Integrated Silicon Photonics

by

Daniel Knight Sparacin

Sc.B. Materials Science and Engineering, with Honors
Brown University, 2000

Submitted to the Department of Material Science and Engineering in Partial Fulfillment of the Requirements for the Degree of

Doctor of Philosophy in Electronic, Photonic, and Magnetic Materials
at the
Massachusetts Institute of Technology

June 9, 2006

© 2006 Massachusetts Institute of Technology. All rights reserved.

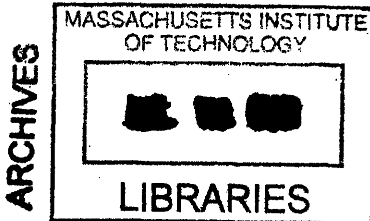

Signature of Author: ______________________
Department of Material Science and Engineering
May 22, 2006

Certified by: ______________________
Lionel C. Kimerling
Thomas Lord Professor of Material Science and Engineering
Thesis Supervisor

Accepted by: ______________________
Samuel M. Allen
POSCO Professor of Physical Metallurgy
Chair, Departmental Committee on Graduate Students

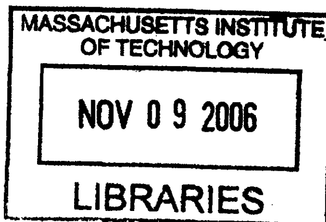

Process and Design Techniques for Low Loss Integrated Silicon Photonics

by

Daniel Knight Sparacin

Abstract

Microprocessors have truly revolutionized the efficiency of the world due to the high-volume and low-cost of complimentary metal oxide semiconductor (CMOS) process technology. However, the traditional scaling methods by which chips improve are soon to end. The continued drive towards smaller circuit elements and dense chip architecture has yielded to power consumption, heat production, and electromagnetic interference (RC-delay) limitations. A logical solution to surmounting this electronic interconnect bottleneck is to utilize photonic interconnects. Photonic interconnects (waveguides) offer high data bandwidths with low signal attenuation and virtually zero heat dissipation. Strategic replacement of RC speed-limited electronic interconnects with photonic interconnects is a logical step to improving data processing performance in future microprocessors. Integration of photonic circuits onto electronic chips also enables sought after networking technologies that have higher complexity and unique functionality. Similar to the integrated microchip, the employment of CMOS technology in the fabrication of integrated photonic chips enables high yield, low cost, and increased performance. Essentially, the development of an integrated CMOS compatible photonic circuit technology is an enabler of improved communication.

However, there are many challenges in realizing a viable, integrated [illegible] technology. The constraints associated with fabrication of CMOS compatible, high-index-contrast, planar, thin-film photonic devices add difficulty in realizing the necessary components for a complete photonic circuit. Of these components: light source, waveguide, modulator, splitter, filter, and detector; all are limited in performance and functionality by optical transmission loss. As a result, this thesis has focused on diagnosing and addressing the various loss mechanisms that exist in fabricating CMOS compatible channel waveguides. As the building block of higher order photonic devices, waveguides are useful as diagnostic tools with which one can characterize photonic loss mechanisms. Waveguide test methodologies are developed to accurately diagnose the waveguide loss mechanisms (e.g. bulk absorption and interface roughness-scattering) by analyzing transmission loss (α_T) as a function of signal wavelength (λ), waveguide width (w), waveguide height (h), effective index (n_{eff}), number of bends (N), and optical power (P).

Four high index waveguide materials are investigated: silicon on insulator (SOI), amorphous silicon (a-Si), polycrystalline silicon (poly-Si), and Silicon Nitride. The dominant loss mechanism for each material system is different and as a result, unique process and design techniques are developed for each. For SOI waveguides, the loss is dominated by sidewall roughness. As a result, a novel post-etch wet chemical oxidation smoothing method is developed to reduced sidewall roughness and improve waveguide transmission. The employment of a hybrid waveguide design further reduces SOI waveguide losses to 0.35 dB/cm. For a-Si waveguides, loss is dominated by bulk absorption arising from dangling bonds. Loss reduction is achieved by increasing the H-content in the films, thereby satisfying the dangling bonds and reducing the number of absorption sites. Amorphous silicon bulk losses are reduced from 15.2 ± 2 dB/cm to < 1 dB/cm, representing a tractable path for integrating high index contrast waveguides onto multiple chip levels. For SiN waveguides, N-H bond absorption at λ=1510 nm is the

dominant loss mechanism. Here the use of low H-content precursors is investigated to reduce the number of N-H bond absorption sites. A total of six SiN materials are compared with losses as low as 1.5 dB/cm.

Ring resonator devices, comprised of channel waveguides, are also investigated. Ring resonators serve as filters for multiplexing and demultiplexing broadband optical signals, dispersion compensators for accurately controlling phase, lasers, and ultrafast all-optical switches. In realizing these devices a ring trimming method is developed to compensate for non-deterministic pattern transfer errors which limit dimensional precision and preclude the fabrication of identical devices across an entire wafer. In this work, a novel photo-oxidation trimming method, using a UV-sensitive, polysilane top cladding material, is employed. The UV-induced refractive index decrease of polysilane (4%) enables accurate and localized trimming of ring resonators. Ring modulator devices are modeled as well. The employment of integrated SiGe ring modulators that utilize the fast Franz-Keyldish effect is discussed.

The design constraints involved in monolithically integrating photonic and electronic components are discussed. In particular, the CMOS process challenges: material limitations, epitaxial compatibilities, thermal-budget imposed process order, and device communication requirements are utilized in arriving at an optimal application specific, electronic-photonic integrated chip (AS-EPIC) architecture.

Thesis Supervisor: Lionel C. Kimerling
Title: Thomas Lord Professor of Material Science and Engineering

Acknowledgements

First I would like to thank my parents and my sister for always being supportive of my studies. As the son of an engineer I was exposed to problem solving skills early on. Anything broken in our house was promptly fixed, thanks Dad for always explaining how things work and making me feel like I helped by handing you the correct screwdriver. Thank you for suggesting material science as a field to pursue and giving me confidence in my pursuit of the doctorate. Mom, thank you for showing me how to be imaginative and creative in my work. I am always impressed with your prize winning quilts and other crafts; they leave me feeling as though I have the potential to do better. Also thank you for wiping down the kitchen table after dinner every night, it made it that much easier to do my homework. Maggie thanks (although you didn't really have a choice) for acting as my childhood mental sparring partner and keeping me sharp.

At Ossining High School, my interest in science reached a new level with Mr. Howard ("Howie") Myers, my physics and AP chemistry teacher. His lectures were incredibly clear and filled with apt and ingenious demonstrations for which I am still in awe, thank you. After high school, I attended Brown University and worked as an undergraduate researcher under Prof. David C. Paine. Prof. Paine let me get my feet wet, spoiled me with my own lab, and always made the time to discuss anything (including sailing). I also have to thank Dr. Darren Cairns who showed me how one takes experimental results to analysis to publication.

I arrived at MIT in September 2000 and joined Prof. Lionel C. ("Kim") Kimerling's group shortly after the New Year. I am truly thankful to Kim for giving me the freedom to learn at my own pace. Once I built my research toolset, Kim gave me the opportunity to work on several cutting-edge research projects with which I could establish myself. I benefited from his depth of experience and learned how to see the big picture under his guidance. I am continually amazed at how quickly Kim can distill a problem into its fundamental parameters and hope that I can someday reach that lucidity. Kim, it's been a pleasure to learn from you and thank you for sharing your vision of integrated photonics.

As a member of the EMAT group I had the pleasure of working with many gifted scientists and engineers. Dr. Kazumi Wada acted as my co-advisor for my first couple of years at MIT. Kazumi was instrumental in teaching me about waveguides and thinking outside the box, a trait he excelled at. Dr. Jurgen Michel was a tremendous help in using and understanding any piece of equipment, a real asset to the group. Dr. Anu Agarwal welcomed me to EMAT and was very helpful in waveguide processing ideas. Anu also enabled the upgrade of our waveguide measurement equipment thanks to her brief EMAT hiatus and insider knowledge. Mark Beals acted as the MIT project manager and architect on the EPIC project. Mark's knowledge of the CMOS process flow and AMAT processing tool specifications was quite helpful in realizing this work. Not only did I learn a lot from Mark on our trip down to BAE Systems in Virginia, but he bought me lunch, what a guy. I am indebted to Dr. Ching-yin Hong for the many, many waveguides she processed and the help in making photolithography masks. Ching-yin is a critical gear in the EMAT machine.

My time at MIT overlapped with more than 25 EMAT students. Dr. Shoji Akiyama and Dr. Victor Nguyen were always willing to help and impart wisdom gained from fabricating state of the art SiN waveguide devices. Dr. Sajan Saini, physicist extraordinaire, played a crucial role in helping me understand guided optics through many conversations, typically over coffee or tea. Sajan is one of those rare people who can hold a conversation on any topic and relate any topic back to science. Perhaps the most energetic EMAT member and defacto social chair is Dave Danielson, science always seemed cooler when working with him. Many of our enlightening conversations took place over beer. Mike Stolfi, my long time officemate, was always willing to help and ensured EMAT was safe (thank you). Wojtek Giziewicz, our resident electrical engineer and high speed measurement expert, kept the rigor up. Wojtek, thanks for your comments and keeping me honest. Team Ge: Doug Cannon, Jifeng Liu, Nok Jongthammanurak, and Donghwan Ahn, were always willing to discuss the issues involved in integrating

Ge devices. Rong Sun, my protégé, helped with some of the waveguide measurements and is primed to continue this work.

I also had the opportunity to interact with other waveguide researchers at MIT. From the MIT-Pirelli project, I had the pleasure of interacting with Milos Popovic, Peter Rakich, Tymon Barwicz, Mike Watts, Prof. Ippen, Prof. Kaertner, and the late Prof. Haus. I learned a lot from these guys, just check out my references.

I had many collaborators who helped me with the work in this thesis. Dr. Steven Spector of Lincoln Labs provided me with Si and SiN waveguide samples with which I honed my waveguide measurement skills and developed the wet chemical oxidation smoothing technique. He graciously invited me up to Lincoln Labs and brought me up to speed on his measurement and sample preparation techniques which saved me a lot of time. I would also like to thank Dr. John LeBlanc of Draper Labs for useful waveguide discussions and helping me test out flame polishing as a possible post-etch smoothing technique. Dr. John P. Lock and Prof. Karen K. Gleason from the Department of Chemical Engineering developed and provided me with the polysilane material used in the ring trimming experiments. John, it was a pleasure working with you, I can only hope that my future collaborations move as smoothly as ours did. A special thanks to Chuck Mullen from Claredon Photonics for bringing me up to speed on using the Newport-JDS measurement system. Most recently, I have had the pleasure of collaborating on the EPIC project with colleagues at Lucent – Doug Gill, Mahmoud Rasras, Sanjay Patel, and Alice White; and colleagues at BAE Systems – Tim Conway, Andy Pomerene, Dan Carothers, and Mike Grove. Doug, thank you for the many insightful conversations and inviting me down to Bell Labs, it was a great experience.

I would like to thank my friends who made sure that I had a good time outside MIT. Joe, Josh, Ryan, Nate, and Dave it's been great hanging with you at our weekly "meeting of the minds" at the Muddy. Forrest Café Trivia and 99 Marion St. were good times as well. A back of the envelope calculation indicates that we've had hundreds of beers together, you guys are great and the conversations rocked. I should also thank your better halves – Vanessa, Jasmine, Kate, and Lisa (Dave you're not fitting the trend). Josh, thanks for running all those river loops, it really helped me de-stress. Cody, you're a scholar and shoot from the hip, we've had some good adventures, and I still can't believe you're a professor. Nava, thank you for always being there to chat, it's always a pleasure. Mindy, our conversations always brought me to new understandings, it's been fun. Fitzgerald Crew: Dave, Carl (The Dohrminator), and Saurabh you guys were great office neighbors and always helpful. Fellow Nth Years: Edwin, Jason, Shandon, Jorge, Zil, Will, Chacha, John G., it was great hanging out and discussing the notion of IHTFP. Duncan, Peter, and Aunt Ruth, thanks for all the lunches and dinners. Fellow O-town transplants: Eric, Kitty, Patrick, and Peter; it's amazing how long we've known each other. Eric, Alissa, Hudson, and Danielle, the future looks bright.

Finally, I would like to acknowledge my funding sources: The Rosenblith Fellowship, The National Science Foundation (NSF), and the Defense Advanced Research Projects Agency (DARPA).

This thesis was brought to you by the letters P, Q, and the number 9.

Table of Contents

1 Introduction

1.1 Motivation 14

1.1.1 Communication..14

1.1.2 Computation..15

1.1.3 The Limitations of Electronic Interconnects.......................................16

1.1.4 The Benefits of Integrated Photonics..18

1.2 Integrated Photonic Circuits...20

1.2.1 Photonic Components 20

1.2.2 Material Platform Considerations 21

1.2.3 Silicon Photonics 23

1.3 Thesis Work 24

2 Theory

2.1 Maxwell's Equations 28

2.2 Plane Waves 29

2.3 Phase and Group Velocity 31

2.4 Polarization 32

2.5 Interface Boundary Conditions 33

2.6 Dielectric Waveguides 34

2.6.1 Slab Waveguide 34

2.6.2 Other Planar Waveguide Geometries 38

2.6.3 Effective Index Method 39

2.6.4 Numerical Techniques 40

2.6.5 Single Mode versus Multiple Mode Waveguides 41

2.7 Single-Mode, High Index Contrast, Channel Waveguides 42

2.7.1 Asymmetric Boundary Conditions 42

2.7.2 Effective Index versus Width 44

2.7.3 Mode Size 45

3 Waveguide Measurement

3.1 Transmission Loss 48

3.2 Insertion Loss 49

3.2.1 High Index and Lens Tipped Fibers 51
3.2.2 Estimating Coupling Loss 51
3.2.3 Input Couplers 52
3.2.4 Inverted Taper Coupler 53
3.2.5 Asymmetric GRIN Taper Coupler 54
3.2.6 Vertical Grating Coupler 54
3.2.7 Input Coupler Comparison 55
3.3 Sample Preparation 55
3.4 Cutback Loss 57
3.5 Fabry-Perot Loss 59
3.5.1 Determining the Waveguide Facet Reflection Coefficient 60
3.6 Experimental Apparati 61
3.6.1 Table 3 System 62
3.6.2 Newport-JDS System 63
3.7 Effective Experimental Design........ 64
3.7.1 Cutback Measurement Concerns 64
3.7.2 Fabry-Perot Measurement Concerns 65

4 Waveguide Loss Mechanisms

4.1 Planar Waveguide Fabrication 68
4.1.1 Waveguide Process Flow 68
4.1.2 High Index Contrast Waveguide Processing Concerns 70
4.2 Loss Mechanisms Overview 74
4.3 Roughness Scattering 76
4.3.1 Mathematically Describing Roughness 76
4.3.2 Measurement of Sidewall Roughness 77
4.3.3 Roughness Scattering Theory 78
4.3.4 Experimental Identification of Roughness Scattering 86
4.4 Absorption 88
4.4.1 Common Thin Film Absorption Loss Mechanisms 89
4.4.2 Measuring Material Bulk Loss 91
4.4.3 Calculating Waveguide Absorption Loss 92
4.4.4 Experimental Identification of Waveguide Absorption Loss 94
4.4.5 Experimentally Finding Bulk Loss Values by Waveguide Loss Measurement.. 95

4.5 Non-linear Processes 96
4.5.1 Stimulated Raman Scattering 97
4.5.2 Two Photon Absorption 97
4.5.3 Non-linear Thresholds in Integrated Si Waveguides 98
4.6 Waveguide Coupling 99
4.6.1 Coupled-Mode Theory Between Two Waveguides 99
4.6.2 Evaluating the Coupling Coefficient 102
4.6.3 HIC Directional Coupler 102
4.6.4 Experimental Evidence of Waveguide Coupling 104
4.7 Substrate Leakage 106
4.7.1 Substrate Leakage in Silicon Waveguides 107
4.7.2 Experimental Evidence of Substrate Leakage 108
4.8 Mode-to-Mode Coupling 109
4.8.1 Experimental Evidence of Mode-to-Mode Coupling 111
4.9 Bend Loss 114
4.9.1 Bend Loss Theory 114
4.9.2 Experimental Identification of Bend Loss 115
4.9.3 Experimental Measurement of Bend Loss 117
4.10 Loss Mechanism Summary 118

5 Crystalline Silicon Waveguide Processing

5.1 Silicon on Insulator (SOI) Wafers 120
5.1.1 SOI Substrate Fabrication 120
5.1.2 Silicon Material Properties 121
5.2 Crystalline Silicon Waveguide 123
5.2.1 Fabrication 124
5.2.2 Experimental Results 124
5.2.3 Comparison of Experimental Results with Barwicz-Haus Theory 126
5.2.4 Comparison to Literature 128
5.3 Thermal Oxidation Smoothing 129
5.3.1 Oxidation Smoothing Kinetics 130
5.3.2 Experimental Details 131
5.3.3 Experimental Results 131
5.3.4 Oxidation Smoothing Simulation 133

5.3.5 Multiple Oxidation Smoothing Method 134
5.4 Wet Chemical Oxidation Smoothing 135
5.4.1 Wet Chemical Selection 135
5.4.2 Experimental Procedure 136
5.4.3 Comparative Results and Discussion 137
5.4.4 RCA Clean Iterations 140
5.4.5 Conclusions 141
5.5 Other Post-Etch Smoothing Techniques 141
5.5.1 Anisotropic Etch Smoothing 142

6 Deposited Waveguide Processing
6.1 Silicon Nitride (SiN) 146
6.1.1 Previous Work 146
6.1.2 Fabrication 147
6.1.3 Loss Results 148
6.1.4 Increased Wavelength Range Measurements 153
6.1.5 Waveguide Loss Results Comparison 154
6.2 Amorphous Silicon (a-Si) 155
6.2.1 Waveguide Fabrication 156
6.2.2 Initial Waveguide Results 157
6.2.3 Amorphous Silicon Deposition Variation Waveguide Results 159
6.2.4 Bulk Loss Measurement 161
6.3 Polycrystalline Silicon (poly-Si) 164
6.3.1 Previous Work 164
6.3.2 Waveguide Fabrication 165
6.3.3 Post-Etch Annealing 165
6.3.4 Slab Annealing 166

7 Waveguide Design for Low Loss
7.1 Geometric Techniques 170
7.1.1 Roughness-Limited Waveguides 170
7.1.2 Absorption-Limited Waveguides 174
7.2 Cladding Design 176
7.2.1 Roughness-Scattering Loss Reduction 176

7.2.2 Diffusion Barrier 179
7.2.3 Poly-Silicon Oxidation Smoothing 179
7.3 Crystalline Substrate Optimization 180
7.3.1 Anisotropic Etching and Smoothing 180
7.3.2 Substrate Optimization 181
7.3.3 Integration Issues 182

8 Ring Resonator Devices
8.1 Ring Resonator Basics 186
8.1.1 Resonance 187
8.1.2 The Quality Factor – Q 188
8.1.3 Coupled Mode Theory (in Time) of a Ring Resonator and a Single Bus Waveguide 188
8.1.4 Evaluating the Coupling Coefficient 193
8.1.5 Coupling Regimes 194
8.2 Ring Resonator Trimming 197
8.2.1 Thermal Trimming 197
8.2.2 Photo-Oxidation Trimming Using a Polysilane Cladding 198
8.2.3 Experimental Procedure 199
8.2.4 Modeling the Resonance Shift 200
8.2.5 UV-induced Index Change in PECVD Polysilane 201
8.2.6 Optical Characterization 201
8.2.7 Discussion of Trimming Results 203
8.3 Ring Resonator Modulators 207
8.3.1 Ring Modulator Operation 207
8.3.2 Modulation Speed 208
8.3.3 Extinction Ratio 209
8.3.4 Extinction Ratio Optimization 211
8.3.5 Modulator Material Considerations 212
8.3.6 CMOS Compatible Integrated Ring Resonators 213

9 Waveguide Integration
9.1 The EPIC Project 220
9.1.1 Device Operation 220

9.1.2 The Need for Low Loss Waveguides ... 221

9.2 CMOS-Compatible Process Challenges ... 222

9.2.1 Materials ... 223

9.2.2 Epitaxial Constraints ... 224

9.2.3 Thermal Budget Limitations ... 225

9.2.4 AS-EPIC Architecture ... 227

9.3 Waveguide Selection ... 228

9.3.1 Desired Characteristics ... 228

9.3.2 Bend Radius ... 229

9.3.3 Aspect Ratio ... 230

9.3.4 Evanescent Field Decay ... 230

9.3.5 Modal Area ... 232

9.4 Contributions of This Work to the AS-EPIC design ... 233

9.4.1 Waveguide Integration ... 234

9.4.2 Improved Filter Response ... 235

10 Conclusions and Future Work

10.1 Chapter by Chapter Review ... 238

10.2 Future Work ... 243

10.2.1 Silicon-on-Insulator (SOI) Based Waveguides ... 243

10.2.2 Deposited Waveguide Materials ... 244

10.2.3 Ring Resonator Devices ... 244

10.2.4 Integration ... 245

Appendix A – Fabry-Perot Loss ... 247

Appendix B – Snell's Law ... 251

References ... 255

Chapter 1 – Introduction

1.1 Motivation

Knowledge is a measure of civilization. Correspondingly, communication, or what may be regarded as knowledge transfer, reflects the growth of civilization. Since time began, communication technology has evolved in leaps and bounds with the introduction of disruptive technologies. The advent of our historical record is marked by the introduction of written communication which supplanted oral record keeping. The ability to accurately record data with written language facilitated the access to ideas and facts whereby knowledge could be built upon. The invention of the printing press by Johan Gutenburg in the 1450s was another disruptive technology that further enabled economic and large-scale storage and distribution of information in the form of books. In the 19th century, the invention of the telegraph paved the way for real-time communication by using an electric signal to impart a binary data stream of information. In the 20th century, this revolutionary electronic communication paradigm was improved with newer technologies to realize data rates sufficient for voice, radio, television, and internet applications.

1.1.1 Communication

The use of electronic communication has facilitated the ability to quantify the information capacity of communication in terms of binary data rates measured in bits per second. For a majority of the 20th century, the improvement rate or learning curve, as measured by the exponential rate increase of the information capacity versus time (see Figure 1.1), has remained constant. That is until the introduction of optical fiber systems, another disruptive technology, which shifted the information capacity improvement rate and is ultimately responsible for the high information capacity applications our communication relies upon today. The use of ultra-low loss (< 0.1 dB/km) optical fibers with compatible lasers, both developed in the 1960s, ushered in a new learning curve and pushed the information capacity capabilities of communication to record levels. More recently, the application of wave division multiplexing (WDM) technology increased these bandwidths by utilizing multiple data streams on the same fiber.

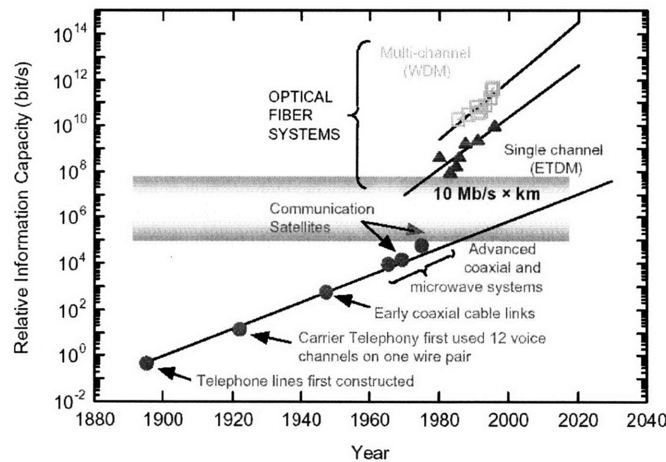

Figure 1.1: Communication data rates versus time [1]

The shift towards photonic technologies has also improved the distance of communication. Electronic technologies, like all technologies, exhibit a tradeoff between data rate and distance of communication. Hence, the product of bandwidth and distance, for a given communication technology, represents a more relevant figure of merit for communication technologies than data rate alone. It turns out that the resistance and capacitance bandwidth-distance limitations in electronic connections are much greater than that of dispersion in photonic connections. This deficiency in electronic connections has manifested itself as a technology crossover point where optical communication is preferred for technologies with a bandwidth x distance product that exceeds 10 Mb/s•km [1]. This figure is significant in that it represents an electronic-photonic technology cross-over for communication applications. When extended to computers, where the length scale of interconnects is on the order of a meter, this metric implies a shift to optical interconnects will be required to uphold efficient data communication as processor speeds approach 10 GHz.

1.1.2 Computation

High speed communication is only relevant when the transmitted information can be processed or computed in a proficient manner. Gene Amdahl, an early American computer architect, coined a rule of thumb which states that one byte per second of input/output (data communication) is required for each instruction per second supported by a computer (data computation) [4]. In other words, an efficient computer, whether it is a person, a machine, or society as a collective, is one that communicates as fast as it processes the data. Fortunately, the improvements in high speed communication have also been closely followed by improvements in data processing. The invention of the transistor in 1947, followed by the development of the electronic integrated circuit in the 1950s, set the stage for the microelectronics

revolution. The integration of individual electronic components onto a single platform via parallel fabrication techniques enabled unrealized and scalable data processing functionality.

Monolithic integration of electronic circuits with scalable fabrication technologies has been largely responsible for the incredible performance gains in computation. First and foremost, shrinking dimensions of the various components, such as transistors, increases the overall performance (speed) of the electronic circuit. Secondly, in comparison to discrete components, integrated circuits utilize less power, occupy less volume, and weigh less. Thirdly, the wafer real estate saved by shrinking the circuit allows more chips per wafer, lowering individual chip cost and increasing fabricated chip output volume and yield. These performance and economic incentives have led to the rapid development and improvement of many data processing technologies such as: calculators, radios, radar, telephones, and televisions to name a few. Furthermore, the development of standardized Silicon (Si) wafers and thin-film process technologies, such as the dominant complementary metal oxide semiconductor (CMOS) technology used in our computer processors, has truly elevated the benefits of integrated circuits to a new level. Yesterday's supercomputers are today's personal computers. For example, the cutting edge microprocessor in 1970 had 20,000 transistors and operated at 100 kHz, whereas today it has nearly 1,000,000,000 transistors and operates at greater than three GHz. As shown in Figure 1.2, the pace of microprocessor improvement over this time period, as measured by clock speed, has increased at a steady exponential rate, a phenomenon often referred to as Moore's Law [2].

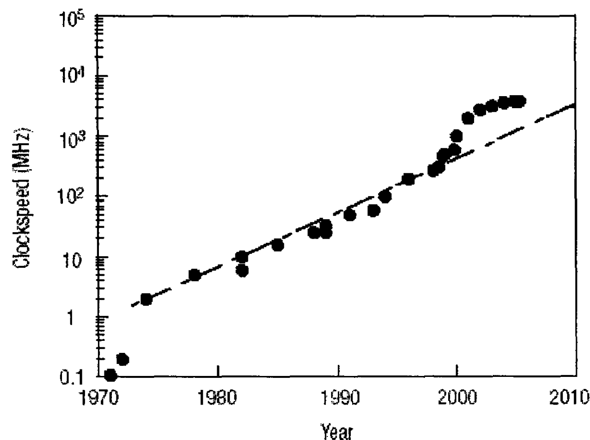

Figure 1.2 – Microprocessor clock speeds versus time [3].

1.1.3 The Limitations of Electronic Interconnects

Over the past thirty years, clock speed increases have accounted for a majority of the performance gains in microprocessors. However within the last couple of years, as observed in Figure 1.2, clock speed scaling has stalled, due to fundamental physical barriers associated with electronic interconnects, resulting

in a clock speed ceiling of a few GHz. The two major causes of this limitation are power consumption and electromagnetic interference.

Power consumption is problematic both practically, where excessive power consumption limits usage and application of the chip, and in terms of heat which is detrimental to chip performance and lifetime. Put simply, as chip geometries shrink and clock frequencies rise, the transistor leakage current increases; summing this leakage over an ever increasing transistor count results in a substantial waste of power that is ultimately dissipated as heat. While this problem has always been known, and thought to be a design issue, the detrimental effects have recently made an impact. In 2004, Intel shelved its plan to introduce a 4 GHz processor, the next iteration of the then current Pentium 4, with excessive power consumption cited as the cause [6]. Moreover, the excessive heat produced from Apple's G5 processors has required water cooling and precluded its use in laptops [7]. These events have led to the recently coined "performance per watt" metric in evaluating a microprocessor.

The continued drive towards smaller circuit elements and dense chip architectures has also led to electromagnetic interference in the form of resistive-capacitance (RC) delays that limit both intra- and extra-chip communication. This RC delay is the cause of the so-called interconnect bottleneck and restricts the maximum frequency of operation for an electronic circuit. As seen in figure 1.3, the intra-chip delay – defined as the combined gate and interconnect delay – is increasing with each chip generation. Even with the switch to lower resistance copper interconnects, the interconnect delay dominates the intra-chip delay (chip makers are presently using 90nm processes) and limits the potential computing performance of current and future microprocessors.

Likewise, extra-chip communication (i.e. chip-to-chip or board-to-board communication) is RC-limited to a few GHz. The combination of relatively long interconnect lengths (10 – 100 cm) with increasingly higher data rates is approaching the historic 10 Mb/s•km bandwidth x distance product communication limitation of electronic interconnect materials. As it stands, the memory to processor communication (arguably the limiting speed of computation) is nearly an order of magnitude slower than on-chip communication. This discrepancy between data communication and data processing is inefficient and reduces the advantages gained by high clock speeds.

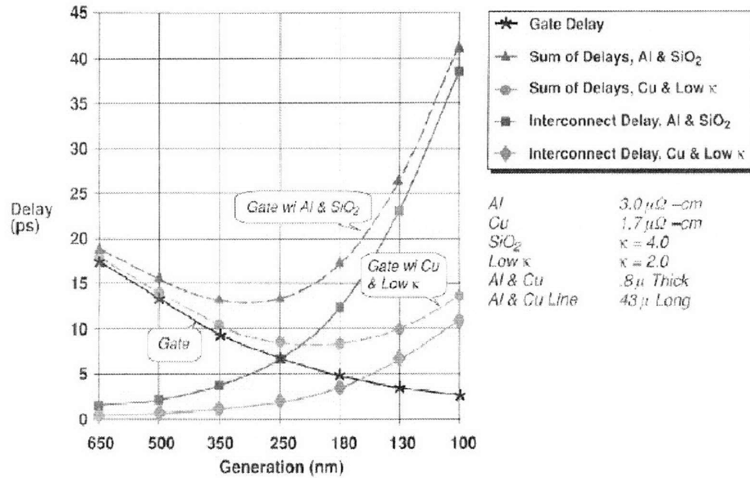

Figure 1.3 – Gate and Interconnect Delay versus Chip Generation [12].

As a result of the limitations in clock speed scaling, chip manufactures will have to increase computing performance by parallelism. This is echoed with the recent interest in and development of multiple-core chips where data is processed in parallel at lower clock frequencies, rather than serially at high clock frequencies in a single-core chip. Intel has plans to offer dual-core in 2006 and quad-core chips by 2007 [8] with long term plans of hundreds of cores on a single chip [5]. Another performance enhancing technique is to increase the cache size (on-chip memory) thereby limiting the reliance on slow, off-chip memory communication. The "Cell" processor developed by IBM, Toshiba, and Sony for the upcoming Playstation 3 is a drastic redesign in chip architecture that uses both multi-core and large on-chip cache to provide a power-efficient, high-performance processor [9]. While these approaches will improve computation bandwidths, there still remains the problem of high speed communication between the cores and off the chip.

1.1.4 The benefits of integrated photonics

As a collective, our information technologies have the potential to supply the bandwidth requirements for future communication and computation applications. Practically though, integration of these technologies is difficult. As it stands, our best computation technologies are electronics-based, whereas our best communication technologies are photonics-based. On the computation side, the continual shrinkage of integrated electronic circuits with standardized Si-compatible processes has yielded high-performance, low-cost chips that are communication limited due to the fundamental physics of dense electronic interconnects. On the communication side, the development of fiber optics and corresponding III-V semiconductor lasers, modulators, and detectors has enabled incredible communication bandwidths; but the components are large, discrete, expensive, and have minimal computation abilities. Ideally, we could take the best from both worlds and seamlessly integrate electronic and photonic components onto a single

platform, where data would be processed with high-performance, low-cost microelectronics, but transported with high bandwidth optical interconnects; thereby enabling *improved communication* – this is the promise and motivation for integrated photonics.

The prospects for integrated photonic circuits are immense. Photonic interconnects offer high data-transportation bandwidths with low signal attenuation and virtually zero heat dissipation; and therefore excel where electronic interconnects are limited. Strategic replacement of speed-limited electronic interconnects, such as off-chip memory input/output bus or board-to-board connections in cluster computers, with photonic interconnects will dramatically improve data processing performance. Similarly, the shift towards multi-core architectures will also necessitate photonic interconnects as high-speed, cross-chip interconnects are implicit in this technology. Another advantageous application of photonic interconnects is in the clock signal distribution system, where reduced jitter, skew, delay, crosstalk and power consumption will all benefit microprocessor performance.

Integration of photonic circuits onto electronic chips will also enable networking technologies that have higher complexity and unique functionality. Similar to electronics, an integrated photonic circuit benefits from lower cost, higher reliability, and increased functionality in comparison to linking discrete components. These attributes will undoubtedly benefit and enable network router and transceiver technologies, which are currently comprised of multiple discrete photonic components, by increasing performance and ultimately driving down the cost.

The added integration benefits of reduced weight, volume, and power consumption also enable technologies where these savings are crucial. The Department of Defense currently funds several electronic photonic integrated chip (EPIC) research projects that focus on realizing this prospect [11]. One such project, the subject of Chapter 9, is to build an EPIC that acts as a broadband radio frequency (RF) channelizer, or what may be thought of as a fast fourier transform (FFT) chip. The goal is to replace a filing cabinet of electronic components with a single chip: a feat that can only be realized by the unique properties of integrated photonics.

In summary, the bandwidth-distance limitation of electronic interconnects has led to a bottleneck in our ability to transport data as fast as it can be processed. The implementation of integrated photonic interconnects holds the promise of bridging microelectronics-based computation technologies with photonics-based communication technologies, thereby eliminating this bottleneck. Ultimately, the unique and cost-effective data processing abilities that accompany integration of photonic circuits with conventional microelectronic circuits will enable the realization of superior communication and computation technologies.

1.2 Integrated Photonic Circuits

1.2.1 Photonic Components

As a technology, a complete integrated photonic circuit has yet to be realized in any materials platform. The tradeoffs and constraints for each material platform are unique and many times unknown. To further understand these integration issues, it is important to appreciate the necessary components and accompanying functions of an integrated photonic circuit. These components include:

- Light source(s) – A device that emits light, preferably a tunable laser or several single wavelength lasers.
- Couplers – Devices that efficiently transfer power between small on chip waveguides and optical fibers
- Waveguides – Devices that can route and evenly split optical signals with low attenuation.
- Filters – Devices that can separate an optical signal as a function of its wavelength or in the time domain. High fidelity and tunability are desirable attributes for these filters.
- Switches – Devices that can change the optical signal path, typically from one waveguide to another waveguide.
- Modulators – Devices which facilitate electrical-to-optical signal conversion.
- Detectors – Devices which facilitate optical-to-electrical signal conversion.

When integrated, these components contain all the rudimentary functions necessary to realize a photonic circuit: create light, guide it, perform a signal operation, and detect it.

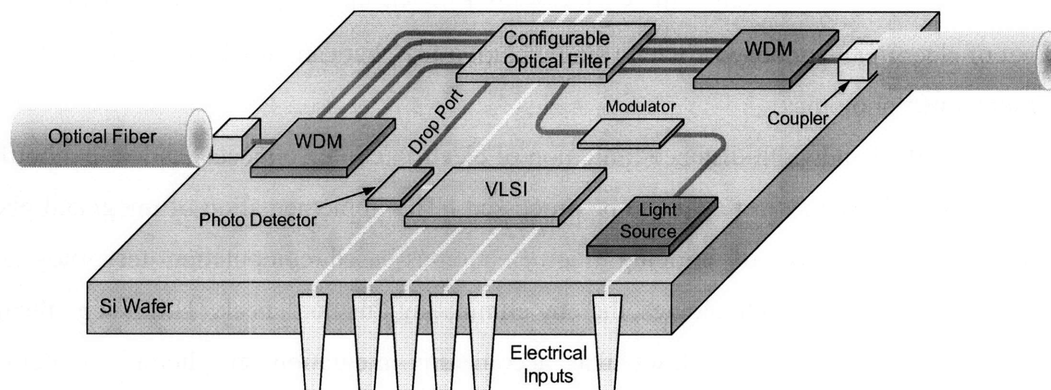

Figure 1.4: Layout of an integrated photonic circuit.

Figure 1.4 depicts a generalized example of an integrated electronic/photonic circuit. In this layout, light enters the chip from the left optical fiber, where it is coupled with a mode converter (coupler)

for efficient power transfer to the on-chip waveguide. The signal then enters a wave division multiplexing (WDM) module, where a set of wavelength filters sort the optical signal as a function of wavelength into four output waveguides. The filtered signals then enter a configurable optical filter, where a variety of optical signal processing can occur. In this example, an optical add/drop module is chosen. Light from an input channel (one of the four wavelengths in our example) is "dropped" and switched to a drop port where it is guided into a photodetector and converted into an electrical signal. The spectral channel vacancy created from this dropped channel can be "added" to with another input. In this example, an on-chip light source in conjunction with a modulator is used to create the input channel. The ability to selectively configure this filter, process the detected drop signal, and modulate the input signal requires integrated electronic data processing and is depicted with the very large scale integration (VLSI) microprocessor component with accompanying electrical connections to the photonic components. Post-filter, the four photonic signal channels are recombined into a single waveguide and coupled off-chip to the optical fiber on the right. The depicted example is closer in layout to a network transceiver than a microprocessor, but the general principles remain the same: data is transmitted optically, converted to electrical signals where the data is computed with microelectronics, and then reconverted to optical signals for further communication. In this way, the electronic bottleneck is alleviated for improved data computation and communication.

1.2.2 Material Platform Considerations

In deciding the material platform – the materials, process flow, and fabrication technologies – it is important to take into account the desired characteristics of an integrated photonic circuit. As with most technologies, cost and assimilation with existing technologies are imperative for product adoption. The desired characteristics for integrated photonic circuits are:

- Low Insertion Loss – Optical power attenuation is problematic in that it reduces photonic device functionality. Therefore, light propagation and coupling in optically transparent materials with high quality interfaces will be needed for an optimized integrated photonic circuit.
- Polarization Independence – Light in optical fibers networks typically travel in a mixed polarization. Interfacing these networks with integrated photonic components that exhibit birefringence or polarization dependent loss (PDL) will require methods of compensation.
- High In-Plane Integration Density – A higher concentration of photonic devices will increase circuit complexity and enhance functionality. Increased circuit density also has the economic benefit of allowing more chips per wafer. A high index of refraction difference between waveguide core and cladding materials will be necessary to realize this.

- Multiple Level Integration – The ability to guide light through multiple chip levels is an effective increase of chip real estate which will increase circuit density, complexity, and enhance functionality. Increased circuit density also has the economic benefit of allowing more chips per wafer. Epitaxy and stress constraints will need to be considered in realizing multiple photonic layers.
- Low-Cost, High-Volume Assembly Methods – Economic viability is essential to the realization of integrated photonic technology.
- Compatibility with Electronic Data Processing Components – Electronic components will be necessary to control active photonic devices and perform "intelligent" data processing. Material and size constraints will need to be addressed.
- Optical-to-Electrical and Electrical-to-Optical Signal Conversion – Seamless and high speed signal conversion between electronic and photonic circuits is necessary to realize the high bandwidth benefit of photonic interconnects.

The ability to meet these desired characteristics hinges on the feasibility of integrating the various photonic components into a cohesive material platform. As with most complex problems, there exist many tradeoffs in reaching the goal of an integrated electronic/photonic chip. Many of the tradeoffs are due to material compatibility issues – reactivity, stress, inter-diffusion; and processing compatibility issues – epitaxy, thermal budget, and contamination.

For example, the ability to guide and detect light requires the material and processing compatibility of an optically transparent waveguide material with an absorptive detector material that efficiently transforms photons into electrons. Within this constraint lies an epitaxy requirement in that the semiconductor detector material must be lattice-matched to the substrate (for good electrical properties). If amorphous materials, which do not have epitaxy constraints, are used as waveguiding layers (which is probable for integrated photonic waveguides), the detector placement will be limited to chip levels below the amorphous waveguides – restricting photonic component layout.

Another constraint lies with the need for high in-plane photonic device density, which requires waveguide core and cladding materials with a large index of refraction difference – limiting material selection. Yet another constraint is the melting temperatures of the various photonic and electronic materials. The lowest melting point material depositions and anneals will have to occur at the end of the process flow order – limiting process order. Perhaps most importantly, photonic and electronic circuit materials must be compatible with low-cost, high-volume processing methods. This constraint is imperative for product adoption in the marketplace. In combination, the material and processing

constraints associated with a chosen material platform represent a majority of the hurdles in realizing an integrated electronic/photonic chip.

To be practical and economic, the selection of a material platform really boils down to two options: 1) build electronic circuits on an existing photonic circuit materials platform, or 2) build photonic circuits on an existing electronic circuit materials platform. Option one has the problem in that an existing integrated photonic circuit material platform does not exist, at least in totality. However, if one were to choose, it would have to be the III-V material platform that has been extensively used for electronic and photonic components in the telecommunications industry. III-V materials possess an arguably superior set of photonic (direct bandgap, quantum well growth) and electronic (high carrier mobility, well suited bandgap) material properties. Integration of lattice-matched, quaternary III-V semiconductor alloys on InP substrates has yielded light emitter, detector, and electro-absorption modulator devices that have driven optical network bandwidths to world record levels. However, the major detriment of utilizing the III-V material platform is cost. In comparison to Si–based CMOS wafer processing, III-V wafer processing does not have the market volume to realize the cost benefits that accompany the necessary economy of scale [1]. In the end, the development of potentially superior III-V integrated photonic technologies and products will hinge on whether or not a cheaper alternative exists. In all likelihood, III-V integrated photonic devices will exist for high performance photonic applications, where alternatives do not exist.

The second and more practical option is to build an integrated photonic circuit that is compatible with the popular Si-based CMOS process and materials platform used in a majority of microprocessors. The ability to fabricate high performance integrated photonic circuits with the high-volume and low-cost of CMOS fabrication technology enables integration of complex electronic and photonic circuits on a single Si chip, eliminates the need for the multiple material platforms currently used where electronic and photonic applications coincide, and provides a seamless interface between photonic and electronic devices – these are the advantages of silicon photonics. The challenge is to realize all the necessary components for an integrable photonic circuit within this material platform.

1.2.3 Silicon Photonics

Silicon photonics is the use of CMOS compatible material and processing technology in the fabrication of photonic devices. The field of integrated silicon photonics, also known as nano/microphotonics, is a subset of the field of silicon photonics, in which compact, high optical confinement photonic components and circuits, with feature sizes that range from tens of nanometers to several microns, are researched and developed for intended use in dense photonic circuit applications such as an electronic/photonic integrated chip.

As an optical material, Si – the workhorse material of the Microelectronics industry, has the detriment of having an indirect band gap, which precludes its use as a light source by traditional methods. Despite this setback, Si benefits from extensive processing knowledge, an electrically superior quality insulating/amorphous oxide, a high index of refraction difference ($\Delta n=2$) with its oxide (critical for high device density), and transparency in the telecommunications spectrum ($\lambda=1470$-1620 nm). Similarly, SiO_2 (the material used in fiber optics), SiON, and Si_3N_4 exhibit excellent optical properties and benefit from compatibility with and the extensive knowledge base of Si processing. Finally, the use of Ge, with its high carrier mobility and absorption in the telecom spectrum, provides an optimal material for photo-detection.

Over the past decade, a near-complete set of CMOS compatible integrable nanophotonic devices have been demonstrated: silicon based optical waveguides with low losses and small curvature radii [13], splitters [14], tunable optical filters [15], fast optical modulators [16], and fast integrated Ge photodetectors [17]. The only missing component is a light source, however research in this area is promising [18], and off-chip light sources offer an adequate substitute. At present, research is focused on integrating silicon nanophotonic components to demonstrate photonic circuit functionality. However, the material and processing constraints associated with fabrication of CMOS compatible, high-index-contrast, planar, thin-film photonic devices add difficulty in realizing a high performance photonic circuit. Ultimately, these constraints lead to optical loss mechanisms which limit photonic device functionality and hamper integrated circuit performance.

1.3 Thesis Work

In an effort to address the deficiencies in integrated silicon nanophotonics, this thesis focuses on diagnosing and addressing the various loss mechanisms that exist in fabricating CMOS compatible photonic circuits. We start by exploring the prerequisites for understanding and measuring waveguide loss, along with methods with which to identify the various fundamental photonic loss mechanisms. As the building block of nearly all higher order photonic devices (filters, splitters, modulators, detectors), waveguides are an essential diagnostic tool with which to characterize fundamental photonic loss mechanisms. From there, we report methods with which loss can be reduced in integrated silicon photonic devices by 1) researching and optimizing the processing of high index core materials: silicon (amorphous, crystalline, and polycrystalline) and silicon nitride; 2) developing waveguide design techniques to optimize optical signal transmission; and 3) devising CMOS compatible process techniques to improve nanophotonic device performance. Finally, we explore the tradeoffs involved in the monolithic integration of electronic and photonic circuits in the CMOS materials platform as well as in some higher order photonic devices. The ultimate goal of this work is to enable monolithic integration of

complex and high performance photonic and electronic devices that exhibit unique and superior data processing and communication performance.

Chapter 2 – Waveguide Theory

Fabrication and design of functional waveguides requires an understanding of electromagnetic radiation propagation through a waveguiding structure. In this chapter, the relevant physics and calculation methods needed for determining an accurate view of the interactions of light and matter in a waveguide are reviewed.

2.1 Maxwell's Equations

Maxwell's equations represent first principle interactions of electric and magnetic fields.

$$\nabla \cdot \vec{D} = \rho \tag{2.1}$$

$$\nabla \cdot \vec{B} = 0 \tag{2.2}$$

$$\nabla \times \vec{E} = -\frac{\partial \vec{B}}{\partial t} \tag{2.3}$$

$$\nabla \times \vec{H} = \frac{\partial \vec{D}}{\partial t} + \vec{J} \tag{2.4}$$

Here ρ is the charge density, J is the current density, E is the electric field, B is the magnetic induction, D is the electric displacement field, and H the auxiliary field (often referred to as the applied magnetic field). In terms of experimentation, E and H are quoted, as they are what are varied. Conveniently, we can express Maxell's equations in terms of the E and H fields, for linear and homogeneous materials, using the relations

$$\vec{D} = \varepsilon \vec{E} = \varepsilon_0 \left(1 + \chi_e\right) \vec{E} \tag{2.5}$$

$$\vec{B} = \mu \vec{H} = \mu_0 \left(1 + \chi_m\right) \vec{H} \tag{2.6}$$

where ε is the electric permittivity of the medium, ε_0 is the permittivity of free space, χ_e is the electric susceptibility, μ is the magnetic permeability of the medium, μ_0 is the permeability of free space, and χ_m is the magnetic susceptibility. Maxwell's equations become:

$$\nabla \cdot \varepsilon \vec{E} = \rho \tag{2.7}$$

$$\nabla \cdot \mu \vec{H} = 0 \tag{2.8}$$

$$\nabla \times \vec{E} = -\mu \frac{\partial \vec{H}}{\partial t} \tag{2.9}$$

$$\nabla \times \vec{H} = \varepsilon \frac{\partial \vec{E}}{\partial t} + \vec{J} \quad (2.10)$$

In optics, we can restrict ourselves to a source-free medium ($\rho=0$ and $J=0$) for most applications. With these simplifications, we can construct a wave equation by taking the curl of (2.9). Using the vector identity $\nabla \times \left(\nabla \times \vec{A}\right) = \nabla\left(\nabla \cdot \vec{A}\right) - \nabla^2 \vec{A}$, we obtain the Helmholtz wave equation for E:

$$\nabla^2 \vec{E} - \mu\varepsilon \frac{\partial^2 \vec{E}}{\partial t^2} = 0 \quad (2.11)$$

A similar equation holds for H.

The index of refraction is defined as:

$$n = \sqrt{\frac{\mu\varepsilon}{\mu_0 \varepsilon_0}} \quad (2.12)$$

The index of refraction of free space is unity (i.e. $\varepsilon=\varepsilon_0$ and $\mu=\mu_0$). For a medium, the index of refraction describes the degree to which the medium polarizes in the presence of the electric and magnetic fields. The extent of this polarization is a function of the frequency (ω). In general, the permittivity and permeability of a material are functions of ω, $\varepsilon=\varepsilon(\omega)$ and $\mu=\mu(\omega)$. Thus $n = n(\omega)$, indicates that the material is dispersive.

At optical frequencies (high ω), magnetic dipoles simply can not oscillate as fast as the magnetic field frequency, resulting in $\mu \rightarrow \mu_0$. This simplifies (2.12) to $n = \sqrt{\frac{\varepsilon}{\varepsilon_0}}$.

2.2 Plane Waves

Solutions to the wave equation can be obtained if we consider time harmonic functions of the electric and magnetic fields ($\vec{E} = E(\vec{r})e^{i\omega t}$ and $\vec{H} = H(\vec{r})e^{i\omega t}$), yielding a more tractable form of (2.11):

$$\nabla^2 \vec{E} - \omega^2 \mu\varepsilon \vec{E} = 0 \quad (2.13)$$

Plane wave solutions of the Helmholtz wave equation can be found for E and H by assuming a spatial dependence in both forwards and backwards propagation (corresponding to the – and + signs of the exponential) in the direction of k, the wave vector.

$$\vec{E}(\vec{r}) = \vec{E}_0 e^{\pm i\vec{k}\cdot\vec{r}} \tag{2.14}$$

$$\vec{H}(\vec{r}) = \vec{H}_0 e^{\pm i\vec{k}\cdot\vec{r}} \tag{2.15}$$

The magnitude of the k is equal to $2\pi/\lambda$, where λ is the wavelength of the light in a medium. Reinserting the wave equation solution (2.14) into the wave equation (2.13) allows us to realize the dispersion relation for a plane wave.

$$k^2 = \omega^2 \mu\varepsilon \tag{2.16}$$

For optical materials we observe that the magnitude of the wave vector in a medium is a factor of n greater than k_0, the wave vector in free space.

$$k = \sqrt{\omega^2 \mu\varepsilon} = \sqrt{\frac{\mu\varepsilon}{\mu_0\varepsilon_0}} k_0 = nk_0 \tag{2.17}$$

Thus the wavelength of light in a material is reduced from its free space wavelength λ_0 by a factor of n.

$$\lambda = \frac{\lambda_0}{n} \tag{2.18}$$

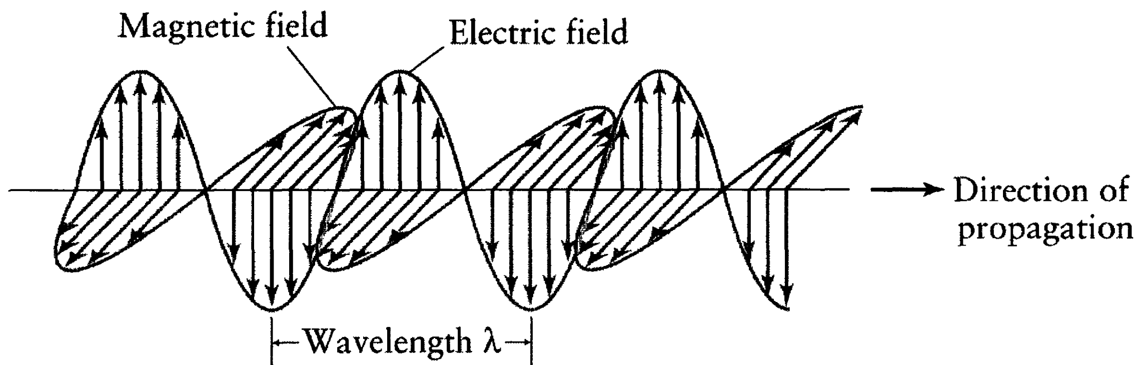

Figure 2.1 – Artist rendering of an electromagnetic wave [19]

Electromagnetic plane waves are categorized as transverse waves because the oscillation energy, in the form of electric and magnetic fields, is orthogonal to the propagation direction (figure 2.1); in other words, E and H oscillate orthogonal to k. This orthogonality relationship is demonstrated, in a source free medium, by first plugging a forward propagating wave into equation 2.7,

$$\nabla \cdot \vec{E} = -i\vec{k} \cdot \vec{E} = 0 \tag{2.19}$$

confirming that k and E are orthogonal. In a similar manner, H can be related to E and k using 2.1.9:

$$\vec{H} = \frac{i}{\omega\mu} \nabla \times \vec{E} = \frac{i}{\omega\mu}\left(-i\vec{k} \times \vec{E}\right) = \sqrt{\frac{\varepsilon}{\mu}}\, \hat{k} \times \vec{E} \tag{2.20}$$

where $\hat{k}$ is a unit vector in the propagation direction. We find that the magnetic field is orthogonal to both the electric field and the propagation vector such that $\vec{E} \times \vec{H}$ is the propagation direction. The magnitude of H differs from E by a factor of $\sqrt{\varepsilon / \mu}$, which is known as the inverse of the characteristic impedance of the medium.

The power of a given electromagnetic wave can be determined by the pointing theorem. At optical frequencies, it is only possible to measure the time averaged power of the wave. Hence, it is convenient to know the time averaged power flux:

$$\langle P \rangle = \left\langle \vec{E}(t) \times \vec{H}(t)^* \right\rangle = \tfrac{1}{2}\sqrt{\tfrac{\varepsilon}{\mu}} \left|\vec{E}\right|^2 \hat{k} \tag{2.21}$$

2.3 Phase and Group Velocity

The phase velocity of light is defined as the velocity of a plane of constant phase. For a plane wave, this velocity is defined as:

$$v_p \equiv \frac{\omega}{k} = \frac{1}{\sqrt{\mu\varepsilon}} = \frac{c}{n} \tag{2.22}$$

In free space ($\varepsilon=\varepsilon_0$, $\mu=\mu_0$, $n=1$), this velocity corresponds to the speed of light and is denoted as c. In a medium, electromagnetic waves travel at a velocity less than c by a factor of n, the refractive index of the medium.

However, because waves of different frequency move at different velocities in dispersive mediums $n=n(\omega)$, the phase velocity relation is not always useful; even lasers have finite spectral line widths that exhibit dispersion. Instead, the aggregate velocity of a set of frequencies, known as the group velocity is desired. The group velocity of a 'wave packet' is defined as:

$$v_g \equiv \frac{d\omega}{dk} = \frac{1}{\frac{d(\frac{\omega n}{c})}{d\omega}} = \frac{1}{\frac{n}{c}+\frac{\omega}{c}\frac{dn}{d\omega}} = \frac{c}{n-\lambda\frac{dn}{d\lambda}} = \frac{c}{n_g} \tag{2.23}$$

where n_g is the group index. If a material does not exhibit dispersion, $\frac{dn}{d\lambda} = 0$ then we observe that $v_g = v_p$, as one might expect.

2.4 Polarization

The polarization direction is defined as the direction of the electric field (E); however the nomenclature as to the type of polarization is dependent on the frame of reference. Polarization can be broken down into two categories: linear and circular. Circular polarizations arise when the plane, comprised of the E and H fields, rotate as the wave propagates and are denoted as being either right handed or left handed elliptical states. In contrast, linear polarizations do not rotate and are denoted as being vertical, horizontal, or a mix of the two. It is easy to get confused when discussing polarization as it is a relative concept to a frame of reference.

The Poincaré sphere (Figure 2.3) is a graphical tool that allows convenient description of polarized signals and of polarization transformations that may occur within optical devices. Any state of polarization can be uniquely represented by a point on the sphere. Orthogonal polarizations that form the basis of polarization are diametrically opposite on the sphere. A change in polarization state can be represented as a continuous path on the sphere.

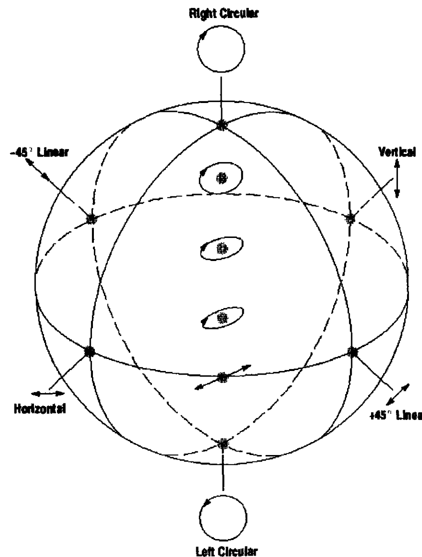

Figure 2.3 – Poincaré Sphere [20]

Waveguides with rectilinear cross-sections do not support circularly polarized modes, unlike radially symmetric fiber optics, and are consequently restricted to linearly polarized modes. Thus the possible polarization states on the Poincaré sphere are confined to the equatorial plane for rectilinear waveguides. Depending on convention, the linear polarization horizontal and vertical states are often referred to as trans-electric (TE) and trans-magnetic (TM) polarizations. Within this thesis, the TE/TM frame of reference will be with regard to the direction of E relative to the substrate in a given waveguide cross-section. A waveguide mode with the electric field parallel to the substrate will be regarded as TE and orthogonal as TM. Figure 2.4 depicts this polarization nomenclature. To be rigorous, the polarization of light in a waveguide is not strictly TE or TM, but rather a majority of one with the balance of the other. Strictly speaking, we will refer to these "TE-like" modes and "TM-like" modes as TE and TM.

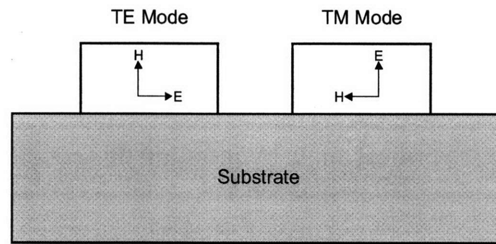

Figure 2.4 – Frame of reference used for describing the polarization of light in a waveguide cross-section.

2.5 Interface Boundary Conditions

In optics, an interface is defined as the boundary between media with differing refractive indices. The reflection and transmission of light at an interface is governed by conservation of the wave vector and boundary conditions for E and H. Perpendicular to the interface D and B are conserved:

$$\varepsilon_1 E_{1\perp} = \varepsilon_2 E_{2\perp} \qquad \mu_1 H_{1\perp} = \mu_2 H_{2\perp} \tag{2.24}$$

where 1 and 2 indicate the two interfacing media. Parallel to the interface E and H fields are conserved.

$$\vec{E}_{1\parallel} = \vec{E}_{2\parallel} \qquad \vec{H}_{1\parallel} = \vec{H}_{2\parallel} \tag{2.25}$$

It is because of these boundary conditions that interaction of light on an interface is polarization dependent. At optical frequencies $\mu = \mu_0$ which results in an asymmetry of the field distributions for the TE and TM polarizations.

The angular dependence of reflected and transmitted light at an interface, or what is known as refraction, is governed by the conservation of momentum of the wave vector (see appendix B). Conserving the wave vector allows one to assume that the angle of incidence is equal to the angle of reflection ($\theta_I = \theta_R$) at an interface. It also allows one to derive Snell's law:

$$n_1 \sin(\theta_1) = n_2 \sin(\theta_2) \tag{2.26}$$

which describes the angular trajectory of light as it passes through an interface, where the subscripts represent the two media that form the interface and angle θ_i is with respect to the interface normal for medium i.

The phenomenon of total internal reflection, the basis of guiding light in a waveguide, arises out of Snell's law when $n_1 > n_2$. For light incident at angles greater than a critical angle θ_c, the transmission component becomes imaginary and all light is reflected at the interface. This phenomenon occurs when θ_2 exceeds $\frac{\pi}{2}$, allowing us to define the critical angle by inserting this condition into (2.31):

$$\theta_c = \sin^{-1}\left(\frac{n_2}{n_1}\right) \tag{2.27}$$

2.6 Dielectric Waveguides

Dielectric waveguides operate on the principle of total internal reflection and are comprised of two components: a core and a cladding. The higher index core material acts as the guiding medium, which facilitates internal reflection with the surrounding cladding material. Unlike metallic waveguides, the boundary conditions for dielectric waveguides do not limit light to the core only, as a substantial fraction of power is evanescently guided in the cladding and referred to as the evanescent field. In this section we briefly review the analytical solutions to the symmetric dielectric slab waveguide, which is illustrative in understanding the characteristics of light in a guided structure. Methods of extending these solutions to other waveguide geometries will also be discussed. From here in out, the term waveguide will be synonymous with dielectric waveguide.

2.6.1 Slab Waveguide

The simplest form of waveguiding occurs when a slab of high index material is surrounded by lower index material(s). More detailed explanations of waveguiding theory can be found in textbooks [21-23]. In this case, we will examine the symmetric slab waveguide where the cladding materials have identical indices. As seen in figure 2.6, a slab of material of thickness 2d and $n=n_1$, is clad with a material with

$n = n_2$, such that $n_1 > n_2$. The width of this structure as well as the thickness of the cladding layers are regarded as infinite for this analysis.

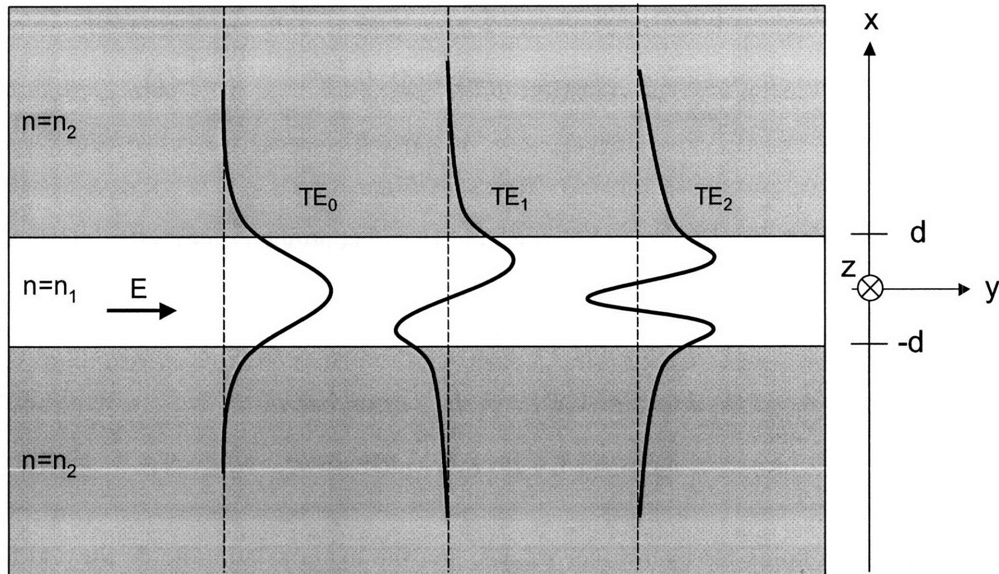

Figure 2.6 – Symmetric slab waveguide with the first three TE mode field distributions

Superimposed on the slab waveguide in Figure 2.6 are schematics of the field distributions that correspond to the first three modes. These modes represent eigenvalue solutions to the wave equation and are indexed by the order of the mode. For example TE_m is the mth order mode. The guided light propagates in the z direction and is TE polarized. Consequently, the E-field distribution in this slab only has components in the y-direction and solutions have the form:

$$E_y(x) \quad \begin{cases} E_0 \cos(\phi) e^{\gamma_x (x+d)} e^{-i\beta z} & (x \le -d) \\ E_0 \cos(k_x (x+d) - \phi) e^{-i\beta z} & (-d \le x \le d) \\ E_0 \cos(\phi + m\pi) e^{-\gamma_x (x-d)} e^{-i\beta z} & (x \ge d) \end{cases} \tag{2.28}$$

Here a standing wave solution of order m and period k_x is used in the waveguide core with amplitude E_0 and propagation constant β. Outside the core, the field exponentially decreases with a decay coefficient of γ_x. The phase shift ϕ of the standing mode solution is slab thickness and mode dependent. From the orthogonality relation found in (2.19), we can find the H-field distribution as well:

$$
H_z(x) \begin{cases} \frac{i}{\omega\mu}\gamma_x E_0 \cos(\phi) e^{\gamma_x(x+d)} e^{-i\beta z} & (x \le -d) \\ \frac{-i}{\omega\mu} k_x E_0 \sin(k_x(x+d)-\phi) e^{-i\beta z} & (-d \le x \le d) \\ \frac{i}{\omega\mu}\gamma_x E_0 \cos(\phi + m\pi) e^{-\gamma_x(x-d)} e^{-i\beta z} & (x \ge d) \end{cases} \tag{2.29}
$$

Now if we assume boundary conditions such that E_y and H_x are continuous across the interfaces at x=d and x=-d, which is valid given (2.24) and (2.25) and assuming that $\mu=\mu_0$, it can be shown that:

$$
\begin{aligned} k_x d \tan(k_x d) &= \gamma_x d \qquad m = even \\ -k_x d \cot(k_x d) &= \gamma_x d \qquad m = odd \end{aligned} \tag{2.30}
$$

where the upper relation holds for even order modes, and the lower relation holds for odd order modes. Additionally, from conservation of the wavevector, it can be shown:

$$
\gamma_x = \sqrt{\beta^2 - n_{clad}^2 k_0^2} \tag{2.31}
$$

$$
k_x = \sqrt{n_{core}^2 k_0^2 - \beta^2} \tag{2.32}
$$

and with a bit of algebra, the combination of (2.31) and (2.32) yields:

$$
(\gamma_x d)^2 + (k_x d)^2 = k_0^2 \left(n_{core}^2 - n_{clad}^2\right) d^2 \tag{2.33}
$$

Now, to find the propagation constant of the guided mode (β), we use the guided wave relations (2.30) and (2.33) to solve for k_x and γ_x, which are related to β by (2.31) and (2.32). The resulting transcendental equation has no analytical solution and must be solved by other means, such as graphically. As shown in Figure 2.7, the eigen-equations (2.30) and (2.33) are plotted on axes of $\gamma_x d$ versus $k_x d$. The intersections of the two relations are eigenmode solutions to the guided wave equations and correlate to the different modes supported by the slab waveguide. The number of modes is equivalent to the number of intersecting points, which is dependent on the thickness of the slab and the index difference between the core and cladding materials (Δn). The example depicted in Figure 2.7, has only two solutions, indicating that the slab waveguide core thickness is too thin to support a third waveguide mode.

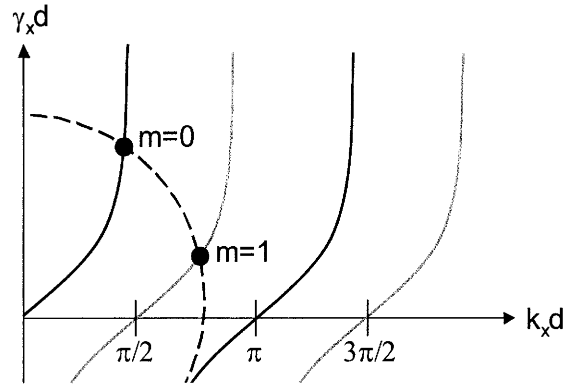

Figure 2.7 – Graphical representation of the guided mode equations (2.30) and (2.33) and solutions (dots) that correspond to the propagation constant β for each mode.

Each eigenmode solution β corresponds to a unique eigenfunction Φ that describes the spatial field distribution of the mode (see Figure 2.6 for examples) and is also a solution to the Helmholz wave equation (2.13). The set of Φ represent a basis set with which guided light can be characterized. Thus we can view the E-field distribution of the guided wave in the mth mode as:

$$\vec{E}(x,z,t) = E_0\ \Phi_m(x)\ e^{-i(\beta_m z-\omega t)} \tag{2.34}$$

where E_0 is the field amplitude, Φ_m is the normalized field distribution for the mth mode, and β_m is the propagation constant of the mth mode, and ω is the angular frequency of light. By definition, the mode field profiles, defined by the eigenmode solutions to the wave equation for a uniform waveguide, are orthogonal and thus

$$\int \Phi_m \Phi_n^* dx = \delta_{mn} \tag{2.35}$$

where δ_{mn} is the Kronecker delta function – which equals unity when m = n and zero otherwise.

The speed at which each waveguide mode propagates (c/n_{eff}) is inversely proportional to its effective index (n_{eff}), which is related to β by:

$$\beta = n_{eff} k_0 = \frac{2\pi}{\lambda_0} n_{eff} \tag{2.36}$$

In a sense, the effective index is just a weighted average of the guided optical power distribution in the core and cladding of the waveguide. This limits the range of values for n_{eff} to:

$$n_{clad} < n_{eff} < n_{core} \tag{2.37}$$

which makes intuitive sense when viewing the guided mode as a uniformly propagating phase front. If the speed of light in the cladding is c/n_{clad} and the speed of light in the core is c/n_{core}, then the speed of the guided mode must be at some in-between value c/n_{eff}.

2.6.2 Other Planar Waveguide Geometries

There are several other classes of planar waveguides used in photonic circuits. The most common waveguide structures are listed in Figure 2.8. As noted in the figure caption, a strict nomenclature has not been established and thus each structure is known under several aliases. In addition, the difference between the waveguide types is not strict. For example, the difference between (a) and (c) is really a matter of how much optical power is confined in the dark strip section – if the mode is highly confined, it is considered waveguide (a), whereas if the mode is not well confined in the strip, and consequently most of the optical power is in the material below, it is considered waveguide (c). In addition, many of the waveguide type illustrations have been generalized, as many permutations, such as adding top cladding index or high index substrates, exist within each classification.

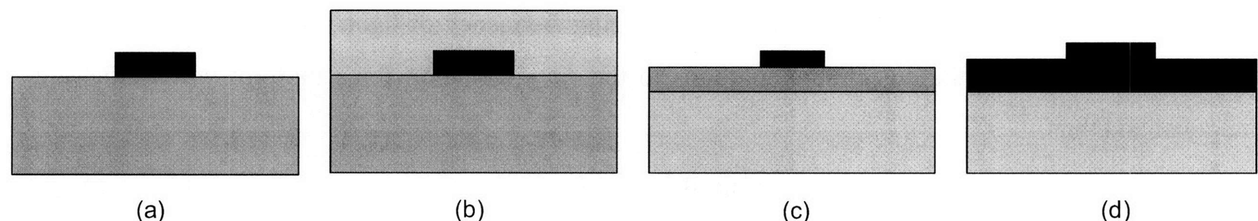

Figure 2.8 – Various waveguide types: (a) rectangular, wire, strip, or channel waveguide (b) rectangular, wire, (buried) channel, or (embedded) strip waveguide (c) strip loaded waveguide (d) ridge or rib waveguide. The shading is proportional to the index.

Unlike the slab waveguide, which only confines light in the out-of-plane direction, the waveguide geometries depicted in Figure 2.8 confine light in both the in-plane and out-of-plane directions, and facilitate in-plane optical routing.

2.6.3 Effective Index Method

The approach used in section 2.6.1 to solve for the propagation constant of the one dimensional slab waveguide can be extended for two dimensional waveguide geometries as well. Essentially, the effective index method approximates a given waveguide structure as a set of slab waveguides.

For a ridge waveguide, the solution to the propagation constant can be well approximated by reducing the ridge into three vertical slab waveguide sections with differing slab thicknesses, as show in Figure 2.9. Ridge waveguides are intrinsically low confinement waveguides, despite the use of high index contrast materials. The three resulting effective indices are then used to form a fourth transverse slab waveguide with thickness w. The cladding indices of the final slab are the effective indices found in the original slab approximations to the left and right of the ridge (steps 1 and 3 in the Figure), while the core index is the original slab approximation at the ridge (step 2 in the Figure). The resulting solution is the effective index of the ridge waveguide.

The effective index method can also be used on channel waveguides, however in this case the approximation is only well suited when W/H >>1 (i.e. when the channel waveguide is nearly a slab waveguide). The steps, detailed in Figure 4.10, are very similar to the ridge waveguide approximation for the case where H1→ 0. First the channel waveguide is approximated as a slab waveguide in the direction of the smaller waveguide dimension. Next, a second slab waveguide in the direction and dimensions of the thicker dimension is created with the core index equivalent to the effective index found in the first step. The resulting solution is the effective index of the channel waveguide.

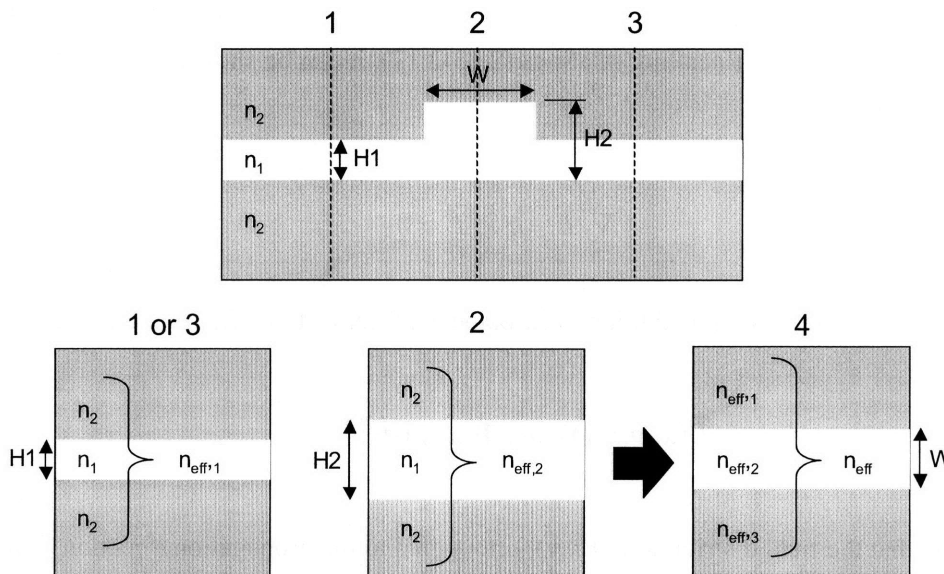

Figure 2.9 – Effective Index Method for a ridge waveguide. Step 1 to 3 – Reduce the ridge waveguide into three vertical slab waveguides. Steps 1 and 3 are identical due to the symmetry of this structure. Step 4 – Use the

effective indices found in steps one to three to construct a transverse slab waveguide with cladding indices $n_{eff,1}$ and $n_{eff,3}$ and core index $n_{eff,2}$ and thickness w.

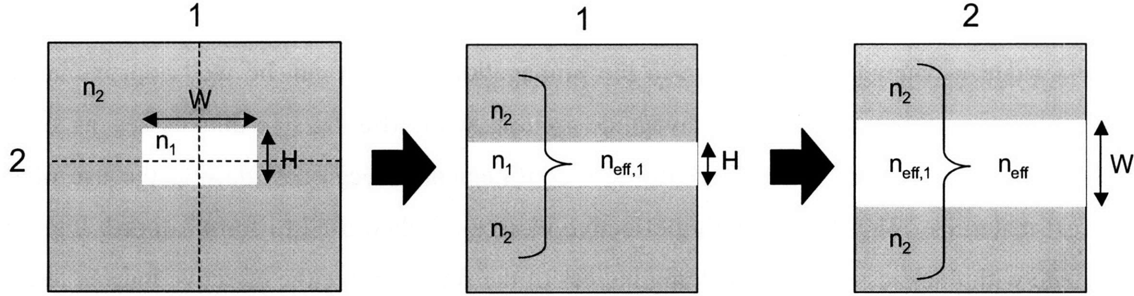

Figure 2.10 – Effective Index Method for a symmetric buried channel waveguide. Step 1 – Approximate the channel waveguide as a slab waveguide across the smaller of the two dimensions. Step 2 – Use the effective index from step 1 as the index of the core and approximate the slab in the transverse direction to find $n_{eff.}$

The effective index method is a reasonable approximation for low confinement waveguides but is inaccurate for many waveguide structures, particularly high index contrast, single-mode, channel waveguides well-suited for integrated applications and the focus of this work. Hence, numerical methods of calculating the effective index and propagation constant are often employed for these cases.

2.6.4 Numerical Techniques

A more accurate method of finding eigenvalue β and eigenfunction Φ(x,y) solutions for a given, arbitrary waveguide structure is to use a finite-difference technique to solve the Helmholtz wave equation for a given index distribution n(x,y). Recalling relations (2.13-2.17), it can be shown that the Helmholtz wave equation has the form of (2.38).

$$\nabla^2 \vec{E} - n^2 k_0^2 \vec{E} = 0 \tag{2.38}$$

Similar to a slab waveguide, but with addition of in-plane confinement, the field for a guided wave will be of a form:

$$\vec{E}(x,y,z,t) = E_0 \; \Phi(x,y) \; e^{-i(\beta z - \omega t)} \tag{2.39}$$

where we assume that the field distribution Φ(x,y), orthogonal to the propagation direction, is normalized.

$$\iint \left| \Phi\left(x,y\right) \right| dxdy = 1 \tag{2.40}$$

Inserting (2.39) into (2.38), we find for the x-y plane:

$$\frac{\partial^2\Phi(x,y)}{\partial x^2}+\frac{\partial^2\Phi(x,y)}{\partial y^2}+k_0^2\left[n^2(x,y)-n_{eff}^2\right]\Phi(x,y)=0 \tag{2.41}$$

Hence, we again find that n_{eff} is the eigenvalue to the wave equation for a uniform waveguide of index profile n(x,y).

Using a computer, one can use the discretized form of relation (2.41) in combination with a finite-element approach to numerically solve the wave equation for both β and $\Phi(x,y)$. This approach, is the basis of many mode solvers, and requires the use of a mesh overlay on the index distribution n(x,y), where (2.41) is evaluated at each node. The accuracy (and computation time) of this calculation is proportional to the mesh density and size of the computation window. Most algorithms assume that the field approaches zero at the boundaries of the computation window and thus the window size must be large enough to ensure sufficient evanescent field decays outside the waveguide core.

2.6.5 Single Mode versus Multiple Mode Waveguides

Single mode waveguides have geometries that only support the first eigenmode solution to the wave equation (for each polarization). In contrast, multiple mode (or multi-mode) waveguides have larger dimensions, for a given core/cladding materials system, and support many eigenmode solutions to the wave equation. The transition point between single-mode (m=0) and multi-mode waveguides corresponds to the second-mode (m=1) cutoff. For slab-waveguides, the mth order mode cutoff occurs when:

$$(\gamma_x d)^2+(k_x d)^2=\left(\frac{m\pi}{2}\right)^2 \tag{2.42}$$

and thus a slab waveguide near the m=1 cutoff condition will transition from single mode to multi-mode if the thickness (2d) increases or if the index difference (Δn) increases such that $(\gamma_x d)^2 + (k_x d)^2 > (\pi/2)^2$. Qualitatively, this behavior is extended to all dielectric waveguides.

Aside from simplicity of modeling, there are many advantages to using single mode waveguides. Single mode waveguides avoid the detriments of using higher order modes (m > 1), which travel at different propagation constants and are less confined in a given waveguide structure. Differing propagation constants result in modal dispersion, where the differing propagation velocities limit the speed with which an optical signal can be modulated. In addition, many photonic devices are optimized

for a particular β (usually for m=0). The lower confinement of the higher order modes within the waveguide core is problematic for two reasons. First, the evanescent field of the higher order modes decays at a slower rate resulting in physically larger modes, where the size scales with m. Second, the lower confinement results in a larger bend loss for a given bend radius and increased substrate leakage for a given waveguide structure, both losses also scales with m. The combination of these two effects results in lowered photonic interconnect density to maintain low loss propagation.

2.7 Single-Mode, High Index Contrast, Channel Waveguides

The majority of this work focuses on processing, designing, and characterizing single-mode, high index contrast (HIC), channel waveguides for integrated photonic applications. This category of waveguides exhibits high confinement of light in small waveguide cross-sections and low loss transmission through compact bends with small bend radii – making it well suited for electronic-photonic integration. The following section will review some of the physical phenomena that arise as a result of high confinement in HIC waveguides.

2.7.1 Asymmetric Boundary Conditions

The boundary conditions (2.24) and (2.25) for E and H fields at a dielectric interface, such as the core-cladding interface of a waveguide, result in pronounced effects on the mode shape and field distribution of a waveguide mode as Δn is increased. The dependence of material index n on permittivity ε and *not* permeability μ at optical frequencies results in an asymmetry in the mode shape that leads to increased polarization dependent behavior as Δn is increased. Quantitatively, this can be observed by rewriting the boundary conditions (2.24) and (2.25) in terms of material indices at optical frequencies. Perpendicular to the interface the boundary conditions change:

$$n_1^2 E_{1\perp} = n_2^2 E_{2\perp} \qquad H_{1\perp} = H_{2\perp} \tag{2.43}$$

while parallel to the interface they remain unchanged.

$$E_{1\parallel} = E_{2\parallel} \qquad H_{1\parallel} = H_{2\parallel} \tag{2.44}$$

Hence, a field discontinuity only exists when the E-field is perpendicular to the interface. In this situation, the magnitude of the field on the cladding side will be larger than the magnitude of the field on core side by the ratio of their indices squared:

$$E_{clad\perp} = \left(\frac{n_{core}}{n_{clad}}\right)^2 E_{core\perp} \quad (2.45)$$

For low index contrast systems ($n_1 \approx n_2$), this discontinuity is minimal and can be ignored in calculations, however for HIC waveguides the effect can be substantial. For Si/SiO_2 waveguides the difference in field magnitudes is ~ 6.

Ultimately, the boundary conditions result in a large difference in modal properties for the TE and TM polarizations in a given waveguide structure. This deviation is minimized for symmetrically-clad, square waveguide geometries and most pronounced in asymmetrically clad rectangular waveguides with aspect ratios far from unity. Figure 2.11 depicts contour plots of the field profile for the TE and TM modes in a 200x500 nm^2 Si/SiO_2 channel waveguide, where both plots are plotted on the same scale with the same number of contours. Both field contour plots clearly show the polarization dependent field discontinuities, which occurs on the waveguide sidewalls for the TE mode, and the top and bottom waveguide surfaces for the TM mode. In contrast, the fields are continuous across the top/bottom and sidewall interfaces for the TE and TM modes respectively.

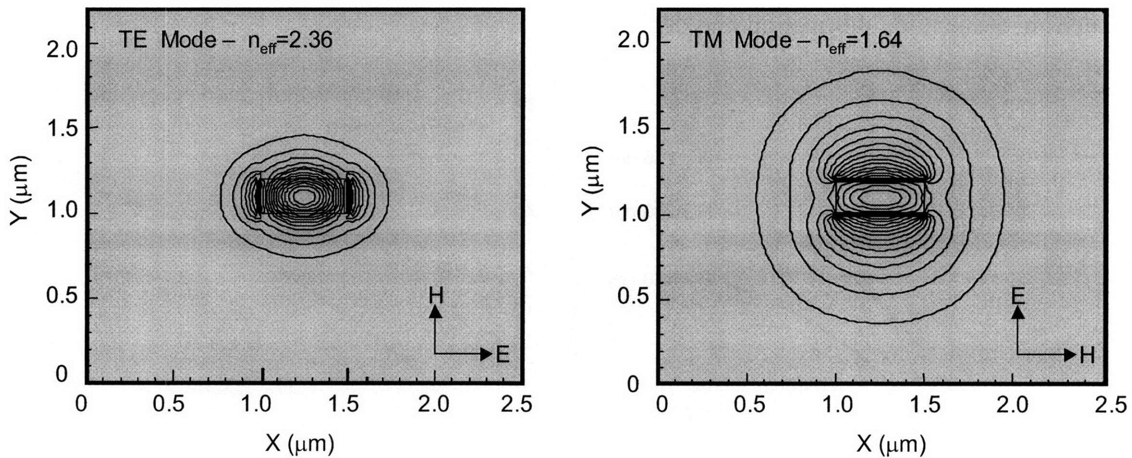

Figure 2.11 – Field contour plots of the TE and TM mode profiles for a 200x500 nm^2 Si (n=3.48) channel waveguide clad with SiO_2 (n=1.445) for λ=1550 nm, simulated with FIMMWAVE

The large difference in mode size, shape, and effective index for the two polarizations in the short-wide rectangular waveguide geometry is a consequence of satisfying the boundary conditions. The field distributions in the X and Y directions must balance to resolve an equivalent effective index. Thus, if the field discontinuities are closely spaced, such as in the Y-direction for the TM mode, the optical power in the core must decrease to meet conditions (2.43) and (2.44) at the interfaces. Thus the TM mode will have considerably more guided optical power in the cladding, which reduces the effective index and

increases the mode size. In comparison, the field discontinuities for the TE mode are farther spaced, resulting in a higher proportion of the optical power in the core, which results in a higher effective index, smaller mode size, and increased confinement.

For the case of a rectangular waveguide with an inverse aspect ratio (500x200 nm^2) to the example in Figure 2.11, the modal properties would be totally reversed. The TE solution would be the larger of the two, with a field distribution identical to the 200x500 TM solution, but rotated 90°. Likewise, TM solution would be mode confined and smaller with a field distribution identical to the 200x500 TE solution, but rotated 90°.

2.7.2 Effective Index versus Width

The range of effective index values, as discussed in section 2.6.1, is bounded by the core and cladding indices. Therefore the effective index range is maximized for a large Δn, such as the HIC waveguides studied in this work. For planar circuits, the waveguide width is comparatively less controlled than the waveguide height as a result of the relative tolerances associated with the deposition and etching techniques used in defining each parameter. As a result, it is useful to know the functional nature of a given waveguides effective index versus width in the single-mode regime to understand the sensitivity and tolerances in waveguide fabrication and design.

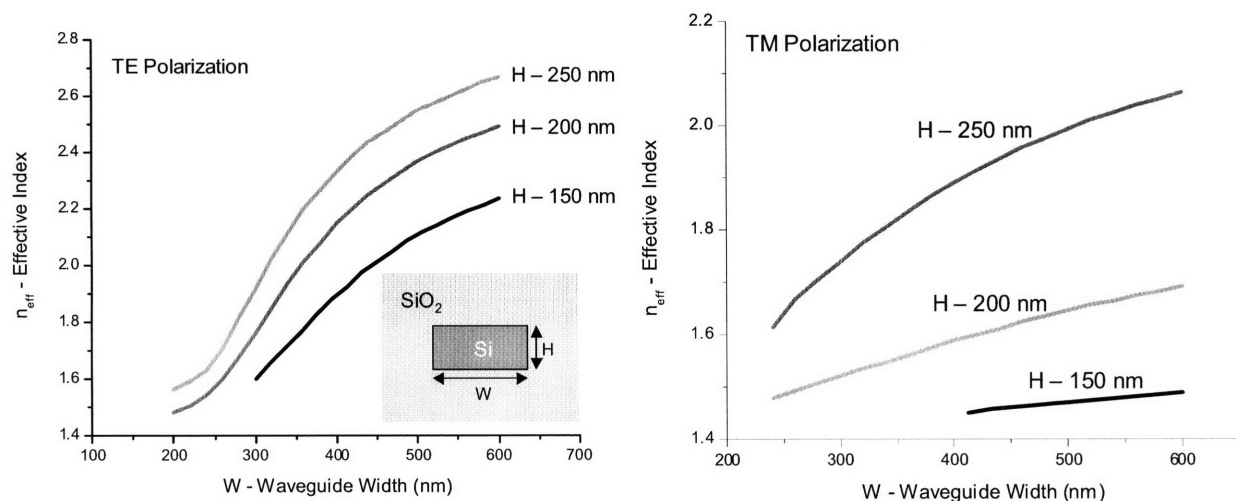

Figure 2.12 – Effective index of Si (n=3.48) channel waveguides of different dimensions clad with SiO_2 (n=1.445) for the TE and TM polarizations, λ=1550 nm. Calculations performed with FIMMWAVE Mode Solver software.

Figure 2.12 shows the effective index of Si/SiO_2 channel waveguides for a range of dimensions. As one may expect, the highest effective index in each plot is found for the waveguide with the largest dimensions, corresponding to the highest fraction of power inside the waveguide. Likewise, the effective

index decreases as the dimensions shrink, as the mode is squeezed out into the cladding. For the smallest widths, the effective index asymptotically approaches the cladding index. For the largest widths, the effective indices plateau at a level proportional to the waveguide height.

Similar to altering the waveguide dimensions, varying the signal wavelength λ, results in a similar change in effective index. For single-mode waveguides, increasing the wavelength is analogous to decreasing the waveguide dimensions, and vice-versa for decreasing the wavelength. In most cases, this effect is limited by the range of available tunable lasers, and thus the change in effective index for a given wavelength scan can be approximated as linear.

2.7.3 Mode Size

The size of a field distribution for a given mode is inversely proportional to the effective index. Recalling (2.31), the decay constant of the evanescent field, can be rewritten as (2.46) in terms of n_{eff}.

$$\gamma_x = k_0\sqrt{n_{eff}^2 - n_{clad}^2} \tag{2.46}$$

Hence, if we approximate the exponential decay length as the inverse of the decay constant, the effective height (H_{eff}) and width (W_{eff}) of the mode are given by:

$$H_{eff} = H + \frac{2}{\gamma_x} \tag{2.47}$$

$$W_{eff} = W + \frac{2}{\gamma_x} \tag{2.48}$$

Again, this approximation works well for low index contrast waveguides, where the field discontinuities are minimal, and the evanescent field magnitude at the core-cladding interface is approximately polarization independent. For HIC waveguides, the evanescent field magnitude is not polarization independent, resulting in an underestimation of the mode height or width (depending on the polarization) for the interfaces with field discontinuities. This effect can be observed in the field contours in Figure 2.11.

Chapter 3 – Waveguide Measurement

There are several methods of measuring the transmission loss of waveguides (α_T), in this chapter Cutback and Fabry-Perot loss measurement techniques are reviewed in the context of high index contrast (HIC) waveguide measurement. Reduction of insertion loss to HIC waveguide chips is imperative to loss measurement and details on how to surmount this problem are discussed as well.

3.1 Transmission Loss

Transmission loss is a summation of loss mechanisms associated with the propagation of electro-magnetic radiation through a waveguiding structure; these include, but are not limited to, scattering from interface roughness or bulk inhomogeneities, leakage to the substrate, radiation due to bend loss or abrupt dimensional changes in the waveguide, and absorption.

$$\alpha_T = \sum_i \alpha_i = \alpha_{scattering} + \alpha_{leakage} + \alpha_{radiation} + \alpha_{absorption} + \ldots \qquad (3.1)$$

As a result of these loss mechanisms, the optical signal exponentially decays, as defined in equation 3.2, where P(z) is the power as a function of the propagation length z and P_0 is the initial power at the beginning of the waveguide, neglecting coupling losses.

$$P(z) = P_0 \, e^{-\alpha_T z} \qquad (3.2)$$

For planar waveguide circuits, the relevant length-scale is the centimeter (cm) and thus α_T, as defined in equation 3.2, has the units of inverse length [cm^{-1}]. However in keeping with convention (in our base ten society); α_T is typically quoted in decibels (dB) per length scale or [dB/cm] for planar waveguide circuits. It should be noted that loss in terms of dB/cm, is defined in equation 3.3, where P_0 and P_{final} are the initial and final transmission power over L, the waveguide length difference.

$$\alpha_T \left[\tfrac{dB}{cm}\right] = \frac{10 \log\left(\frac{P_{final}}{P_0}\right)}{L} \qquad (3.3)$$

In comparison, rearranging equation 3.2 solved for α_T yields:

$$\alpha_T \left[\tfrac{1}{cm}\right] = \frac{\ln\left(\frac{P_{final}}{P_0}\right)}{L} \qquad (3.4)$$

Thus by comparing equations 3.3 and 3.4 one finds the conversion factor between the two units of transmission loss.

$$\alpha_T\,[\tfrac{dB}{cm}] \cong 4.34\,\alpha_T[\tfrac{1}{cm}] \tag{3.5}$$

3.2 Insertion Loss

Insertion loss is the total loss that occurs between insertion and extraction of light from an optical device often referred to as the device under test (DUT). In general, the insertion loss ($\alpha_{Insertion}$) is the sum of the coupling loss ($\alpha_{Coupling}$), and the transmission loss (α_T) multiplied by the length of the optical path (L) of the DUT.

$$\alpha_{Insertion} = \alpha_{Coupling} + \alpha_T L \tag{3.6}$$

Ideally, coupling loss, defined as the loss associated with coupling in and out of a given waveguide structure or chip, is negligible. Quantitatively, the coupling loss ($\alpha_{Coupling}$) is given by equation 3.7, where R is the facet reflection and the Φ_{fiber} and $\Phi_{waveguide}$ terms are the E-field distributions of the respective guided modes. The factor of two in equation 3.7 accounts for the two facets, R accounts for reflection losses, and the overlap integral accounts for coupling losses due to mode mismatch.

$$\alpha_{Coupling} = 2\left[R + \left(1 - \iint \Phi_{fiber}(x,y)\,\Phi^*_{waveguide}(x,y)\,dxdy\right)\right] \tag{3.7}$$

Measurement of planar waveguides is typically performed by butt coupling an optical fiber to a waveguide chip at both the input and output facets. Optical fibers are inexpensive, robust, and have extremely low attenuation rates for near infra-red light. The "standard" optical fiber, known as SMF-28 single is used for telecommunication, cable television, submarine, and private network applications in the transmission of data, voice, and video. A plot of attenuation versus wavelength for a typical silica fiber is shown in figure 3.1. The key wavelengths of operation are at 1310 nm, where there is low loss and zero dispersion, and at 1550 nm where the loss is at a minimum. Other notable wavelengths are at 1380nm, which corresponds to the O-H bond resonance and thus an increased loss, and 850 nm where cheap, reliable GaAs based lasers emit.

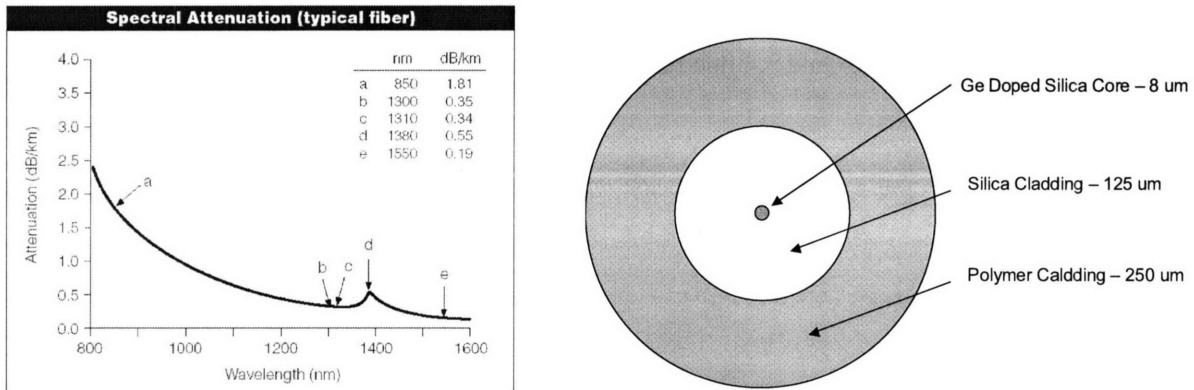

Figure 3.1 – Optical fiber loss as a function of wavelength [24] (left) and cross-sectional components and diameters (right).

Fiber butt coupling to large modal area waveguides, as is the case with most low index contrast waveguides, yields low coupling loss due to the low modal mismatch and typically low facet reflection. The use of an index matching fluid applied to the tip of a fiber can further reduce R and improve coupling. In contrast, fiber butt-coupling to HIC waveguides, with small modal areas, results in high insertion losses dominated by the modal mismatch term. In other words, the ratio of the cross-sectional area of a single-mode, HIC waveguide to the modal area of a SMF-28 fiber can be as low as 10^{-3}, resulting in very low coupling of optical power. Besides being impractical, high insertion losses can result in the inability to characterize waveguides if they surpass the noise level of detection. Figure 3.2 illustrates the relative mode field diameter (MFD) of SMF-28 fiber and two lens tipped fibers used to measure waveguides in this thesis, as compared to the cross-sectional areas of a single-mode Si and SiN waveguide. For Gaussian power distributions, such as in optical fibers, the MFD is defined as the diameter at which the electric field is at reduced to 1/e and correspondingly the optical power is reduced by $1/e^2$ of the maximum value.

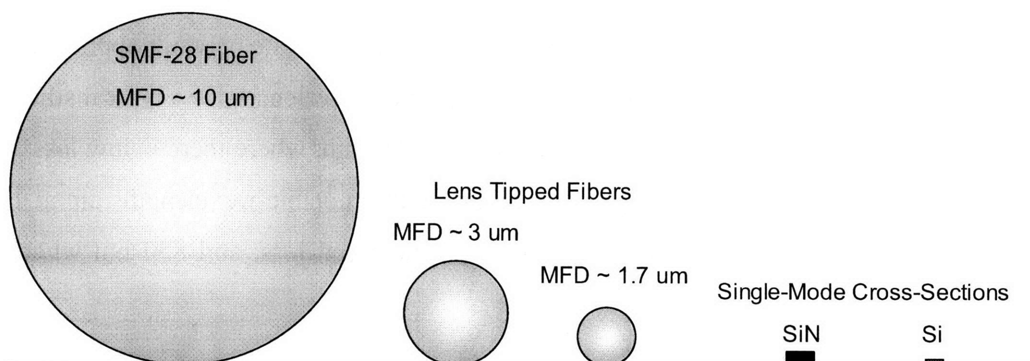

Figure 3.2 – Relative sizes of three optical fiber Modal Field Diameters (MFD), for λ=1550nm, as they compare to the single-mode cross-sectional areas of Si and SiN high-index contrast waveguides.

Fiber coupling to HIC waveguides can be improved in two ways: 1) reducing the fiber MFD and 2) fabricating waveguide input couplers. Both approaches aim at improving the modal overlap between the modes of the fiber and the HIC waveguide.

3.2.1 High Index and Lens Tipped Fibers

One approach to improving HIC waveguide insertion loss is to modify the fiber geometry to shrink its MFD to more closely match the waveguide mode. This can be accomplished by either increasing the index contrast of the fiber or by tailoring the fiber end to act as a lens. The former can be achieved by increasing the doping of the fiber core, enabling the fiber to support a smaller MFD. This method works well to reduce the MFD from 10 μm to as small as 4 μm (for λ=1550nm) where the resulting fibers have very low loss and can be easily spliced to SMF-28 fibers with minimal loss.

Alternatively, a lens tipped fiber can be utilized to reduce the MFD of the input and output fibers. Lens tipped fibers are commercially available from Nanonics Imaging Ltd. with MFDs as low as 1.7 μm at λ=1550nm. One detriment to using lens tipped fibers is the cost, in terms of loss, that scales inversely with MFD. Theoretically, the loss from a lens should be negligible; however the lens tipped fibers used in the experiments were fabricated by a thermal process that results in a sub-optimal fiber taper and lens. Nonetheless, what is lost in terms of input power is gained in input flux with lens tipped fibers. A comparison of the throughput and flux of two lens tipped fibers and SMF-28 fiber is listed in figure 3.3. The input flux is calculated by dividing the fiber-to-fiber power by the modal area (approximated by a circle with the MFD as its diameter) and can be viewed as a figure of merit for HIC waveguide insertion loss minimization.

Fiber Type	MFD (um)	Fiber-to-Fiber Power (uW)	Input Flux (W/cm^2)
SMF-28	10	610	777
Lens Tipped Fiber	3	400	5660
Lens Tipped Fiber	1.7	150	6610

Figure 3.3 – Modal field diameter (MFD), fiber-to-fiber power and calculated input flux for three fibers used in the experiments.

3.2.2 Estimating Coupling Loss

If the field distributions of the fiber mode and the waveguide mode are known, the coupling loss can be estimated with relation (3.7). This approach, if accurate, presents a method with which to estimate transmission loss from insertion loss data.

To understand the accuracy of simulating coupling loss with lens tipped fibers, experimental and theoretical coupling loss data was compared. Coupling loss values were obtained from experimental data,

as observed in relation (3.6), by subtracting the loss associated with transmission from insertion loss data. FIMMPROP, a commercial waveguide simulation tool, was used to simulate the mode profile in the waveguide, the mode profile projected from the lens tipped fiber onto the waveguide facet, and the coupling loss.

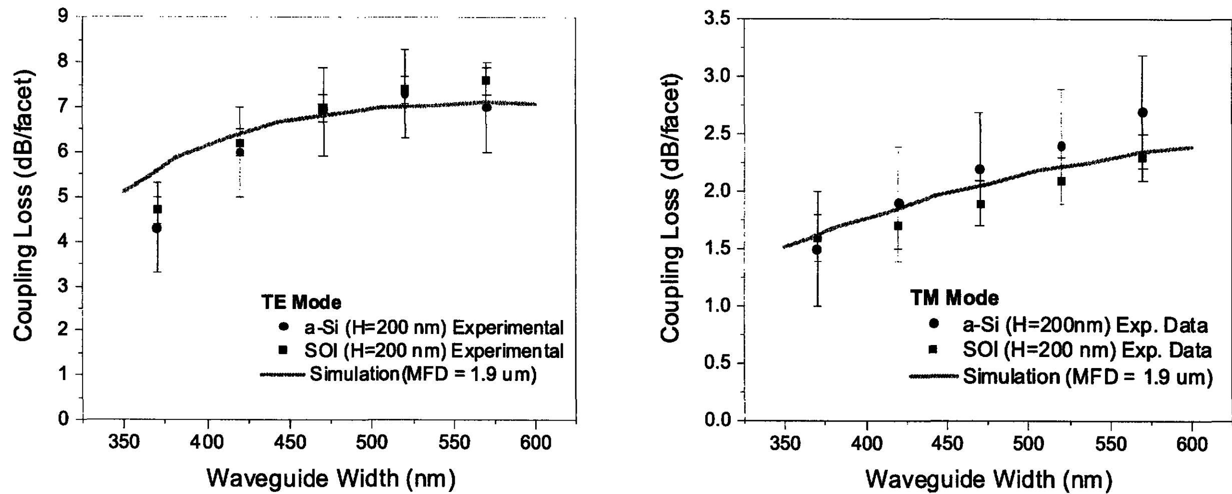

Figure 3.4 – Comparison of experimental and simulated coupling loss data, using lens tipped fibers. The lens tipped fiber field distribution is well approximated by a Gaussian distribution with a waist equal to its modal field diameter (MFD = 1.9 μm).

The plots in Figure 3.4 depict experimental and theoretical coupling loss data. Experimental waveguide data was measured for several waveguide geometries of crystalline and amorphous Si channel waveguides clad with SiO_2. The transmission loss (α_T) was measured by the cutback technique for each geometry (to be discussed in section 3.4). Insertion loss was measured for straight waveguides with known length, and the respective transmission loss, associated with each geometry, was subtracted to find the coupling loss. Each experimental data point is an average of four waveguide loss measurements, the error bars on the coupling loss data reflects the data range of the transmission loss.

Overall, the comparison of experiment and theory is quite good. The field profile of the lens tipped fiber is well approximated by a Gaussian distribution with a beam waist equal to a modal field diameter of 1.9 μm. Although the lens tipped fibers were quoted as having a MFD of 1.7 μm, the deviation is well within the product specs (spot size tolerance = ± 0.3 μm). The deviation in insertion loss between the two polarizations is related to the difference in mode size; the TM mode is considerably larger than the TE mode and therefore has a better overlap with the lens tipped fiber mode.

3.2.3 Input Couplers

The other approach to reducing insertion loss is to fabricate input couplers at the waveguide terminals. The intuitive solution is to flare the waveguide dimensions near the waveguide facet to match the modal

size of the fiber. Unfortunately, this approach is incompatible with thin film processes, for a variety of reasons including: large facet reflection, out of plane tapering, and multimode behavior for HIC waveguides. Fortunately, researchers [14, 25-27] have been working on this problem for a number of years and have arrived at three categories of input couplers that have been successfully integrated with HIC waveguide structures. Each coupler is ingenious in its own respect and briefly reviewed below.

3.2.4 Inverted Taper Coupler

This coupler philosophy takes the opposite approach of what one might think is an optimal coupler design. Rather than taper out the width of the waveguide to closely match the size mode of the fiber mode, the waveguide width is tapered in, to nearly a point (figure 3.5). The benefits of "inverting" the taper are two fold. First, reducing the waveguide core dimensions, within the single mode regime, causes the waveguide mode to expand, enabling better mode matching with the fiber. Second, for the case of SiO_2 clad HIC waveguides, expanding the mode such that a majority of the mode resides in the cladding results in effective index matching of the waveguide and fiber modes, this reduces the facet reflection coefficient and further reduces the insertion loss. The addition of a large, low index contrast waveguide surrounding this inverted taper coupler alleviates loss that may occur due to dimensional fluctuations along the taper. Reported insertion loss values have been as low as 1.9 dB/cm for Si waveguides [25], and 1 dB/cm for SiN waveguides [26].

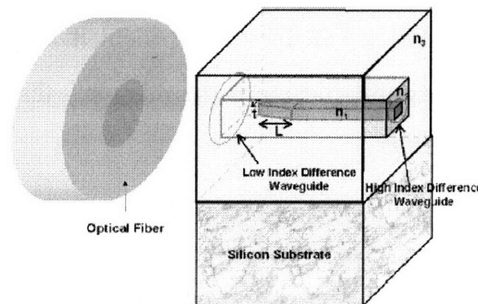

Figure 3.5 – Inverted Taper Coupler for reducing insertion loss in HIC waveguides [26].

Theoretically, the inverted taper coupler should be lossless; however in practice the leakage of power from the waveguide to the Si substrate prevents this. An expanded waveguide mode is prone to substrate leakage losses, especially when a thin undercladding thickness is used. However, this effect is small since the overall lengths of inverted taper couplers are quite short (~100 μm). The most critical parameter to a low loss inverted taper coupler is the width of the taper tip. For silicon waveguides, the optimal width is less than 20 nm [25-26] which indicates that high resolution lithography (i.e. e-beam or deep-UV lithography) is required for fabrication.

3.2.5 Asymmetric GRIN Taper Coupler

The asymmetric GRIN taper coupler is a great example of being clever with standard, thin film technology to surmount a difficult problem. The structure (figure 3.6) consists of a graded index (GRIN) stack that is tapered, in-plane to the width of a single mode waveguide. The GRIN, if designed properly, acts as a lens to shrink the mode to match that of the single mode waveguide, in the out-of plane direction. Similarly, the in-plane taper shrinks the mode laterally. Combined and optimized, the GRIN and taper enable efficient modal size reduction and low insertion loss.

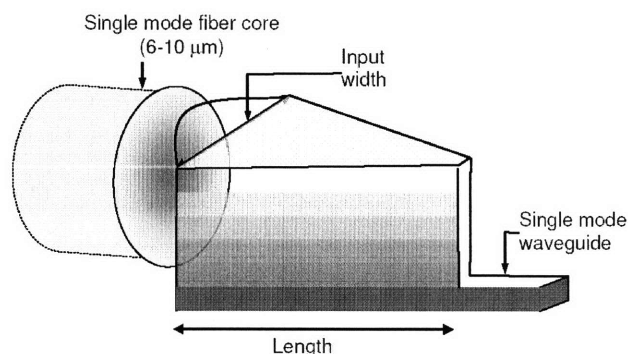

Figure 3.7 – Asymmetric GRIN Taper Coupler for reducing insertion loss in HIC waveguides [14].

The benefit of this design is that it can be fabricated without high resolution photolithography and is quite short (~20 μm). Initial prototypes of this coupler design yielded losses as low as 2.5 dB/cm using standard fibers. A concern using this coupler design is the relatively thick structure, which can result in high stresses and fabrication complications.

3.2.6 Vertical Grating Coupler

As nominally implied vertical grating couplers use a grating to couple light in from a waveguide. While this approach takes quite a bit of design and fabrication work, it offers the ability to vertically couple light to the waveguide. Vertical coupling allows one to avoid timely sample preparation, as measurements can be done without dicing the wafer, and offers an easier geometry to package a fiber pigtail. This coupling approach is particularly attractive to electronic and photonic integrated chips as it allows simultaneous electrical and optical measurement with a single, automated probe station. Detriments of using this coupling approach arise from the physics of gratings [25, 27]. The vertical grating coupler is polarization sensitive, as the grating teeth only vary the permittivity and not permeability in real space. The grating is also sensitive to the input fiber angle and wavelength. Insertion losses of less than 2 dB/cm at λ=1550 nm, have been reported [27].

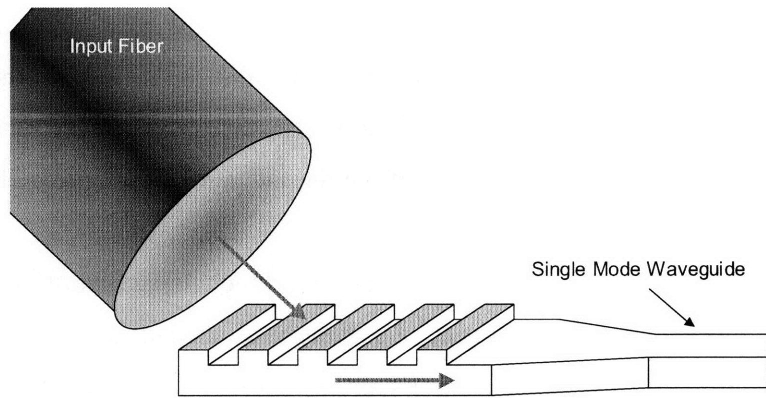

Figure 3.7 – Vertical Grating Coupler for reducing insertion loss in HIC waveguides.

3.2.7 Input Coupler Comparison

A comparison of pertinent coupler criteria is listed in figure 3.8. The relative importance of each category is application dependent and ultimately influenced by the polarization, wavelength range, available lithography, and sample preparation ease of the waveguide chip. Due to the simplicity of fabrication, polarization independence, and available lithography, the only input couplers used in this thesis were the inverted taper couplers.

Input Coupler	Polarization Independent	Broadband	Sensitive to Lithography Resolution	Fiber Insertion Direction
Inverted Taper	Yes	Yes	Yes	Chip Facet
Asymmetric GRIN Taper	Yes	Yes	No	Chip Facet
Grating Coupler	No	No	Yes	Vertical

Figure 3.8– Comparison of HIC waveguide input coupler designs

3.3 Sample Preparation

In this work, waveguide samples are prepared in one of two ways: 1) cut and polish or 2) cleaving. While the cut and polish preparation method is accurate in terms of facet placement, it is timely and laborious in nature. In contrast, cleaving (by hand) is less accurate but with comparatively quick and high quality results.

The cut and polish method uses a diesaw to cut the wafer into individual chips. Diesaws are used in the microelectronic industry to accurately (micron-scale resolution) separate the dense array of chips typical in high-yield microchip processing. The problem in using a diesaw to dice photonic chips is facet roughness (~10 μm). Unless vertical input couplers are used (see section 3.2.6) the waveguide input *is* the diesawed facet whose roughness can scatter optical power and drastically reduce coupling efficiency

to the waveguide. Hence, a polishing step is required to smooth the facet to the sub-wavelength roughness needed to lower insertion loss. Facet polishing is a laborious and timely sample preparation method in that it requires the use of several continually smoother polishing papers to reduce facet roughness. Even when multiple chips are polished in parallel, the net preparation time per chip is on the order of hours. However, many times the accuracy of the diesaw is needed to precisely place the facet, such as when input couplers are used.

Alternatively, cleaving is a quick sample preparation technique where most of the time involved is in placing the scribe mark with a diamond scribe. Cleaving takes advantage of the anisotropic atomic bonding in crystalline substrates. By applying pressure to a defect, created by scribing a line along certain crystallographic directions that correlate with weaker atomic bonding, the crystalline wafer will crack and propagate along a "cleave" plane. Theoretically, a cleaved facet should have atomic smoothness! For {100} silicon wafer substrates, cleaving occurs in the <110> directions, which nicely corresponds to the orthogonal basis that chips are aligned to. The thin films on top of the substrate are of negligible effect and cleave with the substrate. This effect is shown in an SEM image of a cleaved SiN waveguide that is deposited on a Si Substrate (Figure 3.9).

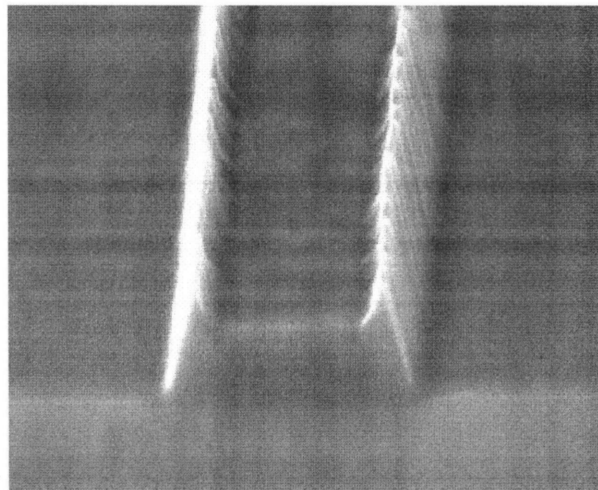

Figure 3.9– SEM image of a cleaved SiN waveguide Facet, courtesy of Dr. Tymon Barwicz, MIT

Many times, it is advantageous to fabricate waveguides without a top cladding when researching waveguides. In these cases, cut and polish techniques cannot be used, as the waveguide facets are inevitably ripped off during the polishing process, leaving cleaving as the preferred method of sample preparation. However cleaving does have some disadvantages. First, it is limited to samples with certain crystalline substrate orientations. Second, the cleave placement is limited by the scribe mark resolution, which is human precision (±500 μm) in our case, and the spacing between cleaves is limited to several

mm, for handling reasons. Third, most photolithography masks are designed with a space between chips to accommodate for the width of the diesaw blade. Therefore, if one were to cleave a perfectly placed scribe at the edge of one chip, the waveguide inputs on the adjacent chip would not be exposed on the adjoining facet, thereby rendering the adjacent chip useless, or needing polishing. This effectively reduces the sample preparation yield from cleaving to 50%.

3.4 Cutback Loss

Cutback is a technique where the transmission loss of a waveguide is determined by comparing the optical power throughput of identical waveguides with varying lengths. This can be observed by differentiating (3.6) by L, yielding:

$$\alpha_T = \frac{\partial\left(\alpha_{Insertion}\right)}{\partial L} \tag{3.8}$$

By plotting this data on a logarithmic plot, where each data point corresponds to a transmission measurement of a different waveguide length, the loss coefficient α_T is found by measuring the slope (see Figure 3.10).

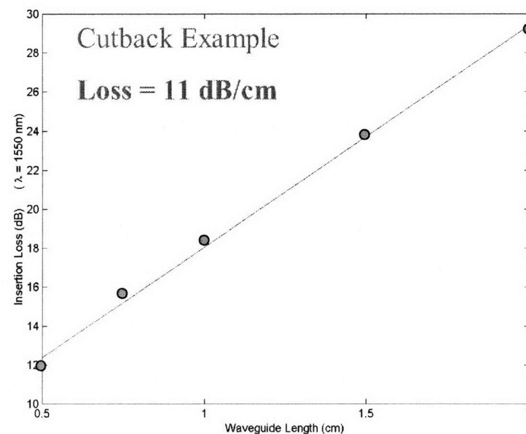

Figure 3.10 - Experimental data from a set of silicon waveguides, where transmission in terms of insertion loss [dB] is plotted versus the waveguide length [cm], yields a slope which is equivalent to a transmission loss of 11 dB/cm.

In the traditional sense, cutback is a method of physically reducing a waveguide by known length increments, what one might call “cutback”, to determine the functional dependence of optical power versus length. This method is destructive and can result in variable waveguide facet transmission properties after each length reduction step. For the case of HIC planar lightwave circuits, physically

reducing the length of a waveguide is cumbersome, laborious from an input and output alignment perspective, and expensive. Sample preparation techniques also makes it difficult to consistently create identical waveguide input or output facets after each size reduction, which yields error in finding α_T. However, by cleverly designing the waveguide layout, the cutback method can be used to obtain transmission loss without destroying waveguide samples or creating errors from irregular sample preparation.

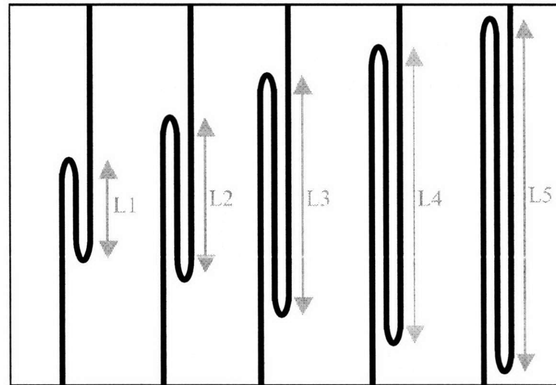

Figure 3.11 – Example of paperclip waveguide structures used for cutback loss measurement, where the distance between the two bends increases from L1 to L5.

The paperclip approach is one such design that avoids the detriments of traditional cutback. As seen in figure 3.11, the arrangement of paperclip-shaped waveguides with identical cross-sections enables measurement of different length waveguides without the need to destructively reduce the size of the sample. The addition of two 180° bends allow the waveguides to have different lengths while maintaining identical input and output facet spacing. Maintaining a constant input to output port spacing facilitates easier sample preparation and reduces the alignment time between waveguide measurements. Additional loss that may arise from the waveguide bends is constant for each waveguide and does not affect the transmission loss value since the cutback is a relative measurement.

The straight-forwardness of the cutback method makes it an ideal experimental technique for measuring transmission loss in waveguides. Errors using this approach result from non-uniformities in the waveguide facets. However, typical fabrication sample preparation techniques (cleaving and polishing) produce very uniform waveguide facets across a given facet. The disadvantages of using this technique are that it requires optimized alignment, to keep P_0 constant, and measurement of several waveguides to obtain α_T.

3.5 Fabry-Perot Loss

The Fabry-Perot Loss technique takes advantage of the fact that a waveguide is essentially a long resonant cavity, where the waveguide facets act as mirrors. The Fabry-Perot Loss relation is given by equation 3.8 and derived in Appendix A.

$$\alpha_T = \frac{1}{L}\ln\left(R\frac{1+\sqrt{\frac{I_{\min}}{I_{\max}}}}{1-\sqrt{\frac{I_{\min}}{I_{\max}}}} \right) \qquad (3.9)$$

Thus to find the loss of a waveguide using the Fabry-Perot technique requires the knowledge of the length of the waveguide (L), the reflection coefficient of the facet (R), and a tunable laser source used to measure the ratio of intensities. Straight waveguides are the best structures for this type of measurement as waveguide bends can cause small internal reflections that influence the resonance condition. Figure 3.12 shows an example of a Fabry-Perot measurement for a silicon waveguide, I_{min} and I_{max} data is obtained from the oscillations in power, what are sometimes known as Fabry-Perot fringes, as the wavelength is scanned.

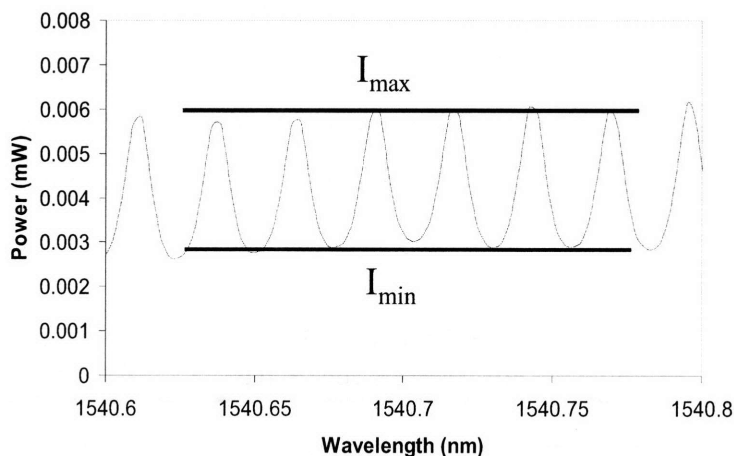

Figure 3.12 – Example of a cleaved silicon channel waveguide Fabry-Perot oscillation.

Fabry–Pérot loss measurements are a bit easier and faster to perform than cutback, although it requires more complex equipment. The data sought from a Fabry-Perot measurement is a ratio of I_{min}/I_{max} and therefore independent of fiber alignment (input power), thereby easing the alignment tolerance. Second, Fabry-Perot measurements yield a loss value after one measurement. However, the ease of Fabry-Perot measurement is countered by the sensitivity and difficulty in determining the reflection

coefficient, particularly for high index contrast waveguides. On one hand, assuming on knows R, Fabry-Perot measurements are an upper bound to transmission loss since facet imperfections negatively affect the transmission data. On the other hand, the lack of an analytical model for properly modeling the high index contrast waveguide facet reflection adds to the uncertainty of this measurement technique.

3.5.1 Determining the Waveguide Facet Reflection Coefficient

There are several ways to calculate the reflection coefficient (R) of a waveguide facet. Accurate values for the reflection of a waveguide facet can be determined by experimentation or simulation by 3D FDTD. However both of these methods can be quite involved. To first order, R can be estimated using the Fresnel equation, where the waveguide facet is modeled as a one dimensional interface between two materials: the incident material, typically air (n=1), and the waveguiding material with a refractive index n_{eff}.

$$R = \left(\frac{n_{incident} - n_{eff}}{n_{incident} + n_{eff}} \right)^2 \tag{3.10}$$

The Fresnel reflection approximates the reflection coefficient as it assumes that the light is in the form of plane waves, normal to the interface. This approximation works well for low index contrast and/or large modal area waveguides. However, the approximation breaks down and leads to an underestimation of the transmission loss for high index contrast waveguides [28-29]. The basic reason for this phenomenon is the reduced phase matching when light, in the form of a plane wave or large Gaussian envelope, is guided into a highly confined waveguide mode. The reduction in phase-matching leads to an enlarged reflection coefficient.

Chip #	Cutback (dB/cm)	Fabry-Perot (dB/cm) Fresnel Reflection (R=6.6%)	Fabry-Perot (dB/cm) 3D FDTD (R=10.5 %)
1	4.3	2.9	6.6
2	6.5	3.4	6.7
3	8.6	3.5	6.7
4	9.5	5.6	9.5

Figure 3.13 – Transmission loss data for SiN waveguides using Cutback and Fabry-Perot loss techniques. Two different facet reflection coefficients were used in determining the loss, demonstrating how the Fresnel reflection approximation is inappropriate for high index contrast waveguides. Ideally, the cutback and fabry-perot loss data should match.

This Fresnel reflection coefficient estimation discrepancy in high index waveguides was clearly seen in a comparison of Fabry-Perot and Cutback measurements. In this study, air-clad, SiN waveguides (n = 2.2) on a 3um SiO_2 undercladding deposited on a Si wafer were used. Four chips from the same wafer, fabricated at Lincoln Laboratory, were measured by cutback with paperclip waveguides and by Fabry-Perot with straight waveguides. All waveguides measured at λ=1550 nm had with identical cross-sections of approximately 400 x 750 nm^2. The results for cutback loss and Fabry-Perot loss with two different facet reflection coefficients are detailed in figure 3.4. It is clear from this data that the Fesnel Reflection approximation for the SiN waveguides (R=6.6%) underestimates facet reflection as this translates into a factor of two difference in loss when compared with cutback. In contrast, the reflection coefficient found by a 3D FDTD simulation (R=10.6%) yielded loss values which were quite close to the cutback ones. Deviations between the two are attributed to experimental errors arising from excessive handling of the air-clad chips. Ideally, the loss obtained from the cutback and Fabry-Perot techniques should be equivalent.

3.6 Experimental Apparati

The experiments performed throughout this document were measured with one of two loss measurement setups. Figure 3.14 lists the relative system data for the two systems. While the Newport JDS-System is preferable in nearly all categories, the Table 3 system has several attributes which make it more attractive for combined electrical and optical characterization, alignment of high transmission loss waveguides, and visual inspection of the waveguide mode.

	Table 3 System	**Newport-JDS System**
Measurement Type	Fiber – Chip – Free Space	Fiber – Chip – Fiber
Dynamic Range (dB)	~ 30	60
Alignment	Manual	Automated
Laser Data		
Laser Manufacturer	New Focus	JDS Uniphase
Wavelength Range (nm)	1473 – 1543	1519 – 1634
Scan Speed (nm/s)	0.01	20
Wavelength Resolution (pm)	10	3
Maximum Power (mW)	25	2

Figure 3.14 – Comparison of the Loss Measurement Systems

3.6.1 Table 3 System

The first loss measurement system, named for its location in the lab as opposed to its makeup (it is constructed of many parts from many manufacturers), utilizes fiber insertion/free space extraction measurement. Light from a tunable laser is guided in a fiber as it transverses a polarizer and chopper to the sample insertion junction. The fiber output is aligned to the waveguide facet, by means of a lens tipped fiber, with a MFD of 3 μm, manipulated by a three axis micrometer (coarse adjustment) and piezeo-electrical controller (fine alignment). At the output of the waveguide chip sample, the guided light is collected, focused, and collimated by a 25X microscope objective to the detector. To increase the precision of detection, a lock-in amplifier used in conjunction with an optical chopper amplifies the laser signal, to distinguish it from other light sources that may be detected in the free space detector. The lens and detector reside on a single two axis translation stage, enabling measurement of several waveguide output ports without needing to adjust the input or refocus the output. Wavelength versus power measurements are collected and controlled by a computer. Alignment of the Table 3 system is implemented by visual imaging of the output with a mirror and an IR camera (not shown in figure 3.15) placed in the beam path between the lens and detector.

Two issues that exist with the Table 3 system are the limited dynamic range and slow wavelength scanning speed. The relatively large collection area of the lens limits the dynamic range, as it focuses power in the form of cladding modes into the detector, thereby increasing the noise floor of the measurement. Increasing the magnification of the objective can help alleviate this issue, but at the cost of increasing the difficulty and sensitivity of alignment. The slow detection response time, limited by the detector response to the chopper, prevents fast wavelength scans and ultimately leads to timely spectral response measurements. Lengthy measurement times tend to add error as system alignment tends to drift with time.

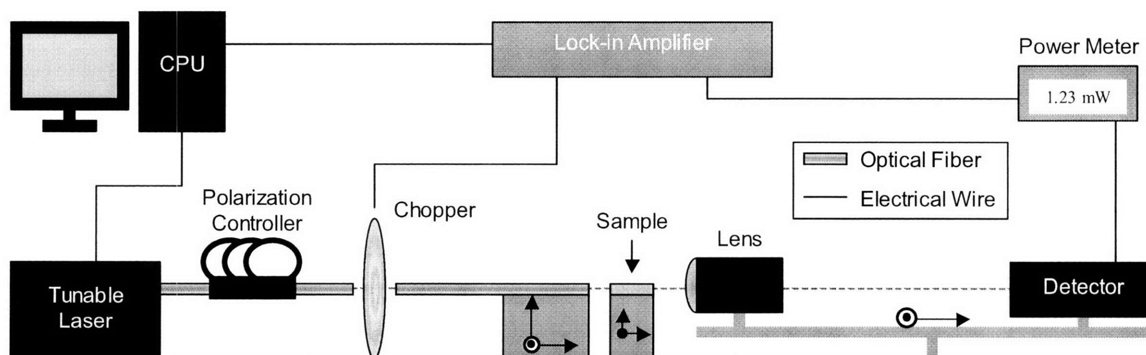

Figure 3.15 – Schematic of the Table 3 Waveguide Measurement System

3.6.2 Newport-JDS System

The Newport-JDS system is made up of a Newport Auto-Align Station and a JDS Uniphase Swept Wavelength System (SWS). This measurement system utilizes a fiber in/fiber out measurement. The Newport Auto-Align station consists of two towers, with four degrees of freedom, to precisely align input and output fibers to the waveguide sample, an alignment laser, and a detector. The alignment procedure involves placing the input fiber near a chosen waveguide and using a lens (mounted to the output tower) and IR camera to ensure that light is guided through the waveguide. Once the input fiber is aligned, the output fiber is aligned to the waveguide output and aided visually by a microscope mounted above the sample and quantitatively with the detector (note: the lens, IR camera, and microscope are not shown in figure 3.16). Once the output fiber is coarsely aligned, the alignment can be optimized with a push of a button. The auto-align process is computer controlled (CPU2) and optimizes output power by independently moving input and output fibers with a precision of ±50 nm in the X, Y, and Z directions.

Once aligned, the two optical switches are activated, changing both the input laser source and output detection to the JDSU SWS unit. The SWS unit contains a tunable laser, polarization controller, and detectors that are computer controlled (CPU1) and designed for polarization dependent loss (PDL) measurement of optical devices. Spectral response measurements across the entire C and L bands (1520 – 1570 nm and 1570 – 1630 nm respectively) are accurate and take a little over a minute to perform. The polarization unit cycles through four polarization states (see section 2.4) enabling the minimum and maximum polarizations to be determined by the Mueller Matrix method. It is important to note that the min and max polarizations correspond to TE and TM modes only in cases of very simple waveguide geometry. In general, waveguides that support several modes will not have TE and TM modes corresponding to min and max polarizations.

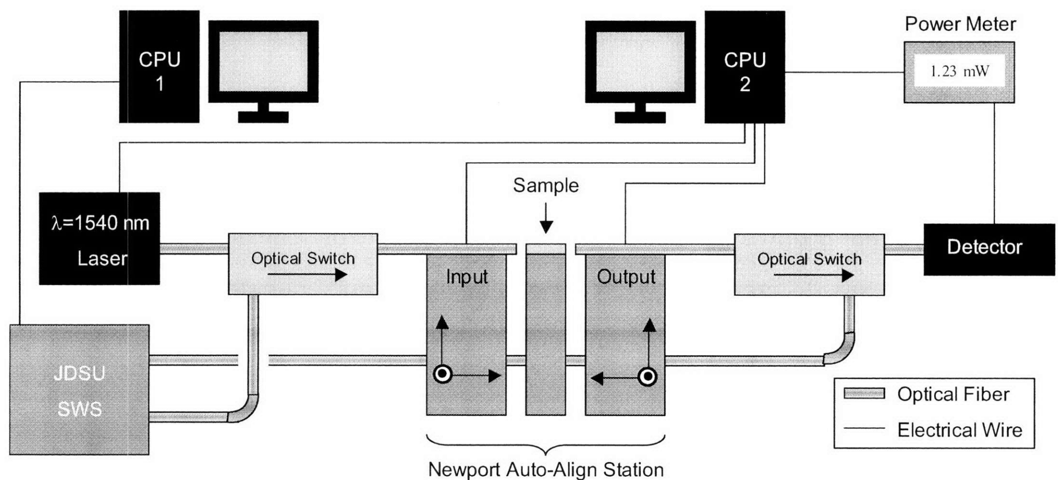

Figure 3.16 – Schematic of the Newport-JDS Waveguide Measurement System

3.7 Effective Experimental Design

Waveguide transmission loss measurements are effective only when the experiments are compatible with the noise level and dynamic range of a given measurement apparatus (see Figure 3.14). The first criterion to check when designing waveguide structures to test for loss is whether the insertion loss (equation 3.6) of the waveguide is less than the dynamic range (detector sensitivity) of the system:

$$\alpha_{Insertion} < Dynamic\ Range \tag{3.11}$$

This does require some knowledge of the losses of the waveguide in question; however order of magnitude estimations are satisfactory. If this criterion is not met, the output cannot be detected unless changes to the waveguide in the form of reducing coupling loss or truncating the length occur. The next option to consider is what type of transmission loss experiment will be used.

3.7.1 Cutback Measurement Concerns

If cutback loss is chosen, the length of the longest waveguide (L_{MAX}) is dictated by equation 3.8, and can be rewritten as equation 3.11.

$$L_{MAX} < \frac{Dynamic\ Range - \alpha_{Coupling}}{\alpha_{Transmission}} \tag{3.12}$$

In general, the longer the waveguide length range used in a cutback loss measurement, the smaller the experimental error, and thus it is preferable to maximize L_{MAX}. In cases where bend loss is negligible, it is possible to add extra bends to the waveguide to increase L_{MAX} without expanding the chip size or adding any significant error to the measurement.

The minimum waveguide length is typically dictated by practical matters such as the minimum chip size that can be easily manipulated and the length at which uncoupled, unguided or cladding guided light can diverge without appreciably elevating detection noise. For cutback measurements to be experimentally valid, the loss difference between the minimum and maximum length waveguides must be larger than the noise level of the measurement. At a minimum, this means that the length difference (ΔL) must meet relation 3.12.

$$\Delta L > \frac{Noise\ Level}{\alpha_{Transmission}} \tag{3.13}$$

Ideally, each waveguide length increment should meet the requirement of equation 3.12. Typical photodetector noise levels are of the order of 1% and dominated by shot noise [30].

3.7.2 Fabry-Perot Measurement Concerns

The ability to measure the fabry-perot resonance of a waveguide is dependent on the signal to noise level of the system, spectral resolution of the system, and the waveguide reflection coefficient. The first thing to check when is the best case scenario, where a waveguide has zero loss, to ensure that the resonance can be detected. Using equation 3.9, and inserting α_T=0, yields the maximum contrast ratio as a function of the facet reflection coefficient (R), which must be much greater than the noise level of the system.

$$\left(\frac{I_{Max}}{I_{Min}}\right)_{\alpha=0} \rightarrow \frac{(1+R)}{(1-R)} >> (1+\textit{Noise Level}) \tag{3.14}$$

Without satisfying equation 3.13, the fabry-perot fringes will be indistinguishable from random fluctuations in the optical system due to noise, and this is for a zero loss waveguide. The addition of transmission loss reduces the fringe contrast further, requiring larger facet reflection coefficients for detection. Large facet reflection coefficients, such as those of HIC waveguides, alleviate this issue. Alternatively, deposition of a reflective material on the facets of a waveguide can be used to increase R [31].

The spectral resolution required for a fabry-perot measurement inversely scales with the length of the waveguide. Consequently it is important to keep track that the length of the waveguide is such that the fringe spacing ($\Delta\lambda_{Fabry\text{-}Perot}$) is larger than the spectral resolution of the laser ($\Delta\lambda_{Laser}$). This relation is shown in equation 3.14 where λ is the wavelength, n is the group index of the waveguide, and L is the waveguide length.

$$\Delta\lambda_{Fabry-Perot} \approx \frac{\lambda^2}{2nL} > \Delta\lambda_{Laser} \tag{3.15}$$

Therefore, reducing the length of a waveguide not only increases the fringe spacing but it also reduces transmission loss. However, reducing the length too much can result in measurement errors in terms of less precision and alignment drift during wavelength scans, where the scan time scales with fringe spacing.

Chapter 4 – Waveguide Loss Mechanisms

This chapter reviews various loss mechanisms that can occur in waveguides within the context of CMOS-compatible, integrated, HIC waveguides. First, a review of planar waveguide fabrication is presented to provide the background necessary in understanding the limitations that exist in thin-film processing. Second, various loss mechanisms, of which many arise due to process limitations, are identified and illustrated with experimental data. In addition, the pertinent theory and methods with which to identify each loss mechanism are discussed. In understanding the various waveguide loss mechanisms, the critical process and design parameters can be identified and optimized for improved optical transmission.

4.1 Planar Waveguide Fabrication

4.1.1 Waveguide Process Flow

The following is a basic process flow for a single level HIC waveguide. This process can be generalized to most planar, thin-film waveguides. Each step is depicted sequentially in figure 4.1.

1. *Deposit an undercladding layer.* This layer is intended to optically isolate the waveguide from the substrate. The required thickness is dependent on the light confinement of the waveguide, which is dependent on the index difference (Δn) between this underclad layer and the waveguide core material as well as waveguide geometry. SiO_2 is an optimal undercladding material for Si wafer substrates due to its low index of refraction ($n = 1.445$), optical transparency, and electrically insulating properties. We used both thermal and PECVD SiO_2 in our experiments. One detriment to using SiO_2 is its amorphous structure which precludes the growth of crystalline waveguide materials on top of the amorphous layer. To surmount this problem, Silicon-on-Insulator (SOI) wafers were purchased for crystalline Si waveguide experiments. For cases where the waveguide core material has a larger index than the substrate, such as when using silica substrates, this step may not be necessary.
2. *Deposit the waveguide core material.* The deposition parameters of the waveguide core materials can have a large impact on material microstructure which can affect material scattering, absorption, or surface roughness. The a-Si, poly-Si, and SiN waveguide materials used in this study were largely deposited with PECVD. This step was not needed for SOI wafers as the top Si and SiO_2 undercladding layers are wafer bonded to a Si substrate by the manufacturer. The waveguide material thickness is determined by waveguide design (i.e. waveguide type: ridge or channel, and waveguide mode: single or multi-mode).
3. *Deposit photo-resist.* Photo-resists are photosensitive polymers that react in the presence of ultraviolet light. The chemistry and thickness of the photoresist are optimized for the wavelength of light used in the exposure. Deposition occurs through spin-on techniques where the thickness

of the resist is determined by the rate at which the wafer rotates. Photoresist thickness is set primarily to be compatible with minimum feature size and processing requirements, such as etch depth at a known selectivity and exposure time for a given UV-irradiation dose. After the spin-on step a soft-bake is used to dive out the carrier solvent to give mechanical and chemical stability.

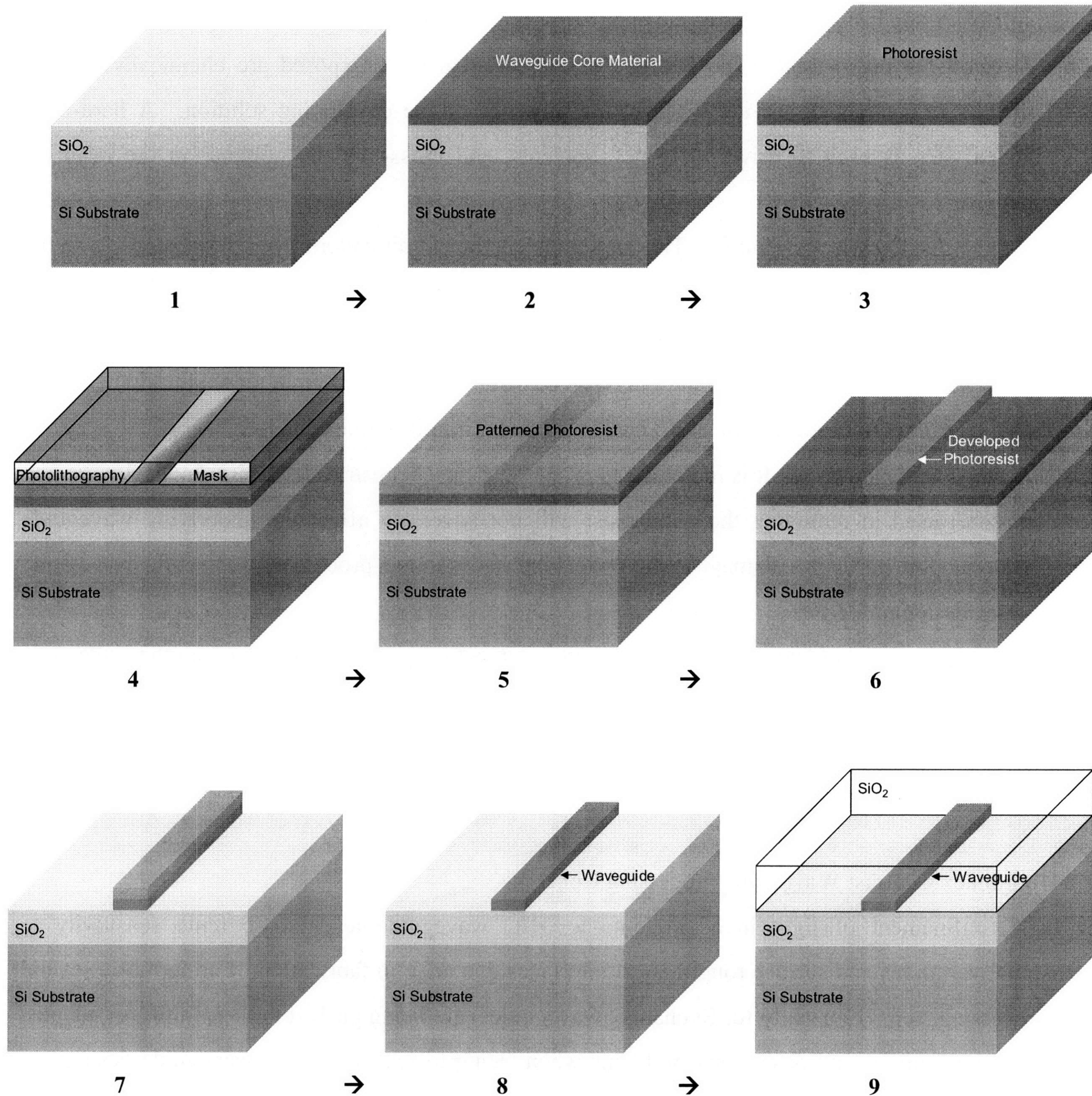

Figure 4.1 – Basic process flow schematic for CMOS-compatible integrated HIC waveguides. Steps are detailed above and below.

4. *Align the photolithography mask to the substrate.* The mask is typically comprised of a slab of high optical quality quartz with a metallic chrome pattern in the shape of the circuit. The pattern

is written with nm-scale accuracy with an e-beam. Alignment of the mask is critical when multiple chip levels are used; alignment error will result in reduced photonic device performance.

5. *Expose the photoresist.* The waveguide pattern is transferred from the mask to the photoresist by exposing and chemically altering the photoresist with ultraviolet light. The resolution of the pattern transfer scales inversely with the wavelength of light used. In most cases, an additional soft-bake step is used to improve the photoresist properties.
6. *Develop the photoresist.* The portions of the resist that are exposed are chemically altered, thereby selectively dissolving when in the presence of the developing solution. A hard-bake anneal step is used to drive out water, solvents, and cross-link the polymer in the resulting pattern.
7. *Etch and define the waveguide.* This step transfers the circuit pattern from the photoresist to the waveguide material. Here the etch chemistry is used to remove the waveguide material that is not protected by the photoresist. Etch selectivity between the waveguide material and photoresist is critical in ensuring dimensional integrity. Etch chemistry and polymerization on the sidewalls are also important to ensuring a near 90° etch angle and minimized line edge roughness.
8. *Remove the photoresist.* It is important to ensure that the chemistries (e.g. piranha, or dry oxygen plasma) used in removing the photoresist will not adversely affect the underlying waveguide materials. In particular, damage to the optical interfaces in this process may affect the waveguide transmission properties.
9. *Deposit the top cladding.* This final processing step is to deposit a top cladding on the waveguide structure. There are many advantages to using a top cladding: it shields the waveguide surface from contamination, reduces the amount of birefringence by providing a symmetrical structure for the guided mode, and facilitates easier sample preparation.

4.1.2 High Index Contrast Waveguide Processing Concerns

The high confinement of light in a single-mode, HIC waveguide leads to extreme sensitivity to dimensional variations and surface roughness at interfaces that arise in fabrication. Furthermore, several of the processing steps (especially for Si channel waveguides) are being pushed to their limits, or adapted from other applications, and pose many problems when trying to realize a given waveguide design. In particular the process concerns that relate to etch profile, lithographic resolution, and interface smoothness are the major challenges in HIC waveguide fabrication.

Etch Profile

A straight etch profile as drawn in figure 4.2a is important in that deviations in waveguide etch angle will result in altered group velocity, transmission loss, bend loss, and perhaps most importantly polarization coupling. Slanted sidewalls as shown in Figure 4.2b and 4.2c can break symmetry in the mode shape and lead to coupling between the TE and TM modes within and between waveguides [32].

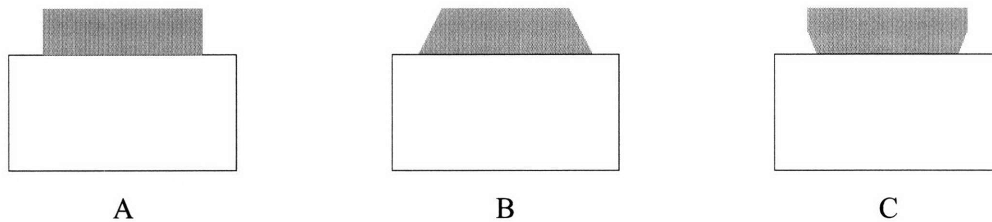

A B C

Figure 4.2 – Ideal waveguide etch profile (A) and non-ideal slanted (B) and inverted (C) waveguide etch profiles as viewed in cross-section.

The non-ideal, slanted waveguide etch profile depicted in Figure 4.2b, is typical of photoresist mask erosion during the etch process in which the selectivity between the waveguide material and photoresist is not total. The use of a hard-mask or improved etch chemistry can remedy this situation. In contrast, the inverted etch profile depicted in Figure 4.2c is typical of excessive waveguide etch time. In this scenario, the waveguide etch does not etch the undercladding layer and by exceeding the needed etch time, the waveguide etch attacks the bottom portion of the waveguide, as it has the least amount of protective polymerization on the sidewall.

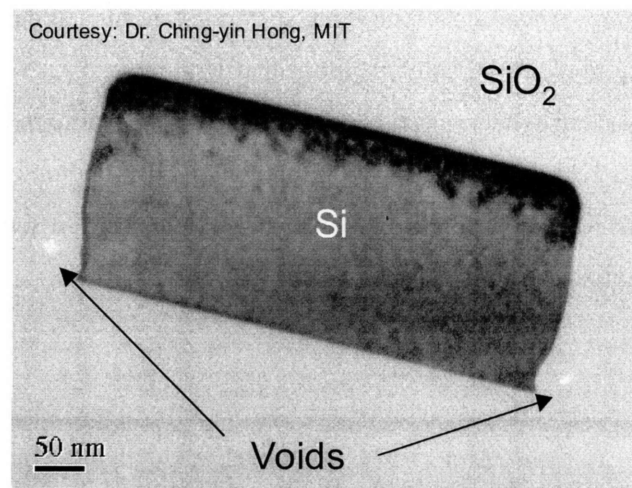

Figure 4.3 – TEM cross-section of a SOI waveguide with SiO2 top cladding, the inverted etch profile in combination with rapid top cladding deposition resulted in the formation of air voids.

The inverted etch profile can also result in other fabrication complications. Figure 4.3 is a TEM cross-section of an SOI waveguide that was over-etched so as to create the inverted etch profile. As seen in this figure, the formation of voids was observed in several wafers in this process run. The voids are believed to be a result of rapid, top cladding deposition in combination with a shadowing effect from the inverted etch profile. In terms of waveguide transmission loss, the voids are disastrous, as they presumably vary in size and shape in the propagation direction of the waveguide and scatter light.

Lithographic Resolution

The lithographic resolution needed to realize HIC waveguide devices is astonishingly many times smaller than the wavelength of light (λ_{signal}) that the waveguides are designed to support. To first order, waveguide dimensions scale with the index of refraction (n_{core}) and thus HIC waveguide should expect the needed resolution to be at least a fraction of $\lambda_{signal}/n_{core}$. As an example, Si waveguides designed for single-mode operation with 1.55 μm light have a cross-section of roughly 200x500 nm^2. However, for more complex HIC devices – waveguide ring resonators and multimode interferometers (see Figure 4.4), there are even smaller feature sizes (particularly the gap between the waveguide and ring) which drive the required lithographic resolution to as low as tens of nanometers. To accommodate these needs, deep ultra violet (deep-UV) or electron beam (e-beam) lithography is needed to fabricate optimized HIC waveguide circuits.

While e-beam lithography offers more or less the best possible resolution, it is not well suited for manufacturing purposes as it is a time-consuming, serial processing method. Notwithstanding, e-beam is an excellent research tool for fabricating individual devices and small circuits with the added cost bonus of not requiring a photolithography mask. Despite these research benefits, all devices in this thesis were fabricated and measured using photolithographic methods that lend themselves to low cost, high volume manufacturing. Ironically, this research approach is more expensive, but more in line with the fabrication issues that will arise with large scale fabrication of integrated HIC photonic circuits. The limited photolithographic resolution of MIT's clean room facilities necessitated the outsourcing of our fabrication to Lincoln Labs and British Aerospace Engineering (BAE).

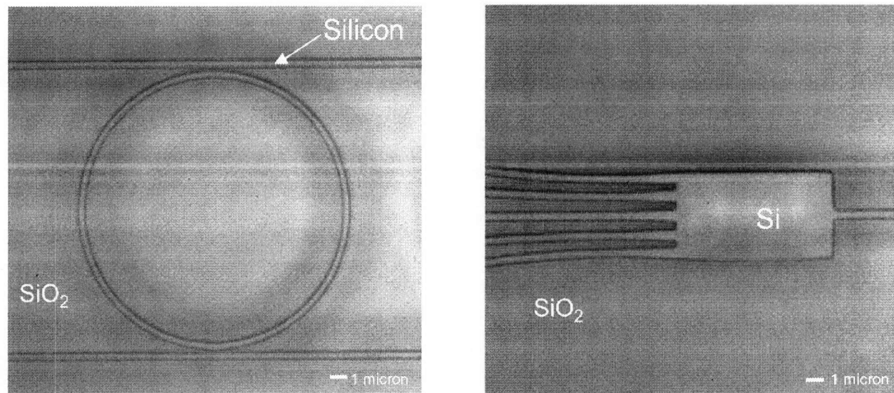

Figure 4.4 – Si ring resonator structure (left) and 5X1 MMI (right). Courtesy: Andrew Pomerene, BAE Systems

Interface Smoothness

Light is debatably the most accurate measuring tool that we possess. By the same token, the small-scale dimensional variations (roughness) that occur as a consequence of imperfect pattern transfer from the photolithography mask to the waveguide affect the transmission of light through a waveguide. In thin film processing, the top and bottom surfaces of waveguides tend to be smooth whereas the sidewalls tend to exhibit roughness that arises from the etch process. This can be seen in figure 4.5, where a freshly etched SiN waveguide is viewed from two perspectives. The 45° view clearly shows that the waveguide sidewall roughness is made up of vertical striations that exhibit some periodicity, whereas the top surface is comparatively smooth. The overhead view in Figure 4.5 reveals the effects of etching two closely spaced waveguides: increased roughness and dimensional variation near the gap. The edges of the top waveguide should be parallel, however comparing the bottom edge to the dashed line reveals that it is not. This phenomenon is caused by proximity effects that occur in the photolithography exposure step and the etch step.

For the photolithography step, as the width of the gap between the two waveguides approaches the lithographic resolution, the impinging optical flux on the photo-resist in the gap diminishes, resulting in reduced exposure, underdevelopment of the resist, and thus reduced gap size. For the etch step, the flux of chemical etch species is reduced, as a result of the high-aspect ratio gap geometry, and results in a reduced etch rate in the gap. Large feature size differences are often the cause of differential etch rates across the wafer and can be remedied by adding features to the mask to ensure isotropic etch fluxes that balance the etch rate, a phenomenon known as etch loading. In combination, the optical and etching proximity effects result in under-etched gaps with increased sidewall roughness: a problem that must be compensated for in HIC photonic circuit design.

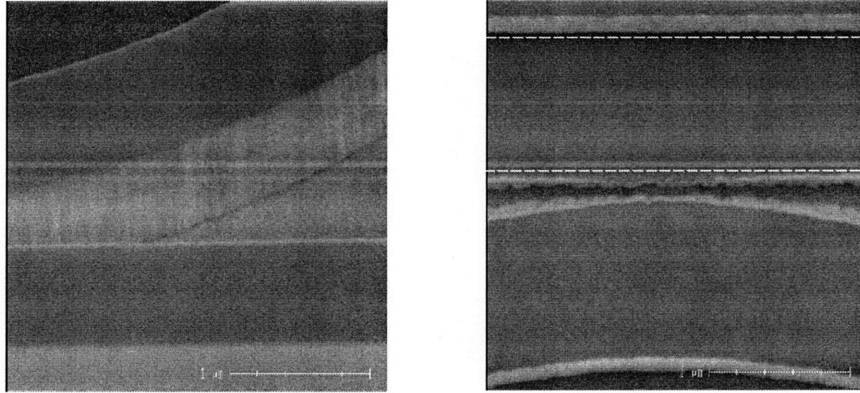

Figure 4.5 – SEM of a SiN waveguide 45° view (left) and overhead view (right). Courtesy: Dr. Steven Spector, Lincoln Laboratories

4.2 Loss Mechanism Overview

In general, waveguide transmission loss is caused by one or more of the following: light scattering, absorption, and coupling to radiation or other guided modes. Some losses are inherent to fabrication or waveguide material properties, whereas other losses can be attributed to waveguide design. The following sections will detail the various loss mechanisms in terms of the variables listed below.

Material Properties

- α_{bulk} – Bulk Material Absorption
- B – The two photon absorption (TPA) coefficient
- n_{clad} – The index of refraction of the cladding
- n_{core} – The index of refraction of the core

Interface Properties

- σ – The standard deviation or root mean square (RMS) of the roughness
- L_c – The correlation length of the roughness
- Δn – The index of refraction difference between the waveguide core and cladding – $f(n_{clad}, n_{core})$

Design Properties

- n_{eff} – The effective index of the waveguide – $f(n_{clad}, n_{core}, h, w)$
- h – The height of the waveguide
- w – The width of the waveguide
- R – The bend radius
- Γ – The fraction of power in the waveguide core
- P – The optical power
- $t_{underclad}$ – The thickness of the undercladding

δ – The distance between adjacent waveguides

θ – The angle between the substrate and etched waveguide sidewall

The waveguide loss mechanisms detailed in this chapter can be classified by loss type:

1. Radiation – Roughness Scattering and Bend Loss
2. Absorption – Linear and Non-linear
3. Coupling – Waveguide-to-Waveguide, Mode-to-Mode, and Substrate Leakage

Alternatively, the loss mechanisms can be classified under loss origin:

1. Processing – Roughness Scattering, Material Absorption
2. Design – Bend Loss, Waveguide-to-Waveguide coupling, Substrate Leakage, Non-linear Absorption

The loss mechanisms that are processing-based remain as the major challenges to realizing low-loss waveguides. However, in research, unknowns in using new materials and processing methods can lead to deviations in design and a full understanding of all waveguide loss mechanisms is necessary to interpret waveguide transmission data. Hence in the following sections, methods of understanding and identifying each loss mechanism are detailed.

4.3 Roughness Scattering – f (Δn, σ, L_c, h, w)

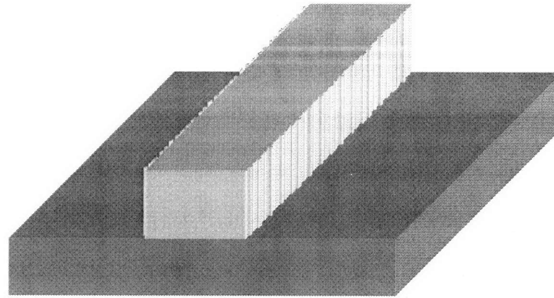

Figure 4.6 - Waveguide with sidewall roughness

Light scattering from a rough core/cladding interface is often the dominant transmission loss mechanism for high index contrast waveguides. The roughness is usually confined to the waveguide sidewalls, as shown in Figure 4.6, and is a consequence of the etching step, wherein the roughness appears as vertical striations and can be characterized as a one dimensional roughness f(z) along the waveguide axis.

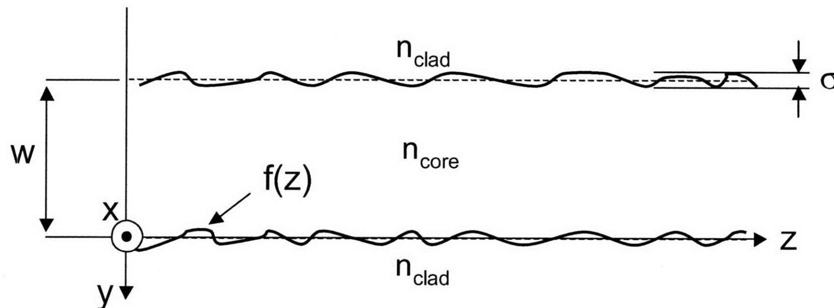

Figure 4.7 – Overhead view of a symmetric waveguide with sidewall roughness f(z)

4.3.1 Mathematically Describing Roughness

Waveguide sidewall roughness is a random fluctuation in the waveguide width that can be characterized by its amplitude and distribution of spatial frequency components. It is mathematically convenient in roughness scattering analysis to define the waveguide width such that the roughness distribution has zero-mean:

$$\int_{-\infty}^{\infty} f(z)\, dz = 0 \tag{4.1}$$

The roughness amplitude can be characterized by σ, the standard or root-mean-squared deviation of f(z) from the waveguide width w. Roughness measurement by SEM or AFM will result in a discrete distribution, in these cases, σ can be characterized by:

$$\sigma = \sqrt{\frac{1}{N-1}\sum_{i=1}^{N}\left(y_i - \bar{y}\right)^2} \tag{4.2}$$

where N is the number of measurements, y_i is the value of f(z) for each measurement, and $\bar{y}$ is the average value of y_i over N. For the f(z) depicted in Figure 4.7, $\bar{y}=0$.

The degree of periodicity in a given roughness can be characterized by the autocorrelation function R(u).

$$R(u) \equiv \langle f(z)f(z+u)\rangle = \lim_{T\to\infty}\left[\frac{1}{2T}\int_{-T}^{T} f(z)f(z+u)dz\right] \tag{4.3}$$

The autocorrelation function is simply a way of measuring the amount of similarity a function has to itself when displaced by u. If f(z) = sin(z), R(u) would have maxima when u = 2mπ and minima when u = (2m+1)π, where m is an integer. For random distributions, R(u) is typically a smooth function with a single peak, such as a Gaussian distribution.

The distribution of spatial frequency components can be obtained from the power spectral density (PSD) function of the roughness. The PSD is given by $\tilde{R}(\xi)$ the Fourier transform of R(u) the autocorrelation function.

$$\tilde{R}(\xi) = \int_{-\infty}^{+\infty} R(u)\, e^{i\xi u}\, du \tag{4.4}$$

The PSD can be viewed as the amount of each spatial frequency component (ξ) contained within f(z). For the example of f(z)=sin(z), $\tilde{R}(\xi)$ has a single value that corresponds to the spatial frequency 2π/z.

4.3.2 Measurement of Sidewall Roughness

Direct measurement of waveguide sidewall roughness to find f(z) is experimentally difficult. As a result, there have been only a few studies on the subject. Ladoceur et al. [38] estimated the sidewall roughness for silica waveguides by measuring the line edge roughness (LER) of the photolithography mask with an AFM. This study was the first to identify the analytical form of the autocorrelation function in thin film processing. Practically, the large step height and steep angle of ideally etched waveguides all but

prevents AFM measurement of actual waveguide sidewalls. However, Kuribayashi et al. managed to overcome this difficulty by cleaving the wafer next to the etched surface [41]. Lee et al. used TEM to examine the LER of Si-SiO_2 waveguides [43]. In another study, Barwicz et al. [39] used an SEM to measure the LER at various stages during HIC waveguide fabrication. Each waveguide roughness study [39, 41, 42] agreed that the autocorrelation of the sidewall roughness can be well approximated by:

$$R(u) \approx \sigma^2 e^{-\left(\frac{|u|}{L_c}\right)} \tag{4.5}$$

where σ is the RMS roughness and L_c is the correlation length of the roughness. It is interesting to note that the autocorrelation of Si-SiO_2 interface roughness is also found to be well approximated by an exponential form [33].

The magnitude of L_c is related to the length scale of the roughness. For HIC waveguides, L_c values are typically below 200 nm [39] and in the neighborhood of 50 nm [39, 42]. SEM pictures that show the vertical striated sidewall roughness with a characteristic period, such as in Figure 4.5, can be used to approximate the order of the L_c. Inserting (4.5) into (4.4), we find that the PSD of sidewall roughness will have a Lorentzian form with a half width of $1/L_c$.

$$\tilde{R}(\xi) \approx \frac{2\sigma^2 L_c}{1 + L_c^2 \xi^2} \tag{4.6}$$

4.3.3 Roughness Scattering Theory

Mathematical modeling of the roughness scattering loss was first devised by Marcuse [34], who used a coupled mode theory approach to model the coupling between the guided modes and the radiation modes from a slab waveguide with a random sidewall roughness. The solutions to Marcuse's approach were exact but were rather involved and did not have an analytical form. In efforts to make waveguide loss evaluations more tractable, Payne and Lacey [35-36] utilized the volume current method (VCM) to arrive at an analytical method of calculating roughness scattering loss. VCM theory [37] is a perturbation technique for calculation of small transmission loss and assumes that the roughness is small in comparison to the waveguide dimensions. All that is needed for VCM theory is the electric field inside the guide, the waveguide dimensions, and the roughness distribution.

Payne-Lacey Theory of Roughness Scattering Loss

The Payne-Lacey approach models the interaction of the primary waveguide mode with two rough sidewalls in a symmetrically clad slab waveguide geometry [35]. The two sidewalls are assumed to be randomly distorted with identical distributions that are uncorrelated with each other and can be characterized by a one dimensional roughness function f(z) with a zero-mean distribution along the waveguide axis (see figure 4.7). The loss is calculated by comparing the far-field radiation from roughness scattering to the guided power within the waveguide. In this theory the wave equation (Eq. 2.13) refractive index distribution is rewritten to accommodate the varying roughness:

$$n^2 = n_{clad}^2 + \left(n_{core}^2 - n_{clad}^2\right)U\left[f(z) - |y|\right] \tag{4.7}$$

where the perturbation is accounted for with the unit step function $U\left[f(z)-|y|\right]$ such that:

$$\begin{aligned} U\left[f(z)-|y|\right] &= 0 \qquad |y| > f(z) \\ U\left[f(z)-|y|\right] &= 1 \qquad |y| < f(z) \end{aligned} \tag{4.8}$$

which yields:

$$\begin{aligned} n^2 &= n_{clad}^2 \qquad |y| > f(z) \\ n^2 &= n_{core}^2 \qquad |y| < f(z) \end{aligned} \tag{4.9}$$

Inserting (4.7) into the source-free wave equation and assuming that the field in the slab is of the form $\vec{E} = \vec{E}_x\left(y,z\right)e^{i\omega t}$ we find:

$$\nabla^2 \vec{E}_x\left(y,z\right) + k_0^2 n_{clad}^2 \vec{E}_x\left(y,z\right) = k_0^2\left(n_{clad}^2 - n_{core}^2\right)U\left[f(z)-|y|\right]\vec{E}_x\left(y,z\right) \tag{4.10}$$

In this form, equation (4.10) cannot be solved analytically, however by approximating the E-field as that of an ideal, single-mode waveguide with no roughness (E_{ideal}); a solution can be found. This assumes that the roughness amplitude is such that it does not appreciably affect the electric field distribution in the guide (i.e. it is a small perturbation). In this analysis, E_{ideal} can be obtained from the E-field distribution of a slab waveguide:

$$\vec{E} = \Phi(y)e^{i(\omega t - \beta z)} = \vec{E}_{x,ideal}\left(y,z\right)e^{i\omega t} \tag{4.11}$$

where both β and Φ can be determined from our derivation of the slab waveguide mode in chapter 2.3. Inserting E_{ideal} into the right hand side of (4.4) is a reasonable approximation in that it only contributes for the case when U=1, $n^2 = n^2_{core}$, and is thus only dependent on the field inside the waveguide. Applying (4.11) to (4.10):

$$\nabla^2 \vec{E}_x(y,z) + k_0^2 n_{clad}^2 \vec{E}_x(y,z) = k_0^2 \left(n_{clad}^2 - n_{core}^2\right) U\left[f(z) - |y|\right] \vec{E}_{x,ideal}(y,z) \tag{4.12}$$

The right hand side of (4.12) is mathematically equivalent to a current source and acts as the source of radiation from the waveguide. In other words, the interaction of the waveguide E-field with the rough sidewall effectively creates an oscillating charge at the core-cladding interface which radiates power from the guided mode. Solutions of (4.12) take the form of Green functions, yielding $E_x(y,z)$ the far-field pattern of the radiated field in space. Since the guided mode does not contribute to the far field, the integration of the ensemble average of the radiated field intensity $\langle |E_x(y,z)|^2 \rangle$ over space, is equal to the power radiated. After several algebraic steps, Fourier transforms, and switching coordinate systems, Payne and Lacey found that the loss associated with roughness scattering, defined as the radiated power per unit length divided by the guide power, as:

$$\alpha = \Phi^2(w)\left(n_{clad}^2 - n_{core}^2\right)^2 \frac{k_0^2}{4\pi n_{clad}} \int_0^{\pi} \tilde{R}\left(\beta - k_0 n_{clad}\cos(\theta)\right) d\theta \tag{4.13}$$

where $\Phi^2(w)$ is the normalized E-field intensity at the sidewall.

From this analysis, one can ascertain several insights into how light is scattered by a randomly distributed roughness at a waveguide interface. First we see that roughness scattering loss (α) is proportional to the integral of $\tilde{R}\left(\beta - k_0 n_{clad}\cos(\theta)\right)$, the power spectral density function (defined in (4.4)). Thus, the total radiated power can be viewed as a sum of the power carried by each of the radiated plane waves. Second, the angle (θ) at which each plane wave radiates from the core/cladding interface, corresponds to a specific spatial frequency component. If the roughness were sinusoidal, the guided light would only scatter at a single angle, identical to how grating couplers function. Third, the limits of the integral imply that there is a limited set of spatial frequencies (4.14) that scatter a given wavelength of light out of the waveguide.

$$\beta - n_{clad} k_0 < \xi < \beta + n_{clad} k_0 \tag{4.14}$$

Recalling that $\beta=n_{eff}k_0$, elucidates that the spectrum of spatial frequencies that contributes to roughness scattering loss is simply dependent on the wavelength of light (λ) and the difference between n_{eff} and n_{clad}. Therefore, the range of spatial frequencies ξ and spatial wavelengths Λ decrease with Δn for single mode channel waveguides; some examples are listed in Figure 4.8.

Waveguide Core (n_{core}), Cladding (n_{clad})	$n_{eff}=\beta/k_0$	Spatial Frequencies $\xi(\mu m^{-1})$		Spatial Wavelengths $\Lambda(\mu m)$	
		Minimum	Maximum	Minimum	Maximum
Si (n=3.5), SiO_2 (n=1.45)	2.5	4.3	16.0	0.39	1.48
SiN (n=2.0), SiO_2 (n=1.45)	1.7	1.0	12.8	0.49	6.2
SiON (n=1.7), SiO_2 (n=1.45)	1.6	0.6	12.4	0.51	10.3

Figure 4.8 – The range of spatial roughness frequencies ξ and wavelengths Λ which contribute to scattering of λ=1550 nm light for three single mode waveguides with different core indices. ($\Lambda=2\pi/\xi$)

It is interesting to note that the minimum spatial roughness wavelength that contributes to scattering of λ=1550 nm light is nearly constant for all three waveguide systems in figure 4.8. Short wavelength roughness is particularly difficult to control on etched surfaces.

Applying Payne-Lacey Theory to Rectangular Waveguides

In an effort to expand their theory to other waveguide geometries, Payne and Lacey presented a method of applying the scattering profile of a slab waveguide (as just described) to that of a rectangular waveguide [36]. Basically, the radiation profile of a rectangular waveguide is approximated by a slab waveguide with the same effective index. To improve accessibility to this theory, (4.13) was rewritten in terms of fundamental waveguide properties. In this derivation, a TE_0 slab mode field distribution and an exponential correlation function similar to (4.5) were used. The resulting closed form solution is defined in terms of normalized waveguide parameters

$$U=\frac{w}{2}\sqrt{n_{core}^2k_0^2-\beta^2} \quad V=k_0\frac{w}{2}\sqrt{n_{core}^2-n_{clad}^2} \quad W=\frac{w}{2}\sqrt{\beta^2-n_{clad}^2k_0^2} \tag{4.15}$$

and dimensionless parameters,

$$\Delta=\frac{n_{core}^2-n_{clad}^2}{2n_{core}^2} \quad x=W\frac{2L_c}{w} \quad \gamma=\frac{n_{clad}V}{n_{core}W\sqrt{\Delta}} \tag{4.16}$$

to find the Payne-Lacey Loss equation:

$$\boxed{\alpha = \frac{\sigma^2}{\sqrt{2}k_0\left(\frac{w}{2}\right)^4 n_{core}} g(V) f_e(x,\gamma)} \tag{4.17}$$

where:

$$g(V) = \frac{U^2V^2}{1+W} \qquad f_e(x,\gamma) = \frac{x\left\{\left[\left(1+x^2\right)^2 + 2x^2\gamma^2\right]^{\frac{1}{2}} + 1 - x^2\right\}^{\frac{1}{2}}}{\left[\left(1+x^2\right)^2 + 2x^2\gamma^2\right]^{\frac{1}{2}}} \tag{4.18}$$

Equation (4.17) is a closed form solution that furthers our understanding of how sidewall roughness affects the transmission loss (α) of a waveguide. In particular, the σ^2 and w^{-4} variations with α are key relationships to optimize for reduced transmission loss. Reducing σ, the roughness amplitude, can be achieved by improving the waveguide etch process. Thus a reduced roughness will decrease the radiation efficiency of the roughness and lower loss. Alternatively, increasing w, the width of the waveguide, will decrease the intensity of the E-field at the rough sidewall and reduce the relative amount of scattered light. However, this latter approach is often not feasible in that increasing w past the second mode cutoff width will cause multi-mode operation in the waveguide. The g(V) and $f_e(x,\gamma)$ terms vary slowly with changes in waveguide parameters and do not have a dramatic impact on loss for a given waveguide system.

Applying Payne-Lacey Theory to HIC waveguides

In order to evaluate this theory, a single-mode, 200x500 nm^2 cross-section, SiO_2 clad, Si channel waveguide is used in calculating the loss as a function of roughness statistics σ and L_c. The plots are shown in Figure 4.9, here the plot limits were chosen to match the ranges typically found in good HIC waveguide processing: $\sigma < 5$nm and $L_c < 200$ nm. The left plot of Figure 4.9 clearly shows that nm-scale σ and L_c have a large impact on the transmission loss, with particularly high sensitivity to σ. As expected, the loss is zero when roughness is nonexistent – when σ and L_c equal zero. Thus, to minimize loss for a given waveguide structure will require reduction of both σ and L_c.

In reality, improved processing techniques only reduce σ, as L_c seems to be fundamental to the pattern transfer process; the exact mechanism is still debated in the literature. With this in mind, the loss was plotted as a function of σ, with L_c= 50nm (a typical value found by [39,42]) in the right plot of Figure

4.9. The plot suggests that the roughness amplitude σ is incredibly sensitive to roughness scattering requiring sub-nanometer roughness to achieve losses that are adequate for use in integrated chips.

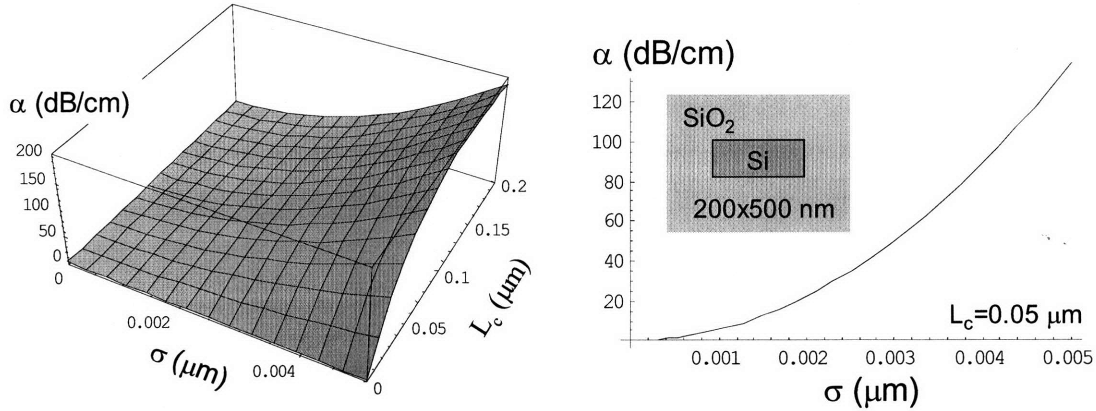

Figure 4.9 – Loss calculation using Payne-Lacey theory equation (4.17) for a single-mode Si channel waveguide with SiO_2 cladding (see right inset) for λ=1550 nm light as a function of σ the (RMS) roughness amplitude and L_c the correlation length of the roughness.

This extreme sensitivity and corresponding incredibly high predicted losses are not congruent with separately reported experimental results for loss and roughness; which brings into question the validity of the loss estimate method for rectangular waveguides as proposed by Payne and Lacey in [36]. As will be discussed in Chapter 5, experimental measurements of σ and α for Si waveguides suggest that the Payne-Lacey theory greatly overestimates the loss for HIC waveguides. In addition; the analysis of [36] and the equations in section 4.3.3c are only formulated for TM polarized light.

Barwicz-Haus Theory of Roughness Scattering Loss

In recognizing that the Payne-Lacey theory incorrectly applies two-dimensional radiation profiles to rectangular waveguides, Barwicz and Haus devised a method of calculating the proper three-dimensional radiation profiles and corresponding loss coefficients for symmetrically clad rectangular HIC waveguides [40]. Barwicz and Haus do so by a leading-order, three-dimensional waveguide analysis utilizing VCM theory. The analysis is in agreement with the results from Payne and Lacey in [35], however it deviates from the Payne-Lacey loss equation derived in [36] in three major ways to accommodate rectangular waveguides:

1. A three-dimensional radiation profile is calculated for a given rectangular waveguide.
2. Effects from radiated power scattered into the waveguide is accounted for – this is an issue for high Δn waveguides.
3. Both TE and TM polarization radiation profiles are calculated.

As one might expect, the mathematical analysis becomes quite complicated and as a result, a closed form analytical solution is not obtained as it was in [36]. Consequently, the loss results are graphically posed in two forms.

The first graphical result (not shown here) is a comparison of the radiated power from the 3D model (developed by Barwicz and Haus) to the 2D approximation (developed by Payne and Lacey) as a function of height and width of a rectangular waveguide for three HIC waveguide systems (Si/SiO_2, Si_3N_4/SiO_2, and $SiON/SiO_2$). There are two notable trends to this analysis. First, the deviation between 3D and 2D radiation efficiency increases with index difference, where the 3D model always radiates less power than the 2D model (i.e. the scattering efficiency is less for a given σ in the 3D model) for every waveguide type and geometry. The $SiON/SiO_2$ system ($\Delta n = 0.05$) deviates for most geometries by approximately a factor of two, whereas the Si/SiO_2 ($\Delta n = 2$) system is about a factor of ten. This suggests that approximating the radiation of a rectangular waveguide sidewall roughness with the radiation profile from a slab waveguide increasingly overestimates the loss with increasing Δn for channel waveguides. The second notable trend is that the short, wide waveguides have a larger deviation from the 2D model than the tall, skinny waveguides. This makes intuitive sense, since the 2D model is essentially approximating the waveguide as an infinitely tall waveguide. In a sense, the short, wide waveguides have less roughness to interact with and should radiate less power as a result. The take away message from this comparison is that short, wide HIC waveguides, that are well suited for integrated photonic applications, are inadequately approximated by the Payne-Lacey approach used in [36] and detailed in section 4.3.3c, however many of the qualitative aspects of [36] still hold.

The second graphical result (Figure 4.10) is a plot of loss coefficients as a function of height and width of a rectangular waveguide for three HIC waveguide systems (Si/SiO_2, Si_3N_4/SiO_2, and $SiON/SiO_2$), where the loss is obtained by multiplying the coefficient by σ^2. The correlation length is assumed to be 50 nm in this analysis; however a correction factor can be used to estimate the loss for another value of L_c. The plots are limited to single-mode dimensions for each waveguide system. In effect, these graphical results are relative values of the integrated E-field intensity along the sidewalls for the various waveguide geometries and systems. As expected, the increased confinement, and therefore E-field intensity at the sidewall, of high Δn waveguides results in corresponding higher sensitivity to a given sidewall roughness. This can be seen by comparing the loss coefficients for the different waveguide systems.

One nice aspect about modeling two uncorrelated rough sidewalls is that the losses are additive (this is true for the Payne-Lacey modeling as well). For example, if the two sidewalls have different roughness statistics, the loss from each sidewall can be calculated from the plots in Figure 4.10 and added to find the total loss. Similarly, top or bottom surface roughness loss can be calculated by considering the

waveguide as on its side for the opposite polarization. For example, the loss resulting from the rough top surface of a 200x500 nm^2 waveguide in the TE polarization is the same as half the sidewall loss of a 500x200 nm^2 waveguide in the TM polarization. A factor of ½ is included in this case to account for only one radiating surface (the top, not bottom surface).

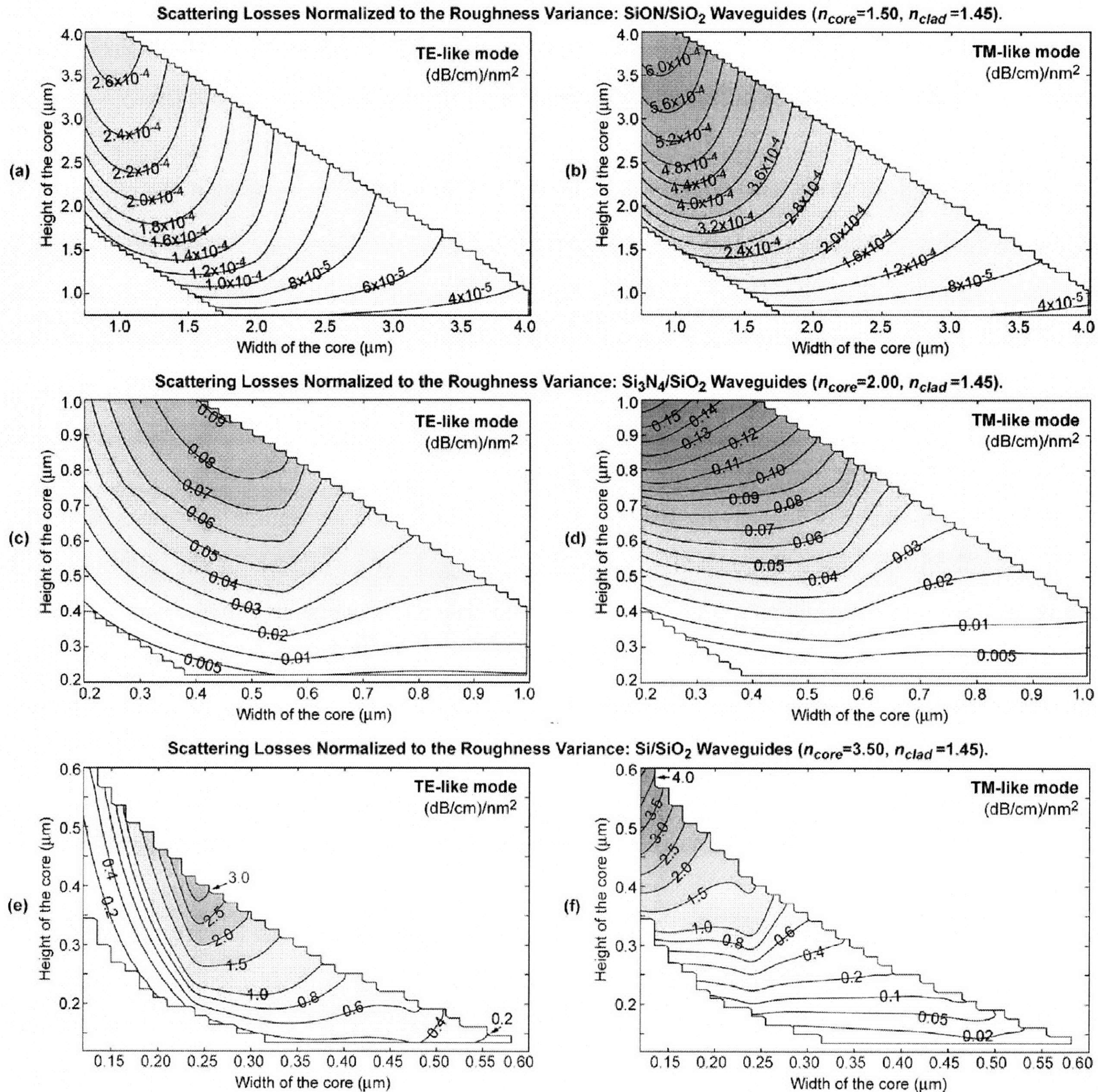

Fig. 12. Scattering losses in decibels per centimeter normalized to the roughness variance in square nanometers for (a) the TE-like mode and (b) the TM-like mode of SiON ($n_{\rm core} = 1.50$) waveguides, for (c) the TE-like mode and (d) the TM-like mode of Si_3N_4 ($n_{\rm core} = 2.00$) waveguides, and for (e) the TE-like mode and (f) the TM-like mode of Si ($n_{\rm core} = 3.50$) waveguides. All waveguides are embedded in an SiO_2 ($n_{\rm clad} = 1.45$) cladding. $\lambda = 1550$ nm and an exponential model of roughness with $L_c = 50$ nm are assumed. The scattering losses can be restored by multiplying the given quantity by the expected variance in square nanometers. For instance, if one expects $\sigma^2 = 10$ nm^2, the expected loss in the TE-like mode of a 200-nm-high and 400-nm-wide Si waveguide will be around 7 dB/cm.

Figure 4.10 –Roughness Scattering Losses calculated by Barwicz and Haus [40]

One particularly interesting aspect of this analysis is the polarization dependence of roughness scattering loss. As can be seen most clearly with the Si/SiO_2 system, the TM loss is less than the TE loss for all but the tall, skinny waveguide geometries. This observation fits well with the notion that the highest scattering loss occurs when the E-field is concentrated at the rough interface. For the TM mode, the intensity at the interface continually increases with decreasing waveguide width. This is not the case for the TE mode, though. The TE mode E- field distribution exhibits a discontinuity at the waveguide sidewall interface as a result of the electromagnetic interface boundary conditions (see Figure 2.11). This asymmetric behavior of the two polarizations is a direct result of only varying the permittivity ε and not the permeability μ at the core-cladding interface. As a result, the TE mode passes through a maximum in E-field interface intensity as the waveguide width decreases. This behavior is mirrored in the plots above, where the Si/SiO_2 loss exhibits a maximum loss for the TE polarization at $w \sim 0.25$ μm. Incidentally, this maximum loss width corresponds to the maximum mode confinement (i.e. highest field intensity). As the width shrinks past this maximum, the mode expands and the E-field interface intensity at the core/cladding interface decreases.

4.3.4 Experimental Identification of Roughness Scattering

There are several methods of identifying roughness scattering loss as a waveguide loss mechanism. If possible, it is useful to image the etched waveguides with SEM, to get a feel for the amplitude and wavelength of the sidewall roughness. It is also useful to inspect the waveguide to make sure the etched dimensions and film thicknesses for the waveguide layers match the design; large deviations from design can often result in other waveguide loss mechanisms.

Loss versus width

The most common method of identifying roughness-scattering loss is to plot the transmission loss as a function of waveguide geometry. By doing so, it is possible to gain insight into the magnitude of the roughness. Since our focus is on planar integrated circuits, it is generally easiest to vary the waveguide width, although this procedure can be readily extended to waveguides with different thicknesses. As discussed earlier, increasing the waveguide width decreases the intesity of the E-field at the core-cladding interface (for most waveguide geometries), resulting in less radiated power and thus less transmission loss. Therefore waveguide transmission loss is inversely proprtional to waveguide width.

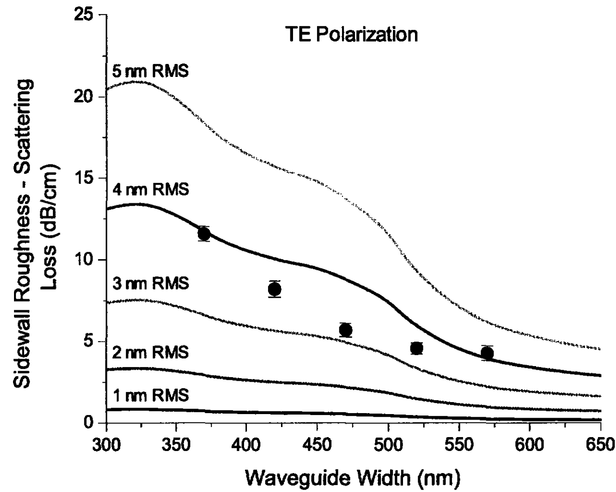

Figure 4.11 – Experimental Si/SiO_2 waveguide loss data (dots) and Barwicz-Haus sidewall roughness scattering theory predictions (lines) for different RMS roughness values. The waveguide height is 200 nm, λ=1550nm, TE mode.

Fitting the waveguide loss versus waveguide width data to the loss theory estimates listed above allows one to obtain the RMS roughness of the waveguide sidewall (σ). As seen in Figure 4.11, the fit between experiment and theory for waveguide loss versus width suggests a sidewall roughness of 3 – 4 nm.

Backscattering

Another characteristic of roughness-scattering loss, particularly for HIC waveguides, is that some of the light can be backscattered into the waveguide. This effect can be seen in the Fabry-Perot resonances (see appendix A). In Figure 4.12, the Fabry-Perot resonances from a straight Si/SiO_2 waveguide are plotted for both polarizations around λ=1550nm. The effect of backscattering is more evident in the TE mode, which is expected given the higher roughness sensitivity (due to the higher confinenment of light and thus higher integrated E-field insensity over the sidewall) in the 200x500 nm^2 waveguide geometry.

The oscillations in power versus wavelength (Fabry-Perot resonances) are a result of reflections at the waveguide facets and correspond to the constructive and destructive interference of forward and backward propagating light in the waveguide. For straight waveguides, the power oscillates between two powers and should closely fit a sinusoidal curve. However in practice, the Fabry-Perot resonances for high Δn waveguides exhibit amplitude peaks that randomly vary, where the extent of variation is correlated with the scattering efficiency of the waveguide. This is seen in Figure 4.12, where the more highly confined TE mode Fabry-Perot resonances have a wider variation in peak amplitudes than the less confined and thus less efficient scattering TM mode. Explaining the power fluctuation as a result of

measurement noise is dismissed given the 20 dB distance from the noise floor and the smoothness of the oscillations.

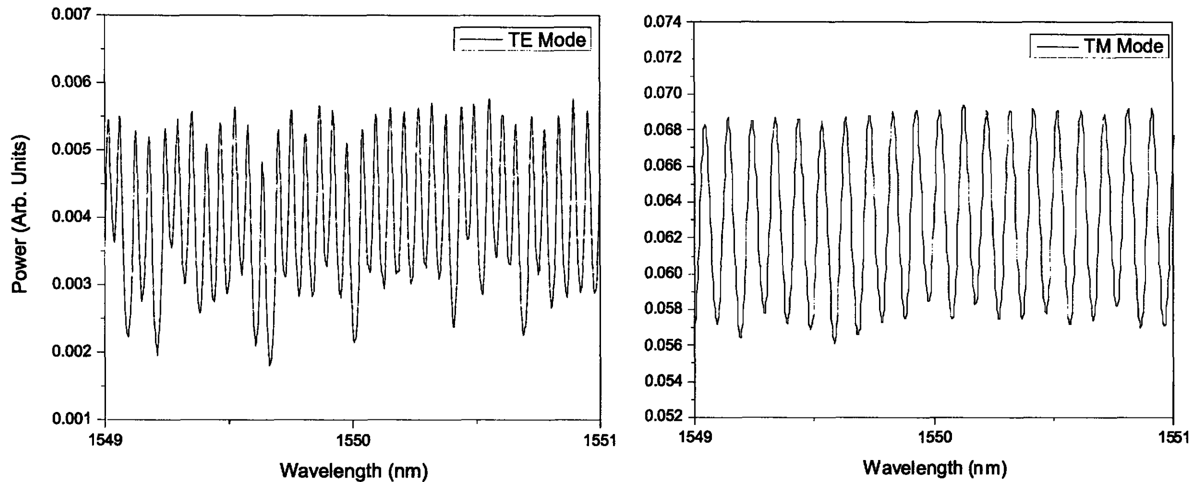

Figure 4.12 – Fabry-Perot Resonances of the TE (left) and TM (right) modes, for a straight 200x500 nm^2 Si/SiO_2 waveguide with a length of 0.5 cm.

Randomly backscattered light with varying amplitude and phase is one of the few reasonable mechanisms that can explain the peak resonant power fluctuation seen in Figure 4.12. The cause of this phenomenon is a direct result of light guiding in a high Δn waveguide with a random sidewall roughness. As discussed previously, the magnitude and direction of light scattered from a randomly distributed roughness is wavelength dependent and consequently, the magnitude of the backscattered light with be a similar random function of the wavelength. For backscattered light to affect the Fabry-Perot resonance output, its power must be on the same order as the reflected light from the waveguide facet. Just recently, Spector et al. reported measuring as much as 3% of the guided power as backscattered light from a 220x500 nm^2, TE polarized, Si channel waveguide [43]. This finding is a validation of this argument as it provides evidence that the magnitude of the backscattered light is indeed a non-negligible contributor to Fabry-Perot resonance. In comparison, the amount of guided light reflected at the waveguide facet, as calculated with 3D FDTD, is about 30 %. Thus, the varying peak amplitude of Fabry-Perot resonances in high Δn waveguides is a consequence and an indication of roughness scattering.

4.4 Absorption – f (α_{bulk}, Δn, h, w)

Material absorption is another common waveguide loss mechanism. In most cases, waveguide materials are chosen for their optical transparency, however there are certain photonic devices such as detectors or modulators where it is advantageous for the waveguide materials to absorb. Absorption is an

encompassing term that covers all loss mechanisms by which optical energy is transferred to the material as light traverses it. In particular, integrated HIC waveguides are susceptible to absorption mechanisms that arise from consequences of imperfect material deposition: dangling bonds, bond-resonances, nano-crystals; as well as fundamental optoelectronic properties such as bandgap absorption.

4.4.1 Common Thin Film Absorption Loss Mechanisms

Bandgap Absorption

Bandgap absorption occurs when the photon energy ($\hbar\omega$), exceeds the bandgap energy (E_g) of the waveguide core or cladding materials. For the case where $\hbar\omega > E_g$, the photon energy is absorbed by an electron in the valence band and promoted to the conduction band. This mechanism is the fundamental principle by which photo-detectors operate. For the case where $\hbar\omega < E_g$, the material is optically transparent, barring other loss mechanisms. For the telecom spectrum, most CMOS compatible dielectric materials have sufficient bandgap energies for optical transparency with the exception of Ge (which can be conveniently used as a detector material).

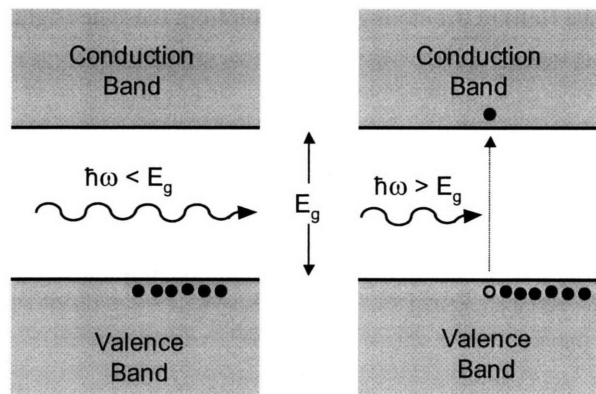

Figure 4.13a – A material is optically transparent for $\hbar\omega < E_g$ (left) absorbing for $\hbar\omega > E_g$ (right)

CMOS Compatible Material	Ge	SiGe	Si	SiN	SiON	SiO_2
E_g (eV)	0.67	0.67-1.1	1.1	4.7	4.7 - 9	9

Figure 4.13b – Bandgap energies for CMOS Compatible Materials at 300 K.

Dangling Bonds

Non-ideal deposition conditions of thin films can result in material defects that cause absorption loss. One particularly problematic defect occurs for amorphous depositions of crystalline materials in which some of the atomic bonds are not satisfied. These non-satisfied or "dangling" bonds contain an unbonded

electron which represents a state within the bandgap of the material. Hence, the presence of dangling bonds will result in absorption for photons which exceed the energy of the dangling bond energy state in the bandgap. In crystalline materials, the defect states are well defined. In amorphous materials, the heterogeneous space-charge environment experienced by dangling bonds results in a variety of inter-bandgap energy level states.

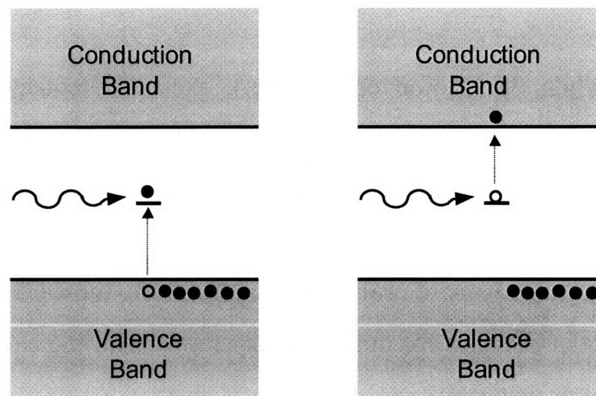

4.14 – Dangling bonds represent states within the bandgap that can act as absorption sites. Light absorption occurs by promoting an electron to the state (left) or promoting an electron from the state (right).

Bond Resonance

Bond-resonance absorption occurs for photons, with a frequency ω, that are closely matched to the resonant frequency ω_0 (or a harmonic) of a given atomic bond. Qualitatively, an atomic bond can be modeled as a harmonic oscillator, where the resonant frequency is characterized by:

$$\omega_0 = \sqrt{\frac{k}{m}} \tag{4.19}$$

where k is the spring constant or strength of the bond and m is the average mass of the bonded atoms. Hence, bonds between heavy atoms will resonate at lower frequencies and stronger atomic bonding will cause atoms with similar mass to resonate at higher frequencies. The spectral shape of an atomic bond resonance is Lorenzian and the spectral width is a function of the atomic bonding. For crystalline materials, the resonance will be sharp and thin, while for amorphous materials the inhomogeneous bonding results in a broad resonance.

For silicon compatible materials, the presence of N-H and O-H bond resonances can cause considerable absorption loss in integrated waveguides. The presence of H in waveguide materials is an unintentional remnant of the precursors (SiH_4 and NH_3) used in the deposition of silicon compatible

waveguide materials (a-Si, SiN, SiON, SiO_2). The N-H bond resonance absorption in SiN and SiON materials peaks at λ=1510 nm and has a rather large spectral width $\Delta\lambda \sim 60$ nm over which this loss is significant [44]. N-H bond absorption is particularly bad since it extends over a substantial portion of the telecom spectrum. One method of averting this issue is to use deuterium (D) based precursors in film deposition. In comparison, the heavier D atom pushes the N-D bond resonance towards higher wavelengths outside the telecom spectrum. In contrast, the O-H bond in SiON and SiO_2 materials is centered at a shorter wavelength λ=1380 nm [44], despite the heavier O atom. In this case the bonding strength difference exceed the mass difference in the bond resonance energy.

Nano-Crystals/Clusters

The recent interest in Si nanocrystals as a potential, Si-compatible light source has led to many studies of how they are formed [45] and optimized for light emission [46] and energy transfer to rare earth ions [47]. Si nanocrystals (Si-ncs) and amorphous Si nanoclusters form at elevated temperatures as a result of phase segregation in Si-rich SiO_2 and SiN films. The size and distribution of nanocrystals/clusters is a function of excess Si and anneal temperature. Amorphous nanoclusters form at lower temperatures than nanocrystals [45]. The presence of Si-ncs in the core or cladding of a waveguide is problematic because they act as dielectric inhomogeneities and scatter light [48].

4.4.2 Measuring Material Bulk Loss

Measurement of bulk loss in a thin film is not simple. Traditional optical characterization equipment – reflectometers and ellipsometers – can yield material loss data, however the sensitivity is very low since the light only traverses the thickness of the film and thus only films with very high loss (~ 100 dB/cm) can be measured with some precision. Another approach is to approximate the bulk loss of the thin film with that of optical loss measurements performed on bulk material samples. This method works well for some known crystalline materials, but is limiting and impractical for most deposited films as they do not necessarily have bulk material equivalents. In even fewer cases, such as free electron absorption in crystalline semiconductor materials [49], the loss can be theoretically estimated with reasonable accuracy. In short, there is no standard way of measuring bulk optical loss of thin films.

Perhaps not surprisingly, the most accurate method of measuring bulk loss in a thin film is to make a waveguide out of it. This is precisely the premise behind the Metricon system [50], depicted in Figure 4.16. The Metricon system is designed to measure the index of refraction and absorption of a thin film. The thin film must be thick enough to accommodate several slab waveguide modes and reside on a lower index material to guide the light by internal reflection. In this setup, a prism is used to couple light into a slab waveguide mode. Once the light is coupled to the film, a fiber attachment scans along the

surface of the thin film material to measure the evanescent field present at the surface of the film. Thin film bulk loss is obtained from fitting an exponential curve to the detected power versus scan length data similar to the cutback method detailed in section 3.4.

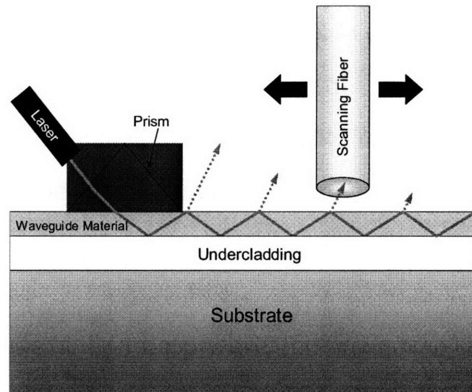

Figure 4.16 – Metricon Measurement Setup – Light is coupled to a slab waveguide by a prism and the evanescent field is scanned to obtain the loss of the thin film waveguide.

The accuracy of the Metricon system is largely dependent on the surface conditions of the thin film. Rough surfaces will scatter light, contribute to the evanescent field, and add error to the measurement. Similarly, contamination from dust can also lead to erroneous results. For these and other practical reasons, the Metricon system is viewed as a good way to qualitatively compare similarly deposited films and not an absolute measurement of bulk loss.

4.4.3 Calculating Waveguide Absorption Loss

The amount of loss from absorption is dependent on the relative distribution of power and loss coefficients of the core and cladding materials. The normalized fraction of power in the waveguide core is described by the fill factor:

$$\Gamma = \frac{\int_{-\frac{h}{2}}^{\frac{h}{2}} \int_{-\frac{w}{2}}^{\frac{w}{2}} \left|\Phi(x,y)\right|^2 \, dxdy}{\int_{-\infty}^{\infty} \int_{-\infty}^{\infty} \left|\Phi(x,y)\right|^2 \, dxdy} \tag{4.20}$$

where Φ(x,y) is the cross-sectional E-field distribution of the waveguide mode, h is the height of the waveguide, and w is the width of the waveguide. Similarly, the fraction of power in the cladding is the balance of the fraction in the core and is given by 1-Γ for most waveguide structures. Values of Γ for several, single-mode, Si/SiO_2 and SiN/SiO_2 channel waveguide geometries are given in Figure 4.15.

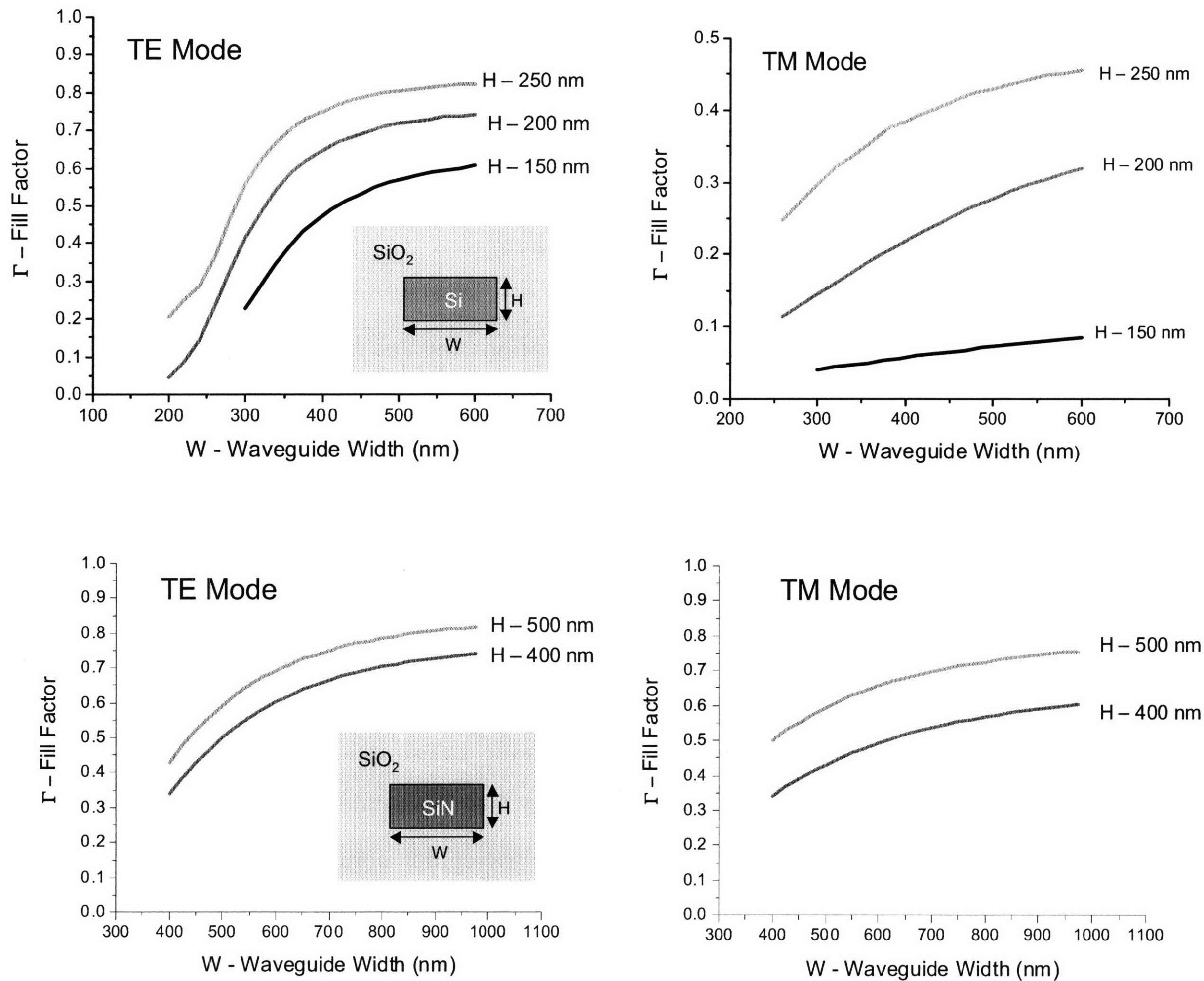

Figure 4.15 – Fill Factor (Γ) values for several geometries of Si/SiO_2 waveguides (top plots) and of SiN/SiO_2 waveguides (bottom plots) for the TE mode (left) and TM mode (right). The plots are calculated with FIMMWAVE mode solver software.

As one might expect, the fill factor ranges from zero to one and scales with waveguide core dimensions and Δn. For the waveguide geometries plotted in Figure 4.15, the fill factor for the TE mode is considerably higher than for the TM mode, indicating that the TE mode is more confined. This behavior is explained by both the aspect ratio of the waveguide and the asymmetric boundary conditions that occur when the permeability is uniform across the core/cladding interface ($\mu_{core} = \mu_{clad} = \mu_0$) but the permittivity is not ($\varepsilon_{core} \neq \varepsilon_{clad}$). Another interesting point is that the fill factor appears to plateau before approaching unity, and the level is dependent on the thickness. Thus even an infinitely wide waveguide will not approach Γ=1. In addition, the plots in Figure 4.15 also yield qualitative information on the relative mode

size, where a small fill factor indicates a greater proportion of power in the cladding and thus a large mode size.

The absorption loss for a waveguide is given by the sum of the core and cladding absorption losses, weighted by the fraction of power in each:

$$\alpha_{abs} = (1-\Gamma)\alpha_{bulk}^{clad} + \Gamma\alpha_{bulk}^{core} \tag{4.21}$$

where α_{bulk}^{core} and α_{bulk}^{clad} are the aggregate bulk material absorptions for the waveguide core and cladding materials respectively. In this work, the SiO_2 cladding material (the same material used in low-loss optical fibers) has a negligible contribution to absorption loss in the telecom spectrum ($\alpha_{bulk}^{clad} = 0$) and thus (4.20) reduces to:

$$\alpha_{absorption} = \Gamma\alpha_{bulk}^{core} \tag{4.22}$$

4.4.4 Experimental Identification of Waveguide Absorption Loss

As indicated by (4.22), the absorption portion of waveguide transmission loss, for the case of a transparent cladding, is simply the function of power within the waveguide core (Γ) multiplied by the optical loss coefficient corresponding to the bulk loss for the waveguide core material (α_{bulk}). Thus, the loss will scale with all variables that scale with Γ, such as the waveguide width (w), height (h), core index (n_{core}), and wavelength (λ). Of these, it is often easiest and most practical to vary the waveguide width.

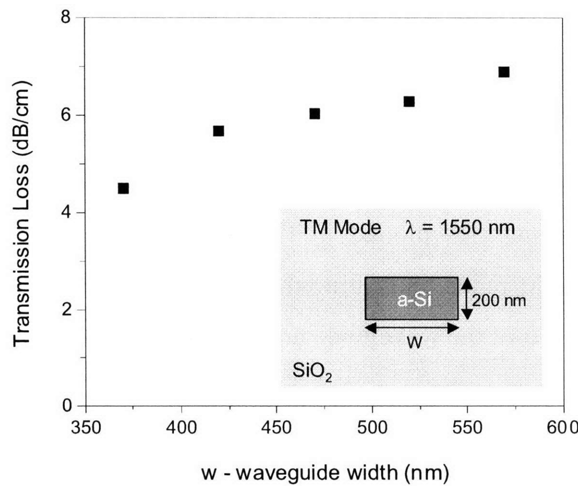

Figure 4.16 – Transmission loss versus waveguide width for an amorphous silicon waveguide (see inset for waveguide structure), increased transmission loss with waveguide width is an indication of greater confinement within the core and hence greater core absorption.

As seen in Figure 4.16, the loss increases with increased width for amorphous silicon (a-Si) waveguides. The TM mode was chosen for this example because of its relative large change in Γ as the width is increased (see Figure 4.15) and low sensitivity to roughness-scattering loss for these waveguide geometries (see Figure 4.10). The positive loss versus width relation is the opposite of that found in section 4.3 with roughness-scattering loss.

4.4.5 Experimentally finding bulk loss values by waveguide loss measurement

Waveguides are an excellent tool with which to measure the bulk loss of materials, especially for low loss materials. Assuming accurate material and processing data is available, it is possible to directly obtain bulk loss data from waveguide transmission measurements. It is preferential to use waveguides that are dominated by absorption loss; otherwise all other loss mechanisms will need to be taken into account.

The easiest way of estimating bulk loss from waveguide loss data, for the case of absorption-dominated loss, is to divide by Γ, as can be observed with (4.22). However, whether or not the waveguide loss is truly absorption-dominated is often in question as well. One way of identifying this condition is to plot waveguide loss versus waveguide width, or any other variable that scales with Γ (as just previously discussed). The waveguide is assumed to be absorption dominated if the transmission loss as a function of width – $\alpha_T(w)$ has the same form as the fill factor as function of width – Γ(w). If other loss mechanisms are present in the waveguide, the form of $\alpha_T(w)$ will alter from Γ(w).

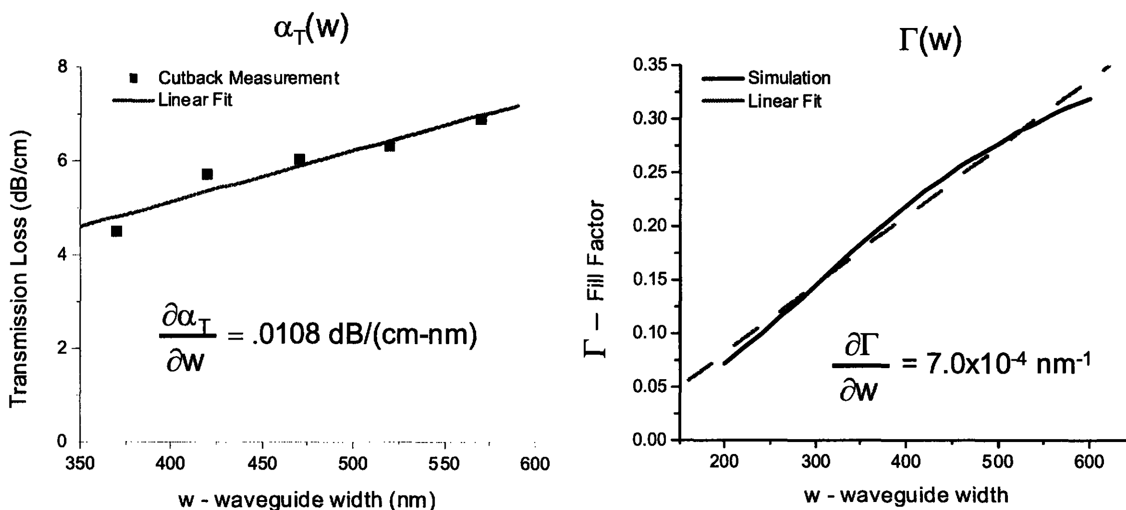

Figure 4.17 – Transmission loss (left) and Fill Factor (right) versus waveguide width for amorphous silicon waveguides (see inset of Fig 4.16 for waveguide structure), both relations can be linearly approximated.

Continuing with the example shown in Figure 4.16, both $\alpha_T(w)$ and $\Gamma(w)$ have similar forms and can both be well approximated with a linear fit for this range of waveguide geometries (see Figure 4.17). Thus, this set of waveguides is thought to be absorption loss dominated and we assume $\alpha_T = \alpha_{absorption}$. Once the functional forms of $\alpha_T(w)$ and $\Gamma(w)$ are known, a_{bulk} can be found by differentiating (4.22) with respect to w:

$$\frac{\partial\left(\alpha_{absorption}\right)}{\partial w} = \frac{\partial\left(\Gamma\right)}{\partial w}\alpha_{bulk}^{core} + \Gamma\frac{\partial\left(\alpha_{bulk}^{core}\right)}{\partial w} \tag{4.23}$$

Assuming that the bulk loss is homogeneous throughout the material $\left(\frac{\partial\left(\alpha_{bulk}^{core}\right)}{\partial w} = 0\right)$ we find that:

$$\alpha_{bulk}^{core} = \left(\frac{\partial\alpha_{absorption}}{\partial w}\right)\left(\frac{\partial\Gamma}{\partial w}\right)^{-1} \tag{4.24}$$

From the data in Figure 4.17, the bulk loss of the a-Si is found to be 15.2 ± 2 dB/cm. The data is an average of three measurements and the error is the range of values found using (4.24) for each data set. This value of bulk loss is in close agreement with the bulk loss value found in a hybrid waveguide structure (discussed in chapter 6) made from the same material, where a single mode was maintained in a 200 x 3000 nm^2 waveguide and thought to be dominated by absorption loss. The hybrid waveguide has an average transmission loss of 13.8 dB/cm and Γ=0.75, which yields a bulk loss value of 18.5 dB/cm. It should be noted that the hybrid approach may include loss contributions from top surface roughness.

4.5 Non-linear Processes – f (B, Δn, h, w, P)

For the purposes of waveguide loss analysis, non-linear processes refer to the non-linear scaling of transmission loss with optical power/intensity. Typically, non-linear processes involve the interaction of two or more particles (i.e. photons, phonons, electrons, holes). The probability of interaction between these particles is low (assuming $\hbar\omega \ll E_g$), however as the density of particles increases, the numbers of interactions increases as well, and thus non-linear processes tend to take place when high optical power densities are employed. In particular, silicon waveguides suffer from both Stimulated Raman Scattering (SRS) and Two Photon Absorption (TPA) at elevated optical powers in the telecom spectrum.

4.5.1 Stimulated Raman Scattering

Raman scattering occurs when photons and optical phonons interact resulting in a transfer of energy and momentum between the two particles [51]. The anti-Stokes component of Raman scattering corresponds to a photon absorbing a phonon, whereas the Stokes component corresponds to a photon emitting a phonon. In practice, phonons have an energy that is of the order 10^{-2} eV, and only cause a small shift in energy to photons in the near infra-red ($\hbar\omega \sim 0.8$ eV). Strictly speaking, Raman scattering is a linear process, however at elevated optical densities, the number of photon-phonon interactions raises to sustain a population sufficient for stimulated emission; a non-linear process known as Stimulated Raman Scattering (SRS). SRS is independent of whether or not the electronic band structure is direct or indirect, and offers a unique optical lasing mechanism for indirect bandgap semiconductors.

Indeed, SRS has been observed in a variety of Si waveguide geometries [52,53]. For crystalline silicon waveguides, the phononic density of states is greatest at the center of the Brillouin zone, where a three-fold degenerate optical phonon state corresponds to the strongest Stokes peak. Researchers at UCLA [52] have theoretically estimated and experimentally measured the SRS gain coefficient (g_{SRS}) for a large Si ridge waveguide to be 3.7 and 2 cm/GW respectively; where the discrepancy is attributed to four wave mixing in the experimental measurements. Similarly, researchers at Columbia University and IBM [53] have measured g_{SRS} = 2.9 cm/GW in a much smaller cross-section Si channel waveguide. In both studies, the signal wavelength (λs=1435 nm) was offset from the SRS wavelength (λ_{SRS}=1550 nm) by $\Delta\lambda$=115 nm, which corresponds to the first order stokes peak. As a non-linear process, the efficiency of SRS scales with the optical power density in the waveguides. Hence observation of SRS gain in Si ridge waveguides with large mode sizes requires orders of magnitude larger power to achieve similar gain in Si channel waveguides.

Recent efforts in creating a laser based on SRS in silicon waveguides has been stifled by TPA-induced free-carrier absorption [54]. To alleviate this problem, Intel designed and fabricated a unique Si ridge waveguide structure that surmounted this problem by applying an electric field across the waveguide cross-section to sweep away the induced free carriers and thereby diminish any losses that prevent Raman lasing [56]. While impressive, the Intel Raman laser is essentially an inefficient wavelength converter and not suitable as an integrated photonic light source.

4.5.2 Two Photon Absorption

Two photon absorption (TPA) involves the interaction of two photons and an electron (sometimes mediated by a phonon) that results in the promotion of the electron from the valence band to the conduction band, despite the photon energy having an energy less than the band gap, but greater than half the bandgap ($E_g/2 \leq \hbar\omega < E_g$). The TPA effect is a two-fold problem in that not only are photons

absorbed in promoting electrons, but the free charge carriers that are generated in the process further attenuate the optical signal [54].

As nominally implied the TPA effect requires two photons to occur and should therefore scale with the optical signal intensity squared. To account for the TPA effect, relation (3.2) is rewritten as:

$$\frac{\partial I}{\partial z} = -\alpha_T I - BI^2 \tag{4.25}$$

where I is the optical intensity, α_T is the linear transmission loss, B is the TPA coefficient, and z is the propagation direction in the waveguide. The value of B can be determined experimentally by plotting the ratio of input and output intensities (I_{in}/I_{out}) versus the input intensity (I_{in}). As can be seen by rewriting (4.25) as (4.26), B is simply the slope of I_{in}/I_{out} versus I_{in}.

$$\frac{I_{in}}{I_{out}} = e^{\alpha_T L}\left(1 + \frac{B\,L_{eff}}{A} I_{in}\right) \tag{4.26}$$

where L is the length of the waveguide, A is the effective area of the waveguide mode in the waveguide core (hw/Γ), and L_{eff} is defined as $\left(1 - e^{-\alpha_T L}\right)/\alpha_T$.

TPA has been observed in Si waveguides [52, 53, 56] and B has been experimentally measured to range from 0.4 – 0.9 cm/GW for λ= 1550 nm. In comparison, the TPA coefficient for GaAs and InP are 10.2 cm/GW [55] and 32 cm/GW [57] respectively for λ= 1550nm. The large difference in TPA coefficients, aside from the differences in E_g (B scales with E_g^{-3} [57]), is mainly because TPA in Si is phonon mediated, while TPA in direct gap semiconductors (GaAs and InP) are not.

4.5.3 Non-linear thresholds in integrated Si waveguides

To get a better understanding of how much optical power is needed to observe the effects of SRS and TPA in waveguide transmission loss, an integrated Si waveguide is examined. By comparison, non-linear effects in SiN and SiO_2 occur for much higher thresholds as a result of the amorphous structure and large bandgap for both materials. In this example a 200x500 nm^2 {100} SOI waveguide symmetrically clad with SiO_2 is assumed. Loss coefficients for both SRS and TPA phenomena are obtained from [52] (g_{SRS} = 2.9 cm/GW and B=0.44 cm/GW) and the input is TE-polarized, λ= 1550nm light.

SRS is dependent on the optical input flux in the Si core, and if we assume that the gain coefficient for the photon-phonon interaction is the same magnitude as the loss to the signal wavelength, we find:

$$\alpha_{SRS} = g_{SRS}\frac{\Gamma P}{hw} \tag{4.27}$$

where Γ is the fraction of power in the waveguide core, P is the power coupled into the waveguide, h is the waveguide height, and w is the waveguide width. Similarly, the loss from TPA is also dependent on the optical input flux in the Si core:

$$\alpha_{TPA} = B\frac{\Gamma P}{hw} \tag{4.28}$$

If we use 0.1 dB/cm as the threshold transmission loss at which each non-linear process commences (i.e. we solve for P with $\alpha = 0.1$ dB) the Si waveguide described above will show the effects of **SRS** when the coupled power (P) reaches **P = 11 mW**. Likewise, the effects of **TPA** will commence at **P = 73 mW**.

Therefore, for low loss, integrated Si waveguides, the throughput power will need to be less than 11 mW to ensure minimal non-linear absorption from stimulated Raman scattering. Consideration should be taken when utilizing resonant waveguide devices, where optical power is concentrated, thereby reducing the threshold power used in the circuit. Additionally, the use of multiple wavelength channels will also lower the threshold by a factor of the number of channels that reside in a single waveguide. The minimum throughput power will most likely be limited by other aspects of the photonic circuit such as the photo-detector sensitivity.

4.6 Waveguide Coupling– f (Δn, h, w, δ)

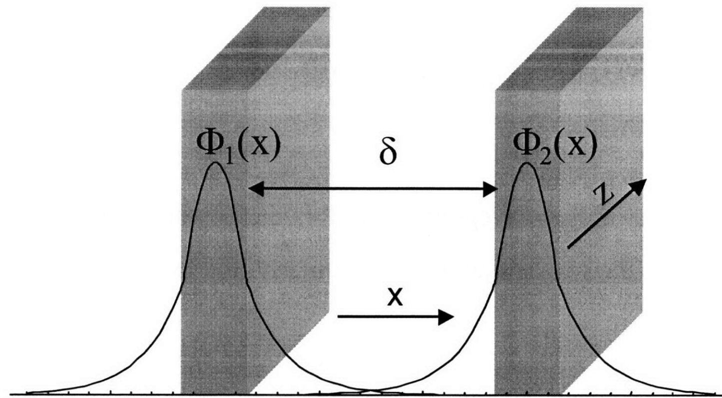

Figure 4.18 – Field distribution of two waveguides closely spaced.

If waveguides are brought sufficiently close to each other, it is possible to completely couple the optical power from one waveguide to the other. This phenomenon, which is quite similar to electron tunneling in quantum wells, is known as waveguide coupling and is the fundamental operating mechanism behind many waveguide switches, modulators, filters, and detectors. As a potential loss mechanism (albeit one that can be easily avoided), waveguide-to-waveguide coupling is quite similar to substrate leakage and mode-to-mode loss mechanisms. The following description utilizes coupled mode theory [58] to describe the power transfer from one waveguide to another waveguide and closely follows the description found in [22]; further detail can be found in textbooks [21-23].

4.6.1 Coupled-Mode Theory between Two Waveguides

As a reminder, the E-field in a waveguide can be described as:

$$E(x,y,z,t) = E_0\Phi(x,y)e^{i(\omega t-\beta z)} \tag{4.29}$$

where E_0 is the field amplitude, Φ(x,y) is the normalized field distribution in the waveguide cross-section, and β is the propagation constant. For two closely spaced waveguides, as seen in Figure 4.19, we can view the field distribution as a superposition of the two modes in (4.30), or alternatively known as the "supermode". For the purposes of this analysis, we will assume that each waveguide supports only the first order mode of each polarization, and since we are concerned with steady-state coupling in space, we will only be concerned with time independent equations.

$$E(x,y,z)=E_{0,1}\Phi_1(x,y)e^{i(-\beta_1 z)}+E_{0,2}\Phi_2(x,y)e^{i(-\beta_2 z)} \tag{4.30}$$

Here the subscripts refer to the waveguide each discrete mode is associated with. For clarity, we will also normalize the field amplitudes such that:

$$E(x,y,z)=c_1\, a_1(z)\,\Phi_1(x,y)+c_2\, a_2(z)\,\Phi_2(x,y) \tag{4.31}$$

$$P=|a_1|^2+|a_2|^2=1 \tag{4.32}$$

here c_1 and c_2 are constants, a_1 and a_2 are the normalized field amplitudes, and P is the optical power. Now, if the two guided waves, corresponding to the two adjacent propagating waveguide modes, couple by some means they will obey the following differential equations:

$$\frac{da_1}{dz}=-i\beta_1 a_1-i\kappa_{12}a_2 \tag{4.33}$$

$$\frac{da_2}{dz}=-i\beta_2 a_2-i\kappa_{21}a_1 \tag{4.34}$$

where κ_{ij} is the coupling coefficient from waveguide i to waveguide j. For the case where there is zero coupling ($\kappa_{12} = \kappa_{21} = 0$), relation (4.33) and (4.34) return to forms equivalent to uncoupled modes propagating in respective waveguides. Assuming that the interacting waves propagate in the form $a_1 = a_{1,0}\, e^{-i(\beta c)z}$ and $a_2 = a_{2,0}\, e^{-i(\beta c)z}$, a solution to the coupled mode equations (4.33) and (4.34) is given by:

$$\begin{aligned}\beta_c &= \frac{\beta_1+\beta_2}{2}\pm\sqrt{\left(\frac{\beta_1-\beta_2}{2}\right)^2+\kappa_{12}\kappa_{21}}\\ &=\overline{\beta}\pm s\end{aligned} \tag{4.35}$$

where β_c can be thought of as the propagation constant for the supermode. Inserting (4.35) back into yielding solutions for the respective wave amplitudes:

$$a_1(z)=e^{-i\overline{\beta}z}\left[A_1e^{isz}+A_2e^{-isz}\right] \tag{4.36}$$

$$a_2(z)=e^{-i\overline{\beta}z}\left[B_1e^{isz}+B_2e^{-isz}\right] \tag{4.37}$$

where A_1, A_2, B_1, and B_2 are determined by the boundary conditions of the problem.

4.6.2 Evaluating the Coupling Coefficient

The coupling coefficient κ_{ij} is the rate per length at which power is coupled. For planar waveguides, κ_{ij} can be well approximated with a perturbation method in which the unperturbed guided mode field distribution is used in determining the energy transfer between waveguides [21-23]. This approximation assumes that the overlap of power between the two waveguides is much smaller than the guided power and can be evaluated by:

$$\kappa_{ij} = \frac{k_0^2}{2\beta_i} \int_{wg,i} \left(n_{core,i}^2 - n_{clad}^2 \right) \Phi_i^* \Phi_j \, dxdy \tag{4.38}$$

Essentially, (4.38) is a measure of the overlap of the field distribution i guided by waveguide i on the field distribution j guided in waveguide j. For the case of symmetric waveguides, $\kappa_{ij} = \kappa_{ji} = \kappa$. For asymmetric waveguides, an effective coupling coefficient is found with $\kappa = \sqrt{\kappa_{ij}\kappa_{ji}}$. Since the modes i and j are separated in space, it is clear that κ will decrease with increased distance between the waveguides (δ). In fact, κ has an inverse exponential dependence on δ, mirroring the inverse exponential field distribution outside the waveguide core. Similarly, κ will increase with Δn, as higher index contrast leads to tighter confinement and lower spatial overlaps for a given δ. Practically, $\kappa \ll \beta_i$ as a consequence of this dependence, as well as lithographic limitations which place a minimum δ, and therefore a maximum κ, on fabricated devices.

4.6.3 HIC Directional Coupler

Let us consider the case where light is injected into only one of the two waveguides, such that $|a_1(0)|^2 = 1$ and $|a_2(0)|^2 = 0$.

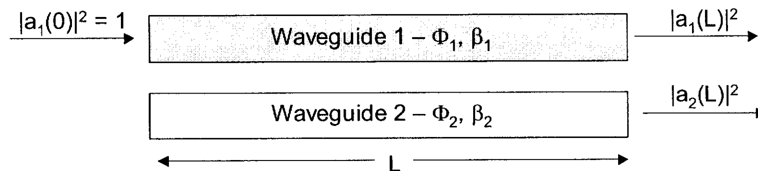

Figure 4.19 – Waveguide layout and input conditions for waveguide coupling

With these input conditions, one can rewrite (4.36) and (4.37) as:

$$a_1(z) = \left[\cos(sz) + i\frac{\beta_2 - \beta_1}{2s}\sin(sz)\right]e^{-i\bar{\beta}z} \tag{4.39}$$

$$a_2(z) = \left[-i\frac{\kappa_{21}}{s}\sin(sz)\right]e^{-i\bar{\beta}z} \tag{4.40}$$

Thus, we can see that waveguide coupling is dependent on the coupling strength (κ) and the difference between the propagation constants (β_1, β_2) for the two waveguides.

If we consider the case of two identical waveguides, such that $\beta_1 = \beta_2 = \beta$ and $\kappa_{12} = \kappa_{21} = \kappa$, relations (4.39) and (4.40) simplify and the power in each waveguide is given by:

$$|a_1(z)|^2 = \cos^2(\kappa z) \tag{4.41}$$

$$|a_2(z)|^2 = \sin^2(\kappa z) \tag{4.42}$$

Using these results, we can plot the distribution of power in the two waveguides, assuming no other loss mechanisms, as a function of propagation distance. As seen in Figure 4.20, the power is completely transferred from waveguide 1 to waveguide 2, for the case of ($\beta_1 = \beta_2$), over a distance known as the coupling length, defined as $\pi/2\kappa$. Input values corresponding to Si/SiO_2 waveguides (β=9.73 μm^{-1} and κ=0.02 μm^{-1}), are used to illustrate typical HIC waveguide behavior.

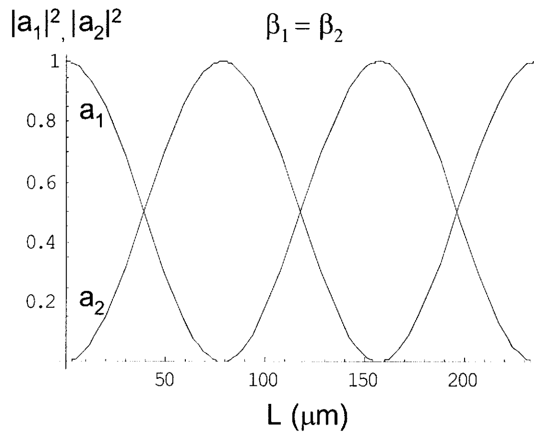

Figure 4.20 – Waveguide Power as function of length for the two adjacent waveguides for $\beta_1 = \beta_2$

Another way to view the coupling length is to think of it in terms of supermode phase, where waveguide coupling occurs when the solutions to differential equations (4.33) and (4.34) are in phase. In

other words, the field amplitude in a waveguide varies with the beating of the two wave propagations solutions: $\beta_c = \overline{\beta} \pm s$.

Alternatively, if the propagation constants are not equivalent ($\beta_1 \neq \beta_2$), the power is no longer fully transferred. This makes intuitive sense, both in terms of phase-matching and velocity-matching the two waveguide modes. The sensitivity of this effect is related to the relative magnitudes of β and κ as can be ascertained from (4.35) and (4.40). For HIC waveguides, weak coupling is assumed ($\kappa \ll \beta$) and thus the coupling of power from one waveguide to another is negligible other than when $\beta_1 \approx \beta_2$. For example, if an error occurred in that only one of the waveguides resulted in a slight change (~10nm) in width, such that $\beta_1 = 9.73\ \mu m^{-1}$ and $\beta_2 = 9.67\ \mu m^{-1}$ (i.e. $\beta_1 \approx \beta_2$) while keeping $\kappa = 0.02\ \mu m^{-1}$, the power distribution between waveguides changes dramatically (Figure 4.21). Here a majority of the power remains in the waveguide in which the power was inserted, but a reasonable fraction is transferred to the second waveguide. As the difference between propagation constants increases, the amount of coupled power decreases. If the width error is larger (~100 nm), such that $\beta_1 = 9.73\ \mu m^{-1}$ and $\beta_2 = 8.92\ \mu m^{-1}$ (i.e. $\beta_1 \neq \beta_2$) while maintaining $\kappa = 0.02\ \mu m^{-1}$, the power coupled to waveguide two is negligible (Figure 4.21).

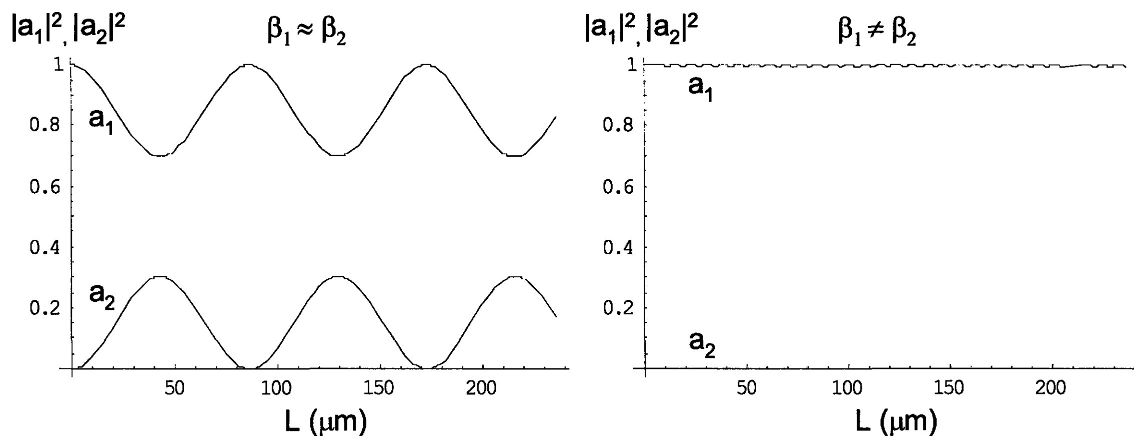

Figure 4.21 – Waveguide Power as function of length for the two adjacent waveguides for $\boldsymbol{\beta_1 \approx \beta_2}$ and $\boldsymbol{\beta_1 \neq \beta_2}$

4.6.4 Experimental evidence of Waveguide Coupling

Although a photonic circuit design which inadvertently contains elements that exhibit waveguide-to-waveguide coupling is unlikely, the phenomenon can manifest itself in fabrication and measurement. In researching new waveguide materials, material indices and thicknesses are often initially unknown, and dependent on material deposition parameters. Additionally, processing unknown materials may result in unoptimized etching and altered waveguide dimensions and spacing.

In one such study, in which the loss of a novel Si rich SiO_2 material was investigated via waveguide measurement, the insertion loss yielded an unusual result that is attributed to waveguide-to-waveguide coupling. To confirm this, the light was inserted in the 4.5 μm wide ridge waveguide (wg1) and the output was measured at the 5 μm ridge waveguide (wg2). The ridge waveguide structures, shown in Figure 4.22, were not designed for this material system as demonstrated by many of the waveguides exhibiting multi-mode behavior. Additionally, the low index contrast of the ridge waveguide structure resulted in considerable mode overlap between the waveguides (facilitating waveguide coupling).

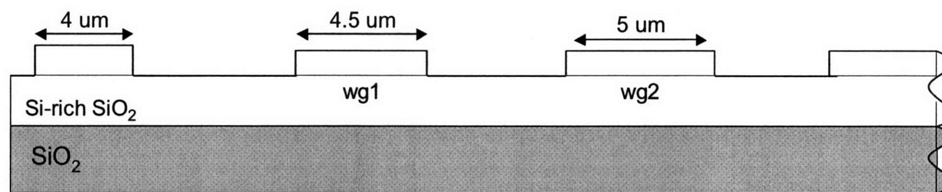

Figure 4.22 – Ridge waveguide structure that exhibited waveguide coupling, measurement was input at wg1 and measured at wg2.

As can be seen in Figure 4.23, the power coupled from to the 5 μm wide waveguide oscillates similar to that of waveguide two in Figures 4.20 and 4.21. While the plots are comparing different variables, waveguide power is plotted versus wavelength rather than waveguide length, the behavior should be qualitatively the same, i.e both variations alter the phase of the coupled mode and thus the coupling length. The increase in amplitude of the coupled power with wavelength is caused by the larger coupling rate between the waveguides that accompanies increased wavelength. The power in wg1 is estimated to be many times larger than that measured in wg2, suggesting that the effective indices of the two waveguides are close but not equal (i.e. $\beta_1 \approx \beta_2$), as is expected.

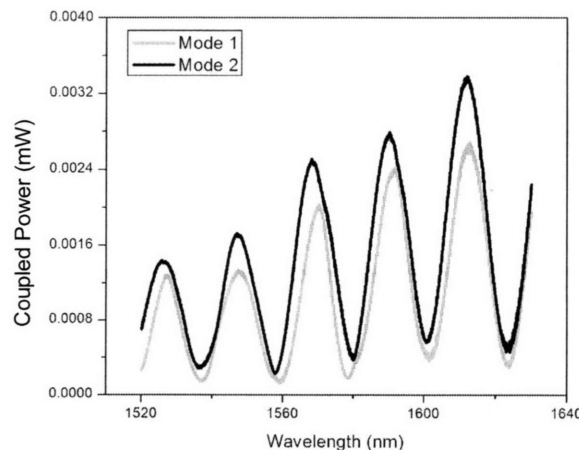

Figure 4.23 – Insertion Loss oscillations due to waveguide to waveguide coupling for structure in Figure 4.22.

Often, insertion loss oscillations are attributed to Fabry-Perot resonances; however a quick calculation will show that the period and amplitude in Figure 4.23 are much too large. The similarity in phase and behavior of the two modes (corresponding to the maximum and minimum insertion losses) indicate that the two modes have similar effective indices and do not interact, ruling out mode-to-mode coupling. Each of these observations is consistent with waveguide-to-waveguide coupling.

4.7 Substrate Leakage – f (Δn, h, w, $t_{underclad}$)

Substrate leakage is the coupling of optical power from a waveguide to the substrate. The phenomenon occurs for waveguide structures deposited on high index substrates, such as Si wafers, in which an undercladding layer intended to optically isolate the power in the waveguide layer, is utilized. If the undercladding layer thickness ($t_{underclad}$) is too thin or the confinement of the waveguide is too weak, the optical power "leaks" into the substrate – a loss mechanism known as substrate leakage or substrate coupling.

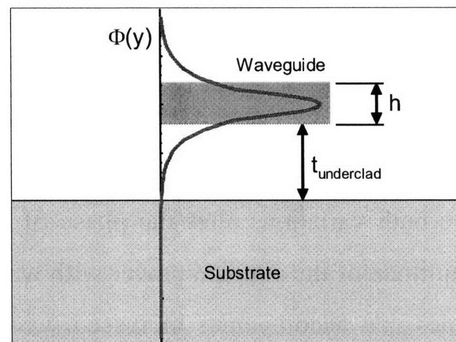

Figure 4.24 – Field amplitude distribution Φ(y) overlaid on a waveguide structure.

Substrate leakage is essentially the coupling of a waveguide mode to slab modes in the substrate. However, unlike waveguide-to-waveguide coupling, the power transfer does not oscillate between waveguides as we saw in section 4.6, rather it is a one-way coupling to the substrate. The major difference between substrate leakage and waveguide-to-waveguide coupling is in the superposition of the fields, which is this case is given by:

$$E(x,y,z) = E_{0,1}\Phi_1(x,y)e^{i(-\beta_1 z)} + \sum_i E_{0,i}\Phi_i(y)e^{i(-\beta_i z)} \tag{4.43}$$

where the left term is the waveguide mode and the right term refers to the multiple modes in the substrate. While the power coupled from the waveguide to any one mode in the substrate may be small, the total

power loss can be substantial. Calculating the substrate leakage for a given waveguide structure is typically performed by a mode solving program, as an analytical solution to substrate coupling would be rather involved and difficult to generalize.

4.7.1 Substrate Leakage in Silicon Waveguides

The substrate leakage for two SiO_2 clad Si waveguide core geometries – 200x400 nm^2 and 200x500 nm^2 – were calculated as a function of undercladding thickness ($t_{underclad}$), for both TE and TM polarizations, in Figure 4.25. As intuitively expected, an increase in $t_{underclad}$ increases the optical confinement from the substrate and reduces substrate leakage. The simulated data was calculated with FIMMWAVE software, and clearly show the exponential behavior that result from the exponential field distribution outside the waveguide core.

The simulations in Figure 4.25 also elucidate the effects of waveguide geometry and polarization on substrate leakage. The comparison of the two waveguide geometries shows that the loss is always higher for the smaller waveguide core, which under single-mode conditions corresponds to a larger modal area. Thus, the 200 x 400 nm^2 Si waveguide geometry experiences more substrate leakage than the 200 x 500 nm^2 geometry, for a given undercladding thickness, as a result of the larger mode size and consequently larger field overlap with the substrate. Similarly, the modal size difference between the TE and TM modes in these waveguide geometries results in orders of magnitude differences in substrate loss (note the different limits on the abscissa axis of both plots in Fig. 4.25).

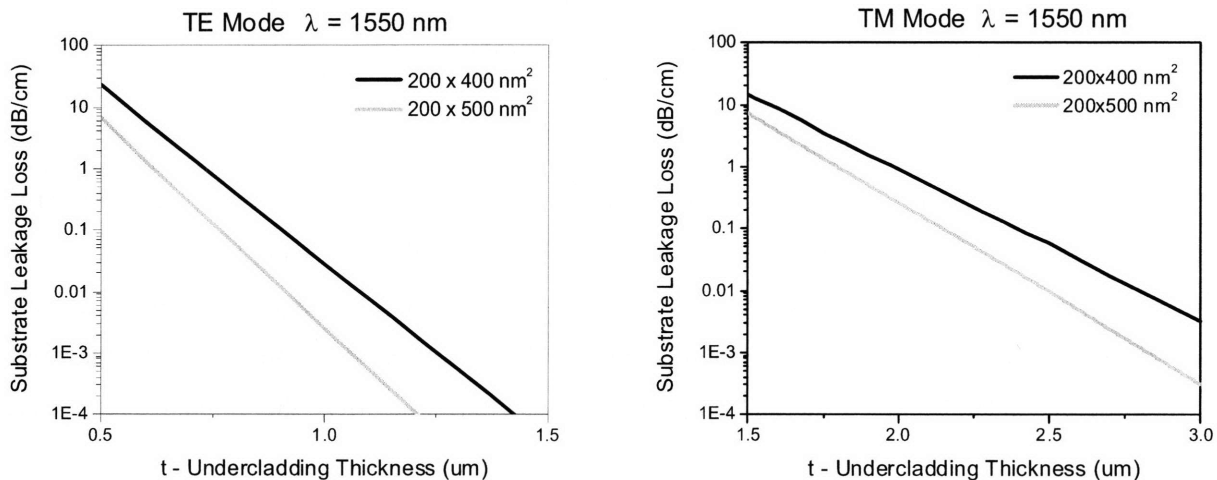

Figure 4.25 – Substrate leakage loss for TE (left) and TM (right) polarized light (λ=1550 nm) in Si waveguides for various SiO_2 undercladding thicknesses, calculated with FIMMWAVE .

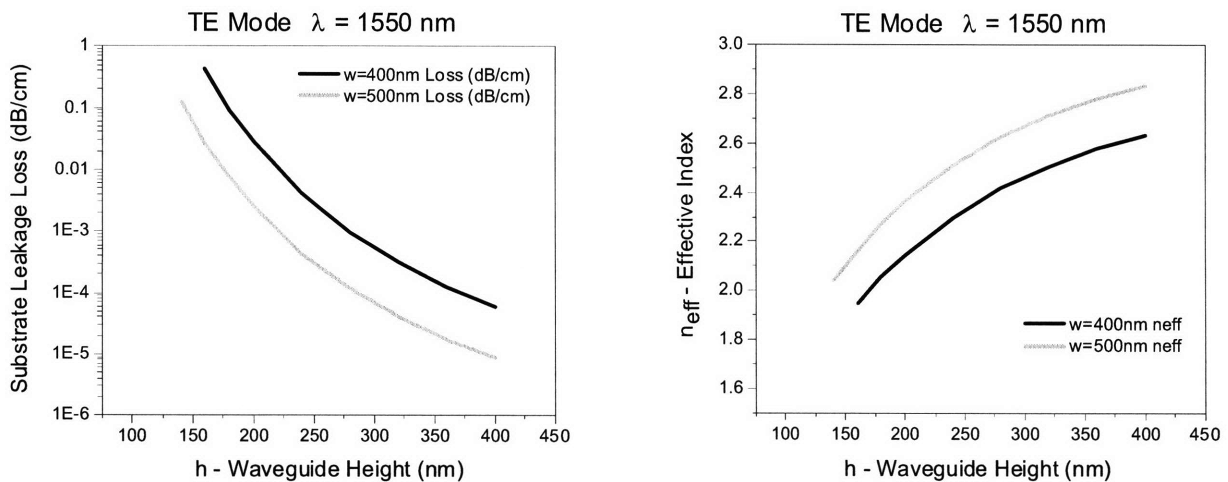

Figure 4.26 – Substrate leakage for TE polarized light (λ=1550 nm) in a Si waveguides with a 1um SiO_2 undercladding as a function of waveguide height (left), and the effect of waveguide height on effective index of the mode (right), calculated with FIMMWAVE

The behavior of substrate leakage on waveguide core height (h) for two waveguide widths (400 and 500 nm) with a constant undercladding thickness ($t_{underclad}$) was also calculated in Figure 4.26. Here the effect of decreasing h results in an increase in substrate leakage that rises faster than an exponential. Essentially, the effect of decreasing h is the combination of two phenomena: 1) the mode center moving closer to the substrate 2) the decrease in waveguide effective index. Moving the mode center closer to the substrate will result in an exponential dependence on loss, similar to moving the waveguide closer. The decrease in effective index alters the coefficient of the exponential decay in the field distribution outside the waveguide core and increases the field overlap with the substrate.

4.7.2 Experimental Evidence of Substrate Leakage

Substrate leakage loss can be identified by insertion loss measurements on straight waveguides. For HIC waveguides made with thin-film processing techniques, the exponentially increasing loss that arises from substrate leakage can be most readily observed by either scanning the wavelength and/or measuring several waveguide geometries. Both wavelength scans and altered waveguide geometries affect the mode size, for a given undercladding material and thickness, and thus can affect the amount of substrate coupling.

As an example, the insertion loss measurements for eight a-Si waveguides, with widths ranging from 300 to 650 nm, were collected for the TM polarization as a function of wavelength and plotted in Figure 4.27. These waveguides are quite similar to the a-Si Waveguides used in the absorption loss example in section 4.4.4, in that they are dominated by absorption and exhibit little roughness scattering.

Insertion loss is the sum of the coupling loss and transmission loss, and thus the spacing between the different waveguide measurements is caused by 1) coupling differences that each respective mode has with the lens-tipped input fiber used for these experiments and 2) the difference in absorption that scales with waveguide core dimensions. The smaller width waveguides have the largest mode sizes and thus the lowest coupling losses. In addition, the smallest waveguide geometries also have the smallest Γ, and thus the least amount of absorption loss. Therefore we should expect the lowest loss a-Si waveguides in this example to be the 300 nm width waveguide. However, as discussed previously, the smallest waveguide geometries have the largest mode sizes and are most susceptible to substrate leakage. Furthermore, this loss behavior, if the waveguide becomes substrate leakage loss dominated, should exhibit an exponential increase with wavelength, since the mode size scales with wavelength as well. Thus, the deviation in spectral shape for the 300 nm, and to a lesser extent the 350 nm wide waveguides, is caused by substrate coupling, where both examples display the exponentially increasing loss with increased mode size consistent with this phenomenon.

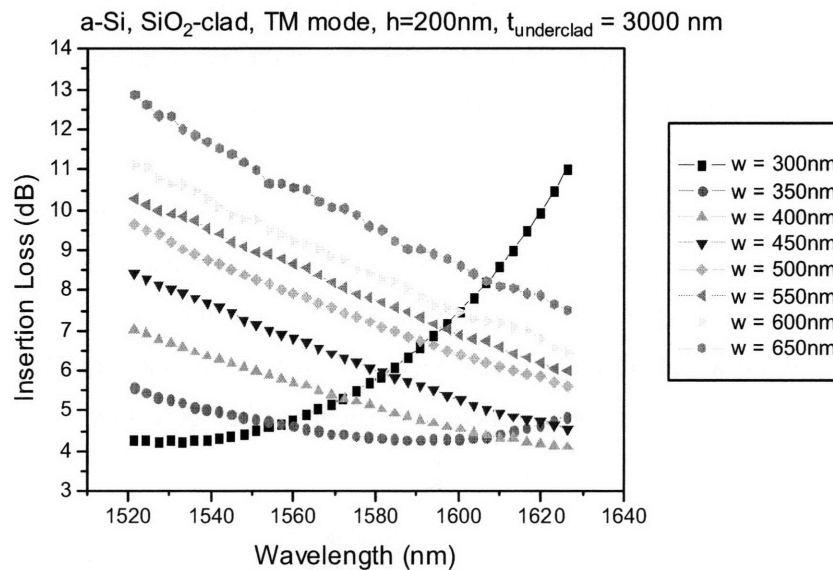

Figure 4.27 – Insertion loss measurements performed with TM polarized light on straight, SiO_2 clad, a-Si waveguides with a height of 200nm and $t_{underclad}$ = 3000 nm. The increase in insertion loss with wavelength is evidence of substrate leakage loss.

In a sense, the presence of substrate coupling is an indicator that the waveguide mode is too large for the waveguide structure. Thus, waveguide geometry and signal wavelength must be taken into account for proper photonic circuit design. As shown with the 300 nm waveguide width in Figure 4.27, substrate leakage can result in considerable loss that, unlike absorption or roughness scattering losses,

scales exponentially with wavelength. Fortunately, substrate leakage can be avoided by using a thick undercladding layer or a tightly confined waveguide mode. However in terms of integration, the tradeoffs that accompany utilizing a thick undercladding (i.e. stress, interfacing devices on the substrate, device density) often result in a maximum $t_{underclad}$ and thus require optimization of waveguide geometry (or an increase in the Δn) to minimize the mode field distribution Φ(y) in the out-of-plane direction.

4.8 Mode-to-Mode Coupling – f (Δn, h, w, θ)

Mode-to-mode coupling is the transfer of optical power between modes within a single waveguide structure. By definition, the mode field profiles, defined by the eigenmode solutions to the wave equation for a given uniform waveguide, are orthogonal and thus:

$$\iint \Phi_m \Phi_n^* \, dxdy = \delta_{mn} \tag{4.44}$$

where δ_{mn} is the Kronecker delta function – which equals unity when m = n and zero otherwise, and Φ_i represents the mode field distribution of mode i. Thus the interaction and coupling of the different modes within a given uniform waveguide structure should be non-existent, since the mode field overlap between different modes is null.

However, there are several situations in which waveguide non-uniformities or asymmetries alter the waveguide modes such that the orthogonality condition between the modes (relation (4.44)) does not hold, and mode-to-mode coupling occurs. In fact, this effect is the fundamental mechanism used in polarization rotators [59-60] which are waveguide devices that convert TE modes to TM modes, and vice-versa. Two examples of polarization rotating structures are depicted in Figure 4.28:

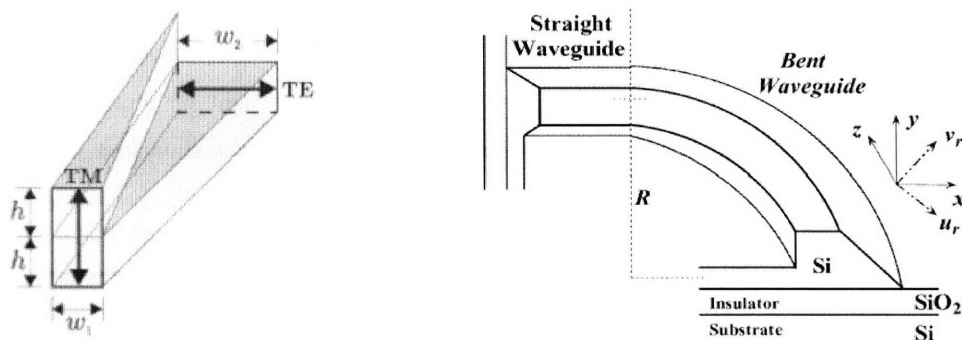

Figure 4.28 – Two examples of polarization rotator structures from ref. [59] (left) and ref. [60] (right).

The polarization waveguide structure on the left of Figure 4.28 utilizes waveguide nonuniformity to efficiently shift the polarization. By adiabatically altering the waveguide geometry in the propagation direction, the waveguide mode field is coupled to the other polarization by matching propagation constants of the two modes and displacing them such that the mode overlap (and thus coupling) is not zero.

In contrast, the polarization rotator on the right of Figure 4.28 uses the asymmetry of the waveguide cross-section to convert polarization. In this device, the asymmetric cross-sectional shape of the waveguide in combination with propagation around a bend results in the rotation of the dominant field vector for both modes such that the orthogonality between modes is no longer conserved and coupling can occur.

4.8.1 Experimental Evidence of Mode-to-Mode Coupling

Mode-to-mode coupling can cause many effects in waveguides, depending on the coupling mechanism and waveguide structure. However, for single mode waveguides, the effect is typically noted by an exchange in optical power between the TE and TM polarization.

Similar to the waveguide-to-waveguide coupling example in section 4.6.4, the example described here is rooted in the use of a material system that differed from design and complicated by processing errors that facilitated coupling. More specifically, PECVD SiN (n=2.2) waveguides were fabricated on a 3 μm thermally oxidized Si wafer and clad with PECVD SiO_2; despite the fact that the photolithography mask was designed for air-clad SiN waveguides. The modified cladding reduced the extent of modal confinement in the waveguide, which in turn resulted in considerable modal displacement (and bend loss) in the waveguide bends. In addition, the pattern-transfer of the photolithography mask to the waveguide layer was not ideal, in that the waveguide sidewalls were angled ($\theta = 75°$) as seen in Figure 4.29. In combination, the large displacement of the mode as it traveled around the bend with angled sidewalls resulted in TM to TE (and TE to TM) mode coupling, similar to the polarization rotator in [60].

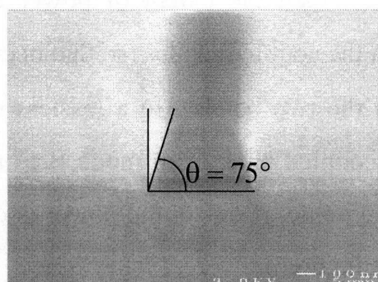

Figure 4.29 – SEM of waveguide etch showing angled sidewalls

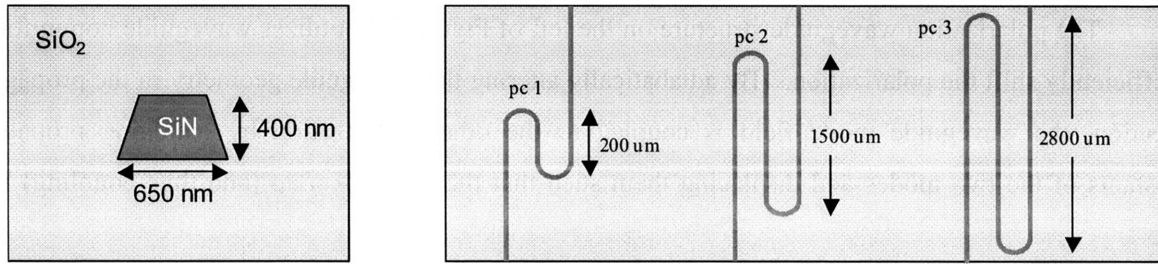

Figure 4.30 – Cross-sectional view (left) and layout of waveguides used in cutback measurement (right).

The mode coupling effect was experimentally observed when performing cutback measurements on waveguide paperclip structures. In this study, 400x650 nm^2 SiN waveguides with 25 μm bend radius paperclip waveguides were measured for the purpose of ascertaining the transmission loss (see Figure 4.30). However upon observing the insertion loss data for these waveguides, shown in Figure 4.31, it was noted that each paperclip exhibited unique oscillations that were inversely proportional to the waveguide length between the two bends.

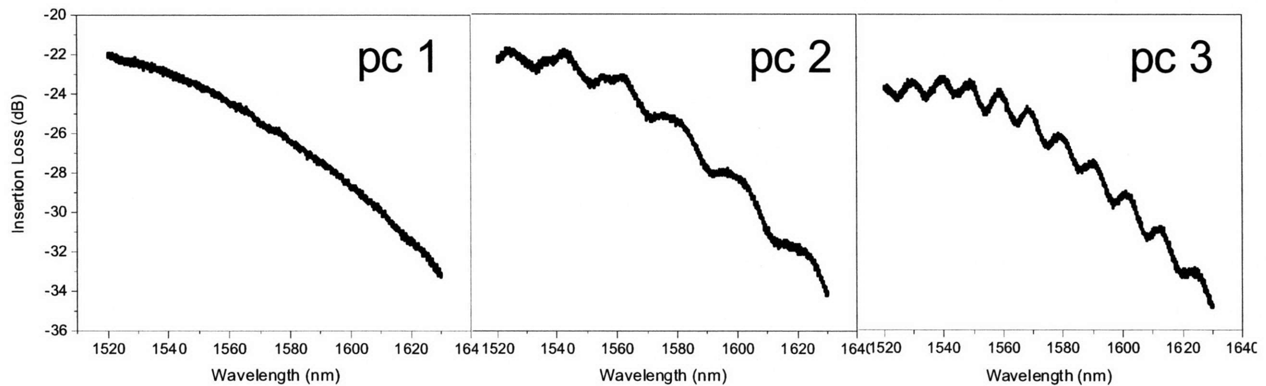

Figure 4.31 – Insertion Loss for the TE polarization in three paperclips depicted in Figure 4.30

If we assume that mode-to-mode coupling occurs in the waveguide bends only (i.e. the bends act as directional couplers between the modes) then the extent of power transferred between the modes is dependent on the phase change between the coupled modes (ϕ) that occurs during propagation through the straight waveguide length (L) between the two bends. In a lossless system, if $\phi=\pi$ the power coupled from mode A to mode B at bend 1 is coupled back from mode B to mode A at bend 2, the throughput power is at a maximum. At the other extreme, if $\phi = 0$, the power is coupled from mode A to B at both bends and the throughput power is at a minimum.

The phase difference between the modes arises from the difference in propagation constants, which result in a differing optical path length. To illustrate this effect, an equivalent photonic circuit model is

depicted in Figure 4.32. The top branch is the TE mode path with an optical path-length of L1= n^{TE}_{eff} L between the bends. Similarly, the bottom branch is the TM mode path with an optical path-length of L2= n^{TM}_{eff} L between the bends. In a sense, one can view this as a Mach-Zehnder device where instead of having two separate waveguides arms in space, the two arms are represented by the different modes traveling within the same waveguide. As the wavelength varies, the phase difference between the modes varies with the path length difference between the TE and TM modes:

$$\Delta L = L_2 - L_1 = \left(n_{eff}^{TE} - n_{eff}^{TM}\right)L = \Delta n_{eff} L \tag{4.45}$$

Therefore, the insertion loss oscillation maxima and minima in the plots in Figure 4.31 occur when this path length difference (ΔL) is in and out of phase with the wavelength.

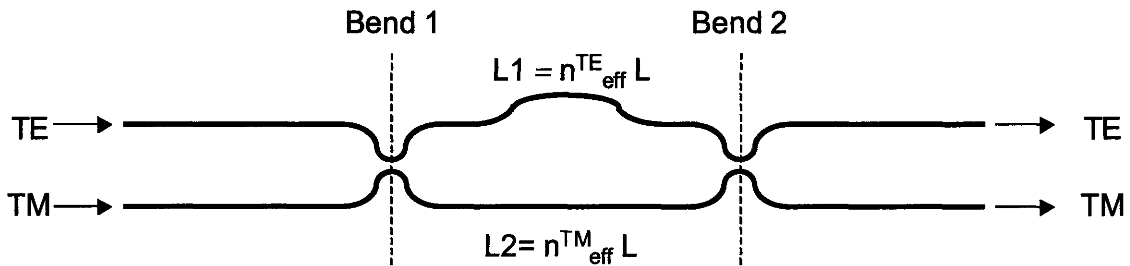

Figure 4.32 – Photonic circuit model of the mode-to-mode coupling paperclip structure, where L is the length between bends 1 and 2.

As a check, one can use the insertion loss oscillation period to estimate the effective index difference between the two modes. As seen in (4.45) the period should scale with the effective index difference between the two modes since the optical path-length difference is Δn_{eff}L. Using the free spectral range relation, we can estimate the effective index difference from our insertion loss data:

$$\Delta n_{eff} = \frac{\lambda^2}{2\,L\,\Delta\lambda} = \frac{(1.55)^2}{2\,(2800)(0.010)} = 0.043 \tag{4.46}$$

This result is a reasonable match to the Δn_{eff}=0.074 found using a mode solver on the ideal rectangular waveguide structure. The difference between these findings is accounted for by the effective index variations for the two modes that arise from the angled sidewall and dimensional variation from design that occur during fabrication.

4.9 Bend Loss – f (Δn, h, w, R)

The loss that occurs at a waveguide bend is caused by two mechanisms. First, there is the loss associated with transitioning from a straight section to a bend. One may think of this as a coupling loss, where the loss is related to the difference in overlap between the mode in the straight section and the mode in the bend, similar to relation (3.7). Second, there is the loss that arises from traveling around the bend, where power is radiated due to a phase mismatch that occurs between the field at the inner and outer radii of the bend. In most cases, it is this latter, phase-mismatch loss mechanism which dominates bend loss.

Figure 4.33 illustrates the primary waveguide mode as it travels around a 180° circular bend of radius R. As the mode propagates around the bend, it maintains a constant phase front, which results in the field on the outside of the curve to travel faster than the rest of the mode. At a certain point, the speed of the outer most portion of the field exceeds the speed of light and the light is radiated. Waveguide bends also cause the field distribution to shift towards the outside of the bend, altering the mode field shape and size. As the bend radius decreases, the phase mismatch increases, which results in the mode shifting further out and a greater percentage of radiated power. Analogous to substrate leakage, bend loss decreases with increased confinement and scales exponentially with R. As a comparison, optical fibers (low confinement waveguides) exhibit negligible bend loss for bend radii as small as several cm, while Si channel (high confinement) waveguides exhibit negligible bend loss for bend radii as small as a few microns.

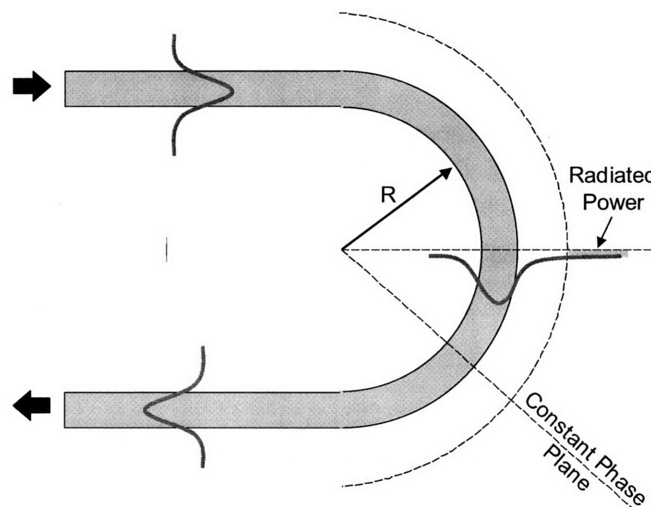

Figure 4.33 – Waveguide bend with circular bend radius R.

4.9.1 Bend Loss Theory

Analytical methods of modeling bend loss were first devised by Macatili [61] and later simplified by Marcuse [62]. While adequate for low confinement waveguides, many of the approximations used in

these analyses are not applicable for HIC waveguides. Another approach to modeling bend loss is to transform the index profile of a waveguide bend to an index profile of a straight waveguide [63] and calculate the mode profile. This method, which is used in many mode solving programs to calculate the modal shape in a slab waveguide bend, is illustrated in Figure 4.34.

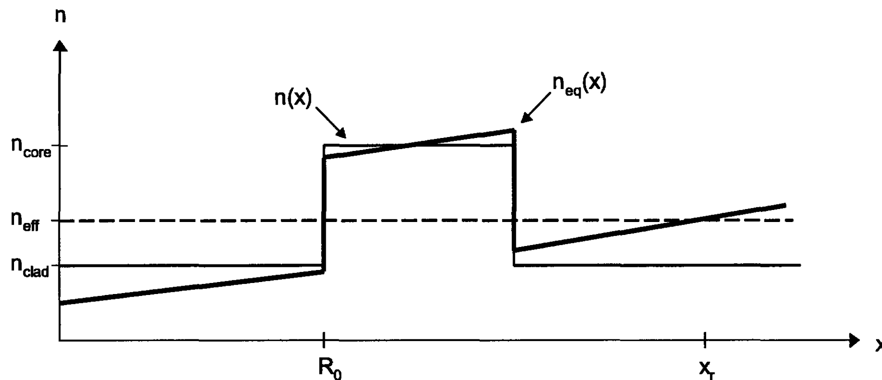

Figure 4.34 – Index profile of a waveguide - n(x) and the equivalent index profile for a bend with circular bend radius R_0 - $n_{eq}(x)$.

Similar to how the velocity of a mode propagating around a bend in a constant phase plane scales with R, the equivalent index profile reflects the varying phase velocity of the wavefront (v_p=c/n). The point, denoted x_r, at which $n_{eq}(x) > n_{eff}$, marks the point at which the mode is no longer guided and beyond which the field radiates. In a sense, the effect of a waveguide bend is comparable to applying an electric field to a quantum well – where the magnitude of the applied field increases the tunneling probability, akin to the magnitude of R with the amount of radiated power.

Accurate methods of calculating bend loss in high index contrast waveguides are limited to computer simulations using discretized meshes with cylindrical coordinate systems [64-65]. Typically, the purpose of simulating bend loss is to find a minimum bend radius, for a given waveguide geometry, that corresponds to a minimum loss threshold for a photonic circuit. Bend loss units are in dB/bend, where the threshold loss is typically and order of magnitude or two less than the propagation loss, such that the addition on N bends results in a negligible increase in loss. If proper waveguide design is used, waveguide bend loss should not be a significant contributor to transmission loss.

4.9.2 Experimental Identification of Bend Loss

The simplest way to test for bend loss is to compare the insertion loss of a straight waveguide with a waveguide with bends. If the two waveguides have similar lengths and the difference in loss is small – bend loss is negligible; if the difference is large – bend loss is significant.

The effect of bend loss can also be observed in insertion loss measurements, where the slope of insertion loss versus wavelength is proportional to the number of bends. For a waveguide with bends, the insertion loss α, is given by:

$$\alpha[dB] = \alpha_{coupling} + L\sum_i \alpha_i + N\alpha_{Bend} \tag{4.47}$$

where $\alpha_{coupling}$ is the coupling loss, α_i is the transmission loss for mechanism i, L is the length of the waveguide, N is the number of turns, and α_{Bend} is the bend loss. If (4.47) is differentiated with respect to λ, the signal wavelength, we find:

$$\frac{\partial \alpha}{\partial \lambda} = \frac{\partial \alpha_{coupling}}{\partial \lambda} + L\sum_i \frac{\partial \alpha_i}{\partial \lambda} + N\frac{\partial \alpha_{Bend}}{\partial \lambda} \tag{4.48}$$

where, holding everything else constant, it is evident that the slope of the insertion loss is proportional to N, the number of bends.

Bend loss, similar to substrate leakage, has an exponential relationship with wavelength. However, if the range of wavelengths used in the measurement is small and the bend loss is not excessive, which is typical in waveguide measurements, the slope of the insertion loss can be approximated as linear. Furthermore, if we assume that the coupling loss is a weak function of λ, i.e. $\frac{\partial \alpha_{coupling}}{\partial \lambda} \approx 0$, we can reduce (4.48) to:

$$\frac{\partial \alpha}{\partial \lambda} = N\frac{\partial \alpha_{Bend}}{\partial \lambda} + L\,C \tag{4.49}$$

where C is a constant reflects the linear wavelength dependence of all the transmission loss mechanisms for a straight waveguide. Hence, bend loss can be identified in insertion loss data by quickly estimating the loss slope to see that it scales with N. This effect is useful in determining the polarization, when it is not known.

Relation (4.48) can be observed in Figure 4.35, where the insertion loss for SiO_2 clad, 200x570 nm^2 SOI ($t_{underclad}$ = 3 μm) waveguides is plotted versus wavelength. Each data set represents the TM-polarized insertion loss for paperclip waveguides with different numbers of 180° circular bends (R=10um). TE-polarized light is more confined in these waveguide structures and consequently exhibits negligible bend loss. The small slope of the straight waveguide indicates that transmission loss in this waveguide geometry is a weak function of λ. Bend loss is evident by the scaling of the slope of insertion loss with the number of bends. Fitting the parameters of (4.49) to this data, we find C = -0.01 dB/cm and $\partial\alpha/\partial\lambda = 0.051 \pm 0.001$ dB/nm.

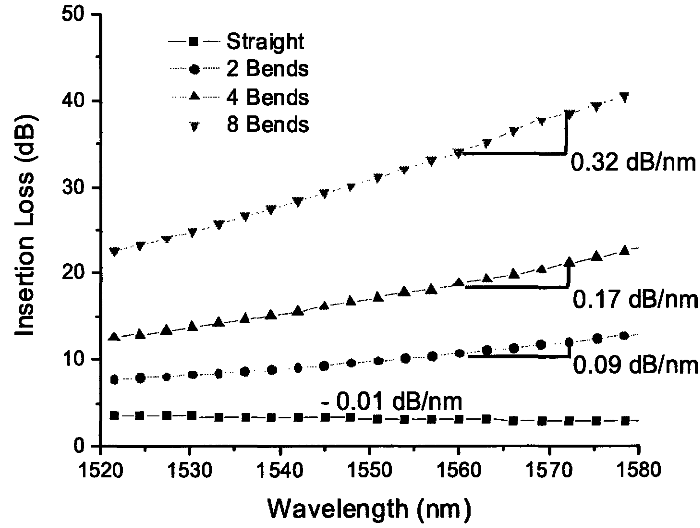

Figure 4.35 – Insertion loss behavior for TM polarized light in 200x600 nm^2 Si/SiO_2 waveguides with R=10 μm bends.

4.9.3 Experimental Measurement of Bend Loss

Bend loss in waveguides with varying numbers of bends can be measured very similarly to how transmission loss is measured for waveguides with different lengths. If the waveguide bends are spaced sufficiently close together, such that the addition of bends contributes a minimal increase to the overall waveguide length (i.e. $\partial L/\partial N \approx 0$), the difference in loss between the waveguides will be dominated by bend loss. Thus, we can differentiate (4.47) with respect to N to find:

$$\alpha_{Bend} = \frac{\partial \alpha}{\partial N} \tag{4.50}$$

Hence, the slope of the insertion loss with respect to the number of bends is equivalent to the bend loss.

Figure 4.35 is an example of bend loss measurement, where the insertion loss versus number of waveguide bends is plotted. As measured by the slope of this plot, the 180° bend loss for TM polarized light in 220x470 nm^2 SOI waveguides overclad with SiO_2 with R=10 μm bend radii, is 0.5 dB/bend. The waveguide layout for this data set is very similar to the inset of Figure 4.35, however it should be noted that this drawing is a zoomed in view of the waveguide bend structure section; in practice the overall length of waveguides, of which a majority is not shown, is much longer.

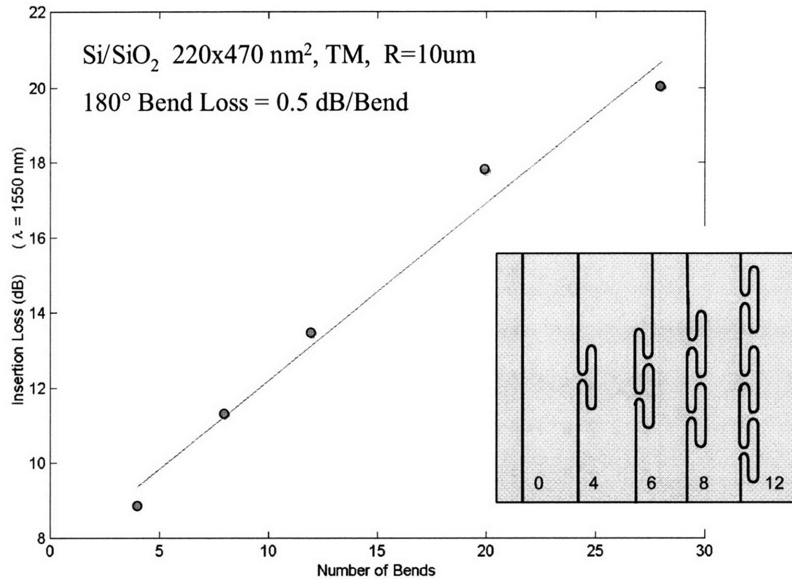

Figure 4.35 – Insertion loss data for waveguides with different numbers of bends (see inset). Bend loss is ascertained from the slope of this plot.

4.10 Loss Mechanism Summary

This chapter has detailed the pertinent details and experimental methods with which to identify roughness-scattering, absorption, non-linear processes, waveguide coupling, substrate leakage, mode coupling, and bend loss. For each of these loss mechanisms, the distribution and magnitude of optical power in the waveguide structure has a direct effect on the overall loss. For waveguide coupling and substrate leakage, the overlap of the evanescent field overlap with other waveguide structures leads to optical coupling loss. For non-linear and linear absorption, the loss is a function of the optical power distribution and intensity within the waveguide materials. While for roughness scattering, the loss is governed by the interface field intensity.

In many cases, losses that arise from non-linear processes, waveguide coupling, substrate leakage, mode coupling, and bend loss can be avoided with minimal design effort; although it is worth recognizing that these loss mechanisms do arise when researching new waveguide materials and processing methods. In contrast, the loss mechanisms that are processing based: roughness-scattering and absorption loss, remain the major challenges to realizing low-loss waveguides and are the topic of many research studies. In the following chapters, roughness-scattering and absorption loss mechanisms will be addressed for CMOS compatible HIC waveguides by improved materials processing, fabrication, and design techniques.

Chapter 5 – Crystalline Silicon Waveguide Processing

Integration of CMOS compatible electronics and photonics was first envisioned nearly 20 years ago [66], coinciding with the emergence of silicon-on-insulator (SOI) substrate technologies. Prior to SOI, only expensive and low-yield wafer bonding techniques were able to provide a method by which thin crystalline Si layers could be selectively positioned within a thin film stack. SOI substrates enable the realization of high index contrast, highly confined, single-mode, crystalline silicon waveguides that are optically isolated from its substrate and amenable to integration with microelectronics. In this chapter, the fabrication of low loss, SOI based, crystalline silicon waveguides is explored. Experimental confirmation of the Barwicz-Haus roughness-scattering theory and process methods developed to minimize sidewall roughness are discussed.

5.1 Silicon on Insulator (SOI) Wafers

Silicon on Insulator (SOI) wafers are a commercially available substrate originally developed for high speed microprocessors. SOI wafers are comprised of a thin (0.05 to 100 μm) crystalline silicon layer bonded to a thermal SiO_2 layer which is bonded to a thicker silicon wafer that acts as a mechanical support. Transistors built on SOI substrates benefit from a reduced active volume, due to the insulating layer below, which lowers the parasitic capacitance and thereby increases switching speed. The insulated active region also enables full depletion of carriers in the gate region which reduces power consumption, current leakage, and heat output. In keeping with Moore's law, the adoption of SOI substrates for high speed microprocessors is almost certain to meet the ITRS roadmap. In fact, SOI substrates are already standard in PowerPC processors.

It is a fortunate circumstance for electronic and photonic integration that SOI is also an ideal photonic platform as well. The configuration and high index of refraction difference ($\Delta n=2$) of the Si and SiO_2 layers enables highly confined, optically insulated, sub-micron cross-section, photonic interconnects which are compliant with the physical and fabrication tolerances utilized in CMOS processing. The high quality interface between Si and SiO_2 also enables atomically smooth interfaces – crucial for low loss optical routing. In addition, the ability to leverage the CMOS processing knowledge base, infrastructure, and economics as well as optical transparency with the telecommunications spectrum further enhances the attractiveness of SOI-based waveguides. The only real detriment to SOI-based waveguides is the single-level restriction imposed by epitaxial constraints.

5.1.1 SOI Substrate Fabrication

The most prevalent SOI fabrication process used nearly exclusively in this work as well as in the literature is the UNIBOND SOI fabrication process [67]; the process is detailed in Figure 5.1. The UNIBOND process joins two Si wafers by an oxidation bonding method. The top Si layer thickness is

tailored by the Smart Cut™ process, where Hydrogen is implanted at a chosen depth, which weakens the Si wafer and forms a cleavage plane by which the unwanted portion of the bonded wafer is removed. The Smart Cut process avoids a costly and timely polishing step. Post-Smart Cut, the top Si layer is polished to sub-nm roughness.

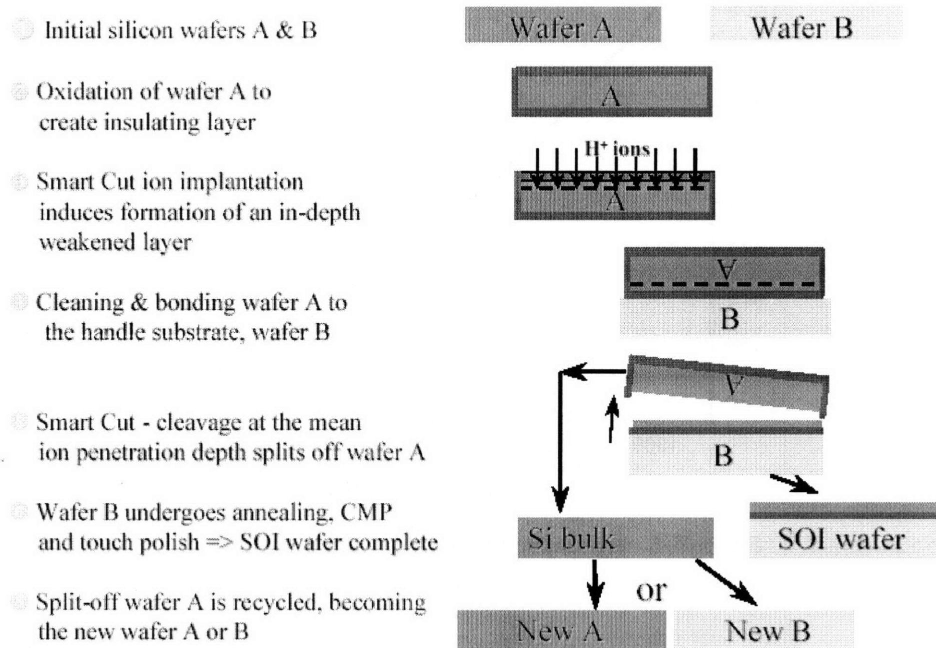

Figure 5.1 – UNIBOND SOI Fabrication process [67]

5.1.2 Silicon Material Properties

The two major material properties relevant to waveguides are index of refraction and optical absorption. In Figure 5.2, the index of refraction of Si across the telecom wavelengths is plotted; data is taken from [68]. Within the telecom wavelengths undoped Si is virtually transparent. However, for doped Si free carriers result in dispersion (Δn) and loss ($\Delta\alpha$). The extent of dispersion and loss (cm^{-1}) is proportional to the free carrier concentration and are calculated for λ=1550 nm using [49]:

$$\Delta n = -\left[8.8\times10^{-22}\Delta N + 8.5\times10^{-18}\left(\Delta P\right)^{0.8} \right] \tag{5.1}$$

$$\Delta \alpha = \left[8.5\times10^{-18}\Delta N + 6.0\times10^{-18}\Delta P \right] \tag{5.2}$$

where ΔN and ΔP are the electron and hole concentrations in units of [cm^{-3}] respectively. These free-carrier dispersion and absorption effects are the basis of many waveguide switching devices, such as the ring modulator detailed in Chapter 7.

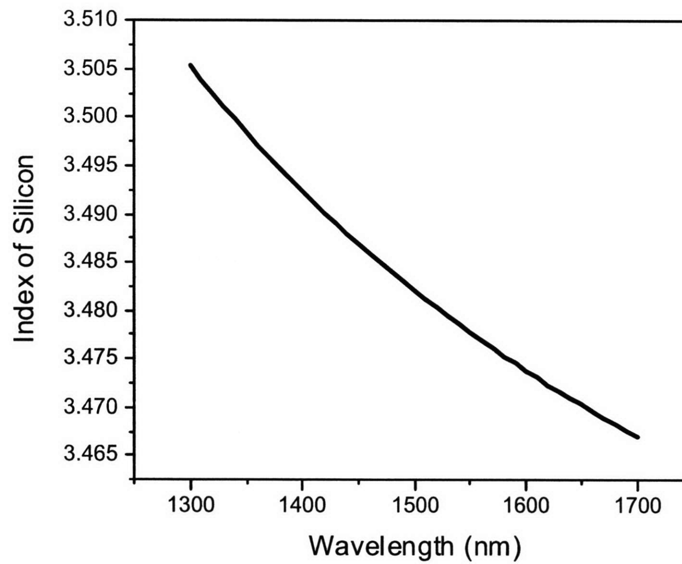

Figure 5.2 – Refractive Index of Crystalline Si [68]

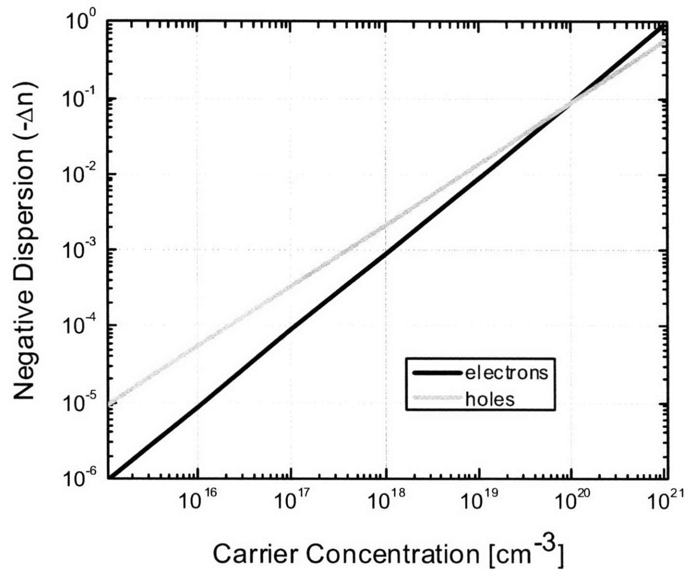

Figure 5.3 – Negative change in the index of refraction for Si as a function of carrier concentration [49]

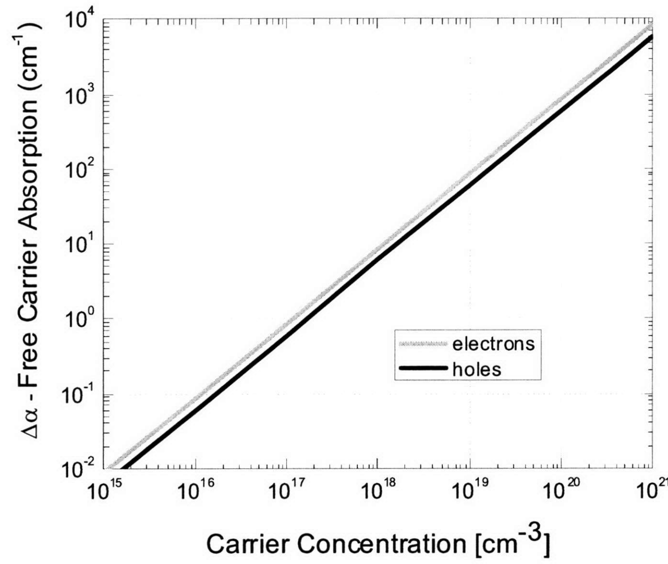

Figure 5.4 – Change in the absorption coefficient for Si as a function of carrier concentration [49]

5.2 Crystalline Silicon Waveguides

As detailed in chapter four, the dominant transmission loss (α_T) mechanisms for an integrated waveguide are roughness scattering at the top and sidewall interfaces, material absorption, and substrate coupling.

$$\alpha_T = \alpha_{sidewall\ roughness} + \alpha_{top\ roughness} + \alpha_{absorption} + \alpha_{substrate\ leakage} \tag{5.3}$$

If we restrict the analysis to a single set of waveguide materials and dimensions, it can be shown that

$$\alpha_T = f\left(\sigma_{Side}^2\right) + f\left(\sigma_{Top}^2\right) + f\left(\alpha_{bulk}^{core}\right) + f\left(t_{underclad}\right) \tag{5.4}$$

where σ_i^2 is the RMS roughness squared for interface i, α^i_{bulk} is the bulk loss of material i, and $t_{underclad}$ is the undercladding thickness. However, for Si waveguides fabricated on SOI substrates, the top surface is polished smooth, virtually eliminating top surface contributions to roughness scattering. In addition if care is taken to ensure that the doping is sufficiently low and the undercladding layer is suitably thick to have negligible effects on the loss, the dominant loss mechanism for crystalline silicon waveguides fabricated on the SOI platform is sidewall roughness.

$$\alpha_T = f\left(\sigma_{Side}^2\right) \tag{5.5}$$

Hence, SOI-based waveguides present a method with which to gauge the photolithographic and etch pattern transfer process.

5.2.1 Fabrication

The Si waveguides reported in this work, unless otherwise noted, were fabricated in at BAE Systems in Manassas, Virginia. The Manassas facility is a six inch CMOS foundry with state of the art CMOS processing tools. In particular, the deep ultra-violet photolithography (λ=248 nm) provides the resolution needed in fabricating the sub-micron dimensions needed for integrated silicon photonics. The limited lithographic resolution available at MIT's Microsystems Technology Lab (MTL) – the shared on-campus cleanroom – is inadequate for this application and precluded it use for nearly all aspects of Si waveguide fabrication.

SOI waveguide fabrication commenced with wafer cleaning, followed by photoresist deposition. Deep-UV photolithography was used to expose the mask and transfer the pattern into the resist. Post-development, the wafer was etched with an AMAT DPS poly etch chamber with an HBr/Cl2/HeO2/CF4 chemistry to define the waveguides with low roughness. Afterwards, the resist was removed by use of an oxygen plasma asher. A 3 μm top cladding layer was deposited by high density plasma (HDP) plasma enhanced chemical vapor deposition (PECVD) from SiH_4 and O_2 chemical precursors. HDP PECVD was chosen for its low temperature deposition and superior high aspect ratio trench filling properties.

In some cases, the sidewall roughness was inspected, prior to the top cladding deposition by an AMAT nanoSEM. The AMAT nanoSEM is a fantastic tool which enables the user to view and measure both the top and sides of etched features, enabling characterization of sidewall roughness and spectral density [69]. The line edge roughness (LER) is measured with nm-scale accuracy yielding the amplitude of the roughness. Since three standard deviations (3σ) of a distribution is approximately 99%, the RMS roughness is obtained by:

$$\sigma = \frac{LER}{3} \tag{5.6}$$

5.2.2 Experimental Results

Silicon waveguides were fabricated from 200 nm thick SOI wafers with a 3 μm buried oxide (BOX) layer. As an initial attempt, the loss results were reasonable and comparable top results; however the etching and top cladding steps resulted in an unforeseen complication – air voids at the waveguide sidewalls, as seen in Figure 5.5.

The presence of voids resulted from a change in the waveguide process flow. The original plan was to use deposited silicon as the waveguide material, where a thin silicon nitride (SiN) layer would be

deposited below the deposited Si layer to act as both an anti-reflection coating (ARC) and an etch stop. However, the inclusion of SOI wafers, as a metric to evaluate the sidewall roughness, precluded the use of the underlying SiN layer. The presence of the exposed, underlying SiO_2 layer during the etch step, complicated with an overextended etch time, led to oxygen radicals attacking the polymerization on the waveguide sidewall. This effect was not seen when the SiN etch stop layer was used for deposited silicon layers. As a result, the etch chemistry undercut the foot of the waveguide and formed a recess at the bottom of the waveguide. In turn, this recess provided a shadowing effect during the top cladding deposition, forming voids in the upper cladding near the waveguide sidewall.

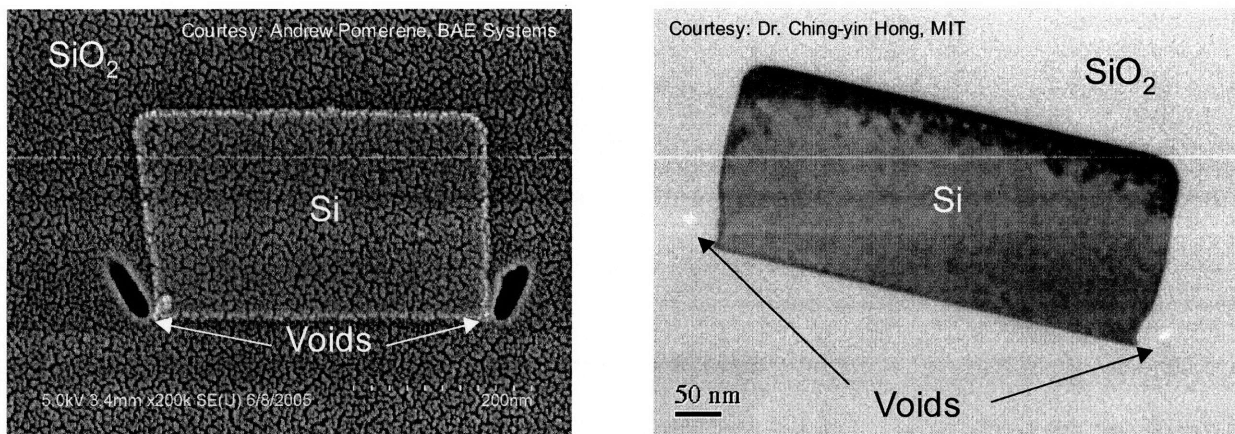

Figure 5.5 – Cross-sections of SOI channel waveguides clad with HDP SiO_2 from the initial BAE process run. On the left is an SEM image taken from the edge of the wafer and on the right is a TEM image taken from the center of the wafer.

As seen in Figure 5.5, the voids reside at the foot of the sidewall, consistent with polymerization removal by oxide radicals, originating from the SiO_2 undercladding layer, interacting with the etch chemistry. The SEM image on the left is taken from the upper left quadrant of the wafer, near the edge, and has seemingly larger voids than the TEM image of a waveguide taken from the center of the wafer. The size distribution and morphology of the voids along the waveguide is unclear and difficult to inspect. However it is likely that the voids vary in size along the length of the waveguide and vary with the waveguide sidewall roughness. Effectively, the altered shape of the voids in the propagation direction of the waveguide results in scattering of the guided light, similar to sidewall roughness scattering. Therefore, the waveguide measurements will have an added loss that is a function of the void size, variation, and distribution.

Interestingly, the waveguide transmission loss measurements from chips located in the upper left quadrant yielded consistently larger losses than those taken from the center of the wafer. As seen in Figure 5.6, the transmission loss measured by the cutback method for a variety of waveguide shows a

nearly 10 dB/cm difference between the losses at each location for the TE mode. Combining this with the difference in void size, as observed in figure 5.5, for the different wafer locations suggests that the voids play a role in considerably increasing the waveguide transmission loss. Each data point is an average of four to six loss measurements and the error bar length is plus or minus the standard deviation of those measurements. The decreasing trend of loss with width is expected as it is indicative of roughness-scattering as the dominant loss mechanism.

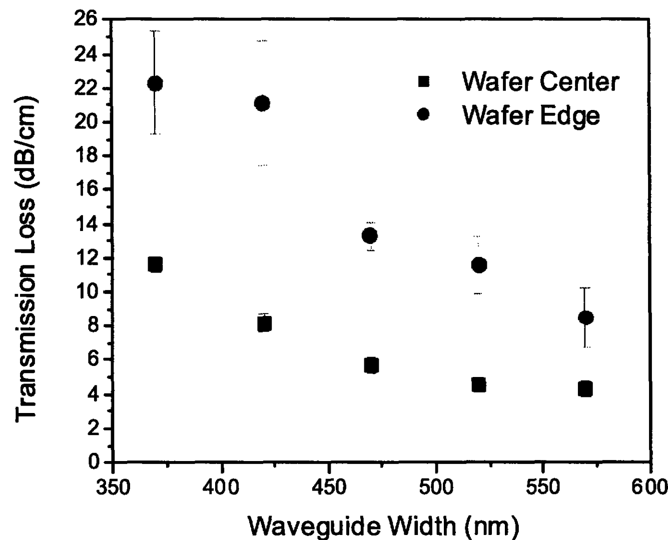

Figure 5.6 – Average waveguide transmission loss for TE polarized light (λ=1550 nm) as a function of width for 200 nm height SOI waveguides with a 3 micron BOX and SiO_2 top cladding.

The small voids at the center of the wafer presumably have a small effect on the loss as they are relatively farther from the sidewall where the evanescent field is minimal. In addition, the small deviation in loss values for the waveguides in the center of the wafer suggests that any variation in the void shape or size is a small effect.

5.2.3 Comparison of Experimental Results with Barwicz-Haus Theory of Roughness-Scattering

In chapter 4, the modeling of roughness scattering was discussed in which the application of Payne-Lacey theory was concluded to overestimate the scattering loss from a rough waveguide sidewall. In short, the Payne-Lacey theory approximates the loss of a channel waveguide by approximating the field intensity at the rough sidewall with the two-dimensional field distribution of a slab waveguide with similar dimensions and roughness. While experimental verification of the Payne-Lacey theory in HIC channel waveguides has been proposed [42], the study is questionable. For one it applies the theory, which was devised for the TM mode, to experimental data measured with the TE mode. Second, the Payne-Lacey

theory is intended for single mode waveguides but the theory is fit to experimental multimode waveguide data. In an effort to find a more accurate model, particularly for the HIC channel waveguides, Barwicz and Haus devised a roughness-scattering theory which takes into account the three-dimensional field distribution of the primary mode in a channel waveguide [40]. In this subsection the Barwicz-Haus Theory of waveguide roughness scattering is evaluated for the first time with experimental waveguide loss data in conjunction with sidewall roughness measurement.

The first step in analyzing the Barwicz-Haus theory is to compare experimental and theoretical loss values for single-mode channel waveguides and estimate the sidewall roughness. Figure 5.7 contains two plots corresponding to the TE and TM mode transmission loss for Si/SiO_2 waveguides. The experimental data, measured by the cutback method, was taken from the BAE processed SOI waveguides (from the center of the wafer, where the voids, if present, have a minimal effect on loss), and compared with theoretical values of the Barwicz-Haus theory for several sidewall roughness values. Theoretical data was interpolated from the graphical solutions of Barwicz and Haus depicted in Figure 4.10 for a waveguide height of 200 nm.

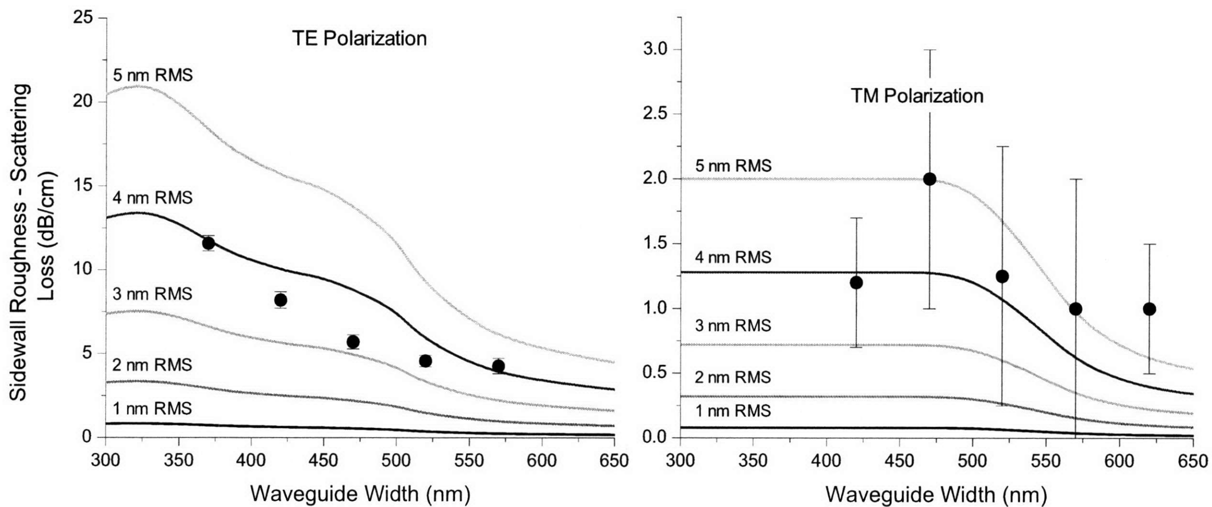

Figure 5.7 – Loss versus waveguide width for the TE mode (left) and TM mode (right) at λ=1550 nm for Si waveguides. The dots represent experimental data from the SOI waveguide fabricated in the initial BAE process run. The curves represent the Barwicz-Haus theoretical loss for different RMS sidewall roughness values.

Overall, the theoretical and experimental results are in good agreement. The data sets have similar loss versus width trends and estimated sidewall roughness values for both polarizations. The polarization dependent behavior is expected as it reflects the relative field intensity at the rough sidewalls for these waveguide geometries. The greater sensitivity of the TE mode reflects the higher mode confinement and therefore higher sidewall field intensity whereas the virtually flat loss response of the

TM mode represents low confinement; the disparity arises from the electromagnetic boundary conditions (see Chapter 2). The larger error bars for the TM mode is due to added loss from bend loss in the paperclip structures. In comparison with theory, the TE experimental data suggests an RMS sidewall roughness value of $\sigma = 3 - 4$ nm, while the low sensitivity of the TM mode to roughness scattering makes it difficult to make a similar estimate. However, the roughness value found in the TE estimate is within the error range of the TM data.

To confirm whether or not the estimate of $\sigma = 3 - 4$ nm is accurate; the AMAT nanoSEM was used to measure the line edge roughness of SOI waveguides etched under the same process conditions. The measured RMS roughness for the unclad SOI waveguide sidewalls ranged from $\sigma = 2 - 3$ nm. This result indicates that the Barwicz-Haus theory is considerably more accurate than the Payne-Lacey Theory. By comparison, the roughness values as estimated by the widely used Payne-Lacey theory ($\sigma \approx 1.0$ nm for the TE mode and $\sigma \approx 0.6$ nm for the TM mode) yield extremely low and unlikely roughness values. The effect of top cladding deposition on sidewall roughness is unknown; however it is believed to not significantly affect the roughness.

5.2.4 Comparison to Literature

The fabrication of low loss single-mode, crystalline silicon waveguides, on SOI substrates has been the focus of many studies [13, 70-73]. However, comparing the loss results is difficult in that each study employs different waveguide geometries which have differing sensitivities to sidewall roughness. While waveguide loss is an important metric in evaluating the application of a photonic technology, the fundamental limit is determined by the sidewall roughness. Figure 5.8 lists Si channel waveguide results from the literature, where the dimensions and transmission loss are used in estimating the RMS roughness (σ) of the waveguide sidewall by applying the Barwicz-Haus Theory.

The extent of scattering is a function of the field intensity at the sidewall and the difference between the effective index (n_{eff}) and cladding index (n_{clad}), as observed in equation (4.13). While the model used in estimating the sidewall roughness is devised for SiO_2 clad Si waveguides, it is applied to air-clad Si waveguides as well. This approximation is reasonable given that for the air-clad case, both the effective index and cladding index are decreased for a given waveguide geometry, resulting in a relatively small change in the difference between the effective and cladding indices, and thus a small change in the scattering potential for the air-clad and SiO_2-clad cases. Likewise, the slightly higher sensitivity to roughness is off-set by the reduced field intensity at the sidewall, when compared to the SiO_2-clad case.

Interestingly, the wide range of losses published in the literature is more a factor of the differing waveguide geometries rather than sidewall roughness. For the most part, the best Si waveguide loss results have approximately the same sidewall roughness ($\sigma = 2.0 - 2.5$ nm). This result is right in line

with a recent line edge roughness study of photo-resists using deep UV lithography, which places the LER of the resist between 5 and 6 nm which corresponds to an RMS roughness of a little less than 2 nm [69]; suggesting that the roughness of the resist is a possible origin of waveguide sidewall roughness during the etch process. The kinetics of mask erosion during etching is also thought to contribute.

Within each study, the waveguides are processed identically and therefore the loss values should correspond to roughness value estimates that vary within a small range of values. This is best seen in the data from this work, where the estimated roughness value for each waveguide geometry is within a range of one nm. The roughness estimates listed for the data from this work can be viewed as effective roughness in light of the processing complications. The only study which does not follow this trend noted that SEM inspection revealed "the narrow wires (waveguides) have more roughness than those of wider wires" [72]. This trend is seen in the roughness estimates and further supports the validity of the Barwicz-Haus theory.

Research Group [Reference]	Height (nm)	Width (nm)	TE Mode Loss (dB/cm)	λ (nm)	Loss Measurement Method	Cladding Type/ Notes	Estimated σ (nm)
Lincoln Labs [70]	210	450 550	2.5 ± 0.5 1.9 ± 0.5	1550	Cutback	SiO_2-Clad Ox. Smoothing	2.0 2.5
IBM [13]	220	445	3.6 ± 0.1	1500	Cutback	Air-Clad SiO_2 Hard Mask	2.3
NTT [71]	300 200	300 400	7.8 2.8	1500	Cutback	SiO_2-Clad SiO_2 Hard Mask	2.2 2.2
Ghent University [72]	220	400 440 450 500	33.8 ± 1.7 9.5 ± 1.8 7.4 ± 0.9 2.4 ± 1.6	1550	Fabry-Perot	Air-Clad	6.9 4.0 3.5 2.0
This Work SOI Control (possibly with influence of voids)	200	370 420 470 520 570	11.6 ± 0.5 8.2 ± 0.5 5.7 ± 0.5 4.6 ± 0.5 4.3 ± 0.5	1550	Cutback	SiO_2-Clad	4.1 3.7 3.1 3.3 4.6
This Work 10 nm SiN nanocladding Chapter 7	200	370 420 470 520 570	10.2 ± 0.5 6.3 ± 0.5 4.3 ± 0.5 3.4 ± 0.5 3.4 ± 0.5	1550	Cutback	SiO_2-Clad	3.8 3.2 2.7 2.9 4.1

Figure 5.8 – Literature comparison of Si channel waveguide losses and estimated sidewall roughness using Barwicz-Haus theory.

5.3 Thermal Oxidation Smoothing

In efforts to reduce Si waveguide sidewall roughness, post-etch smoothing methods have been explored. Oxidation smoothing is one such post-etch process which has successfully reduced the loss in Si waveguides [70, 73]. In this section, the kinetics of oxidation smoothing of Si waveguides is studied.

5.3.1 Oxidation Smoothing Kinetics

There are two kinetic regimes that occur during the oxidation of silicon: reaction-limited and diffusion-limited. Oxidation of a bare silicon surface is initially reaction-limited. The oxidation rate is linear with time and governed by the rate at which the reactant reaches the surface, thus the term reaction-limited regime. However, as the oxidation continues, the oxide layer grows thicker, requiring the oxidizing species to diffuse through the layer in order for oxidation to proceed. This diffusion-limited regime results in a retardation of the oxidation rate, which is proportional to the square root of time. The transition from reaction-limited to diffusion-limited oxidation occurs when the oxide reaches a thickness such that the diffusion rate is less than the reaction rate at the silicon interface. The thickness of the oxide at the kinetics regime transition is dependent on the diffusivity of the oxidizing medium through the oxide and the temperature; typically this thickness can vary from several to hundreds of nm. The linear-parabolic growth kinetics of oxidation smoothing, as just described, is best quantified by the Deal-Grove model [74].

The kinetics of oxidation *smoothing* is dependent on the oxidation kinetics regime. In the reaction-limited regime, oxidation smoothing is thermodynamically driven, as explained by the Gibbs-Thompson relation:

$$\mu(\kappa) = \mu(\infty) + \gamma\Omega\kappa \tag{5.7}$$

where $\mu(\kappa)$ is the chemical potential at a surface of curvature κ, $\mu(\infty)$ is the chemical potential at a flat surface, γ is the surface energy, and Ω is the atomic volume. The Gibbs-Thompson relation signifies that the chemical potential of a surface is dependent on the curvature of the surface. Essentially, the peaks of a rough surface (positive curvature) have a higher chemical potential or reactivity than the troughs of the roughness (negative curvature). For the case of oxidizing a rough Si surface, the Gibbs-Thompson relation implies a differential reaction rate occurring on a rough surface, that results in roughness amplitude reduction (i.e. smoothing) of the surface during the course of oxidation.

Diffusion-limited oxidation smoothing is a flux driven process. Rather than depending on the surface potential, the oxidation rate is dependent on the diffusion rate of oxidizing species. As the oxide thickness grows, the rate of incoming oxidizing species is distributed in a uniform front parallel to the oxide-ambient interface. In the diffusion-limited regime, the incoming oxidizing species smoothes

roughness because diffusion of an oxidizing species to a roughness peak is more probable than to a roughness trough, i.e the oxide thickness is thinner (and thus the diffusion path is shorter) at the roughness peaks. In a sense, diffusion-limited oxidation is a smoothing process that is reaction rate independent.

5.3.2 Experimental Details

Si waveguides were fabricated from SOI wafers with a 200 nm top Si layer and 1 μm BOX layer at Intel, courtesy of Dr. Kevin Lee. The wafers were patterned with a G-line (436nm) 10X stepper and etched with a reactive ion etching (RIE), using an SF_6 etch chemistry, to define the silicon waveguide pattern. All samples were taken from the same wafer to ensure uniformity in the experiment. Dry oxidation of waveguide samples was performed for 30, 60, and 120 minutes at 1050°C. Buffered Oxide Etch (BOE) was used to remove the oxide for roughness measurement.

A Digital Instruments Nanoscope IIIa Atomic Force Microscope (AFM) was used to measure the roughness of the waveguides. Measurement scans (3 X 3 μm^2) were performed parallel to the direction of the waveguides using the tapping mode. This was necessary for distinguishing between waveguide roughness and errors between adjacent scans. Normally, the steep angle of an etched sidewall is too steep to measure with an AFM tip; however the non-ideal etching of the waveguides in this study led to a shallow sidewall etch angle suitable for AFM measurement. Even so, the side of the tip is used when measuring sidewalls, which most likely diminishes the resolution that can be obtained. The lessened resolution results in a smoothing of the surface in terms of amplitude height. Thus the values obtained in our measurements are most likely understated. Care was taken to measure all samples with the same tip orientation.

5.3.3 Experimental Results

The reduction of surface roughness with thermal oxidation is clearly seen in the AFM images depicted in Figure 5.9. As compared to the oxidized waveguides, the as-fabricated waveguide surface roughness contains a greater share of short period roughness and appears rougher. However as oxidation ensues, the roughness is smoothed where short period roughness is reduced fastest, giving way to long period roughness in the oxidized samples. The efficient smoothing of short period roughness is expected as it has a higher curvature compared to long period roughness and therefore a higher chemical potential.

Dimensional shrinkage due to silicon consumption by oxidation is also visible in the AFM micrographs. The scale of all three measurement fields is identical; therefore a direct size comparison can be applied. The width of the 120 minute dry oxidation sample waveguide is roughly 300 nm thinner than the as-fabricated waveguide.

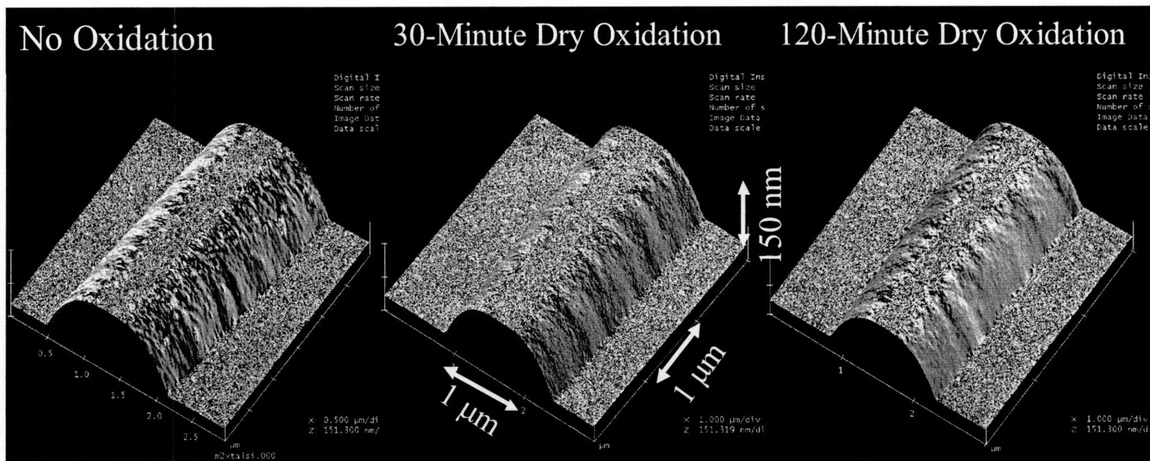

Figure 5.9: AFM images of silicon waveguides, the left image is as-fabricated whereas the center and right waveguides have undergone 30 and 120 minutes of dry oxidation and subsequent oxide etch respectively.

Quantitative measurements of the sidewall roughness as a function of spatial roughness period, obtained from the AFM software, are plotted in Figure 5.10. Again, we see that the overall roughness amplitude decreases for all roughness periods with oxidation time. Hence, oxidation smoothing is effective at reducing roughness on a Si surface and a means of reducing transmission loss for Si waveguides. A comparison of the oxidation time versus the extent of smoothing reveals that the rate of roughness reduction diminishes with oxidation time. This is expected as it indicates that the oxidation kinetics has transitioned from the reaction-limited regime to the diffusion-limited regime. A seen in the plot, more smoothing occurred, as measured by area under each curve, in the first 30 minutes than the following 90 minutes of oxidation.

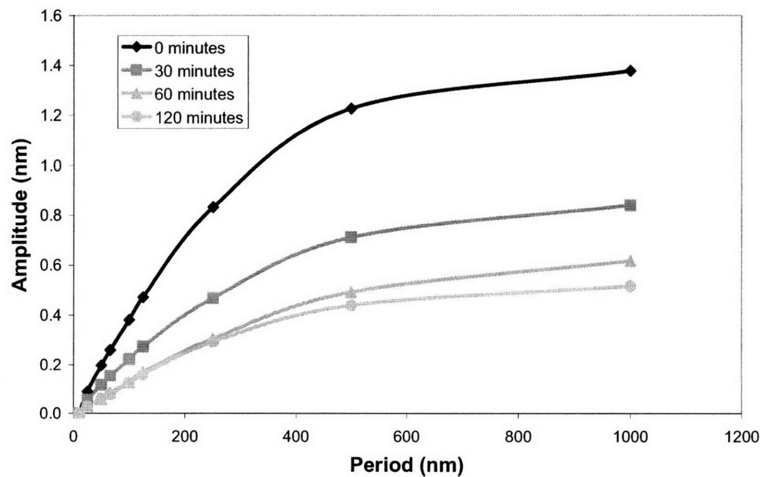

Figure 5.10 - Plot of waveguide roughness amplitude versus roughness period for different oxidation times.

5.3.3 Oxidation Smoothing Simulation

To further our understanding of oxidation smoothing TSUPREM4 – a simulation program used extensively in the microelectronics industry for modeling the structure of CMOS devices during thin film processing – was used to model the oxidation smoothing of the waveguides. In this simulation, a sinusoidal silicon surface was subjected to different oxidation times to evaluate its effect on the surface roughness. The surface roughness was approximated by using trapezoidal cut outs in the silicon surface. This approximation only affects the short-term oxidation behavior, since the high surface energy corners of the trapezoids are oxidized fastest, leaving a sinusoidal profile after only a few minutes of oxidation. Similar to the oxidation experiment described above, the simulated surface was oxidized in a dry O_2 environment at 1050°C.

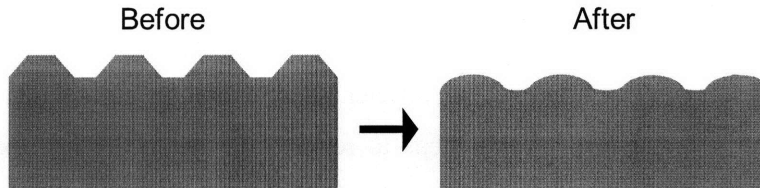

Figure 5.11 – Schematic of silicon surface used in the TSUPREM4 simulation of oxidation smoothing.

Simulation results for a silicon surface with a 2.6 nm roughness amplitude and a 50 nm period (comparable to that found on silicon waveguide sidewalls) is shown in Figure 5.12. As seen in the experimental results, the extent to which the roughness is reduced is a direct consequence of the oxidation kinetics. At the beginning of the oxidation, when the kinetics are reaction-limited, the roughness is smoothed fastest and at a linear rate. However, once the oxide thickness builds and the oxidation kinetics enters the diffusion-limited regime, the smoothing rate decreases and takes on a parabolic dependence with time. Another interesting point to note is that the period of the roughness remains unchanged after these simulations.

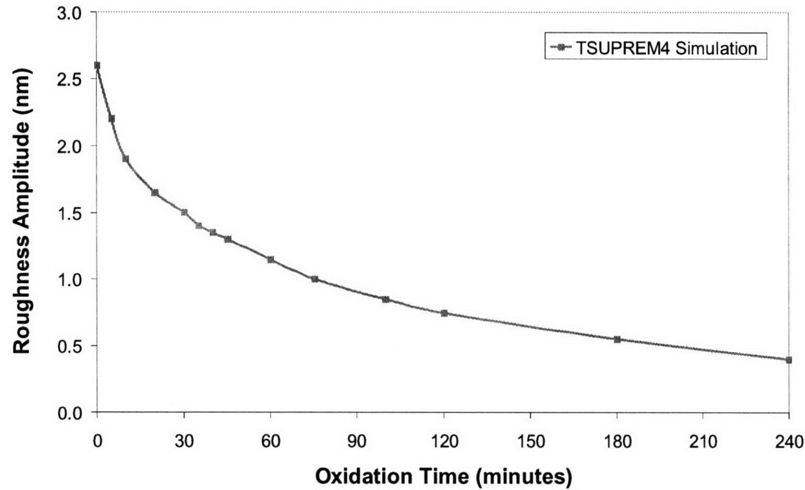

Figure 5.12 –TSUPREM4 simulation of roughness amplitude versus oxidation time.

5.3.5 Multiple Oxidation Smoothing Method

Recognizing that the smoothing rate is fastest in the reaction-limited regime, the multiple oxidation smoothing method was devised to improve the efficiency of oxidation smoothing. In this method, multiple steps of oxidation, separated by etch steps to remove the newly formed oxide each time the oxidation kinetics transitions from the reaction-limited to the diffusion-limited regime, are used to smooth the rough surface. The goal is to continuously oxidize the surface in the reaction-limited regime whereby the total oxidation time is minimized as well as the total exposure time to elevated temperatures.

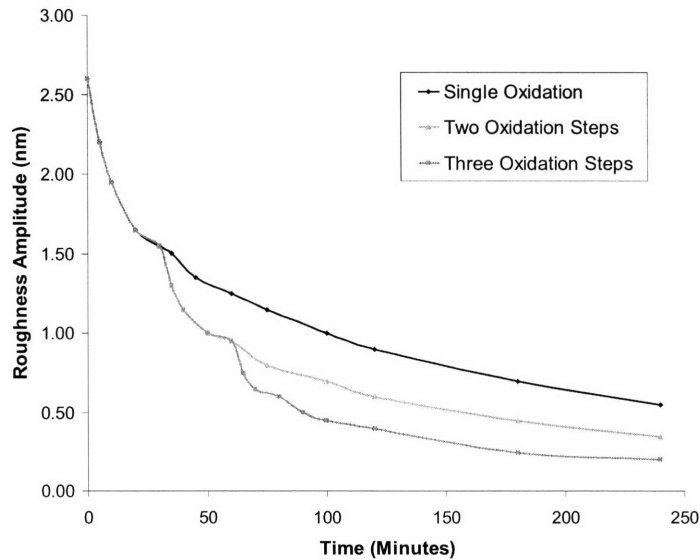

Figure 5.13 –TSUPREM4 simulation of the multiple oxidation smoothing method.

To confirm this idea, the multiple oxidation smoothing method was tested in a TSUPREM4 simulation. A two-step and a three-step oxidation process were employed by removing the oxide after 30

minutes for the two-step process and 30 and 60 minutes for the thee-step process. The simulated results are plotted in figure 5.13. In comparison to the single step oxidation, which transitioned from a linear to a parabolic relation, the MOSM simulations maintained a linear trend until the last etch step. Hence, the oxidation time and thus thermal budget needed to achieve a given roughness amplitude reduction is minimized when employing the multiple oxidation smoothing method.

5.4 Wet Chemical Oxidation Smoothing

In an effort to find a sidewall smoothing process that is compatible with integrated photonic and electronic circuit fabrication, an alternative oxidation smoothing method was developed. Thermal oxidation smoothing is impractical due to the elevated process temperature, which places a strain on the thermal budget and limits the process flow order. Additionally, the considerable cross-sectional size and shape alteration that occurs in thermal oxidation smoothing complicates photonic circuit design. Instead, silicon waveguides are smoothed by wet, oxidizing chemicals, or what we term as "wet chemical oxidation". This method allows greater control in the limiting nature of the reaction and preserves dimensional integrity. Similar to the multiple oxidation smoothing method, wet chemical oxidation involves the periodic removal of the oxide to repeatedly oxidize the Si waveguides in the efficient, reaction-limited regime. In this work wet chemical oxidation is evaluated as a means of smoothing Si waveguides. The effectiveness is characterized by waveguide transmission loss measurements.

5.3.1 Wet Chemical Selection

Fortunately, there are many liquid, oxidizing chemistries available, several of which are already quite common in thin film processing. In most cases, the low temperature wet oxidizing chemistries react with the silicon surface and form a chemical oxide several nm thick, at which point the reaction ends. As a low temperature process, diffusion of the oxidizing chemistries through the oxide is negligible and thus the reaction is entirely in the reaction-limited regime. The choices of oxidizing chemicals range from purely oxidizing chemicals to those that both oxidize and etch. At issue in chemical selection is the quality of the chemical oxide at the Si interface.

In keeping with existing, compatible oxidizing chemistries, three candidates emerge: nitric acid, Piranha, and RCA cleaning chemistries. XPS studies have revealed that the distribution of interface states for Pirahna chemical oxides are nearly identical to that found in thermal dry oxidation [75], while the concentration of interface states is comparatively minimized for nitric acid chemical oxides [76]. However, the standard clean one (SC1) chemistry is particularly attractive because of the continual formation and dissolving of the oxide layer, where H_2O_2 oxidizes while NH_4OH slowly dissolves the chemical oxide, slowly consuming the Si as the oxide front propagates [77].

The oxide removal step is complicated by the presence of the exposed SiO_2 undercladding layer below the Si waveguides. Thus a dilute oxide etch is needed to prevent undercutting of the undercladding layer, otherwise the waveguides can dislodge from the substrate. This constraint is what prevents the employment of many popular Si smoothing chemistries, as they etch SiO_2 as well. Dilute HF chemistries are well known to slowly etch SiO_2 layers with high selectivity over Si, however care should be taken to not use buffered HF solutions, as the presence of NH_4F has been shown to result in anisotropic etching of Si surfaces which can induce roughness on (110) Si surfaces [78-79].

5.4.2 Experimental Procedure

Crystalline silicon waveguides were fabricated from (100) SOI wafers with a 220 nm thick top Si layer on a 1 μm BOX layer, courtesy of Dr. Steven Spector at Lincoln Labs. Photolithography was used to pattern the SOI wafers with a 248 nm stepper on Shipley UV5 resist. Dry etching with $HBr:Cl_2:He_2:O_2$ at flow rates of 135:37.5:6:1.5, sccm, respectively, defined the waveguides at a pressure of 10 mtorr, with 200W source RF and 100 W bias RF. For these experiments, the photoresist was overexposed creating larger sidewall roughness during the etch process. These waveguides were used, rather than our optimal, as-fabricated waveguides with 500 nm width and less than 3 dB/cm transmission loss, to emphasize the effects of wet chemical smoothing.

Once fabricated, the waveguides were subjected to one of four wet oxidizing chemistry recipes (Figure 5.14). In this notation, DI rinse is an abbreviation for a deionized H_2O rinse, HF is an abbreviation for dilute (50:1) HF, SC1 solution consists of DI H_2O, H_2O_2, and NH_4OH in a 5:1:1 ratio heated to 80°C, SC2 solution consists of DI H_2O, H_2O_2, and HCl in a 6:1:1 ratio heated to 80°C, and Piranha solution consists of H_2O_2 and H_2SO_4 in a 1:3 ratio self-heated to ~ 100°C.

Recipe #	Recipe Name	Sequence	Repeated
1	5X RCA	10 min SC-1, DI rinse, 15 sec HF, DI rinse, 15 min SC-2, DI Rinse	5 times
2	5X SC1	10 min SC-1, DI rinse, 15 sec HF, DI rinse	5 times
3	Extended SC1	50 min SC-1, DI rinse, 30 sec HF, DI rinse	1 time
4	5X Piranha	5 min Piranha, DI rinse, 30 sec HF, DI rinse	5 times

Figure 5.14 – Wet chemistry sequences used in this study

Recipe 1 consists of repeating the RCA clean five times. This recipe was chosen because of its widespread use in wafer processing and known oxidizing nature. As a wafer cleaning process, RCA has three steps; the first is standard clean one (SC1) which removes organics and cleans surface impurities by

reacting with Si and traps surface impurities in a chemical oxide. The second step is a dilute HF dip, which removes the oxide created by the SC-1, and passivates the surface. The third step is standard clean two (SC2) which removes residual metals from the surface and leaves a protective hydrous oxide film. Recipe 2 is basically recipe 1 without the SC2 step and is intended to determine what role SC2 provides in smoothing. This recipe was repeated five times for a total SC1 immersion time of 50 minutes. Recipe 3 was used as a control to see the effects of doing multiple chemical oxidations as opposed to a single long SC1 chemical oxidation. In this recipe, a 50 minute, as opposed to five, ten minute SC1 exposures was used. The final recipe used piranha, an alternative wet chemical oxidizer.

Waveguide samples were prepared by cleaving the wafers, subsequently followed by a solvent clean in an ultrasonic bath and N_2 blow drying. Cleaving occurred after wet chemical treatments to ensure consistent facet reflection, waveguide sample lengths varied from 0.4 – 0.6 cm. Once prepared, the waveguides were measured by the Table 3 system. Waveguide loss was determined by the Fabry-Perot method. For these measurements, the output fringe ratios were averaged over a scan from $\lambda = 1550$ - 1551 nm in the TE polarization. Waveguide lengths were determined with ± 0.001 cm resolution using a Tencor P10 Profilometer. For accuracy, the reflectivities of the waveguide facets were calculated with 3D FDTD simulations. Each experimental data point is a collection of several waveguides averaged to find the loss value. Four waveguide geometries were measured in these experiments (220 x 630, 830, 1130, and 1330 nm^2). Multimode behavior was seen in the two widest waveguides, as evidenced by the observance of beating of the Fabry-Perot fringes. For these cases, losses were obtained by measuring fringes of the primary mode at the maxima and minima of the secondary mode.

A Digital Instruments Atomic Force Microscope (AFM) was used to measure the top surface roughness of the waveguides after RCA treatments to evaluate the possibility of surface roughening. Measurement scans (1 X 1 μm^2), in the tapping mode, were performed on the larger waveguides. RMS roughness amplitudes (σ) were obtained from the NanoscopeIII software. All samples were measured with the same tip.

5.4.3 Comparative Results and Discussion

Transmission loss versus waveguide width is plotted for the as-fabricated and wet chemical oxidized waveguides in Figure 5.15. For clarity, error bars were removed from the plot, the average waveguide measurement varied by ± 1 dB/cm, this variance is larger than estimated experimental errors.

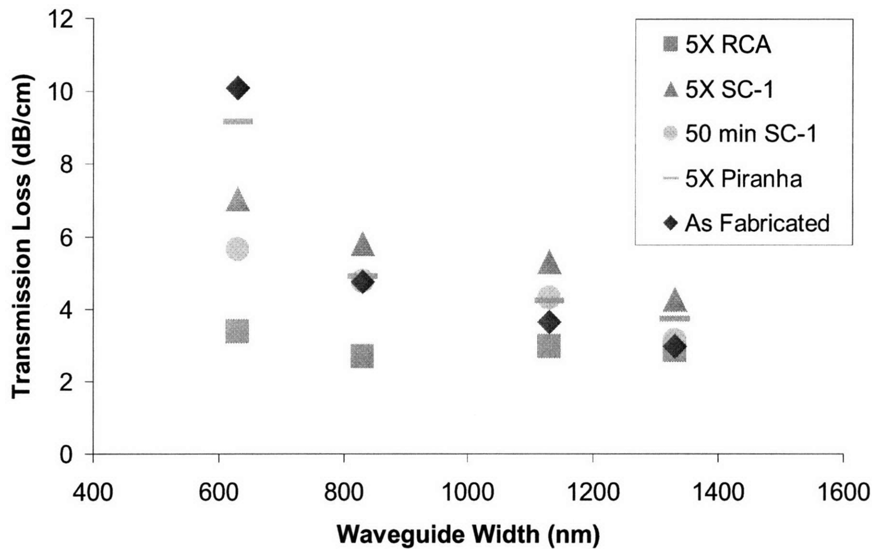

Fig. 5.15 - Transmission loss versus Si waveguide width for the various wet chemical oxidation recipes listed in Figure 5.14. Measurement variance error bars for each data point (± 1 dB/cm) have been omitted for clarity.

As anticipated, the 630 nm width waveguides show the most dramatic reduction in loss (~ 7 dB/cm) due to wet chemical oxidation. This is to be expected since the waveguide sidewall field intensity is comparatively the greatest for the 630 nm wide waveguide, resulting in the highest sensitivity to sidewall roughness smoothing. To illustrate this, the modal profiles for the 630 and 1330 nm width waveguides were calculated using an Apollo mode solver and plotted in Figure 5.16. The superimposed white delineation around each mode is a normalized isopower line.

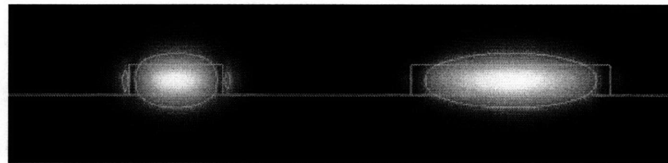

Figure 5.16 - Modal profile of light in the 630 nm and 1330 nm wide Si waveguides. Calculated with Apollo Mode Solver.

The reduced roughness sensitivity with waveguide width can also be seen in the diminishing spread of transmission losses, with respect to waveguide width, among the various wet chemical recipes employed in this study. The small spread of losses for the widest waveguides indicates that the roughness sensitivity is minimal.

Comparatively, the four recipes differed in effectiveness with 5X RCA exhibiting the best (110) sidewall smoothing results. It should be noted that a direct comparison of each recipe is not completely fair given different chemicals and overall recipe times differed. Additionally, each recipe is comprised of

two or three different chemicals which evaporate at different rates, adding another variable to this experiment. This effect is amplified given that the chemical solutions are heated.

Wilmer Kern, the inventor of the RCA clean, documented the differing evaporation rates with regard to the SC1 constituents [77] showing that the NH_4OH decomposes faster than the H_2O_2. According to this study, after 50 minutes at 85°C, NH_4OH and H_2O_2 levels drop to 10% and 50% of their original levels respectively. This effect is important to note since SC1 solutions are known to roughen smooth Si surfaces to sub-nanometer roughness [80-81]. It has also been documented that this roughening is an increasing function of NH_4OH concentration in SC1 [81]. Miyashita et al. has shown that an RCA clean using an SC1 solution with a 1:1:5 ratio of NH_4OH, H_2O_2, and H_2O respectively resulted in a 0.7 nm increase of average surface roughness whereas a 0.05:1:5 ratio showed a 0.1 nm increase. Combining these facts implies that the age of a SC1 solution affects the roughening and perhaps smoothing characteristics of the wet chemical oxidation process. It follows that as the SC1 solution ages, the NH_4OH concentration decreases, yielding a smaller characteristic surface roughness.

Given the variable nature of the wet chemical solutions used in these experiments, comparisons of the recipes is a rough guide to trends. A comparison of recipes one and two suggests that there is a correlation between reducing loss and the use of SC2 for sidewall smoothing. While an additional 75 minutes of SC2 should aid in sidewall smoothing due to its oxidizing nature, the 4 dB/cm loss difference (for the case of the 630 nm waveguide) between using the 5X RCA or the 5X SC1 recipe is rather dramatic. SC2 was originally formulated to remove heavy metals and not expected to have a large impact on sidewall smoothing. It may be that the use of SC2 served to prolong the SC1 aging time and thus NH_4OH concentration, affecting the end surface roughness.

A comparison of recipes two and three, multiple versus single SC1 treatment, reveals that the extended SC1 treatment yields lower loss waveguides. In fact, the extended SC1 treated waveguides have a consistent 1 dB/cm lower loss than the 5X SC1 treated waveguides for each waveguide width. This trend might be caused by the relative NH_4OH concentrations in the SC1 solutions. Whereas the SC1 solution was refreshed after the second 10 minute SC1 treatment during the multiple 5X SC1 experiment, the extended SC1 used only a single uninterrupted treatment.

The use of 5X Piranha recipe was not comparably effective at reducing transmission loss in Si waveguides. The Piranha recipe losses were within the measurement error of the as-fabricated losses, indicating that Piranha does not significantly smooth the sidewalls. It should be noted that the recipe duration was much smaller than the other recipes, reducing the overall oxidation time.

5.4.4 RCA Clean Iterations

Waveguides treated with the 5X RCA recipe were measured after each RCA iteration to document the smoothing process. Figure 5.17 illustrates the effect each RCA clean has on transmission loss for the 630 nm and 1330 nm waveguides respectively. Here it is clear that transmission loss decreases with chemical oxidation treatment for the thinnest (630 nm) waveguide, indicating that sidewall roughness has been reduced.

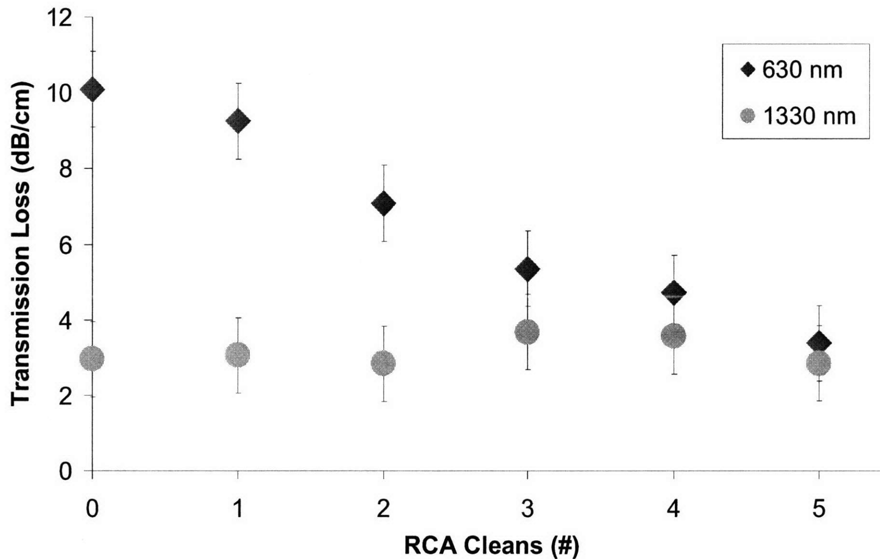

Figure 5.17: Transmission loss versus number of RCA cleans for the 630 and 1330 nm wide Si waveguides

The transmission loss for the widest (1330 nm) waveguide remains constant with respect to wet chemical oxidation treatment. While the roughness sensitivity to smoothing is small in this geometry, the lack of loss reduction may be a consequence of added loss from top surface roughening by the SC1 chemistry. SC1 surface roughening of (100) Si wafers has been noted in several studies [80-81].

The loss sensitivity to the core-cladding interface roughness at the top surface is much higher than at the sidewall for these waveguides. Hence, surface roughening can cause considerable loss, depending on the roughness statistics. AFM measurements reveal a notable increase, in RMS top surface roughness from 0.15 nm to 0.37 nm with RCA iteration.

WET CHEMICAL TOP SURFACE ROUGHENING

RCA #	0	1	2	3	4	5
σ (nm)	0.14	0.23	0.27	0.31	0.31	0.37

Figure 5.18: AFM measurements of the RMS roughness σ for Si waveguide top surface.

While the experimental evidence indicates that oxidizing with wet chemical solutions reduces sidewall roughness, it may also add loss by roughening the smooth Si waveguide top surface. Miyashita et al. [81] have shown that an RCA clean using an SC1 solution with a 1:1:5 ratio of NH_4OH, H_2O_2, and H_2O respectively resulted in a 0.7 nm increase of average surface roughness. In fact, Lai et al. have attributed oxidation roughening of Si to the oxidation reaction and argue that there is a limiting roughness (where equilibrium is reached between oxidation smoothing and roughening) of ~ 0.3 nm RMS [82]. Our AFM measurements confirm this nm-scale oxidation roughening with an increase of top surface RMS roughness. For future experiments, the use of an oxide hard mask can be used as a protective layer to prevent top surface roughening.

5.4.5 Conclusions

In this study, the use of wet chemical oxidation was evaluated as a means of reducing Si waveguide sidewall roughness for more efficient signal transmission. These experiments were designed to continually oxidize the Si in the fast, linear, reaction-limited regime. Of the four wet chemical recipes used, the RCA clean was the most effective at decreasing transmission loss for the waveguides used in this study. The decrease in TE polarized transmission loss was most dramatic for waveguides with the smallest cross-sectional dimensions, where sidewall losses were reduced from 10.1 to 3.4 dB/cm. These experiments represent a proof of concept and have not been optimized. Wet chemical oxidation is a relatively easy, effective method of reducing transmission loss without sacrificing waveguide dimensional integrity or thermal budget; ideal for integrated photonic circuit fabrication

5.5 Other Post-Etch Smoothing Techniques

For silicon waveguides, there are two other post-etch process techniques which have met with varying degrees of success and are worth mentioning: anisotropic etch smoothing [73], and hydrogen ambient induced surface diffusion smoothing [83-84]. While not explored in this research, a brief synopsis is given for both methods.

5.5.1 Anisotropic Etch Smoothing

Anisotropic etch smoothing of silicon waveguides was first demonstrated in [73]. In this study, TMAH was used to preferentially etch the waveguide sidewalls to expose the slow etching {111} crystallographic planes, see Figure 5.9. Anisotropic etching is extremely attractive as it is possible to reduce sidewall roughness to atomic level smoothness (~ 1 Å). In addition, the process is fast and requires virtually no heat: a plus if there is a tight thermal budget.

However, there are several detriments to choosing this smoothing technique. First, the exposure of {111} planes is very limiting to design. Waveguides fabricated from the prevalent {100} oriented SOI wafers result in a trapezoidal waveguide geometry. As discussed in section 4.8, trapezoidal waveguide geometries are susceptible to mode-to-mode coupling. Second, the application of an anisotropic etch to a photonic circuit results in faceting of waveguide bends and ring resonators, or any waveguide that is not conformal to a rectilinear <110> grid, which deleteriously affects the optical transmission.

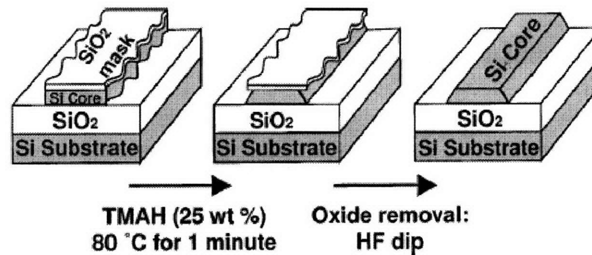

Figure 5.9 – Anisotropic etch smoothing of crystalline silicon waveguides [73]

5.5.2 Hydrogen Ambient Induced Surface Diffusion Smoothing

Another Si surface smoothing method is to anneal in a hydrogen ambient environment [83-84]. At elevated temperatures (T ~ 1000 °C) hydrogen induces Si surface diffusion which smoothes rough surfaces. In one study, the RMS roughness of etched Si trench sidewalls decreased from 1.72 to 0.11 nm, as measured by AFM [83]. In another study, researchers applied the hydrogen smoothing technique to Si waveguides, yielding a loss of 0.9 dB/cm for a 200x500 nm^2 waveguide [84].

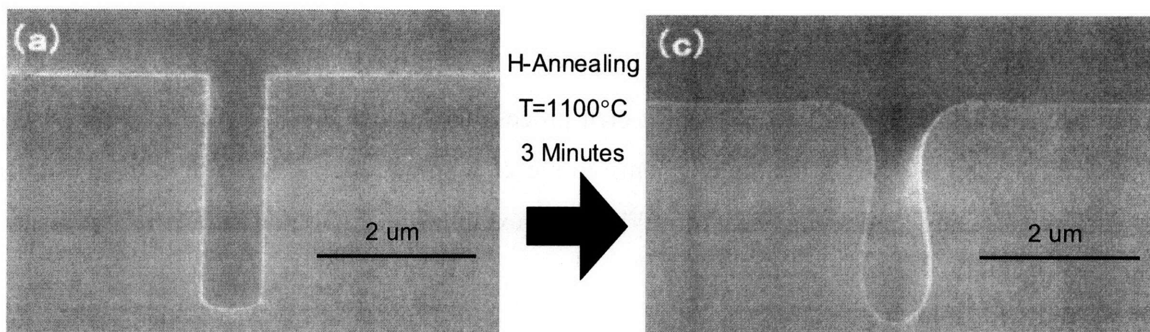

Figure 5.19 – Annealing in a H ambient induces Si surface diffusion which smoothes and alters the shape of etched features [84].

While the effectiveness of hydrogen annealing on Si surface smoothing is very attractive, the process is not easily adapted to integrated photonic circuits. Similar to oxidation smoothing the process temperature is too high for typical thermal budgets. In addition, the induced surface diffusion results in a

rounding of the features, as seen in Figure 5.19. This is problematic for photonic devices which depend on evanescent coupling, as the altered waveguide cross-section alters the evanescent field overlap which governs the coupling characteristics and device operation. However, unlike ambient oxidation smoothing, Si consumption is negligible.

Chapter 6 – Deposited Waveguide Processing

The ability to route optical signals on multiple chip-levels within an integrated electronic-photonic chip adds versatility and design freedoms which can improve data processing and communication. Similar to SOI-based waveguides, deposited waveguide materials must have a high index of refraction and compatibility with SiO_2 to enable a highly confined, optically insulated, sub-micron cross-section, which is compliant with the physical and fabrication tolerances utilized in CMOS processing. In continuing the use of amorphous SiO_2 claddings, the deposited materials are epitaxially restricted to amorphous or polycrystalline morphologies. In this chapter, three CMOS compatible deposited waveguide materials are investigated: silicon nitride, amorphous silicon, and polycrystalline silicon. The dominant loss mechanisms in these materials are roughness-scattering and material absorption.

6.1 Silicon Nitride (SiN)

In many ways, silicon nitride is an ideal deposited waveguide material. The index of SiN ranges from its stoichiometric (Si_3N_4) value of 2.0 to 2.25 for silicon rich SiN. While the index is considerably lower than that of silicon, it is still large enough to sustain sub-micron, single-mode waveguide cross-sections with bend radii on the order of 10 μm. In some ways, the lower index contrast is advantageous as it relieves the high sensitivity to sidewall roughness experienced by Si waveguides. SiN is also transparent over a wide range of wavelengths, including λ=850 nm (unlike Si) at which inexpensive GaAs light emitters exist, and there are multiple methods of depositing SiN, some of which are at low temperatures, a benefit for multiple chip levels when temperature sensitive materials lie beneath. In addition, SiN is amorphous and thermally stable so it does not transform into a polycrystalline material at relevant process temperatures like a-Si does. However, there are some detriments to using SiN waveguide materials. SiN does not exhibit optoelectronic properties and its thermo-optic response, used for trimming the waveguide index, is quite low. However, for passive optical routing applications, these properties are many times not needed. Film stress in deposited SiN films, especially stoichiometric Si_3N_4 films, can preclude the growth of ideal waveguide film thicknesses, due to film cracking [14], however added Si-content relieves this issue (and increases the index). Finally, and most importantly for optical loss, the presence of hydrogen in SiN films results in the presence of N-H bonds which absorb in the telecom spectrum. The degree of hydrogen incorporated in the SiN film is process dependent. In this subsection, a material study of SiN materials is investigated to understand the relative distribution of loss mechanisms.

6.1.1 Previous Work

The SiN waveguide study described herein is an extension of two previous SiN waveguide material studies in Prof. Kimerling's research group [14, 85], of which the focus is to fabricate low loss SiN waveguides. The major obstacle to realizing low loss waveguide and the dominant loss mechanism is

SiN material absorption. SiN material absorption in the telecom spectrum occurs due to the presence of nitrogen-hydrogen (N-H) covalent bonds which arise from imperfect dissociation of gaseous precursors used in the deposition (SiH_4 and NH_3). N-H bonds act as absorption centers in the telecom spectrum which adversely affect waveguide transmission [86-88]. The degree of loss scales with the concentration of N-H bonds and is largely dependent on the deposition method.

Low pressure chemical vapor deposition (LPCVD) and plasma enhanced chemical vapor deposition (PECVD) are the two most popular methods of depositing high quality SiN films. LPCVD films are grown at high temperatures (750 - 900°C) and low growth rates (~ nm/min) with comparatively low H-content, typically less than a few atomic percent [14, 89-90]. In comparison PECVD films are grown at lower temperatures (300-500°C) with higher growth rates (100s nm/min), and higher H-content, ranging from 20-50 atomic percent [14, 91-92]. The large disparity between H-content in the two deposition processes is mostly due to the process-temperature. The higher kinetic energy imparted to the film at higher temperatures drives out the hydrogen from the N-H bonds [14, 86, 90, 93] and reduces the H-content in the films. Consequently, the lowest loss, 0.1 dB/cm, SiN waveguides are made from LPCVD films that are further annealed [93].

However, in the interest of utilizing SiN materials as an upper chip level waveguide, it is imperative to use a low temperature deposition in keeping compatible with lower level devices with low thermal budgets, such as germanium modulator and detector devices, which have melting temperatures near 700°C. This constraint leaves only PECVD deposited SiN materials as a viable option. In aims to reduce the absorption loss in these materials, the PECVD precursor chemistries were optimized to decrease the H-incorporation in the film. By implementing an N_2 precursor instead of NH_3, the atomic percentage of hydrogen decreased from 18.3% to 9.9% corresponding to a SiN (n=2.0) bulk material loss decrease from 4.3 to 2.8 dB/cm for λ=1550 nm, as measured by a Metricon prism coupler [14].

6.1.2 Fabrication

The SiN waveguides reported in this work were fabricated at MIT's Microsystems Technology Lab (MTL) cleanroom facility by Dr. Ching-yin Hong. 400 nm thick SiN films were deposited on (100) silicon substrates, purchased from SQI, with a 3 μm thermal SiO_2 layer. The various SiN materials studied in this work are listed in Figure 6.1, along with process temperature, gaseous precursors, and refractive indices at λ=1550 nm. For the DCVD-400 material the following deposition conditions were used: SiH_4 140 sccm, N_2 4900 sccm, P=3 torr, power = 440W, spacing 640 mils, and T=400°C. For the DCVD-500 material the following deposition conditions were used: SiH_4 157 sccm, N2 4850 sccm, P=3 torr, power=485 W, spacing 640 mils, and T=500°C. For the VTR material, the following depositions were used 250 sccm $SiCl_2H_2$, 25 sccm NH_3, P=250 mT, and T=775°C.

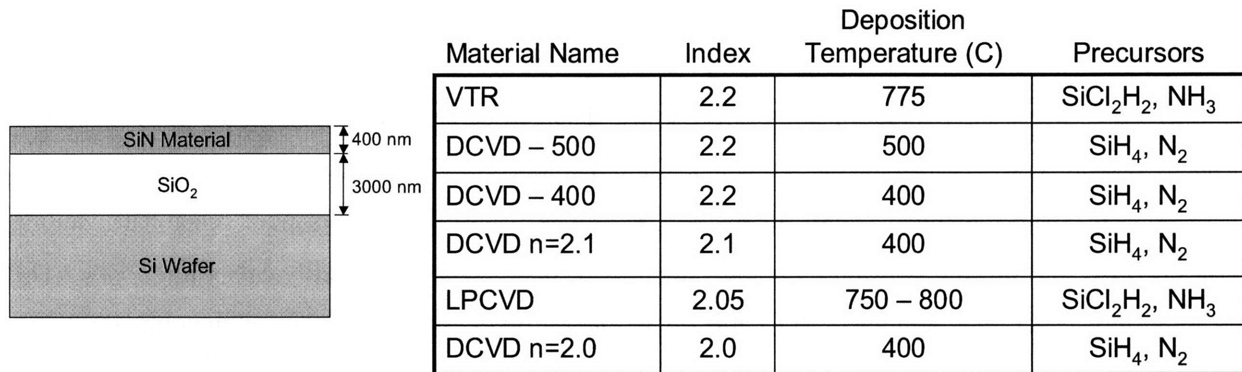

Material Name	Index	Deposition Temperature (C)	Precursors
VTR	2.2	775	$SiCl_2H_2$, NH_3
DCVD – 500	2.2	500	SiH_4, N_2
DCVD – 400	2.2	400	SiH_4, N_2
DCVD n=2.1	2.1	400	SiH_4, N_2
LPCVD	2.05	750 – 800	$SiCl_2H_2$, NH_3
DCVD n=2.0	2.0	400	SiH_4, N_2

Figure 6.1 – Dielectric layer thicknesses (left) and SiN materials used in the SiN waveguide study (right).

The SiN channel waveguides were defined by photolithography with an I-line stepper (λ=365 nm) and etched with the AME5000 with CF4 8 sccm and O2 6 sccm at 50 mTorr, 250W, and 100 Gauss. Post-etch, the photo-resist was removed by an oxygen asher. After a pre-metal clean, 3 µm of PECVD SiO_2 was deposited as a top cladding layer. Waveguide samples were prepared by cleaving the wafer along the input and output facets.

The VTR and LPCVD materials are deposited by two separate LPCVD deposition tools with different refractive indices. The high operating temperature and low deposition rate of these tools are theoretically ideal for low N-H bond concentrations. The DCVD materials are PECVD deposited and employ the N_2 precursor, developed in [14], to minimize the N-H bond concentration. Process temperature and material indices were varied to see their effect on the N-H bond concentration.

This work was motivated by the desire to find the lowest loss SiN material available at MIT. A SiN waveguide study in [85], concluded that the VTR material, the high Si-content/index LPCVD SiN material, was the lowest loss material. However, since this study, conflicting results have been measured which has put the results of this study in question.

6.1.3 Loss Results

The photolithography mask used in this work was originally designed for air-clad SiN waveguides. The decision to include a top cladding was to ensure that the waveguide surfaces were unaffected by contaminants such as dust, as well as facilitate a more direct comparison with the results in [85]. However, the addition of a SiO_2 cladding to a waveguide structure designed for air-cladding led to several undesirable consequences.

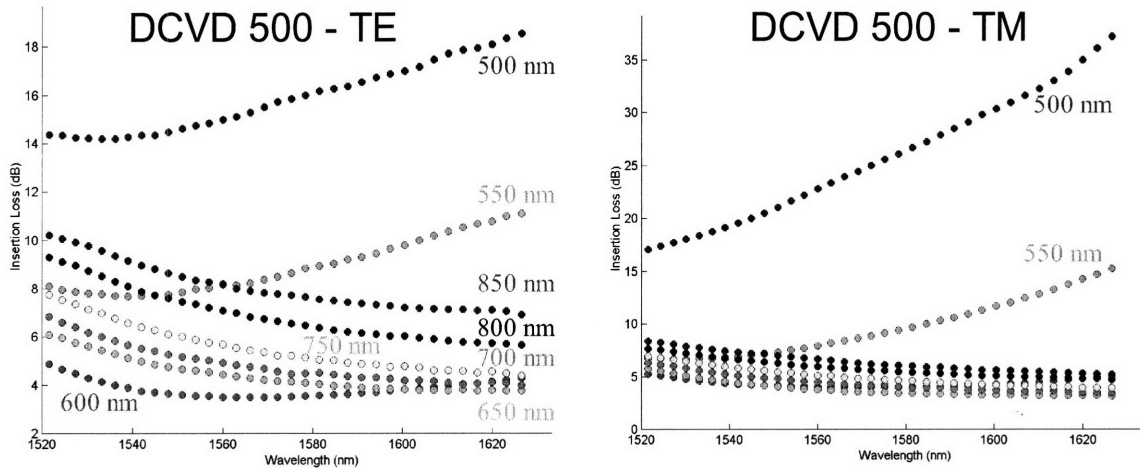

Figure 6.2 – Insertion loss for DCVD-500 SiN (n=2.2) waveguides for different widths. Substrate leakage is evident for insertion loss data which increases with wavelength.

The most problematic issue with the addition of a top cladding was the lowered effective index in combination with a relatively thin undercladding layer which resulted in substrate leakage. Evidence of substrate leakage can be seen in figure 6.2, which compares the insertion loss of straight waveguides fabricated from the DCVD-500 material. In general, the spectral shape of the insertion loss should be similar in form and magnitude for straight waveguides with differing waveguide geometries. However, as discussed in section 4.7, the presence of substrate leakage results in an exponential increase in loss with wavelength. This is seen in the smallest waveguide geometries which have larger waveguide modes and thus an increased overlap with the substrate. For the DCVD-500 material, the 500 and 550 nm width waveguides are substrate leakage loss dominated. The difference in confinement between the two polarizations is observed by the magnitude of the increase. The less confined TM mode, as a consequence of the rectangular geometry, has a larger mode field overlap with the substrate and therefore has a much higher insertion loss for the substrate leakage loss dominated widths; note the ordinate scale axis difference.

The presence of substrate leakage in the higher index SiN materials was negligible for the waveguide geometries used in transmission loss measurements. However, for the lower index SiN materials – LPCVD and DCVD n=2.0 – substrate leakage dominated all waveguide widths, eliminating these materials from the comparison of waveguide transmission losses. A second problem with depositing a top cladding on a waveguide structure intended for air-cladding is bend loss. The decrease in the waveguide effective index, as a consequence of increasing the cladding index, increases the minimum, low-loss bend radius. Fortunately, the widest width waveguides did not exhibit noticeable bend loss for the four remaining materials and thus waveguide paperclips with the 850 nm width were used in the waveguide loss comparison.

Transmission loss of the SiN waveguides was measured by the cutback method. An example cutback fit used in these experiments is listed in Figure 6.3. In light of the relatively low losses measured for most of the SiN materials, the use of only three paperclip structures, and the short length difference between the maximum and minimum length paperclips (0.5 cm), required care to make sure that experimental errors in alignment were less than the loss difference between waveguide paperclip structures. The accuracy of the Newport-JDS system (see section 3.6) proved to be sufficient, as the variation between chips from the same wafer losses was within ± 0.5 dB/cm and the standard deviation of the cutback fits was less than 0.3 dB for nearly all waveguide samples.

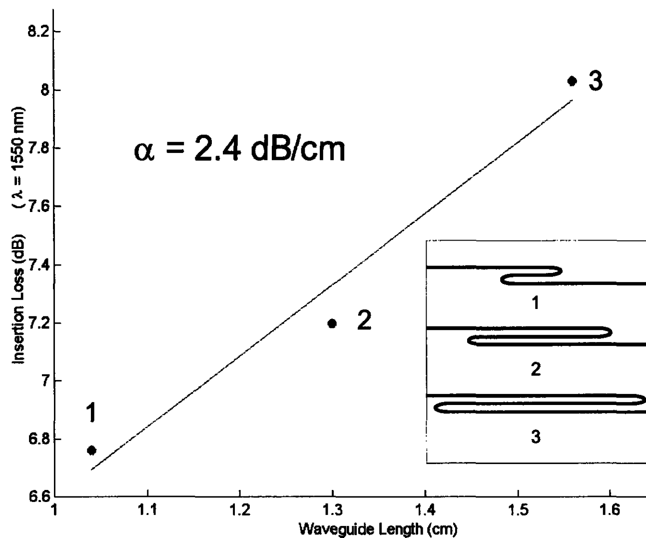

Figure 6.3 – Cutback example for the waveguides used in the SiN study.

Interestingly, the spectral shape of the transmission loss was nearly identical for the VTR, DCVD-500, DCVD-400, and the DCVD n=2.1 materials. An example, measured for a DCVD-400 sample, is illustrated in figure 6.4. Here, the loss is relatively flat for the longer wavelengths and increases at shorter wavelengths. This behavior fits with the presence of hydrogen in the SiN materials. The N-H bond resonance manifests itself as a broad absorption peak centered on λ=1510 nm [86]. The width of the absorption peak is a function of the N-H concentration and can affect the absorption wavelengths out to λ=1580 nm. Therefore, the dominant loss mechanism in SiN waveguides is wavelength dependent. For the long wavelength regime of the telecom spectrum, the waveguides are roughness-limited, whereas on the short wavelength regime, the waveguides are absorption-limited.

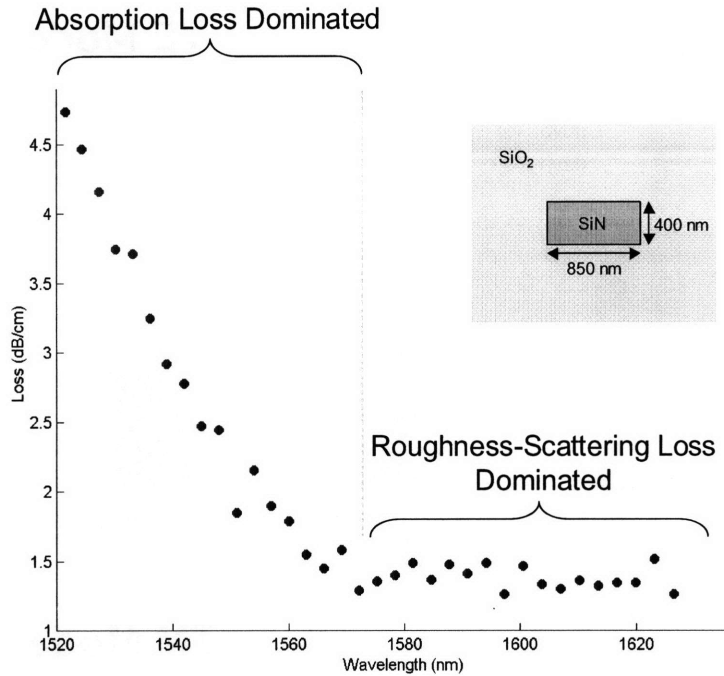

Figure 6.4 – Typical spectral loss behavior of SiN waveguides measured in this work.

The magnitude of the transmission losses, averaged over a minimum of four waveguide chips, for the VTR, DCVD-500, DCVD-400, and the DCVD n=2.1 SiN materials are compiled in Figure 6.5 for λ=1520, 1550, and 1620 nm for the TE and TM polarizations. Over the spectrum measured, each SiN material has its loss maximum at λ=1520nm and its loss minimum around λ=1620, consistent with N-H bond absorption. The losses at λ=1550 nm are listed due to the popularity of this wavelength and reference to other studies.

The three PECVD materials – DCVD-500, DCVD-400, and the DCVD n=2.1 – performed quite similarly in terms of transmission loss magnitude and spectral shape. The difference in loss between these materials is in line with experimental errors and may be affected by slight differences in material indices which affect the optical power confinement in the waveguide core. The difference between the losses measured in the TE and TM polarizations fit with waveguide confinement differences where the ratio of optical fill factors for the 400x850 nm^2 SiN geometry is 1.25; therefore the TE mode should exhibit 25% higher loss than the TM mode in the absorption-limited regime. In the roughness-limited regime, the waveguide losses ranged from 1 – 3 dB/cm, which corresponds to a sidewall RMS roughness around 10 nm.

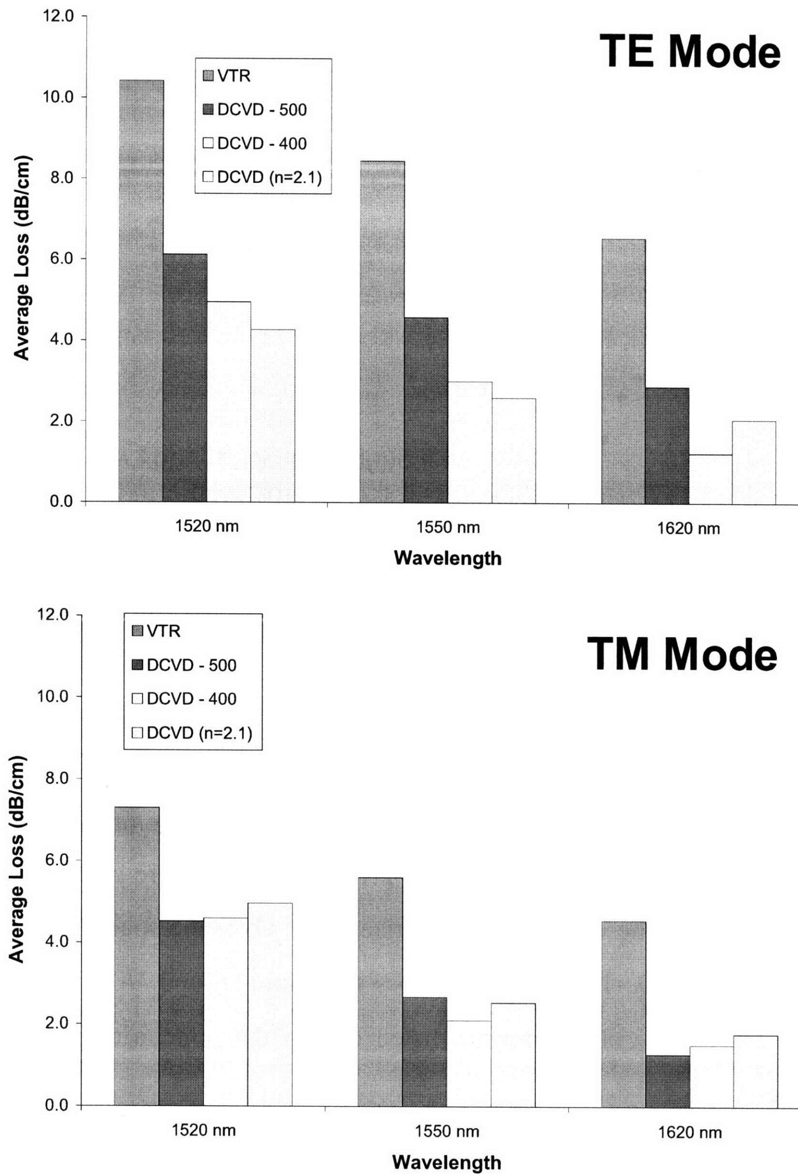

Figure 6.5 – Average Waveguide transmission losses of the SiN waveguide materials.

Fascinatingly, the VTR material, which was previously found to have the lowest loss in comparison to materials from the DCVD tool [85], is observed to have the highest losses in this waveguide study. In addition, the similar spectral shape of the loss is puzzling since the rise in material absorption loss at short wavelengths, thought to correspond to the N-H bond peak, is a weak effect in the VTR material since LPCVD materials generally have low N-H bond concentrations due to the high deposition temperatures. Previously, the spectral loss response of the VTR material was found to be flat with losses around 2 dB/cm [85], fitting with the presumption of very low H-content. However, the considerably higher loss at the longer wavelengths suggests either 1) that the fabrication of VTR

waveguides was less optimal than for the DCVD materials or 2) another loss mechanism is contributing to the waveguide loss.

6.1.4 Increased Wavelength Range Measurements

To fully understand the origin of the loss increase in the SiN materials, waveguide samples were measured with a broadband tunable laser (λ=1250-1650 nm), courtesy of Peter Rakich in Prof. Ippen's lab. Prior to these measurements, it could only be assumed that the loss increase was a result of N-H bond resonant absorption, as the N-H bond resonance peak could not be resolved using the smaller wavelength range on our waveguide measurement apparatus. The waveguide loss for the VTR and the DCVD-400 materials are plotted versus wavelength in Figure 6.6.

The loss behavior of the DCVD-400 sample fits with expected waveguide loss mechanisms. The DCVD-400 loss response is flat and roughness-limited except for the regions of the spectrum near two loss peaks, centered at λ=1380 nm and λ=1510 nm, which correspond to O-H and N-H bond resonance absorption. The presence of O-H bond absorption is a consequence of the evanescent field interacting with the PECVD SiO_2 top claddings, which like the PECVD SiN materials, has hydrogen incorporated in the films as a result of imperfect dissociation of the chemical precursors. Aside from the bond resonance, the waveguide loss magnitude 2-3 dB/cm is within experimental error with that measured earlier. The small differences in power between the paperclips as well as system drift added error to the absolute magnitude of the long wavelength range loss measurements.

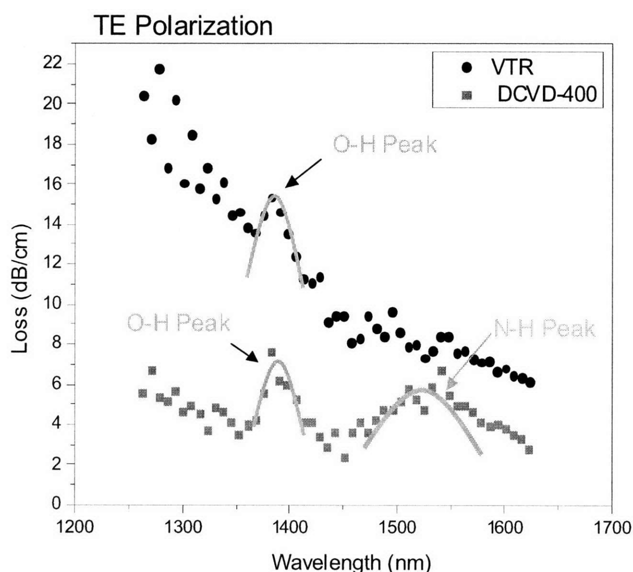

Figure 6.6 –Waveguide loss over a broad λ-range for the DCVD-400 and VTR SiN Materials.

The loss behavior of the VTR material is intriguing. Similar to before, the loss behavior mimicked the shape of the DCVD-400 material from λ=1520 – 1620 nm, at an increased loss with a similar off-set. However, as the wavelength decreases, the loss increases dramatically to greater than 20 dB/cm at λ=1250 nm. The lack of an N-H resonance peak suggests that the H-content is low in the VTR material, inline with findings from the literature. The presence of the O-H peak is expected given that all SiN materials were clad with an identical PECVD SiO_2 material. The dramatic loss difference over the long wavelength range for the VTR material suggests that there is another loss mechanism present most likely a bulk scattering center.

One likely explanation for the loss behavior in VTR is the presence of silicon nanocrystals (Si-ncs). Si-nc formation from SiN materials with excess Si-content has been observed to occur between 500°C and 900°C [94]. In some cases, the formation of nm-size amorphous silicon nanoclusters has been observed to occur without annealing [95]. Therefore the formation of Si-ncs in the VTR material is very likely given the high Si-content and elevated process temperature (775°C). Optically, the presence of Si-ncs can be viewed as dielectric inhomogeneities which scatter light, a bulk analog to sidewall roughness-scattering. It is worthy to note that the increased loss with decreased wavelength rises much faster than Rayleigh scattering which is proportional to λ^{-4}. However, changes in the modal properties and roughness scattering in the waveguide also contribute to added loss with decreased wavelength.

6.1.5 Waveguide Loss Results Comparison

The PECVD SiN waveguides fabricated in this study represent some of the lowest, low temperature deposition, loss results reported. A low temperature waveguide fabrication process is critical for integration of upper chip level waveguides where the thermal budget is a concern. The lowest roughness-limited losses were measured at 1-2 dB/cm, which is inline with a previous SiN waveguide [85]. All studies that report lower transmission loss SiN channel waveguides utilize extremely high temperature fabrication processes (>1000 °C), unsuitable for waveguide integration [93].

In this work, we conclude that VTR SiN is quite lossy, especially at short wavelengths, most likely due to the presence of silicon nanocrystals which scatter light. In contrast, the results reported in [85] found the VTR waveguide loss as quite low across the telecom spectrum, similar in magnitude (1-2 dB/cm) to the roughness-limited loss values found for the PECVD materials outside the N-H bond resonance in this study. It is not clear why the VTR material absorption changed so dramatically between this waveguide study and the results reported in [85]. However, it is thought that equipment maintenance and modification on the VTR LPCVD tool during the two years between waveguide studies is the reason. The VTR LPCVD tool operates in the reaction-limited regime, which makes it quite sensitive to alterations in gas flow, temperature, and pressure.

6.2 Amorphous Silicon (a-Si)

Amorphous silicon (a-Si) is an attractive waveguide material for many of the same reasons that crystalline silicon is. Amorphous silicon has a high index of refraction which can range from n= 3.5 – 4.0 depending on process conditions, CMOS compatibility, and an extensive process knowledge base. In addition, a-Si can be deposited by a variety of low temperature deposition methods which is vital for upper chip level waveguides where thermal budgets are limited due to lower chip level temperature restrictions, such as melting temperature and electrical dopant diffusion.

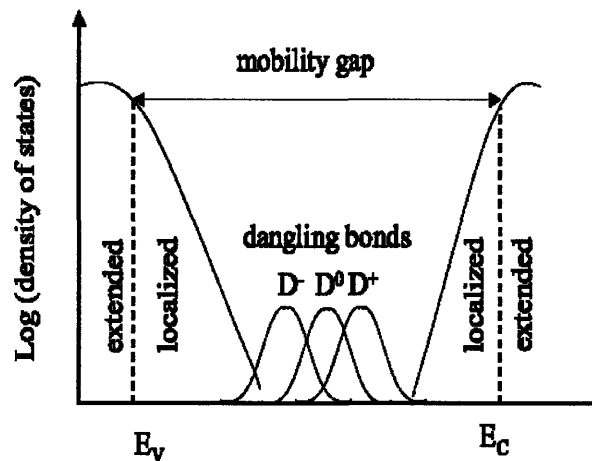

Figure 6.7 – Schematic diagram of an amorphous semiconductor density of states, E_v and E_c denote the valence and conduction band energies [96].

Optical absorption is a major limitation in using a-Si as a waveguide material. Unlike crystalline silicon, where atoms are regularly arranged on a periodic lattice, a-Si only has short-range atomic order which results in structural defects in the form of distorted bond angles, dangling bonds, and altered atomic bonding coordination which drastically alters the density of states near the bandgap. In a crystalline semiconductor, the density of states within the band gap is by definition zero. However, as seen in Figure 6.7, the density of states for an amorphous semiconductor is not identically zero within the bandgap. The long range disorder of the amorphous lattice causes band-tail states which exponentially decay from the valence and conduction bands into the band gap [97]. Additionally, the presence of dangling bonds results in mid-gap electronic states, which can have a negative, neutral, or positive (D^-, D^0, D^+) charge depending on the energy. These mid-gap states act as optical absorption centers for sub-bandgap light and are the cause of infrared absorption in a-Si.

Fortunately, the addition of hydrogen into the a-Si lattice results in the passivation of the dangling bonds, which reduces the number of mid-gap states and absorption centers [98]. Hydrogenated a-Si (a-Si:H) is frequently used in photovoltaic applications where the incorporation of hydrogen improves device performance. As a photovoltaic material, a-Si:H materials behave as direct semiconductor

materials with E_g=1.6 eV [97-98]. In addition, passivation of defects improves the electrical conduction properties of a-Si:H necessary for efficient carrier collection [98]. For passive waveguide applications, hydrogenation of a-Si is crucial in obtaining a low loss waveguide material. To further emphasize this point, fabrication of a-Si waveguides by ion bombardment of SOI substrates, a process which creates unpassivated a-Si (no H), yielded channel waveguides with ~ 300 dB/cm absorption dominated transmission losses [99].

Plasma enhanced chemical vapor deposition (PECVD) of amorphous silicon from the decomposition of monosiliane (SiH_4) is an attractive method of depositing amorphous hydrogenated silicon films. PECVD of a-Si is a low temperature, high deposition rate process that incorporates hydrogen in the film as a result of imperfect dissociation of the SiH_4 precursors. A low temperature deposition is not only important for process integration, it is critical in maintaining a-Si material properties. Above 575°C, a-Si materials crystallize and form polycrystalline silicon materials [74] which are known to be lossy [100].

Most recently, the fabrication and measurement of PECVD deposited a-Si:H yielded ridge waveguides with waveguide transmission losses < 1 dB/cm [103]. This result is inline with the low bulk loss values found here for optimized PECVD a-Si deposition. In this work, the fabrication and measurement of PECVD a-Si channel waveguides is reported.

6.2.1 Waveguide Fabrication

Amorphous silicon waveguides were fabricated at BAE Systems' six inch CMOS foundry in Manassas, Virginia. The fabrication process began with the deposition of a 3 μm undercladding layer of high density plasma (HDP) PECVD silicon dioxide on a Si substrate. The 200 nm thick PECVD a-Si waveguide core layer was deposited with an AMAT P5000 with 100 cc/min SiH_4, 2000 cc/min Ar, T=450 C, spacing 400 mills, P = 4.5 Torr, and Power = 100W to serve as the waveguide layer. Deep UV photolithography (λ=248 nm) was used to define the waveguide pattern. The a-Si layer was etched with an HBr/Cl2/HeO2/CF4 chemistry to define the waveguides with low roughness to form the waveguides. Finally a 3 μm layer of HDP-PECVD was deposited as a top cladding layer.

In some cases, the a-Si waveguides were encapsulated in a thin 10 nm layer of SiN. This required the deposition of a thin 10nm layer of SiN prior the a-Si layer deposition. The lower SiN layer has the added bonus of acting as an etch stop and an ARC layer. In addition, a similar thin conformal PECVD SiN layer was deposited after the waveguide etch step, to encapsulate the a-Si waveguide core prior to the top cladding deposition. In total, the thin, encapsulating SiN layer is termed a "nanocladding" layer and is depicted in Figure 6.8.

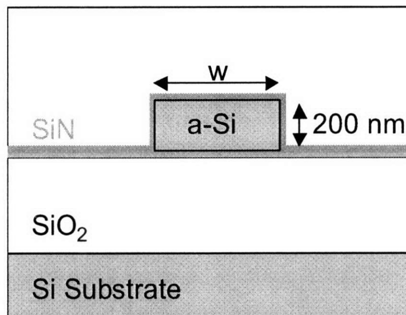

Figure 6.8 – a-Si waveguide structure with SiN nanocladding layer

6.2.2 Initial Waveguide Results

Similar to the initial SOI waveguide process run, the initial a-Si waveguide run (which ran concurrently) was afflicted by the presence of air-voids at the waveguide sidewalls. The waveguide etch step was developed with the SiN etch-stop layer in mind. However for wafers without the underlying SiN layer, the presence of the exposed, underlying SiO_2 layer during the etch step led to oxygen radicals attacking the polymerization on the waveguide sidewall. As a result, the etch chemistry undercut the foot of the waveguide and formed a recess at the bottom of the waveguide. In turn, this recess provided a shadowing effect during the top cladding deposition, forming voids in the top cladding layer near the waveguide sidewall, as seen in Figure 6.9. This effect was not seen when the SiN etch stop layer was used for deposited silicon layers, also seen in Figure 6.9.

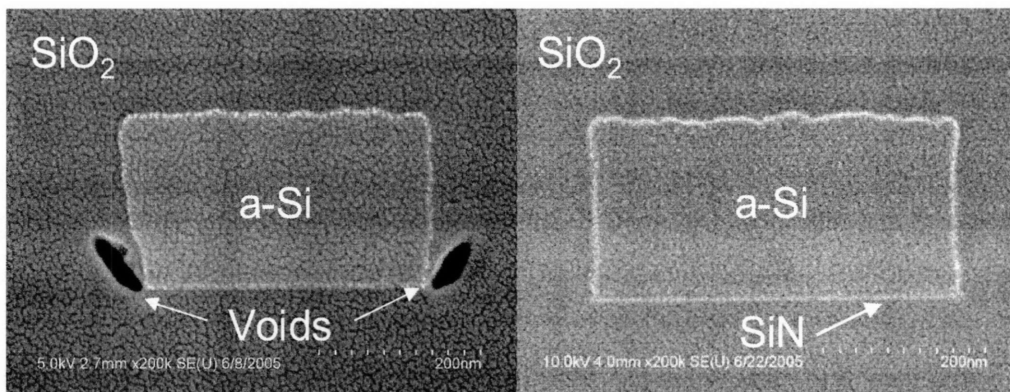

Figure 6.9 – TEM cross-sectional images of a-Si channel waveguides clad with HDP SiO_2. The presence of voids occurred for wafers processes without a SiN etch stop layer (left image). No voids were observed for samples with a SiN etch stop layer; images courtesy of Andrew Pomerene, BAE Systems.

The a-Si waveguide transmission loss data, measured by the cutback method, is plotted in Figure 6.10, as a function of waveguide width. Overall, the transmission losses of the a-Si waveguides were

surprisingly close to that found in SOI-based waveguides. A-Si waveguides exhibit losses from roughness-scattering, both from sidewall and the top surface roughness, as well as bulk absorption.

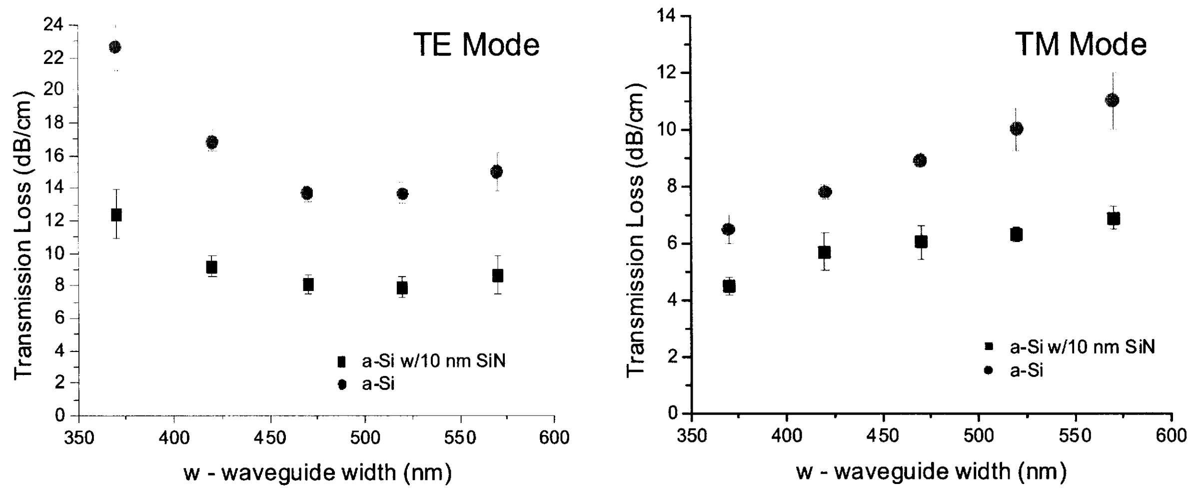

Figure 6.10 – Average waveguide transmission loss (λ=1550 nm) as a function of width for 200 nm height a-Si waveguides with and without the 10 nm SiN encapsulation layer. Error bars reflect the range of losses measured for the different chips.

The presence of air voids is detrimental to the transmission loss; shape and size variation of the voids in the propagation direction of the waveguide results in scattering of the guided light, similar to sidewall roughness scattering. This is evident in the difference in propagation loss between the a-Si waveguides with and without the SiN layer, which correspond to waveguide with and without air voids.

The disparate mode field distributions of the TE and TM modes in rectangular HIC waveguides present a terrific diagnostic for understanding waveguide losses. The most striking aspect of the data plotted in Figure 6.10 is the trend each polarization has with increased width. The TE mode loss has a decreasing trend while the TM mode has an increasing trend. As discussed in chapter 4, a decreasing loss trend with width is indicative of sidewall roughness scattering while an increasing trend is indicative of absorption. This behavior fits with the relative field distributions of the TE and TM modes, as discussed in chapter 3. The absorption-limited behavior of the TM mode is fitting given the relative large change in Γ as the width is increased (see Figure 4.15) and low sensitivity to roughness-scattering loss for these waveguide geometries (see Figure 4.10).

Interestingly, the TE mode loss passes through two loss regimes: roughness-limited and absorption-limited. For waveguide widths less than 500 nm, the TE mode loss decreases, indicating that roughness-scattering loss dominates. This makes sense since these waveguide geometries are most sensitive to roughness-scattering (see Figure 4.10). However, for widths greater than 500 nm, the loss increases, indicating absorption loss in the a-Si core dominates. The field intensity is maximized in the

core and minimized at the sidewalls for these waveguide geometries. The overall loss magnitude for the TE mode is a great deal larger than the TM mode given the higher sensitivity to sidewall roughness and increased optical confinement in the absorptive waveguide core.

For an initial process run, the a-Si waveguide loss results are promising and the lowest channel waveguide losses ever reported. The TM mode transmission loss data indicates that the a-Si material deposited in this process run exhibits significant material absorption. In addition, the presence of voids and top surface roughness increased the loss significantly.

6.2.3 Amorphous Silicon Deposition Variation Waveguide Results

In a second process run, several changes were implemented to improve waveguide loss. To minimize top surface roughness scattering losses, a chemical-mechanical polished (CMP) step was used to smooth the top surface post deposition. For a 10 second hard pad polish, the top surface RMS roughness was decreased from 2.0 to 0.55 nm, as measured by AFM. This roughness reduction is estimated to reduce the loss contribution from top surface roughness scattering to only a few tenths of a dB/cm in the a-Si waveguides. A second change in the waveguide fabrication process was to increase the thickness of the SiN nanocladding layer to 25 nm. This alteration was purely for processing ease, as the 10 nm thickness was found to deteriorate in places and was not thick enough to serve as an effective ARC layer in photolithography. The SiN nanocladding layer was used on all waveguide structures in the second a-Si process run, ensuring that the voids were not present. As will be discussed in further detail, the addition of the thicker SiN added loss to the waveguides due to absorption by the SiN material. The third and most interesting alteration to the fabrication process flow was the alteration of a-Si deposition conditions. Keeping all other conditions identical, the a-Si PECVD deposition power was decreased from 100W (the power used in the initial process run) to 50 W and 25 W. By lowering the deposition power, the kinetic energy used in the dissociation of the SiH_4 is reduced, which increases the H-content in the a-Si films and reduces loss. The increased H-concentration passivates dangling bonds in the a-Si material that are responsible for absorption of light in the telecom spectrum. Even prior to waveguide measurement, the material surface properties were noticeably different. The top surface roughness, as measured by AFM, was smoother (1 nm RMS). This is in line with known smoothing effects that hydrogen has on Si surfaces [84].

Waveguide loss results for the 25 W and 50 W a-Si waveguide structures with 25 nm SiN nanocladding were obtained by the cutback method and are plotted, along with the 10 nm SiN nanocladding sample from the initial process run (deposition power = 100 W), in Figure 6.11. In the TE mode plot, the line connecting each data point is merely to guide the eye. For the TM mode plot, each data set is fit to a line; the slope of this data is useful in estimating the bulk loss of the waveguide core

material, as discussed in section 4.4.5. Each data point is an average of several cutback loss measurements from different waveguide chips.

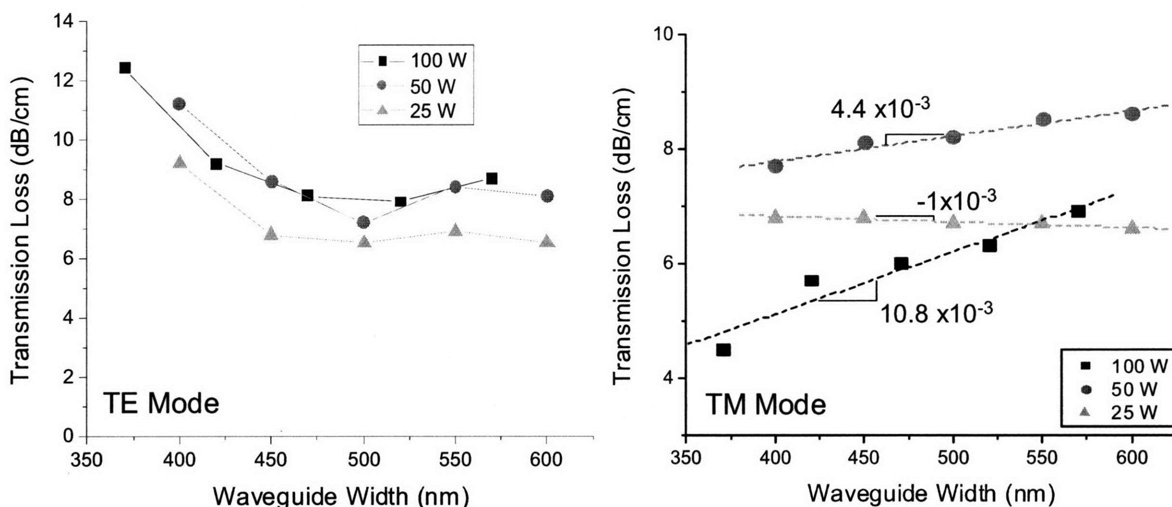

Figure 6.11 – Average waveguide transmission loss (λ=1550 nm) as a function of width for 200 nm height waveguides comprised of a-Si materials deposited with different PECVD deposition powers. The 25W and 50W waveguide samples have a 25 nm thick SiN nanocladding layer, while the 100W sample has a 10 nm thick SiN nanocladding layer.

Similar to the first-process run, the a-Si deposition variants in the second process run exhibited roughness-limited loss behavior in the TE mode and absorption-limited behavior in the TM mode. The loss behavior with waveguide width in the TE mode is very similar for all samples, suggesting that the sidewall roughness is similar in magnitude. Surprisingly, the magnitude of the waveguide losses for the 25 W and 50 W samples in the TM mode are greater than in the 100 W samples. The lowered deposition power should result in lower material absorption and thus waveguide loss. However, regardless of the magnitude, the flat loss response of the 25W TM mode over waveguide geometries w=400 to w=600 nm, which correspond to an increased fraction of power in the a-Si material from Γ=0.35 to Γ=0.45 (see Figure 6.13), suggests that the a-Si material loss is indeed very low. Furthermore, the similarity in loss magnitude between the TE and TM mode losses for the 25W and 50W samples suggests that there is an additional loss mechanism, which is polarization independent.

The increased loss in the second process run is due to the use of a thicker SiN nanocladding layer. SiN materials, particularly those deposited by PECVD, suffer from optical absorption arising from the N-H bond resonance centered on λ=1512 nm [86]. Similar to hydrogenated a-Si, hydrogenated SiN occurs when non-ideal dissociation of the gaseous precursors (SiH_4 and NH_3) occurs during deposition, resulting in the presence of N-H bonds. PECVD deposited SiN materials are reported to have between 20 and 50

atomic percent hydrogen [14, 91-93], this translates to bulk losses of tens of dB/cm. The characteristic N-H bond resonance is evident in the a-Si waveguide loss versus wavelength measurements, as seen in Figure 6.12, for samples with the SiN layer. This behavior is not observed for samples without SiN.

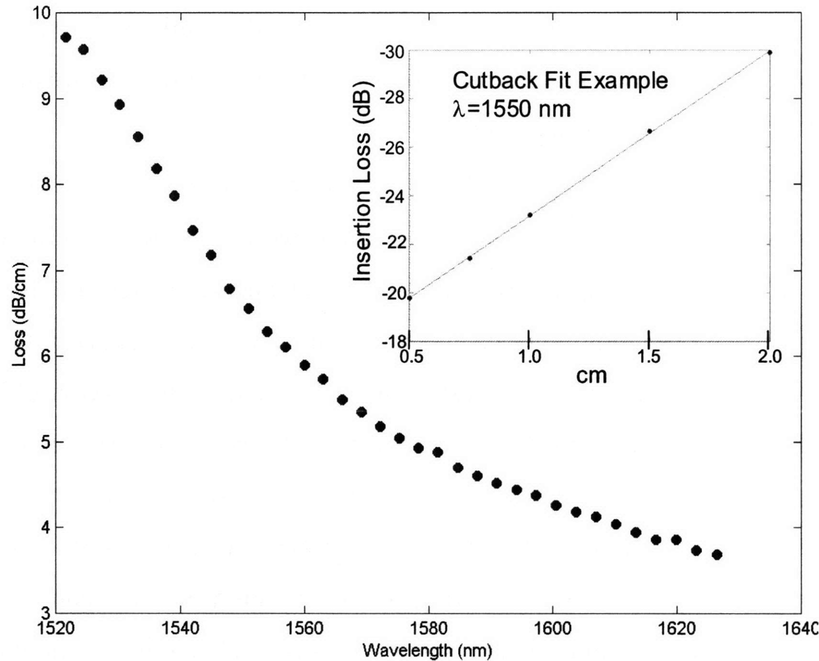

Figure 6.12 – Waveguide transmission loss versus wavelength for a 200x500 nm^2, 25 W a-Si waveguide with a 25 nm SiN nanocladding layer in the TM mode. Loss was obtained by the cutback method, an example fit for λ=1550 nm is shown in the inset. The loss behavior is quite similar to that found in SiN, suggesting that the SiN nanocladding layer contributes significantly to the loss.

6.2.4 Bulk Loss Measurement

While the added loss from the SiN layer is unfortunate, obtaining the bulk loss of the a-Si materials is still possible. Regardless of the absolute value of the waveguide loss, the bulk loss of the a-Si material can be obtained from the slope of the transmission loss versus waveguide width, assuming that the loss is truly absorption dominated and linear with waveguide width, as it is for the TM mode. Using relation (6.1), which was derived in section 4.3.5, we see that the bulk loss is the product of the slope of (absorption-dominated) transmission loss α with respect to waveguide width w and the inverse slope of optical fill factor Γ with respect to waveguide width w.

$$\alpha_{bulk}^{a-Si} = \left(\frac{\partial \alpha}{\partial w}\right)\left(\frac{\partial \Gamma}{\partial w}\right)^{-1} \tag{6.1}$$

To understand how the SiN layer affects the optical confinement in the a-Si layer, the fill factor was simulated by FIMMWAVE for the various waveguide geometries and SiN nanocladding thicknesses. In using relation (6.1) it is important to verify that the nanocladding thickness does not affect $\partial\Gamma/\partial w$ and $\partial\alpha/\partial w$; or in other words, the power within the SiN material remains constant with waveguide width variation. Material indices for the deposited materials were obtained by reflectometry, courtesy of Sanjay Patel at Lucent Technologies, and used in the simulation. The three a-Si process variants all had an index of n=3.64, while the SiN material index was n=2.0.

As can be seen in Figure 6.13, the nanocladding thickness does not significantly affect the value of $\partial\Gamma/\partial w$. This indicates that the slope of the absorption dominated TM mode loss is directly proportional to the bulk loss of the a-Si core for the different nanocladding thicknesses. Interestingly, the confinement of the TM mode increases with the addition of the nanocladding layer. This behavior is unexpected given that this is essentially lowering the index contrast, which should therefore decrease the confinement. However, in light of the asymmetric electromagnetic dielectric interface boundary conditions that occur at optical frequencies (see section 2.7.1), it makes sense. For a TM mode in a short-wide HIC waveguide geometry, such that the thickness is much smaller than the signal wavelength, the fraction of power in the core is limited by the field discontinuity. Lowering the index contrast at the core-cladding interface, decreases the magnitude of the discontinuity and enables an increased fraction of the power in the core. This effect is useful in increasing the effective index of the TM mode for improved bend loss and lowered substrate leakage in rectangular, single-mode, HIC waveguides.

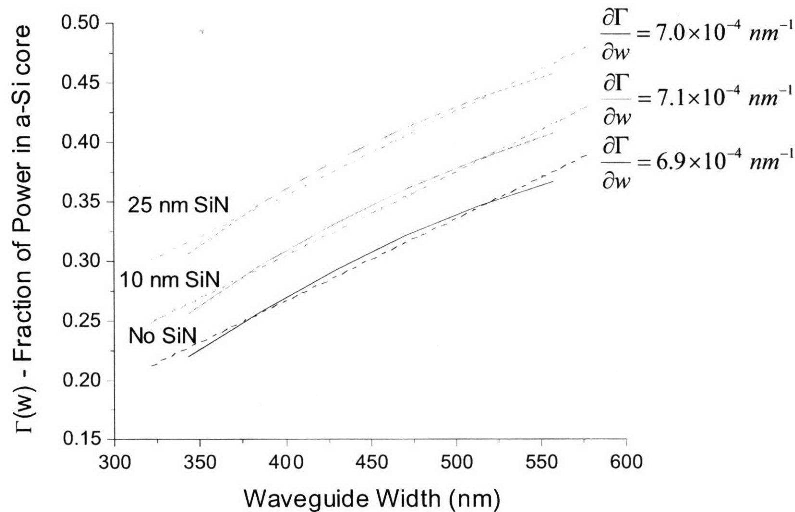

Figure 6.13 – Fraction of power in the a-Si layer as a function of waveguide width and different nanocladding thicknesses for TM mode waveguide, core height = 200 nm, and λ=1550 nm. The solid curves are simulated with FIMMWAVE, while the dashed lines are linear fits.

To ensure that the loss versus width trends for the a-Si deposition variants were purely resultant from the increased optical confinement in the a-Si layer, the fraction of power in the SiN nanocladding layer versus waveguide width was simulated with FIMMWAVE. As seen in Figure 6.14, the fraction of power in the SiN layer is virtually constant with waveguide width, ensuring that any absorption loss arising from the SiN material does not affect $\partial\alpha/\partial w$ - the slope of the waveguide loss versus width data. As expected, an increase in the SiN layer thickness increases the fraction of power within the SiN layer – 3% for 10nm and 9% for 25 nm. Assuming that the SiN material is absorptive, the loss should scale tiwh SiN layer thickness as found with the TM mode loss data.

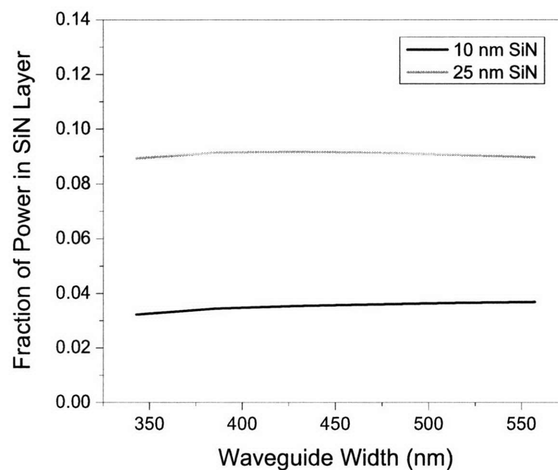

Figure 6.14 – Fraction of power in the SiN nanocladding layer as a function of waveguide width for TM mode waveguides, core height = 200 nm, and λ=1550 nm; simulated with FIMMWAVE.

Now that we have established that adding a nanocladding layer does not affect the bulk loss estimation method used in relation (6.1), the data from Figures 6.11 and 6.13 is used to estimate the bulk loss of the three a-Si deposition variants. The results for this analysis are listed in the right-most column of the table in Figure 6.15. Error in this analysis is estimated from the fitting of each dataset. As hoped for, the lowering of the PECVD deposition power reduced the a-Si bulk loss. The probable mechanism for this is the increased H-content which passivates the dangling bond defects responsible for absorption [100-101, 103].

Intriguingly, the bulk loss for the 25 W a-Si material is very low as observed by its very small slope. This is a fantastic development, in that it provides a very low bulk loss (< 1 dB/cm) deposited waveguide material that is well suited for integrated electronic-photonic chip applications. The fact that $\partial\alpha/\partial w$ is negative for this waveguide structure may be a result of the power distribution in the 25 nm thick SiN which has a slightly negative slope with waveguide width. Future experiments will avoid using the SiN layer to reduce waveguide transmission losses.

Deposition Power [W]	SiN Thickness [nm]	$d\Gamma/dw$ [nm^{-1}]	$d\alpha/dw$ [dB/(cm-nm)]	Estimated a-Si Bulk Loss [dB/cm]
25	25	7.0 X 10^{-4}	-1 X 10^{-3}	~ 0 ± 1
50	25	7.0 X 10^{-4}	4.4 X 10^{-3}	6.3 ± 1
100	10	7.1 X 10^{-4}	10.8 X 10^{-3}	15.2 ± 2

Figure 6.15 – Estimated bulk absorption loss for the three PECVD a-Si deposition variant materials. Data taken from Figures 6.11 and 6.13, bulk loss estimated with relation (6.1) for λ=1550 nm.

Even with the presence of the SiN layer, the loss for the 25W a-Si material waveguide structure is close to the best SOI-based waveguide losses with identical waveguide geometries. The 6.5 dB/cm loss for a 200x500 nm^2 deposited waveguide in the TE mode is low enough for many applications, including upper level waveguide routing. In addition, the dimensional and material index similarities of a-Si and SOI waveguides are ideal for efficient evanescent coupling between the two waveguide structures.

6.3 Polycrystalline Silicon (poly-Si)

Unlike crystalline silicon which is deposition limited, and amorphous silicon which is process temperature restricted (T < 650°C); polycrystalline silicon is restricted by neither deposition limitation. Hence, poly-Si is very attractive for waveguide applications where deposition and process temperature freedoms are necessary. However, light scattering due to rough interfaces and grain boundaries, and bulk absorption from dangling bond defects is truly limiting to poly-Si waveguide performance. In this section, the fabrication of low loss poly-Si waveguides is investigated.

6.3.1 Previous Work

In two previous studies, both originating from Prof. Kimerling's research group, poly-Si waveguide losses were reduced by process improvements from 77 dB/cm to 15 dB/cm [100-101]. The range of losses in these studies represents the lowest losses reported for poly-Si waveguides. In both studies, poly-Si waveguides were fabricated on a 3 μm of SiO_2 from either 1) a deposited poly-Si layer that was subsequently etched or 2) by annealing an etched amorphous silicon waveguide structure for 16 hours at 600°C. Waveguide losses were measured by the cutback method using a multi-mode 1000x8000 nm^2 poly-Si waveguide geometry.

In the first study [100], it was found that the loss was strongly dependent on the top surface roughness, which when reduced by CMP, curtailed the loss from 77 dB/cm to 35 dB/cm. In the second study [101], the use of a hydrogenation step on the fabricated poly-Si waveguides, by means of an electron-cyclotron resonance chamber, was found to further reduce the losses from 35 dB/cm to 15 dB/cm. The hydrogen acts to passivate dangling bonds within the bulk and thus reduce the poly-Si bulk absorption [101]. It was also found that poly-Si waveguide loss is not a strong function of grain size.

6.3.2 Waveguide Fabrication

Polycrystalline silicon waveguides were fabricated at BAE Systems in Manassas, Virginia in two ways. Both fabrication processes began with the deposition of a 3 μm undercladding layer of high density plasma (HDP) PECVD silicon dioxide on a (100) Si substrate. Afterwards, a 200 nm layer of PECVD a-Si waveguide core layer was deposited with an AMAT P5000 with 100 cc/min SiH_4, 2000 cc/min Ar, T=450°C, 400 mills spacing, P = 4.5 torr, and Power = 100W. At this point, the two poly-Si waveguide fabrication methods employed in this study diverged. In one case, the process identically followed the a-Si waveguide process (without the SiN layer) detailed in section 6.2.1, with the exception of a final 650°C anneal for 2 hours. For the second case, the a-Si material was annealed at 650°C anneal for 2 hours prior to the etch step, with all other steps held identical.

6.3.3 Post-Etch Annealing

The first poly-Si waveguide fabrication approach – annealing of fabricated a-Si waveguides – resulted in very high transmission losses that are estimated at >> 30 dB/cm. This is similar to the results in the previous studies [100-101], which without CMP or hydrogen passivation found waveguide losses of 77 dB/cm when a-Si waveguides were crystallized. The losses for the single-mode waveguide geometries, 200 x (400 – 600) nm^2 are expected to have larger losses due to the scattered light from increased field intensity at the core-cladding interfaces.

The propagation loss through all but the shortest paperclip structures exceeded the noise levels of the waveguide measurement apparatus for post-etch annealed poly-Si waveguides. However, to demonstrate the enormous increase in loss that accompanies the crystallization of a-Si waveguides, the insertion loss for a set of straight a-Si waveguides is compared before and after a 2 hour, 700 °C anneal in Figure 6.16. The TM mode data is used since it has lower coupling losses.

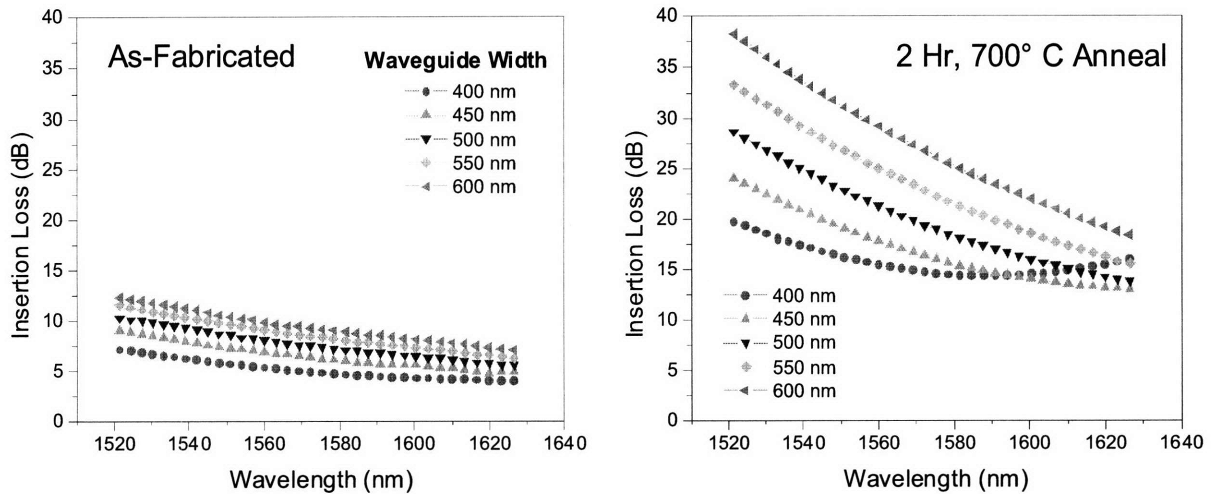

Figure 6.16 – Insertion loss measurements for straight a-Si waveguides of different widths, h=200 nm before (left) and after (right) a 2 hour 700°C anneal in an N_2 environment.

As a reminder, insertion loss is the sum of coupling and transmission losses. The dramatic difference between the insertion loss of the a-Si and poly-Si waveguides is dominated by changes in the transmission loss, as coupling loss variation should be minimal. The increase in insertion and therefore transmission loss is caused by 1) the formation of grain boundaries – bulk scattering 2) increased sidewall roughness from grain boundary grooving – surface roughness scattering, and 3) increased absorption due to dangling bond defects which are no longer passivated by hydrogen. The annealing process also decreased the material index, as can be seen by the w=400 nm insertion loss curve for the poly-Si sample. The increase in loss with wavelength is indicative of substrate coupling, which suggests that the poly-Si material index is less than that of a-Si, as expected.

6.3.4 Slab Annealing

The second poly-Si waveguide fabrication approach – annealing the a-Si layer prior to etching – resulted in high but measurable waveguide losses; see Figure 6.17. This fabrication approach was not tested in the two previous studies in Prof. Kimerling's group. Surprisingly, the losses for these poly-Si waveguides are among the best ever reported, especially for the TM mode. In addition, to the knowledge of the author, these are the only single-mode poly-Si waveguide losses ever reported.

The TE mode loss data is quite high, with a decreasing trend with waveguide width, which suggests that the loss is roughness-limited, presumably resultant from the granular structure. The large error bars are in part due to measurement noise, since the paperclip waveguide output powers were approaching the system noise level. The TM mode losses appear to have an increasing loss trend with waveguide width, which suggests that a bulk loss property, either bulk scattering from grain boundaries or

absorption is dominating. The low loss of the TM mode waveguides is a reflection of the low fraction of power, between 20 and 30 % for these waveguide geometries, in the poly-Si material.

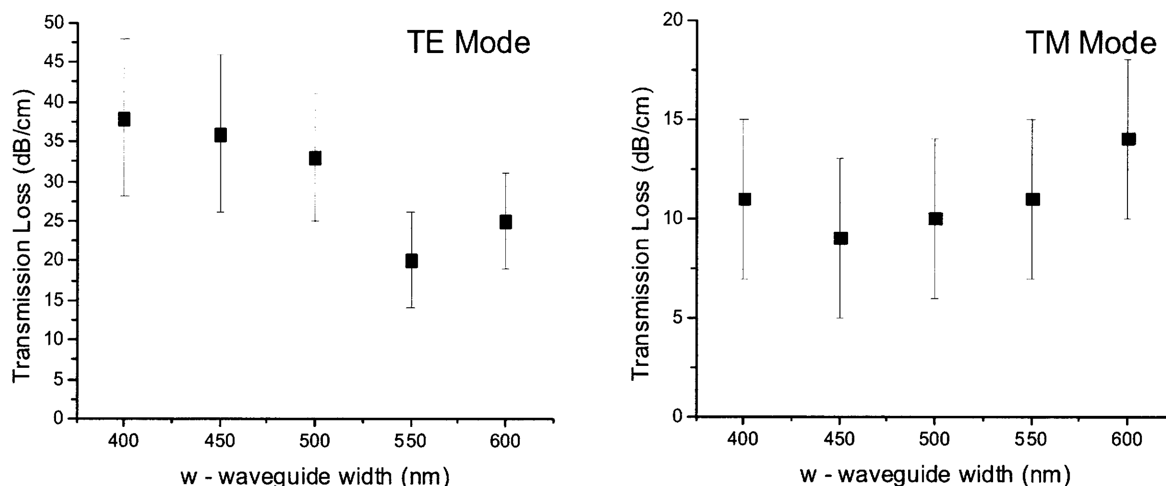

Figure 6.17 – Polycrystalline waveguide transmission loss (λ=1550 nm) as a function of width, h=200 nm. Waveguides were fabricated from an annealed a-Si film that was subsequently etched and clad with HDP PECVD SiO_2.

The mechanism responsible for the large difference in losses between the two poly-Si waveguide fabrication approaches used in this study is not clear. However, the use of the slab anneal approach may serve to comparatively reduce bulk absorption and top surface roughening. In comparison to an etched a-Si waveguide structure, the slab anneal approach has a smaller a-Si surface area to bulk ratio which reduces the extent of hydrogen out-diffusion. Also, the presence of film stresses may serve to suppress surface roughening during crystallization.

Chapter 7 – Waveguide Design for Low Loss

In chapters 5 and 6, improved process techniques were investigated to lower waveguide transmission losses. In this chapter, waveguide design techniques are utilized to optimize waveguide transmission for a given waveguide material and fabrication process. The basic premise of each design technique is to minimize the mode field interaction with the portion of the waveguide structure that is responsible for transmission loss, e.g. sidewall roughness, absorptive materials, or substrate leakage. Experimental results and design tradeoffs are discussed.

7.1 Geometric Techniques

The choice of waveguide geometry is affected by many factors including: index contrast, signal wavelength, thin film thickness limitations, modal confinement, and minimum bend radii. Optimization of the waveguide geometry for low loss is dependent on the material and process limitations in fabrication. Thus, the optimal waveguide geometry depends on the dominant loss mechanism. In this section, waveguide geometries are optimized for high index contrast (HIC), channel waveguides which are designed for operation in the telecom spectrum, however the design principles are applicable to most waveguide systems.

7.1.1 Roughness-Limited Waveguides

Roughness-limited waveguides are roughness-scattering loss dominated and radiate optical power as a result of the waveguide mode scattering optical power from the rough core-cladding interface. In most cases, the interface roughness is only significant at the waveguide sidewalls and therefore the loss is proportional to the field intensity at those interfaces. In section 5.2.5, a literature review of roughness-limited, SOI-based channel waveguides, revealed that the wide disparity in single mode waveguide losses is mostly due to geometric differences rather than differences in sidewall roughness statistics. The reported losses for short, wide waveguide geometries were considerably lower than the taller, thinner waveguides despite nearly identical sidewall roughness values. As discussed in section 4.3.3, short, wide waveguides are less sensitive to loss because 1) the short waveguide height reduces the relative amount of sidewall roughness the mode interacts with and 2) the wide waveguide width results in a relatively, reduced field intensity at the rough sidewall interface. If one extrapolates from these geometric trends, the optimal waveguide cross-sectional geometry for roughness-limited waveguides is a thin, wide structure.

For most photonic circuit applications, the waveguide width and height are restricted to dimensions that only support the primary TE and TM modes. The presence of higher order modes in waveguides results in undesirable dispersion and bend-loss properties which place added complication in

waveguide circuit design. This single-mode requirement places a limitation on the maximum waveguide width. In contrast, the substrate cladding thickness places a minimum waveguide layer thickness requirement to avoid substrate leakage losses. Under these assumptions, the optimum waveguide geometry is restricted such that the width is set at the second-mode cutoff and the height is sufficient such that the mode field overlap with the high index substrate is negligible.

However, just because a given waveguide geometry can support higher order modes, does not necessarily mean it does. In a symmetric channel waveguide each eigenmode solution to the wave equation, which corresponds to a unique mode field distribution, is orthogonal to all other eigenmode solutions. Therefore, the transition of power from a single propagating mode to multiple propagating modes in a higher-order mode, waveguide geometry can only occur due to perturbations in a waveguide structure which facilitate power transfer between the modes; some examples include waveguide bends, abrupt dimensional changes, and excessive interface roughness.

Hence, if the width of a single-mode waveguide is slowly tapered out in a slow, smooth, and controlled manner (what is often referred to as adiabatic tapering) past the second-mode cutoff, the higher order modes will not be excited. By doing this, the low loss nature of wide waveguides can be exploited without the deleterious effects of multi-mode operation. In an analogous manner, if the wide waveguide width is tapered back to single mode dimensions, the high confinement and tight bend radii properties can be utilized to avoid optical losses at bends and other abrupt perturbations which may result in optical power transfer to higher order modes.

This combination of narrow and wide waveguide widths, where the wide width is used in straight, unperturbed waveguide sections and the narrow, single-mode width is used for waveguide bends or any other application where the mode may become perturbed is ideal for ultra low loss transmission. This hybrid scheme of connecting wide and narrow waveguides with adiabatic tapers, depicted in Figure 7.1, was first devised and demonstrated by Spector et al. at Lincoln Labs [70]; the resulting structure is coined a hybrid waveguide.

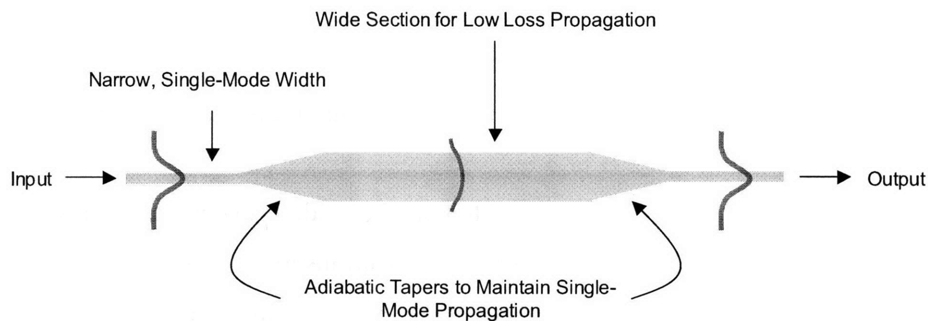

Figure 7.1 – Overhead view schematic of a roughness-limited hybrid waveguide structure.

Several hybrid waveguide structures were included in the initial SOI waveguide process run at BAE. The waveguides were fabricated from a 200 nm thick SOI wafer with a 3 μm buried oxide (BOX) layer. The narrow waveguide width was kept constant at 500 nm, while the wide waveguide width was varied from 3 to 6 μm. The taper angle (~ 2.5°) was kept constant which corresponds to taper lengths that ranged from 50 to 120 μm. The loss of the hybrid waveguide structures were measured by the cutback method. A schematic of a hybrid paperclip as well as an example of a cutback measurement fit are depicted in Figure 7.2.

As one can see in Figure 7.2, the TE mode transmission loss for the 3 μm wide hybrid structure is 0.35 dB/cm, which is considerably smaller than the single-mode SOI waveguide losses (5.7 dB/cm) in the same process run (see section 5.2.2). This result confirms that SOI waveguides are truly roughness-scattering loss dominated. In fact, if the additional loss from single-mode sections in the vicinity of the waveguide bends is subtracted away, the transmission through the wide section is conservatively estimated at 0.1 dB/cm. In order to fit the multiple centimeter length waveguides needed in ascertaining a good cutback fit, the longer hybrid waveguides used up to eight turns to fit on the 0.5 cm length chip.

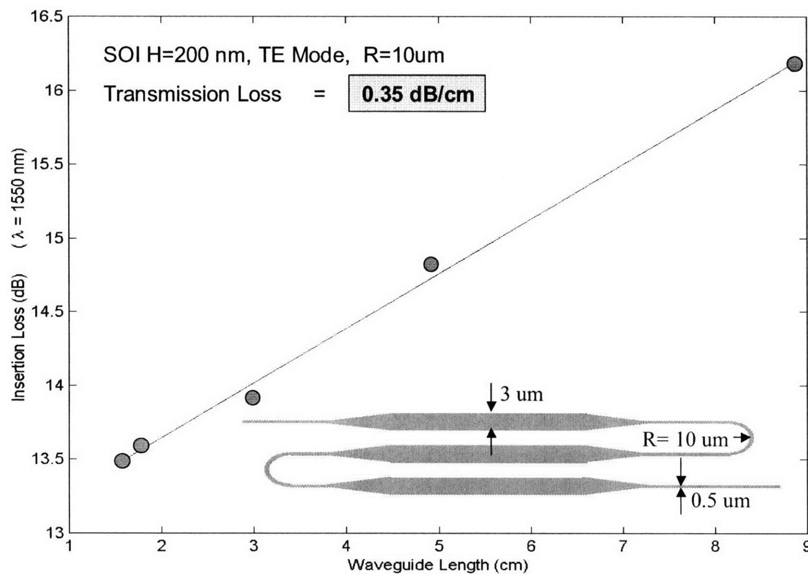

Figure 7.2 – Cutback transmission loss measurement for the roughness-limited hybrid waveguide structure depicted.

Proof that higher order modes are not excited in the wide waveguide sections of the hybrid waveguide structure is observed in Fabry-Perot resonances from insertion loss measurements, see Figure 7.3. Fabry-Perot resonances are a result of reflections at the waveguide facets and correspond to the constructive and destructive interference of the forward and backward propagating light in the waveguide.

For a single waveguide mode, the Fabry-Perot resonance has a distinctive sinusoidal-like pattern with a single period as a function of wavelength. The presence of multiple-modes results in a multitude of Fabry-Perot periods which manifests itself as a beating effect in the Fabry-Perot resonances. However, the lack of a Fabry-Perot beating in Figure 7.3 indicates that the primary mode is maintained throughout the hybrid waveguide structure. The erratic variation of the maxima and minima of the Fabry-Perot resonances in Figure 7.3 is attributed to fact that the fringe spacing is close to the system resolution due to the long waveguide lengths used.

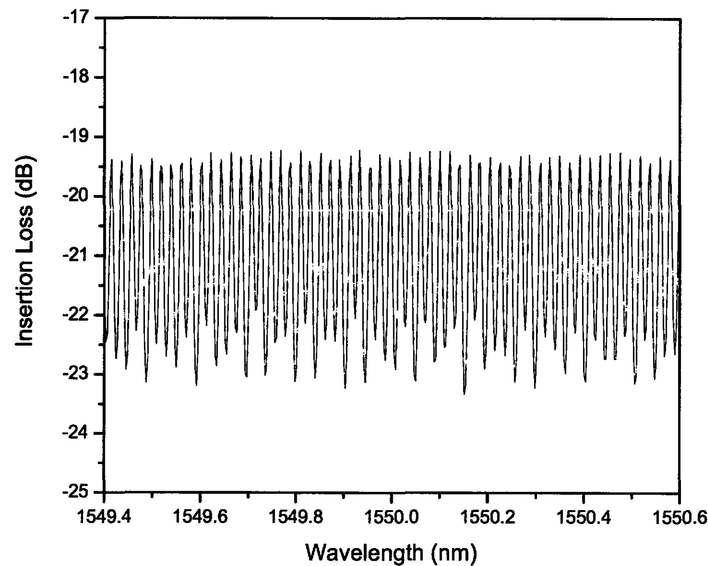

Figure 7.3 – Fabry-Perot Resonance of a hybrid waveguide paperclip structure, the total length is 1.56 cm.

The variation of the width of the wide section in the hybrid waveguides was a small effect on the loss. The average loss values for the different width hybrid waveguides are listed in Figure 7.4. The error bar for these measurements is estimated at ± 0.05 dB/cm. While the losses are much smaller than the narrow, single-mode waveguides, the hybrid waveguide loss results indicate that increasing the width results in a slight increase in loss. This loss increase is attributed to roughness-scattering from the top surface. All chips measured were treated with wet chemistries which were observed to add sub-nm roughness to the top surface. For these waveguide geometries, the field intensity at the top surface is nearly constant with waveguide width, whereas the top surface interface increases significantly with waveguide width. Thus the wider waveguides scatter more light and have higher losses for a constant top surface roughness. This finding suggests that the wide waveguides are top surface roughness-limited.

Hybrid Waveguide Width (μm)	3	4	5	6
Average Loss (dB/cm)	0.38	0.45	0.45	0.63

Figure 7.4 – Hybrid waveguide structure losses as compared to the width of the wide section.

The losses found in this study are nearly identical to that found in [70]. This makes sense since the hybrid design is intended to eliminate the process-dependent losses found in SOI waveguides. To put the loss of 0.35 dB/cm in perspective, 92.3% of the light is transmitted over a one centimeter length. In comparison, the best single-mode waveguide loss (~ 3 dB/cm) results in only 50% of the light transmitted over a one centimeter length. Hence, the hybrid waveguide is best used for "long" distance optical signal transport, where transmission loss is most detrimental. In addition, the large cross-sectional area of the hybrid waveguide is attractive to reduce non-linear absorption losses, since they inversely scale with waveguide dimensions, as detailed in relations (4.27) and (4.28).

One final application of the hybrid waveguide is its use in measuring the bulk loss of a waveguide material. The two most common waveguide losses are roughness-scattering and absorption. The use of a hybrid structure virtually eliminates scattering losses, leaving absorption as the dominant loss mechanism. The waveguide core material bulk loss can then be estimated by dividing the transmission loss by the optical fill factor Γ, as seen in (7.1) and discussed in section 4.4.5.

7.1.2 Absorption-Limited Waveguides

The loss from absorption dominated waveguides is proportional to the percentage of optical power in the absorptive material. For the waveguides studied in the work, the deposited waveguide core materials exhibit absorption. Assuming that absorption from the cladding material is negligible, the absorption loss is given by relation (7.1) where α_{bulk}^{core} is the bulk loss for the core material and Γ is the optical fill factor defined in (4.20).

$$\alpha_{absorption} = \Gamma \alpha_{bulk}^{core} \tag{7.1}$$

The most straight-forward method of reducing loss in an absorption-limited waveguide is to decrease Γ by reducing the waveguide dimensions. Shrinking the waveguide dimensions below the single-mode criteria serves to expand the mode and lessen the field overlap with the waveguide core (i.e. the optical fill factor). The effect is seen in Figure 7.5 where the mode profiles for a typical single-mode Si/SiO_2 waveguide (200 x 500 nm^2) and a reduced dimension waveguide (200 x 200 nm^2) are compared. The

optical fill factor and thus the absorption-limited loss are reduced by 94% in this example! Additional experimental evidence is detailed in section 4.4.5.

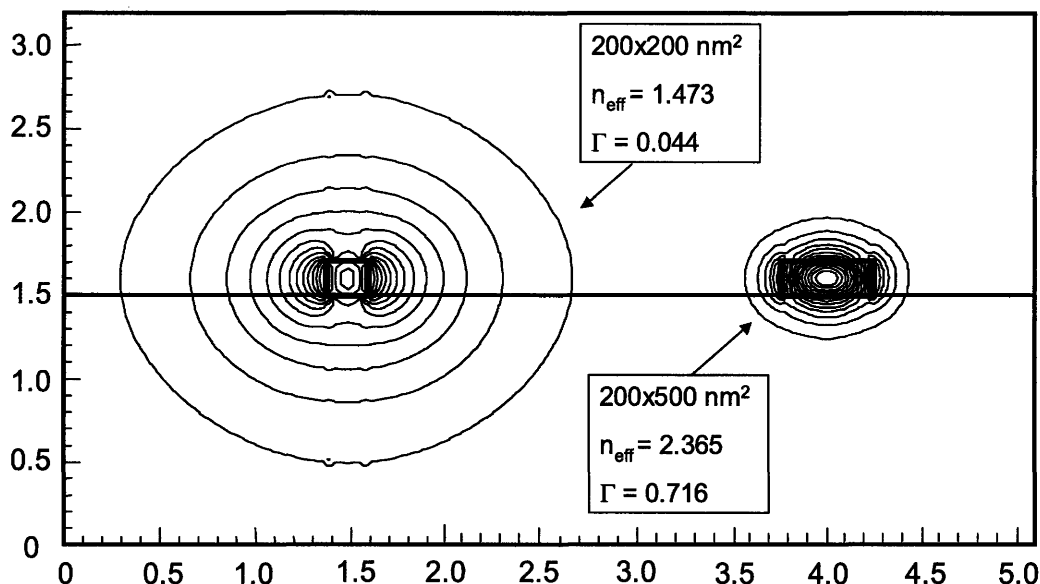

Figure 7.5 – Mode profiles for Si/SiO_2 waveguides, calculated with FIMMWAVE. Grid units are μm.

However, there are several tradeoffs to shrinking the waveguide cross-section. First, the dramatic increase in mode field diameter can be problematic in that it may contribute to substrate leakage loss, as discussed in section 4.7. Expanding the mode increases the field overlap with the substrate for a given undercladding thickness, which induces substrate leakage loss. Thus the undercladding thickness places a limit on the dimension reduction for absorption-limited waveguides.

Second, the decreased effective index, that accompanies the reduced waveguide core dimensions, increases the bend loss for a given bend radius. As discussed in section 4.9, the minimum sustainable bend loss is proportional to the difference between the effective index and the cladding index in the bend. This effect is seen in Figure 7.6, which compares the experimentally measured bend loss for two Si/SiO_2 waveguide geometries; bend loss is plotted versus wavelength for several bend radii. In this comparison, the only difference between the two waveguides is the height 200x500 nm^2 versus 220x500 nm^2, everything else is kept constant. Therefore the effective index is lower and the bend loss is higher in the 200x500 nm^2 waveguide geometry.

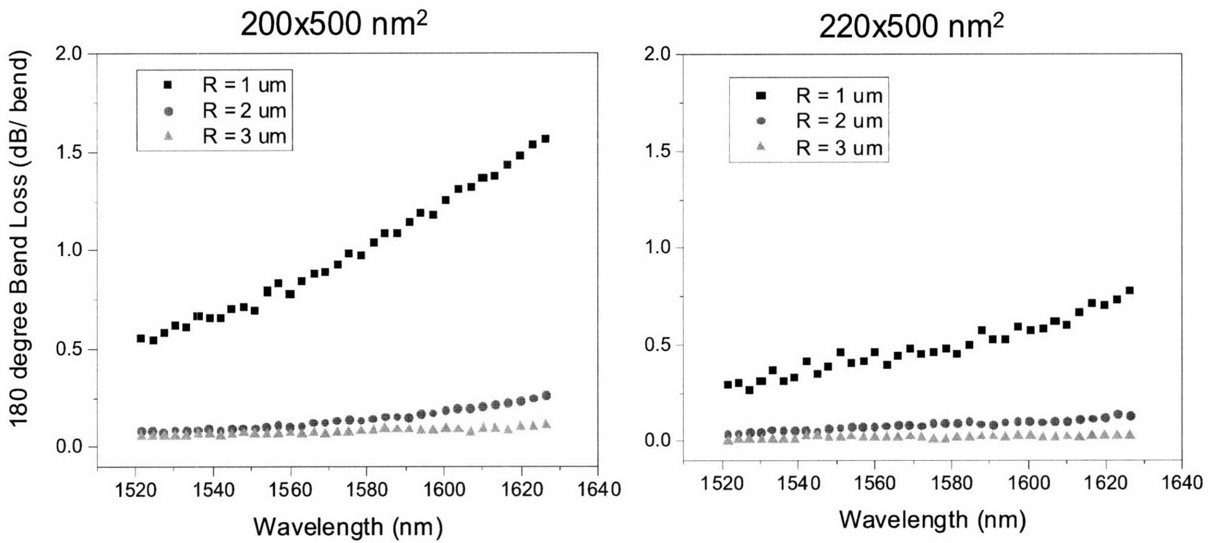

Figure 7.6 – Bend loss measurements for Si/SiO_2 waveguides, 200x500 nm^2 and 220x500 nm^2 geometries

Similar to roughness-limited waveguides, the use of different waveguide geometries in straight and bend sections of the waveguide for absorption-limited waveguides is one method of further optimizing transmission loss. In this scheme, the waveguide is adiabatically tapered to a narrow width for straight sections, to minimize Γ and thus transmission loss, and tapered out to the maximum single-mode size to maximize n_{eff} and optimize bend loss and thus increase device density. A schematic of this absorption-limited hybrid waveguide structure is depicted in Figure 7.7. Experimental demonstration of the absorption-limited waveguide structure, where a 200x500 nm^2 a-Si/SiO_2 waveguide was tapered to a 200x250 nm^2 cross-section, were substrate loss limited for the undercladding thickness (3 μm) used in the experiment.

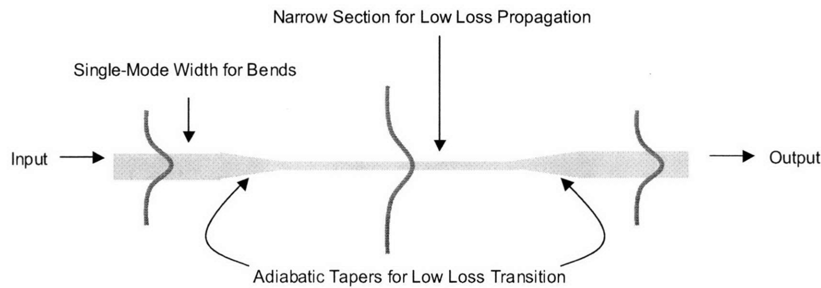

Figure 7.7 – Absorption-limited hybrid waveguide structure for low loss propagation

The mode size limitations of the absorption-limited hybrid waveguide structure may not be an issue for upper chip level waveguides in an integrated chip. Similar to VLSI microelectronic chips, the density of interconnects decreases with chip level. Likewise, upper level photonic interconnects, which are fabricated from deposited waveguide materials which are typically absorption limited, may have the

clearance for large modes in the narrow waveguide sections. For this application, the absorption-limited hybrid waveguide geometry is useful.

7.2 Cladding Design

The choice of waveguide cladding material and thickness has an impact on roughness-scattering loss – both due to the effect on index contrast and interface smoothness. In this section the use of a thin, conformal layer deposited between the core and cladding materials, what is termed here as a "nanocladding" layer, is discussed.

7.2.1 Roughness-Scattering Loss Reduction

For roughness-limited waveguides, the addition of a nanocladding layer with an index between that of the core and cladding materials can act as a desensitizer to scattering-roughness loss. For Si (n=3.5) waveguides clad with SiO_2 (n=1.45), SiN (n=2.0-2.2) is a well-suited material given its index, CMOS compatibility, and optical transparency at the telecom wavelengths (assuming low H content). Such a waveguide structure is illustrated in Figure 7.8.

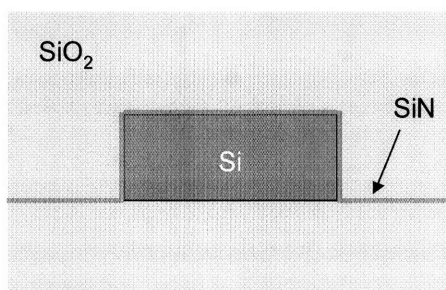

Figure 7.8 – Si/SiO_2 waveguide structure with a SiN nanocladding layer

As discussed in section 4.3.3, the sensitivity of roughness-scattering in channel waveguides scales non-linearly with the index difference between the core and cladding materials (Δn). This effect is observed in figure 4.10, where scattering loss coefficients for the Barwicz-Haus theory for different Δn waveguides are compared. For SiON/SiO_2 (Δn=0.5) waveguides, the scattering loss sensitivity for single-mode geometries is of order 10^{-4} dB/cm-nm^2 whereas for Si/SiO_2 (Δn=2.0) waveguides it is of order 10^{-1} dB/cm-nm^2. By inserting a material of intermediate index, the nanocladding reduces the roughness-scattering for a given sidewall or top surface roughness. Even though the addition of the nanocladding adds another set of dielectric interfaces, the scattering from two low Δn interfaces is less than one high Δn interface, as a result of the hyper-linear scaling. Or in other words:

$$\alpha_{Si\rightarrow SiO_2}^{scattering} > \alpha_{Si\rightarrow SiN}^{scattering} + \alpha_{SiN\rightarrow SiO_2}^{scattering} \quad (7.2)$$

Therefore the addition of an intermediate index nanocladding layer serves to lower roughness-scattering loss. This assumes that the roughness is similar in the two layers.

The nanocladding effect was tested in the first SOI process run at BAE, as described in section 5.2.1. Here, all fabrication steps were held constant except for the addition of a 10 nm thick conformal SiN layer deposited on the etched Si waveguide before the top cladding deposition, yielding the lowest SOI waveguide loss results for this process run. A comparison of average transmission loss data for SOI-based Si/SiO_2 waveguides with and without the SiN nanocladding is plotted in Figure 7.9. The nanoclad sample clearly shows a 1.0 – 1.5 dB/cm reduced loss for all waveguide geometries corresponding to an estimated, effective RMS roughness reduction of 0.5 nm.

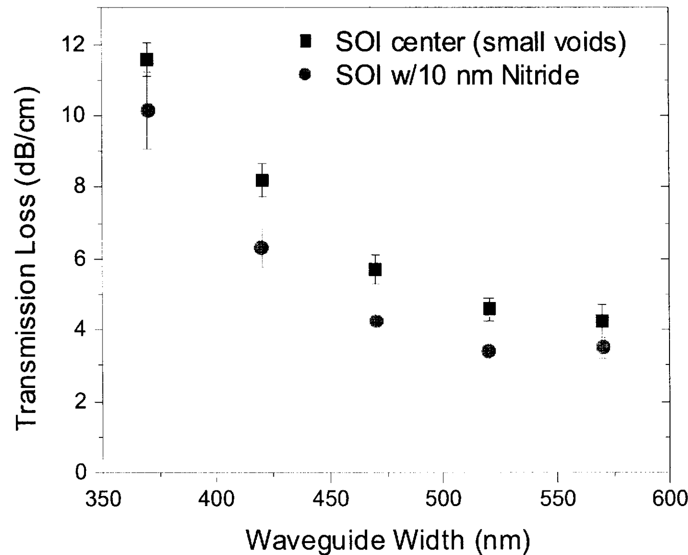

Figure 7.9 – Comparison of average waveguide transmission loss for TE polarized light (λ=1550 nm) for 200 nm thick SOI with and without a nanocladding. The waveguides had a BOX layer and upper cladding thickness of 3 microns.

However, attributing the loss reduction solely to the nanocladding roughness-desensitization effect is not clear. The addition of the SiN layer may serve to fill in the waveguide sidewall recess that occurred in the etch process and thereby prevent the formation of the voids during the top cladding deposition step. On the other hand, the use of a thicker, 25 nm SiN layer in subsequent process runs revealed severe N-H bond absorption in the nanocladding material, adding several dB/cm to the loss, as discussed in section 6.1. Therefore, the roughness-scattering loss reduction may be greater than observed here.

7.2.2 Diffusion Barrier

A second attractive feature of using a nanocladding layer is its use as a diffusion barrier. For deposited materials, unlike SOI-based waveguides, it is possible to cover all four sides of a channel waveguide with a thin-conformal layer that can act as a diffusion barrier. The use of a diffusion barrier layer, such as SiN, can prevent hydrogen, incorporated during film deposition, from out-diffusing. The presence of H in amorphous and poly Si reduces the density of unpassivated dangling bonds – which is a source of absorption loss [101,103]. In addition, H-incorporation in poly-Si, α-Si, and single crystal Si can enhance smoothing effects at elevated temperatures [84].

7.2.3 Poly-Silicon Oxidation Smoothing

The use of a nanocladding diffusion barrier can also facilitate a poly-Si waveguide interface smoothing technique. Thermal oxidation of poly-Si waveguides does not work well to smooth the surface due to the anisotropic oxidizing nature of randomly oriented grains on the surface, as well as intergranular diffusion. Oxidation may actually serve to roughen a poly-Si surface, especially during the reaction-limited regime. However, the use of a diffusion barrier facilitates diffusion-limited oxidation of the waveguide. Diffusion-limited oxidation is a flux driven process. Rather than depending on the surface potential, a diffusion-limited flux rate distributes the rate of incoming oxidizing species as a uniform front parallel to the waveguide-ambient interface. The uniformly distributed front of incoming oxidizing species smoothes roughness because diffusion of an oxidizing species to a roughness peak is more probable than to a roughness trough, i.e the diffusion length is shorter. As a result of this flux behavior, diffusion-limited oxidation is a smoothing process that is reaction rate independent, and thus provides an avenue for smoothing polycrystalline waveguide materials.

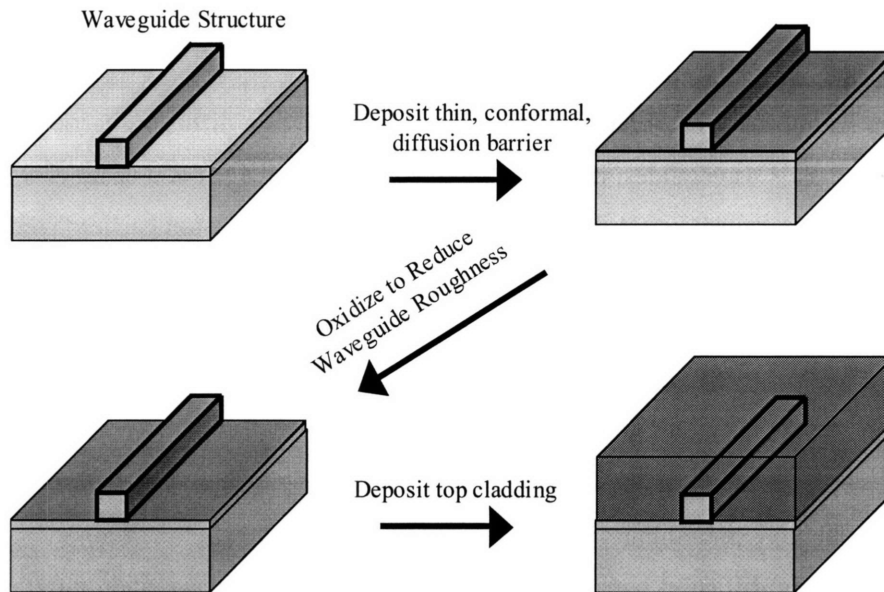

Figure 7.10 – Process flow for Poly-Si smoothing by thermal oxidation

The use of a thin conformal diffusion barrier is necessary to ensure equivalent oxidation fluxes to the waveguide sidewall and top surface interfaces, enabling waveguide shape preservation during the smoothing process. Some oxidation diffusion barrier cladding material candidates for poly-Si waveguides include Si_3N_4, SiON, and SiO_2. The process flow described in this section is illustrated in Figure 7.10.

7.3 Crystalline Substrate Optimization

For crystalline waveguide materials that are roughness limited, such as SOI-based waveguides, it is advantageous to minimize sidewall roughness. In chapter 5, several crystalline silicon interface smoothing techniques that employ modified process conditions were discussed. However, in this section, modification of the waveguide and substrate crystalline orientation in conjunction with some process modifications to optimize surface roughness is discussed.

7.3.1 Anisotropic Etching and Smoothing

The anisotropic nature of crystalline material processing properties is a limiting cause to surface smoothing. For example, even common Si wafer cleaning procedures such as the RCA clean, which is generally regarded as isotropic, leads to nm-scale roughening of non-close-packed atomic surfaces [80-81]. As a reminder, even nm-scale roughness can significantly deteriorate the transmission of light through a HIC waveguides. The roughness arises from differential (anisotropic) etch rates that occur among the various atomic planes, which is an outcome of the atomic arrangement in the crystalline lattice.

For Si, the close-packed {111} surfaces are least reactive and have the slowest etch rates. In fact, the use of anisotropic etches is a common way to expose {111} surfaces with atomically smooth interfaces.

In dealing with the anisotropic nature of crystalline waveguide materials, the use of an anisotropic-etch, post-etch smoothing method has been investigated [73]. In this study, {100} SOI channel waveguides running along the <110> directions with {110} sidewalls were exposed to TMAH whereby the slow etching, close-packed {111} crystallographic planes were exposed on the sidewall interface. A schematic of the resulting waveguide geometry is depicted in Figure 7.11.

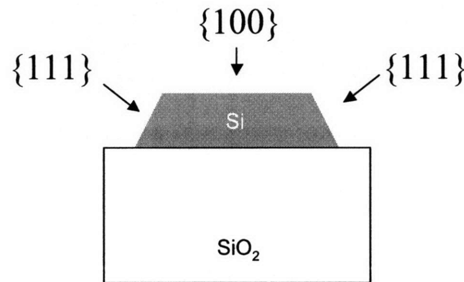

Figure 7.11 – Schematic of {100} SOI waveguide geometry after anisotropic etch exposes {111} sidewalls.

While the loss of the anisotropically etched waveguides was noticeably lowered due to the sidewall smoothing in this study, the resulting trapezoidal cross-section geometry is limiting. As discussed in section 4.8, trapezoidal cross-section waveguides in conjunction with waveguide bends are susceptible to mode-to-mode coupling.

7.3.2 Substrate Optimization

One method to surmounting the geometric limitation that accompanies anisotropic etch smoothing is to choose the wafer orientation such that the fabricated waveguides have {111} sidewalls. In this way, the use of an anisotropic etch will leave the waveguide geometry rectilinear, while maintaining the benefits of the anisotropic etch smoothing technique. Aside from anisotropic smoothing, waveguides fabricated in this fashion will have added resistance to surface roughening during necessary cleaning process steps.

Fabricating a waveguide with {111} sidewalls is dependent on the wafer orientation. Si wafers are commonly available in {100}, {110}, and {111} orientations. Of these three, only the {110} wafer surface is normal to {111} planes – a requisite for fabricating a waveguide with {111} sidewalls. Unfortunately, the commercial availability of SOI substrates is mostly limited to {111} and {100} orientations for relevant photonic layer thicknesses. The lack of {110} SOI is purely due to economic reasons as there are no technical limitations in fabricating these wafers. The gaining popularity of integrated photonics may add demand for this substrate.

A waveguide fabricated from a {110} SOI wafer is depicted in Figure 7.12. The {111} sidewalls are orthogonal to the {110} wafer surface when the waveguide is oriented in the <211> directions.

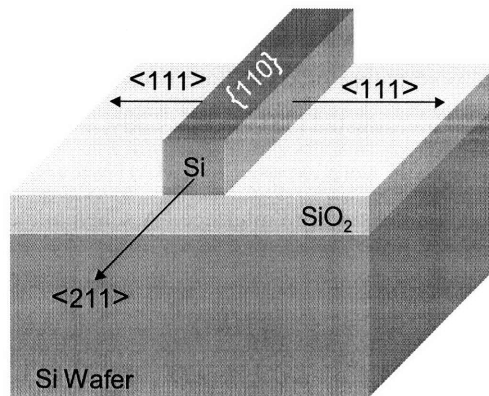

Figure 7.12 – Schematic of {110} SOI waveguide geometry.

7.3.3 Integration Issues

There are several processing issues that accompany fabricating {110} SOI waveguides in the <112> directions. The first issue is that the <112> directions are not orthogonal to each other (as seen in Figure 7.13), this places design restrictions on the waveguide layout. Rather than the orthogonal grid-like circuit layouts typically used, the waveguides in this scheme must run along the <112> directions, which are 70.5° and 109.5° from each other.

If the non-orthogonal layout scheme is too restrictive, a photonic circuit designer may choose to use an orthogonal grid system where one of the grid directions is in the <112> direction, wherein this axis is utilized for low loss waveguide applications. To implement this plan, the wafer or the mask must be rotated 54.7° since the {110} wafer flat is oriented in the <100> direction, which is not parallel or orthogonal to the <112> direction. This is a concern since many lithographic exposure systems are restrictive and do not allow wafer or mask rotation, as these freedoms add error to alignment. To relieve and eliminate this problem, the photolithography mask can be rotated in the CAD software used in drawing the waveguide layout. Alternatively, if this approach becomes popular, the demand for a {110} photonics grade SOI substrate, where the wafer flat is cut along the <112> direction, may become warranted.

One final issue in utilizing an orthogonal grid with one axis in the <112> direction is that it may add extra steps to the process flow, such as a step to protect the non <112> waveguides from faceting during an anisotropic smoothing step. However, the minimization of sidewall roughness and thus transmission loss, especially if atomic smoothness is achieved as it has been previously [73], may be worth the added steps for applications where waveguide loss is crucial.

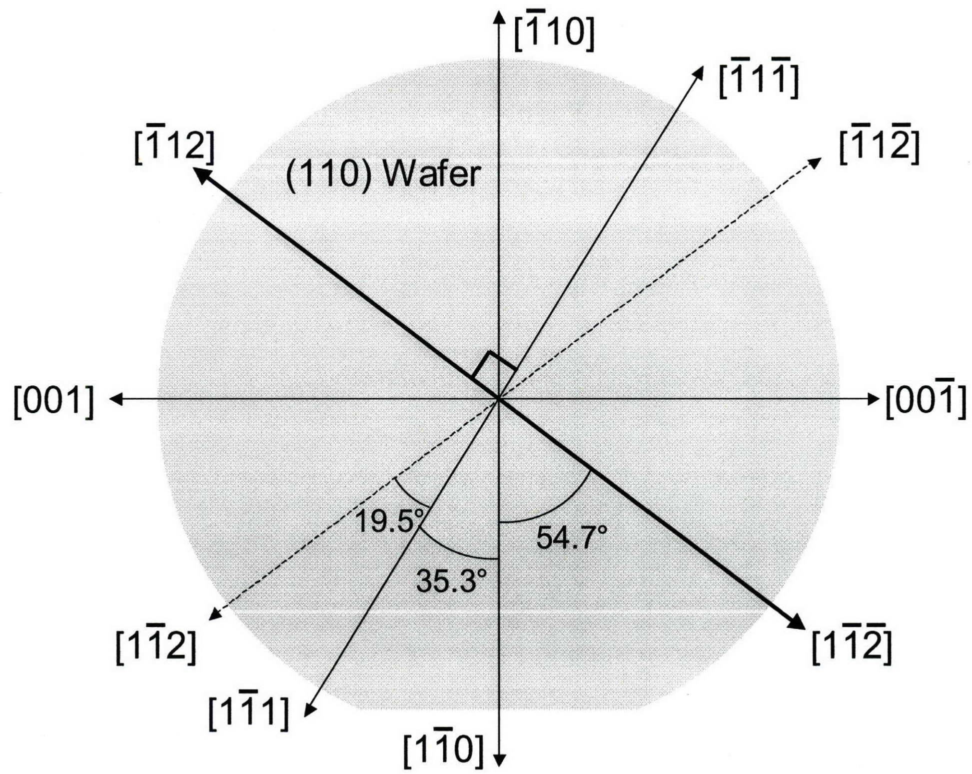

Figure 7.13 – Crystallographic directions of a (110) wafer.

Chapter 8 – Ring Resonator Devices

Ring resonators are a basic building block of photonic circuits, enabling complex functionality for optical systems. Ring resonators can serve as filters for wave division multiplexing and demultiplexing broadband optical signals [15, 104], dispersion compensators for accurately controlling phase [105], lasers [106], and ultrafast electro-optic modulators [107]. In a sense, ring resonators are the do-all analog to the transistor in integrated electronic circuits.

In this chapter, ring resonator devices are analyzed in the context of material optimization and HIC waveguide design where the feasibility and limitations of the devices are surmised for CMOS compatible materials. Particular attention is spent on 1) ring trimming experiments utilizing photo-oxidation of a polysilane top cladding and 2) understanding and optimizimg ring modulator design for SiGe materials. The notation used in this work closely follows the seminal ring resonator modeling work of Little [104] which in turn, follows Haus' textbook notation on generalized resonators [23].

8.1 Ring Resonator Basics

Ring resonator devices are well suited for integrated HIC photonic circuits due to 1) the short evanescent field decay length outside the waveguide core, 2) the small interaction length between the ring and bus, and 3) tight turn radii with low bend loss. In combination, these attributes lead to compact devices with weak coupling between the ring and bus, which facilitates high quality resonators with high spectral selectivity and extinction ratios.

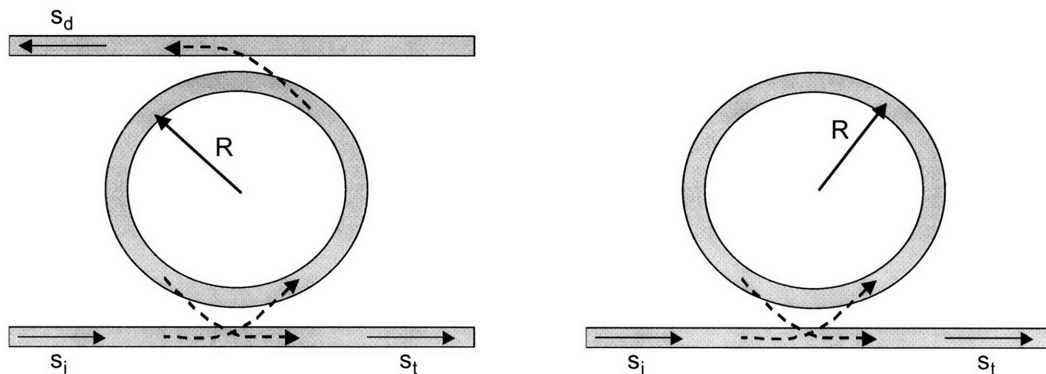

Figure 8.1 – Schematic of two common ring resonator device configurations

There are two basic configurations used for ring resonator devices, both of which are depicted in Figure 8.1. The configuration on the left – a ring resonator with two waveguides – is well suited for filtering applications, whereas the configuration on the right – a ring resonator with one waveguide – is well suited for phase control, modulator, and resonant applications (lasers and amplifiers).

In the two-waveguide-ring configuration, the operation is as follows – resonant light couples from the input waveguide (bottom) to the ring and then to the drop waveguide (top). If the light is not resonant with the ring, the light travels down the input waveguide with a negligible amount coupled to the ring (due to the weak coupling). In the resonant condition, the fraction of light that is coupled to the drop waveguide is dependent on the balance of coupling rates with losses in the system. Similar to the directional coupler, the coupling rates are governed by the gap size and field overlap between the ring and each waveguide. Theoretically, any fraction of light can be transferred from the input to the drop port at resonance by properly choosing the ring-waveguide gap sizes, even when loss is present in the system. Ultimately, ring resonators in this configuration can be designed to have ideal channel dropping characteristics for wave division multiplexing: a broad, steeply sloped, flat-topped spectral response with 100% efficiency. The device physics for this configuration have been well documented in reference [104].

Rather than routing resonant light to a separate waveguide, the single-waveguide-ring configuration takes advantage of the resonator losses (or gain) to manipulate the phase and amplitude of the waveguide output. In operation, light with input field amplitude s_i travels down the waveguide and evanescently couples to the ring, which alters the transmitted field amplitude s_t of the bus waveguide (so called for its ability to carry multiple wavelengths). The extent to which s_t differs from s_i is dependent on the fraction of energy coupled from the bus to the ring, the fraction of energy which is coupled from the ring to the bus, and the phase difference between the ring and bus signals. The device physics for this ring resonator configuration is derived in section 8.1.3 in a similar fashion to the treatment of a ring with two waveguides found in [104].

8.1.1 Resonance

The phenomenon of resonance is the fundamental principle by which all ring resonator devices operate. In a ring resonator, resonance occurs when the optical path length of the ring is an integer number of signal wavelengths. Mathematically, the resonant condition is given by (8.1), where R is the radius of the ring, λ_0 is the free space wavelength of resonant light, m is an integer indicating the resonator mode number, and n_{eff} is the effective index of the ring.

$$\lambda_o = n_{eff}\left(\frac{2\pi R}{m}\right) \tag{8.1}$$

At resonance, the circulating field inside the ring remains in phase with the in-coupled light and consequently the field constructively interferes and the intensity builds. As the amount of power in the

ring builds, the power coupled back to the bus waveguide from the ring increases. A phase shift of $\pi/2$ accompanies each coupling event, as a result of crossing from a low index material to a high index material, and thus the light, which is coupled to and from the ring (two coupling events), is π out of phase with the original bus signal. Consequently, the two signals – the original bus signal, and the signal coupled from the ring, deconstructively interfere. If the coupling rate is properly matched to the damping rate of the resonator, by optimally choosing the distance between the ring and bus, the two signals can be annihilated at the bus waveguide output ($s_t = 0$). Off-resonance, the field inside the ring does not constructively build and the effect of the ring is negligible ($s_t = s_i$).

8.1.2 The Quality Factor - Q

The quality factor Q represents a figure of merit for a resonator and is defined as the maximum energy stored per cycle divided by the dissipated energy per cycle. For a resonator with resonant frequency $\omega_0 = 2\pi c/\lambda_0$, Q is defined as:

$$Q \equiv \frac{\omega_0 \tau}{2} \approx \frac{\lambda_0}{\Delta\lambda} \tag{8.2}$$

where τ is the characteristic time constant of the resonator and $1/\tau$ is the damping rate of the field in the resonator. The Q can also be approximated with the spectral response of the resonator by taking the ratio of the resonant wavelength and the spectral full-width-half-maximum (FWHM) of the resonance $\Delta\lambda$. High Q resonators are efficient energy storage devices which naturally correspond to long τ and sharp spectral responses.

For ring resonators, the quality factor is proportional to the equivalent number of circuits (N) that the waveguide mode sustains before it is dissipated. Here N is estimated by dividing L_{eff}, the effective distance that the waveguide mode travels in the ring, by the circumference of the ring $2\pi R$.

$$N = \frac{L_{eff}}{2\pi R} = \frac{v_g \tau}{2\pi R} = \frac{v_g}{2\pi R}\frac{2Q}{\omega_0} = \frac{Q v_g}{\pi \omega_0 R} \tag{8.3}$$

For compact HIC ring resonators operating in the telecom spectrum, $v_g/\pi\omega R$ is between 10^{-2} and 10^{0}, and thus N is less than or equal to the Q.

8.1.3 Coupled Mode Theory (in Time) of a Ring Resonator and a Single Bus Waveguide

Ring resonators with a single bus waveguide (Figure 8.1 right) are ideal candidates for modulator, amplifier, and laser devices where it is optimal to critically couple light such that the transmitted power of

the bus waveguide is zero. In this section, the device physics of a ring and bus waveguide are derived with coupled mode theory in time, as opposed to space, as was done in section 4.6 for two straight waveguide.

Let us start by assuming that there is only optical power in the ring (i.e. s_i=0). By time reversal symmetry, we know that the power transferred from the bus to the ring is the same as from the ring to the bus and can be conveniently define as:

$$|s_{coupled}|^2 = \chi^2 |A(t)|^2 \tag{8.4}$$

where $|s_{coupled}|^2$ represents the power transmitted coupled to the bus waveguide, $|A(t)|^2$ represents the total power flowing through any cross section of the ring waveguide at time t, and χ^2 represents the normalized fraction of power transferred between the two. This compares to the total power stored in the ring $|a(t)|^2$.

$$|a(t)|^2 = \frac{2\pi R}{v_g}|A(t)|^2 \tag{8.5}$$

Where R is the radius of the ring and v_g is the group velocity of the light in the ring. From (8.4) and (8.5) we obtain the relation between the coupled power in the bus waveguide as a function of the total power in the ring.

$$|s_{coupled}|^2 = \chi^2 \frac{v_g}{2\pi R}|a(t)|^2 \tag{8.6}$$

Utilizing coupled mode theory [104], one can find the relation between the fields of the incoming and transmitted waves is:

$$s_t = s_i - i\,\kappa\, a(t) \tag{8.7}$$

where $|s_i|^2$ and $|s_t|^2$ represent the power in the bus waveguide before and after the ring, and κ is the mutual coupling coefficient between the ring and the bus waveguide and has units of per time. However, if we again set s_i=0 and thus $|s_t|^2=|s_{coupled}|^2$, one obtains a relation for κ when compared to (8.6).

$$\kappa^2 = \chi^2 \frac{v_g}{2\pi R} \tag{8.8}$$

For resonators, the coupling rate κ is inversely related to a given resonators escape time constant τ_e [23] – what can be viewed as the 1/e time it takes to discharge power from the ring.

$$\kappa^2 = \frac{2}{\tau_e} \tag{8.9}$$

Therefore, if we combine (8.8) and (8.9) we find the relation:

$$\tau_e = \frac{4\pi R}{\chi^2 v_g} \tag{8.10}$$

Expression (8.10) gives a relation for determining τ_e the time constant associated with evanescently coupling between the ring and bus. Quite similar to the directional coupler described in section 4.6.3, the extent of evanescent coupling between the bus and the ring is a function of the ring-bus separation and the relative confinement of the modes in each waveguide. As one might intuitively guess, the total power coupled χ^2 is inversely proportional to the escape time constant τ_e and directly proportional to the evanescent coupling rate $1/\tau_e$.

If the ring resonator were lossless, evanescent coupling from the ring to the bus would be the limiting energy dissipation (damping) mechanism resulting in a resonant decay rate of $1/\tau_e$. However, in practice there exist many damping mechanisms, typically in the form of waveguide losses, which affect the power and time dependent behavior of the ring resonator. Let us assume that the roughness scattering, absorption, substrate leakage, bend loss, and all other losses in the ring (α_i) can be lumped together as a single loss α, which further dissipates energy in the resonator at a rate of $1/\tau_l$. The loss time constant (τ_l) and loss (α) are linked by the group velocity of the signal:

$$\tau_l = \frac{1}{v_g}\left(\sum_i \alpha_i\right)^{-1} = \frac{1}{\alpha v_g} \tag{8.11}$$

Then, the overall decay rate $1/\tau$ for a ring resonator with a single bus waveguide is given by the sum of all damping rates:

$$\frac{1}{\tau} = \sum \frac{1}{\tau} = \frac{1}{\tau_l} + \frac{1}{\tau_e} \tag{8.12}$$

Similarly, if we multiply by $2/\omega_0$, we find a similar relationship with quality factors for the respective damping rates:

$$\frac{1}{Q}=\sum\frac{1}{Q}=\frac{1}{Q_l}+\frac{1}{Q_e} \tag{8.13}$$

Thus we can see that each damping term has a related quality factor that contributes to the overall Q of the resonator. Hence the quality factor of a resonator is dominated by the lowest Q process, which corresponds to the fastest damping mechanism and highest loss process.

Now, if we return to modeling the ring as a resonator, the total power stored in the ring $|a(t)|^2$ should obey relation (8.14) where ω_0 is the resonant frequency of the ring and all other variables are held.

$$\frac{d}{dt}a(t)=\left(j\omega_0-\frac{1}{\tau}\right)a(t)-i\kappa s_i \tag{8.14}$$

Assuming that the stored power a(t) is of the form $a(t)=a_0\, e^{i\omega t}$, where ω is the angular frequency of light, one can show that:

$$a(t)=\frac{-i\sqrt{\frac{2}{\tau_e}}}{i(\omega-\omega_0)+\frac{1}{\tau_e}+\frac{1}{\tau_l}}s_i \tag{8.15}$$

Combining (8.7), (8.14), and (8.15) we find the relation between the input $|s_i|^2$ and output $|s_t|^2$ power of the bus waveguide:

$$|s_t|^2=\frac{(\omega-\omega_0)^2+\left(\frac{1}{\tau_e}-\frac{1}{\tau_L}\right)^2}{(\omega-\omega_0)^2+\left(\frac{1}{\tau_e}+\frac{1}{\tau_L}\right)^2}|s_i|^2 \tag{8.16}$$

The spectral response for the single waveguide ring structure is depicted in Figure 8.2 where the normalized output power versus wavelength (rather than frequency since wavelength is what is typically measured) is plotted from relation (8.16). The functional form of the spectral response is lorentzian, where the dip minimum corresponds to the resonant wavelength, which is related to the resonant frequency by $\lambda_0 = 2\pi c/\omega_0$.

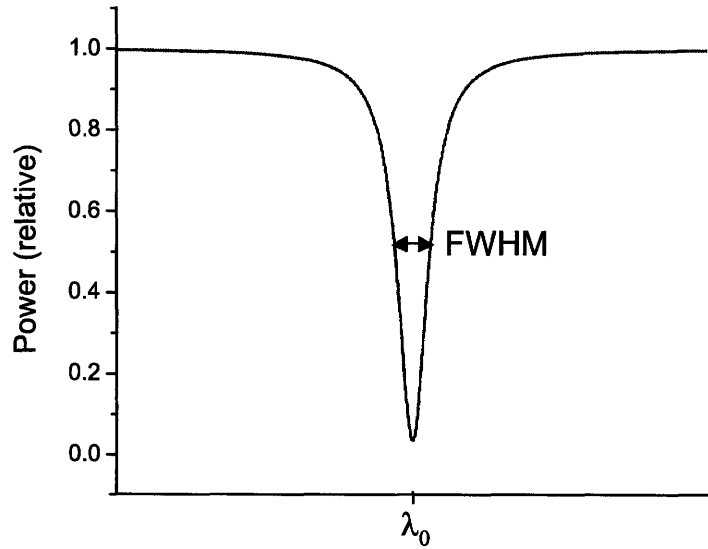

Figure 8.2 – Plot of the spectral response for a single waveguide ring resonator device

At the resonant condition ($\omega = \omega_0$, $\lambda = \lambda_0$), we find the depth of the resonance:

$$|s_t|^2 = \left(\frac{\frac{1}{\tau_l} - \frac{1}{\tau_e}}{\frac{1}{\tau_e} + \frac{1}{\tau_l}} \right)^2 |s_i|^2 \tag{8.17}$$

Thus for the case where coupling and damping rates are equivalent ($1/\tau_l = 1/\tau_e$), the transmitted power in the bus waveguide is canceled ($|s_t|^2 = 0$) due to the equal amplitude but opposite phase of the light coupled from the resonating ring combining with the existing bus signal. In a similar fashion, the Q of the ring resonator:

$$Q = \omega_0 \frac{|a|^2}{|s_t|^2} = \frac{\frac{2}{\tau_e}}{\left(\frac{1}{\tau_e} - \frac{1}{\tau_l} \right)^2} \tag{8.18}$$

is also maximized for the critical coupling condition ($1/\tau_l = 1/\tau_e$).

In terms of more physical variables, the critical coupling condition links the coupling rate with the transmission loss in the ring by a factor of $4\pi R$:

$$\chi^2 = 4\pi R\alpha \tag{8.19}$$

For integrated photonic circuits, the ring radius (R) is typically set to maximize device density by using the minimum radius that corresponds to a bend loss threshold (see section 4.9); this leaves two parameters with which to vary to facilitate a critically coupled ring resonator. The first parameter is the transmission loss of the ring (α) which can be tailored by material selection and processing methods (Chapters 5 and 6). The second parameter is the coupling coefficient (χ^2) which is a function of the ring-bus gap, as will be discussed in the following subsection.

8.1.4 Evaluating the Coupling Coefficient

As opposed to directional couplers, where power is transferred between two waveguides separated by a uniform gap (section 4.6), the spacing between the ring and the bus waveguides continuously changes (as seen in Figure 8.3), leading to a small effective interaction length where a majority of the evanescent coupling occurs at the gap minimum (δ_0). The exponential decay of the evanescent field accentuates this effect as the coupling rate $\kappa(z)$ is a manifestation of the waveguide field distribution Φ, resulting in an exponential dependence on the gap size $\delta(z)$. Since only a small portion of the ring around δ_0 is relevant, a circular ring can be well approximated as parabolic curve near δ_0:

$$\delta(z) \approx \delta_0 + \frac{z^2}{2R} \tag{8.20}$$

Thus the instantaneous coupling in time, very similar to relation (4.38), at any one point is given by:

$$\kappa\left[x = \delta(z)\right] = \frac{\varepsilon_0 \omega}{4} \int_{wg,bus} \left(n_{core,bus}^2 - n_{clad}^2\right) \Phi_{bus}^*\left[x\right] \Phi_{ring}\left[x\right] dx \tag{8.21}$$

where we assume that the coupling rate between the ring and bus is symmetric ($\kappa=\kappa_{12}=\kappa_{21}$). The total coupling for the ring is given by:

$$\chi^2 = \left| \int_{-\infty}^{\infty} \kappa\left[x = s(z)\right] e^{-i\Delta\beta z} dz \right|^2 \tag{8.22}$$

where the $e^{-i\Delta\beta z}$ term accounts for the phase mismatch between the waveguide modes as the light alters its propagation direction around the ring and further decreases the coupling interaction region between the waveguide and ring. Typically, the cross-sections of the ring resonator waveguide and the bus waveguide

are designed to support waveguide modes with equivalent propagation constants, to optimize the coupling at δ_0. For HIC waveguides the typical total coupling is of the range $0.001 < \chi^2 < 0.1$.

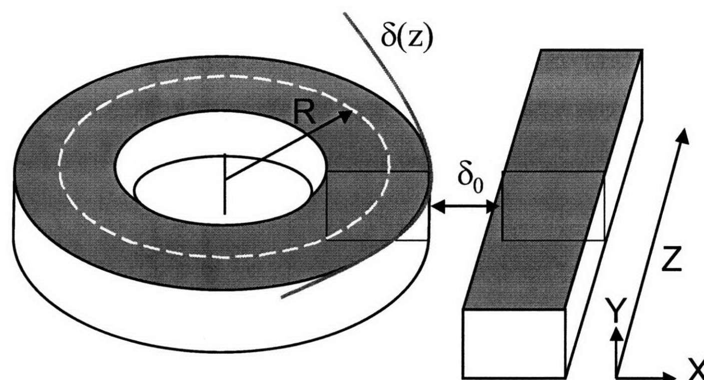

Figure 8.3 – Schematic of ring resonator and bus waveguide layout with minimum gap size δ_0 and gap approximation $\delta(z)$ indicated.

8.1.5 Coupling Regimes

At steady-state, the balance between the coupling and damping rates of a ring resonator at the resonant wavelength can be classified in three ways: over coupled – where the coupling rate exceeds the damping rate, critically coupled – where the coupling rate equals the damping rate, and under coupled – where the coupling rate is less than the damping rate. For the case of weak coupling ($\kappa \ll \beta$) as assumed here, the amplitude of the inserted light (s_i) is relatively unchanged as a result of coupling *to the ring*. Rather, it is the effect of light coupling *from the ring* to the bus that affects the output amplitude and phase of the transmitted light (s_t).

Over Coupled – $1/\tau_e > 1/\tau_l$

An over coupled ring resonator occurs when the coupling rate between the bus and the ring exceeds the damping rate of the ring resonator. From a design perspective, this occurs when the spacing between the ring and bus waveguides is small, resulting in an increased spatial overlap of the modes and an increased coupling rate. Alternatively, over coupled behavior may occur if the damping mechanisms, which are typically waveguide losses, are reduced for a given bus-ring gap; this may occur by improved processing.

As a consequence of over coupling, the amplitude of the light coupled from the ring back to the bus waveguide exceeds the input amplitude ($|s_{coupled}| > |s_i|$). Since the phase of the out coupled light is π out of phase with the input signal, the output amplitude (s_t) will be π out of phase as well ($-1 < s_t / s_i < 0$). Figure 8.4 depicts the behavior of an over coupled resonator, where the output power $|s_t|^2$ is depicted as

the difference between the out coupled power $|s_{coupled}|^2$ and the input power $|s_i|^2$; the dashed and solid lines have opposite phase.

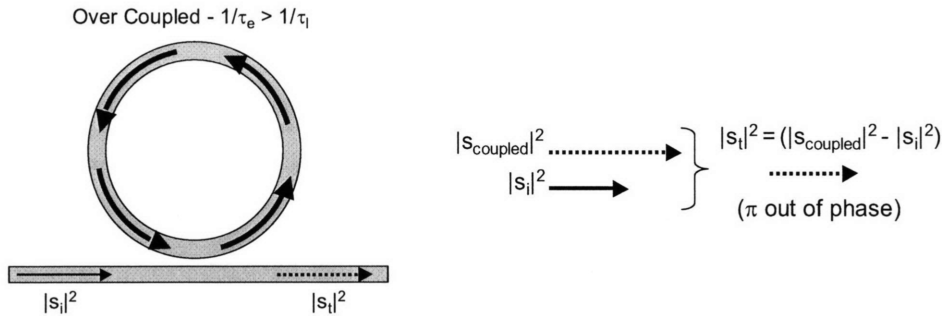

Figure 8.4 – Schematic of an over coupled ring resonator.

Critically Coupled – $1/\tau_e = 1/\tau_l$

A critically coupled ring resonator exists when the coupling rate between the bus and the ring resonator is equivalent to the damping rate of the ring resonator. The amplitude of light coupled from the ring is equivalent to the input amplitude ($|s_{coupled}| = |s_i|$), resulting in absolute destructive interference at the bus waveguide output ($|s_t|^2 = 0$). Figure 8.5 depicts the behavior of a critically coupled resonator; the dashed and solid lines have opposite phase. From a design perspective, knowledge of the losses in the system is critical in defining the proper ring-bus gap to balance the coupling and damping rates. Processing errors that result in a difference in an altered resonator loss affect this balance and modify the coupling regime.

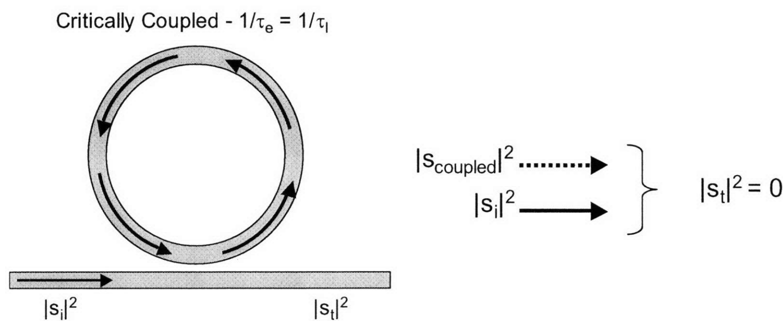

Figure 8.5 – Schematic of a critically coupled ring resonator.

Under Coupled – $1/\tau_e < 1/\tau_l$

An under coupled ring resonator occurs when the coupling rate between the bus and the ring is less than the damping rate of the ring resonator. From a design perspective, this occurs when the spacing between the ring and bus waveguides is large, resulting in a decreased spatial overlap of the modes and a

decreased coupling rate. Under coupled behavior may also occur if the damping mechanisms (waveguide losses) in the ring resonator are larger than expected; as may happen with processing errors.

The amplitude of light coupled from the ring to the bus waveguide is less than the input amplitude ($|s_{coupled}| < |s_i|$) in an under coupled ring resonator. The transmitted light is therefore still in phase ($0 < s_t / s_i < 1$) with the input signal, but reduced by the amplitude of the coupled light from the ring. The ultimate limit of under coupled behavior is when the loss or ring-bus gap approaches infinity; in these cases the ring is effectively absent, similar to off-resonance behavior. Figure 8.6 depicts the behavior of an under coupled resonator, where the output power $|s_t|^2$ is the difference between the input power $|s_i|^2$ and the coupled power $|s_{coupled}|^2$, the dashed and solid lines have opposite phase.

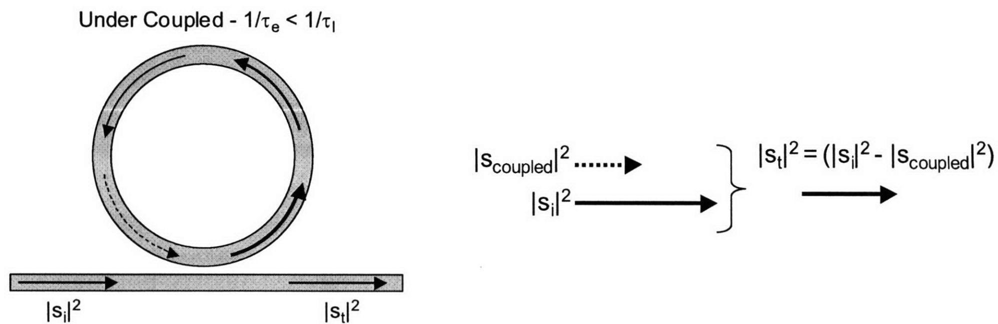

Figure 8.6 – Schematic of an under coupled ring resonator.

8.2 Ring Resonator Trimming

Like all resonant devices, ring resonators are incredibly sensitive to variations that affect the optical path length of the resonant cavity. This is particularly true for highly confined, HIC waveguide ring resonator devices where precise control over the resonant wavelength (λ_0) is critical for integrated photonic circuits. As ring resonator radii shrink to meet high density, HIC, photonic circuit applications, non-deterministic pattern transfer errors limit dimensional precision and preclude the fabrication of identical devices across an entire wafer. Even small deviations in film thickness, index of refraction, and etch processes across a wafer, lead to variation in the effective index and ring radius that shift λ_0 by several nanometers. Hence, a post-production trimming process to modify the effective index (n_{eff}) of the ring to precisely define λ_0 is essential. In this section, a photo-oxidation trimming method using a polysilane top cladding on SiN ring resonators and waveguides is explored. Photo-oxidation of polysilane clad waveguides presents a precise, localized, and controllable technique for specifying the resonance condition of ring resonators.

8.2.1 Thermal Trimming

For resonators, the term "trimming" refers to the act of altering the optical path by modifying the index of a material. For integrated photonic circuits, the most common method of trimming utilizes the thermo-optic response of the waveguide materials (dn/dT). The shift in index of a material (Δn) is given by:

$$\Delta n = \Omega \, \Delta T \tag{8.23}$$

where Ω is the thermo-optic coefficient and ΔT is the change in temperature. Although only small adjustments to the optical path length are needed to change the resonance condition of a ring resonator, the small magnitude of these thermo-optic coefficients limits the trimming range. Figure 8.7 lists thermo-optic coefficients for some common waveguide materials. As a comparison, the right most column lists the equivalent temperature needed to shift the resonant wavelength 25 nm in the telecom spectrum, for a ring resonator of each material with R=100 μm.

Material	Ω - Thermo-Optic Coefficient (K^{-1})	ΔT (K) for 25nm of Trimming
Silicon	4×10^{-4}	150
SiO_2, SiON, Si_3N_4	~ 10^{-5} K	> 1000
Polymers	-1×10^{-4} to -4×10^{-4}	100 - 350

Figure 8.7 – Thermal-optic coefficients for select waveguide materials

Thermal trimming typically employs resistive micro heaters complete with feedback control that are integrated on an adjacent wafer level for each ring resonator [108-109]. This architecture adds several steps to the fabrication of a photonic circuit, limits the density of devices to maintain thermal isolation, and requires significant power consumption to keep the rings "trimmed". For many applications, such as Si_3N_4 waveguide devices which have very small thermo-optic coefficients and thus a curtailed thermal trimming range, an alternative trimming method is desirable.

8.2.2 Photo-Oxidation Trimming Using a Polysilane Cladding

An alternative trimming method, and the focus of the this study, uses a UV-sensitive organosilicon polymer film as the waveguide cladding material. Organosilicon polymers, or polysilanes, are essentially polymers with a silicon or mixed silicon and carbon polymer backbone. The refractive index of this material is altered via photo-oxidation where Si-Si bonds are oxidized to form Si-O-Si bonds when irradiated with ultraviolet light, see Figure 8.10. Polysilanes have a refractive index similar to SiO_2, the predominant material of choice for cladding layers in CMOS compatible waveguides, and can be easily integrated with Si, SiON, and Si_3N_4 high index-contrast microring resonators. The material is transmissive over a broad range of visible and near-IR light [111-112] useful for microphotonic applications [113].

Photo-oxidation trimming was first demonstrated using a dip-coating technique to coat ring resonators with a polysilane material [110]. However, polymers deposited from solution using dip coating or spin coating can be redissolved making the film incompatible with subsequent microfabrication processing steps that involve rinsing. The low degree of crosslinking in soluble organosilicon polymers also makes them prone to swelling when irradiated or contacted with chemical solvents. Furthermore, for the case of thin cladding layers, the resulting change in thickness can inadvertently change the resonant condition of a microring device.

In this study, a plasma enhanced chemical vapor deposition (PECVD) process was used to deposit polymerized 6M2S directly onto ring resonators, yielding an amorphous and highly cross-linked top cladding layer. PECVD 6M2S is insoluble, does not swell in organic solvents, and demonstrates good stability in ambient light, atmosphere, and temperature. Photo-oxidation trimming was tested on single-mode Si_3N_4 ring resonators with PECVD 6M2S top cladding and resulting resonance shifts were compared to a theoretical model.

8.2.3 Experimental Procedure

Si_3N_4 waveguides, designed for single mode operation at λ = 1550 nm, were fabricated from a 0.4 μm Si_3N_4 film deposited (n=2.2), in the vertical tube reactor (VTR) at MTL, on a 3 μm thermal oxide under-cladding layer on a (100) Si wafer. The Si_3N_4 was patterned using a polysilicon hard mask and 365-nm photolithography. The microrings have a diameter of 100 μm and the Si_3N_4 waveguides have cross-sectional dimensions of 400 x 750 nm^2.

After a 30 minute cleaning with an oxygen plasma etch, a hexamethalsilane precursor (6M2S) top cladding layer was deposited directly onto the ring resonator devices using a PECVD process [114]. The 6M2S precursor was obtained from Gelest. A deposition time of 30 minutes achieved films that were approximately 1 μm thick. A schematic of the PECVD deposition equipment, typical deposition parameters and resulting polysilane film are depicted in Figure 8.8.

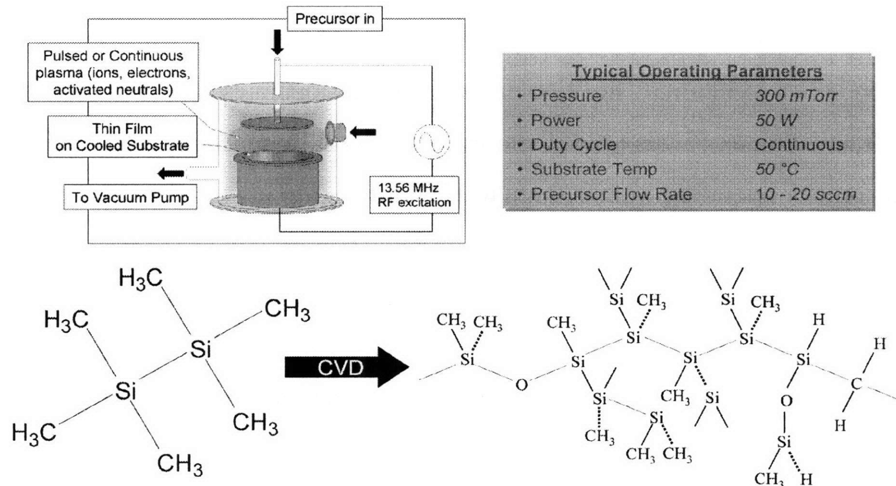

Figure 8.8 – PECVD deposition of 6M2S forms cross-linked polysilane films

Once coated with the organosilane film, spectral characterization of the micro rings was done at the through port in both TE and TM polarizations by a C+L band, JDS Uniphase swept wavelength system (tunable laser and broadband photodetector) used in conjunction with a Newport Auto-Align System (see Section 3.6). A MINERALIGHT® handheld lamp (model UVGL-25) emitting λ=254 nm UV light was used to irradiate samples with a flux of 1.7 $\mu W/cm^2$.

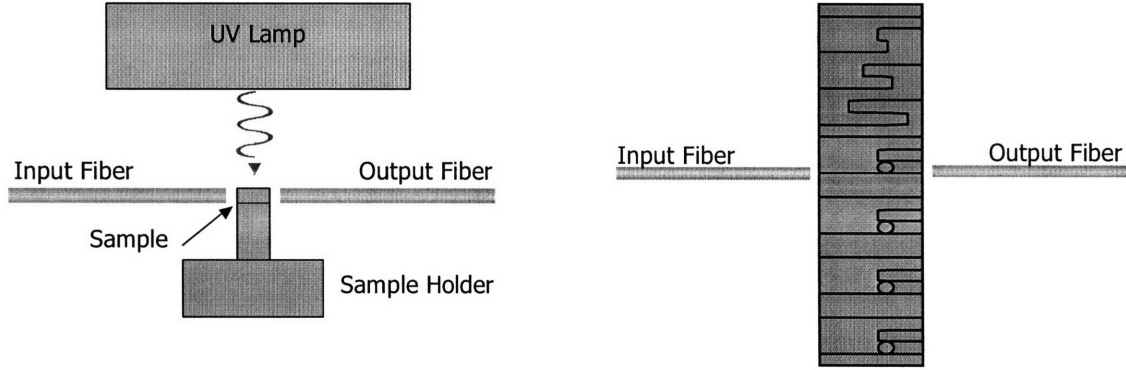

Figure 8.9 – Optical Characterization Setup – side view (left), top view (right).

The same UV irradiation process was repeated on a sample from the same wafer and the refractive index of the 6M2S film was measured after each exposure using a Woolam M-2000 variable angle spectroscopic ellipsometer (VASE). Data was acquired at three angles (65°, 70°, and 75°) and fit to the Cauchy-Urbach model [115] yielding the film thickness and Cauchy constants for the calculation of the film refractive index at 1550 nm. The Woolam ellipsometer operates between 450 nm and 720 nm, but extrapolated refractive index values at 1550 nm were validated by repeating a few measurements with a Sopra GES5 ellipsometer operating from 800 nm to 1750 nm.

8.2.4 Modeling the Resonance Shift

Assuming single mode operation throughout, the predicted resonance shift ($\Delta\lambda$) of the resonance λ_0 after trimming (subscript 2) from the initial state (subscript 1), can be derived from relation (8.1):

$$\Delta\lambda = \lambda_{0,2} - \lambda_{0,1} = n_{eff,2}\left(\frac{2\pi R}{m_2}\right) - n_{eff,1}\left(\frac{2\pi R}{m_1}\right) \tag{8.24}$$

Since the resonant wavelength shift is continuous and small compared to λ_0, the mode number remains fixed.

$$m_1 = m_2 = \frac{n_{eff,1} 2\pi R}{\lambda_{0,1}} = \frac{n_{eff,2} 2\pi R}{\lambda_{0,2}} \tag{8.25}$$

Combining relations (8.24) and (8.25) we find the relation for the resonance shift as a function of the effective index shift (Δn_{eff}):

$$\Delta\lambda = \lambda_{0,1}\left(\frac{n_{eff,2}}{n_{eff,1}} - 1\right) = \frac{\lambda_{0,1}}{n_{eff,1}}\Delta n_{eff} \tag{8.26}$$

Interestingly, Δλ is independent of ring diameter and only dependent on the initial resonant wavelength as well as the initial and final effective indices.

8.2.5 UV-induced index change in PECVD Polysilane

Figure 8.10 shows the controllable decrease in the refractive index of the 6M2S polysilane cladding layer achieved using photo-oxidation induced by UV irradiation. The overall decrease is ~ 4%, from 1.52 to 1.46 at λ=1550 nm. UV light having a wavelength less than about 300 nm causes chain scission in organosilicon polymeric materials and subsequent oxidation converts Si-Si bonds into Si-O-Si bonds [116] (Figure 8.9 insert). The exponential decay in index with UV exposure is a reflection of the Si-Si bond depletion. Incorporation of oxygen reduces the molecular density of the material and causes the refractive index to decrease. The overall index change is about 50% greater than the response observed with dip-coated polysilane material used in an earlier study.

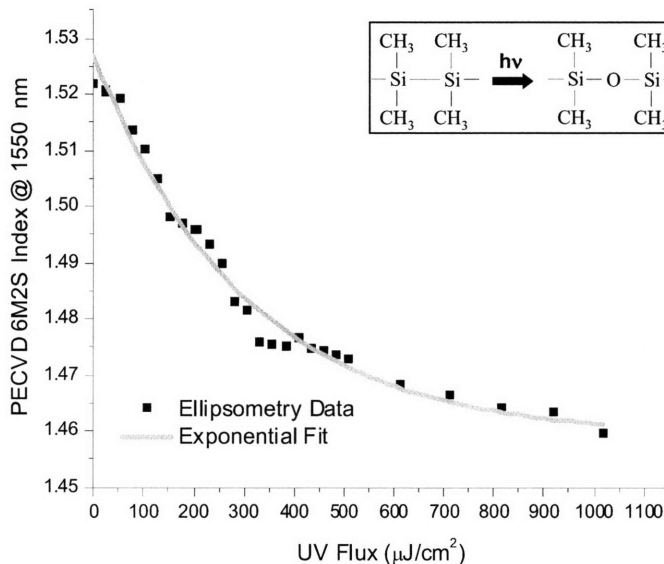

Figure 8.10 – The refractive index of PECVD 6M2S cladding material decreases with UV irradiation as a result of photo-oxidation.

8.2.6 Optical Characterization

Figure 8.11 shows typical spectral responses for a ring resonator with two waveguides. The two curves correspond to output measurements at the through and drop ports. Each dip in the through port power,

and thus peak in the drop port power, corresponds to the resonance condition of the ring. The free spectral range (FSR) – the spacing between resonant wavelengths – is 4.5 and 3.9 nm for the TM and TE polarizations respectively.

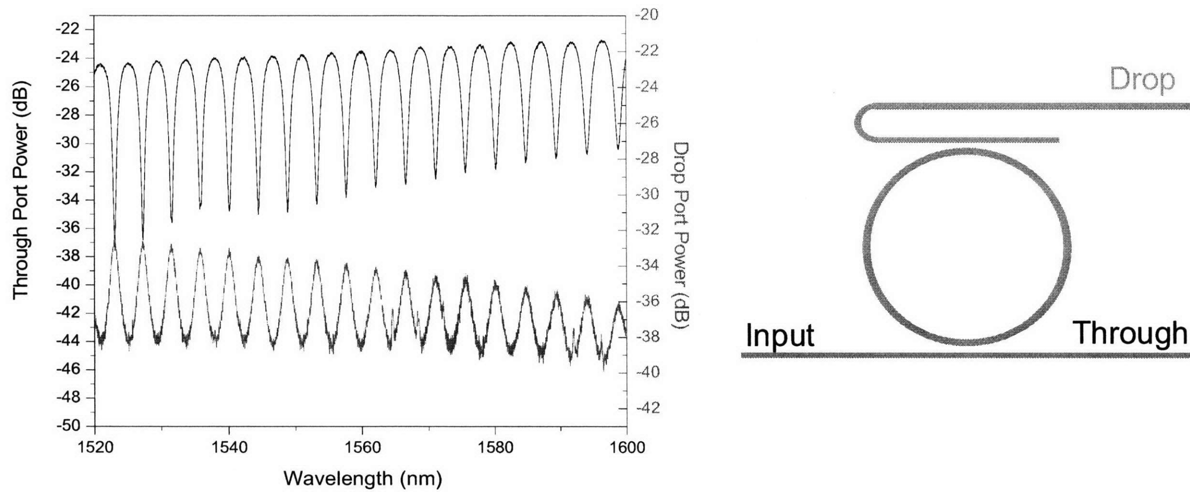

Figure 8.11 – TM spectral response for an untrimmed ring (left) and corresponding ring resonator (R=50 μm) device layout (right)

Output power from the rings was monitored *in situ* during UV trimming. In fact, a probe signal was observed to oscillate in response to the shifting through the resonance during UV exposure. The resonant wavelengths were observed to shift continuously with irradiation of the 6M2S cladding. Figure 8.12 displays the spectral responses for two specific exposure times where minima occur at the resonant wavelengths. The magnitude of the shift exceeded the free spectral range for these ring resonators. The overall resonance shifts, after a UV flux of 1000 μJ/cm^2, were 12.8 nm for the TE mode and 23.5 nm for the TM mode (Figure 8.13). Resonance shifts were not observed for UV-irradiated Si_3N_4 microrings without a PECVD 6M2S top cladding.

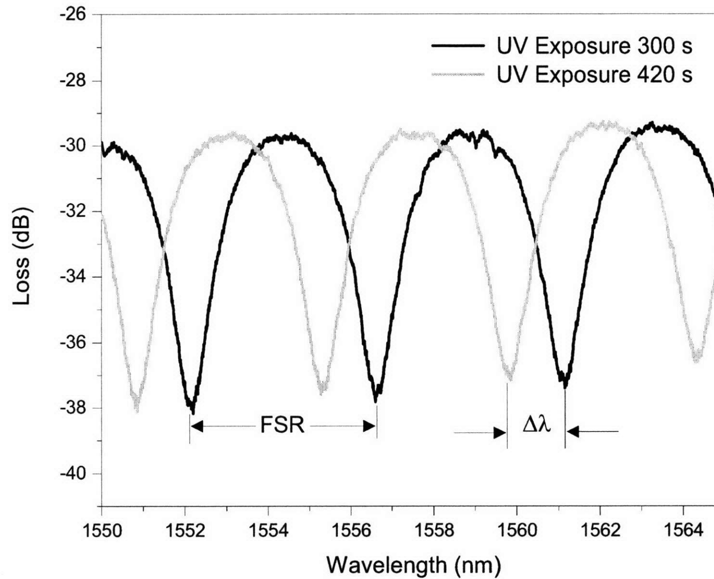

Figure 8.12 – TM spectral response ($\lambda_{0,1}$=1564.5 nm) after 300 and 420 seconds of UV irradiation at 1.7 μW/cm^2 .

8.2.7 Discussion of Trimming Results

To compare experiment with theory, a simulation of the trimming response was created using the relation found in relation (8.26) and the exposure curve data in Figure 8.10. Apollo Mode Solver software was used to correlate the effective index of the ring resonator as the polysilane cladding material was exposed to UV light for each polarization. The simulated resonance shifts (Figure 8.13) agree fairly well with the experimental data in terms of functional form and magnitude for both polarizations. Similar to the ellipsometry data, the experimental resonant shift results exhibited an exponential decay, reflecting the extent of oxidation, with UV exposure.

The larger resonance shift in the TM mode, as compared to the TE mode, is a direct result of the field distribution of the modes in the 400x750 nm^2 waveguide geometry. As a reminder, the effective index is approximatly the weighted average of the core and cladding material indices with respect to the mode distribution. The less confined TM mode has a greater percentage of power in the polysilane cladding and therefore is more sensitive to changes in the cladding index, resulting in a larger resonant shift. The magnitude of the shift is therefore proportional to 1-Γ, where Γ is the fraction of power in the waveguide core.

Deviations between experimental and simulated data are likely caused by uncertainties in the cladding thickness, which can lead to errors in the refractive index values reported by ellipsometry used in the simulation. Although swelling of plasma polymerized 6M2S with oxidation is very minor due to crosslinking, the thickness of the top cladding layer varies by about 1% from the beginning to the end of the trimming process. Additionally, deposition uniformity of the 6M2S thickness can vary by another 1

or 2% from sample to sample. The larger deviation of the TM mode simulation from experiment, when compared to the TE mode, is most likely caused by these thickness variations. The effective index of the TE mode is primarily sensitive to in-plane variations of the core/cladding thickness and or index. Analogously, the effective index of the TM mode is sensitive to variations out of plane (cladding thickness), especially for the thin (relative to the evanescent tail length of the mode) top cladding layer used in this experiment, resulting in an uncertainty in the modeling.

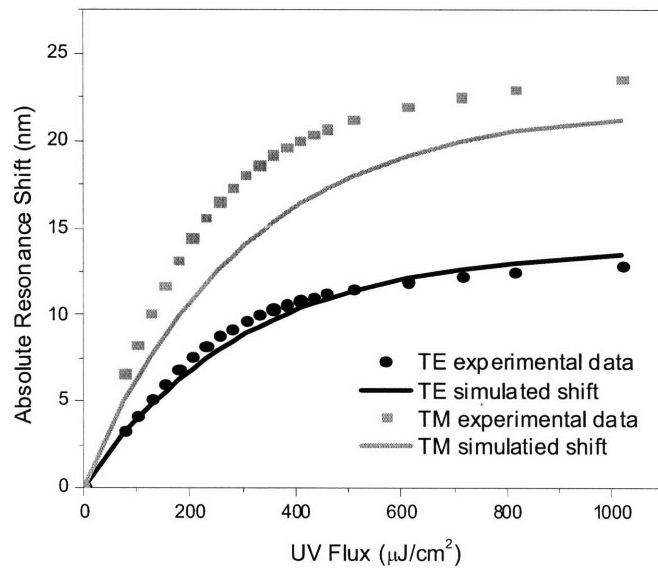

Figure 8.13: The experimental resonance shifts for TE and TM polarizations are compared with modeled results.

Photo-oxidation trimming of plasma-polymerized 6M2S is an irreversible process due to the nature of the reaction. Hence, the term trimming is used in this work rather than tuning – which is a reversible process. However, the photo-oxidation trimming allows for some error. For ring resonators that have small FSRs compared to the maximum desired resonant wavelength shift, as was the case with the rings used in this experiment, overexposing a ring can be remedied by simply using more UV light and shifting the resonance one more FSR length.

The rate of the resonance wavelength shift, ($d(\Delta\lambda)/dt$), is an indicator of the shift resolution. This value ranged from about 0.13 nm/s during the initial steep portion of the exponential curve to as low as 0.01 nm/s in the shallow region. A lower power UV source can reduce this shift rate and presumably increase the precision if needed.

Another benefit of photo-oxidation trimming is the ability to focus UV light and thereby localize trimming to specified areas of a chip. This enables one to preserve the spectral response of higher order

filters that require multiple rings. Differences between ring-to-ring and ring-to-bus coupling require localized index trimming on separate areas of the filter to keep all rings in resonance with each other.

Spectral responses of the trimmed ring resonators were also measured over a range of temperatures from 25 to 70°C (Figure 8.14). The thermo-optic coefficient (Ω) for the device was found to be -1.3×10^{-4} K^{-1} for the TM mode. This value is on par with other polymer based ring resonator devices [108] and an order of magnitude greater than SiO_2 clad Si_3N_4 ring resonators – enhancing the potential thermal trimming/tuning range. Thermal hysteresis effects were not detected over this temperature range. Many polymers used as waveguide cladding materials undergo densification over a span of weeks or months causing drifts in the refractive index on the order of 10^{-4} [116] corresponding to a $\Delta\lambda$ of ~0.1 nm. Although this effect has not yet been quantified for PECVD 6M2S, long-term variances in λ_0 could be counteracted with a global heater, assuming uniform aging of the locally trimmed film.

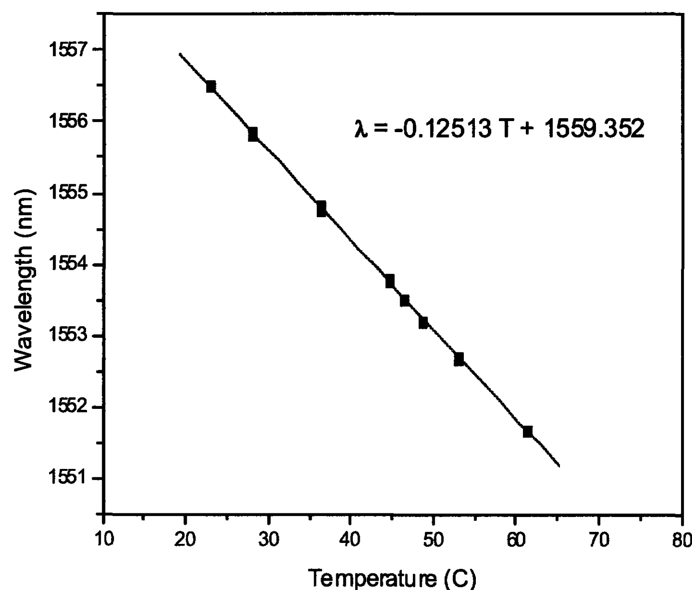

Figure 8.14 – Thermal tuning of the polysilane material.

Trimming microring resonators with UV irradiation of a photosensitive top cladding material provides a less complicated alternative to thermal trimming techniques that require individually controlled microheaters. PECVD 6M2S is a highly crosslinked and insoluble polymeric material with a refractive index that can decrease through photo-oxidation by nearly 4%. This index change allows for resonance shifts as large as $\Delta\lambda$ = 23.5 nm with Si_3N_4 rings. Such a large response is an order of magnitude greater than can be realized with thermal trimming of Si_3N_4 ring resonators and is estimated to be 50% more than what has been shown using a dip-coated polysilane cladding layer. As a quick, localized, and controllable

technique to produce large and precise resonance shifts, photo-oxidation trimming of PECVD polysilane clad waveguides provides an attractive alternative to conventional trimming techniques.

8.3 Ring Resonator Modulators

The sensitivity of ring resonators to variations in cavity length also make them well suited for modulator applications. By utilizing the single waveguide configuration (see Figure 8.1) and a mechanism that varies the index of the core or cladding (similar to ring trimming, but faster and reversible), a ring resonator can act as a modulator device. For integration with electronic circuits ring resonator modulators ideally utilize electro-optic effects to adjust the resonant wavelength (λ_0) such that the signal wavelength of interest moves in and out of resonance. Recently, a GHz-speed silicon ring modulator was demonstrated using free-carrier modification of the silicon index – first by inciting carriers via the two photon absorption effect (see Section 4.5) with short pulses of light [107], and second by building a lateral p-i-n junction for carrier injection and carrier sweep-out [117]. Unlike Intel's Mach-Zehnder modulator [118], the only other GHz-speed CMOS compatible modulator, the ring modulator is ideally suited for integrated photonic applications - negligible insertion loss, high confinement HIC waveguides, small area footprint, high speed, and low power. In this section, the operating physics of a ring modulator are explored from which design principles and material criteria are derived for optimal modulator performance. The validity of these design principles are applied to the feasibility of a SiGe ring modulator.

8.3.1 Ring Modulator Operation

Modulators are essentially optical shutters that have two states: ON - when light passes through and OFF – when light does not pass through. For a ring modulator, the on-state occurs when the signal wavelength is non-resonant with the ring ($\lambda_s \neq \lambda_0$), while the off-state occurs when the signal is resonant with the ring ($\lambda_s = \lambda_0$). The beauty of ring modulators is that the signal negligibly interacts (due to weak coupling) with the "active" ring material in the on state, and thus the insertion loss is dominated by bus waveguide losses.

Figure 8.15 – Ring modulator On and Off States where λ_s is the signal wavelength and λ_0 is the resonant wavelength of the ring.

A modulator is evaluated by two criteria: 1) the modulation speed and 2) the extinction ratio. The modulation speed is dependent on the slower of either the resonator transient power build up time or the time associated with the modulation mechanism. The extinction ratio or the ratio of the off-state to on-state output is dependent on the modulation depth and resonance depth of the off-state. For a ring resonator, the modulation depth is dependent on the resonance line shape, line width, shift, and coupling regime. Hence, to optimize modulator design the parameters which govern modulator speed and depth must be understood.

8.3.2 Modulation Speed

The modulation speed or what can be viewed as the switching speed of a modulator is typically limited by the modulating mechanism, such as the time it takes to inject carriers for the Si ring modulator. However, the fundamental speed limitation of a modulator is optically limited, and governed by the transient response of the total power stored in the ring $|a(t)|^2$ to move in and out of steady-state. The transient response for building power in the ring is given by (8.27), where A_0 is the steady state power.

$$|a(t)|^2 = A_0\left(1-e^{-t/\tau_e}\right) \tag{8.27}$$

Similarly, the transient response for dissipating the power is given by relation (8.28).

$$|a(t)|^2 = A_0\, e^{-t/\tau_e} \tag{8.28}$$

Thus, the operating frequency of a ring modulator (f_{mod}) is proportional to the inverse of the escape time constant $1/\tau_e$. From relation (8.10), we know that the τ_e is inversely proportional to the total coupling χ^2 between the ring and the bus, which in turn, is proportional to the evanescent field overlap between the two guided modes. Interestingly, high Q ring modulators are not ideal as they have long resonant build up times.

Reducing the ring-bus gap (δ_0) is the most straight forward method of decreasing τ_e and therefore increasing the coupling, however lithographic limitations often preclude this option. Alternatively, the evanescent field overlap can be increased by 1) reducing the waveguide width in the neighborhood of the ring, thereby squeezing the mode out of the bus waveguide or 2) increase the interaction length of the bus and ring by wrapping the bus waveguide around the ring, both schematically drawn in figure 8.16. However, by increasing the evanescent field overlap, the weak wavelength dependence of the spectral

response at resonance decreases. In other words, both methods sacrifice the uniform spectral response, exhibited at each resonance condition, for increased coupling.

Figure 8.16 – Methods of increasing the coupling between the bus and ring – shrink the waveguide width to expand the mode in the vicinity of the ring (left) or wrap the waveguide around the ring (right).

The operating frequency of the ring modulator (f_{mod}) is proportional to $1/\tau_e$. As hinted earlier, and to be discussed, it is advantageous to have a critically coupled ring for modulator applications. For this case, the coupling rate is proportional to α, the aggregate loss of the resonator:

$$f_{\text{mod}} \propto \frac{1}{\tau_e} = \frac{1}{\tau_l} = v_g \alpha \tag{8.29}$$

8.3.3 Extinction Ratio

The extinction ratio and modulation depth of a ring modulator are dependent on 1) the depth of the resonance and 2) the magnitude of the resonance shift. This can be seen in Figure 8.17, where the spectral response for the on and off states are depicted with the resonant line width $\Delta\lambda^{LW}$ and wavelength shift of the resonance $\Delta\lambda^{shift}$. In this example, the signal wavelength is λ_s=1550 nm and the output power of the bus waveguide is modulated between 0.65 and 0.05 normalized power as λ_0 is modulated between 1549 and 1550 nm. The spectral response of the shifted on-state is slightly different from the off-state, as a consequence of Kramer-Kroenig relations, reflecting the change in loss $\Delta\alpha$ that accompanies an index change Δn. Adding loss to the ring increases the line width and decreases the depth of the spectral response.

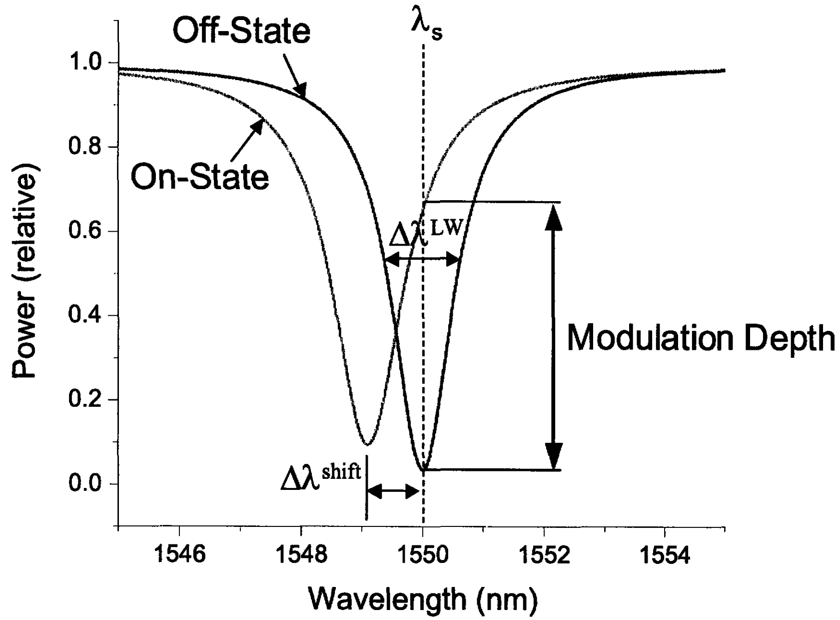

Figure 8.17 – Spectral Response of the Ring Modulator ON and OFF states.

The modulation depth, the difference between the resonance depth in the off-state and the shifted response in the on-state, is optimized when the resonance shift is maximized and the spectral line width is minimized. For the sharp lorentzian spectral response of a ring resonator, the normalized modulation depth approaches unity when $\Delta\lambda_{shift} \geq \Delta\lambda^{LW}$. For this case, the extinction ratio is > 10 dB. Hence, the following figure of merit (FOM) is devised for ring modulators:

$$FOM = \frac{\text{Resonance shift}}{\text{Line width}} = \frac{\Delta\lambda_{shift}}{\Delta\lambda^{LW}} \geq 1 \tag{8.30}$$

Similar to ring trimming, the resonant wavelength shifts due to an effective index change Δn_{eff} of the ring waveguide. Therefore, the magnitude of the resonance shift is identical to that found with the trimming work in (8.26):

$$\Delta\lambda^{shift} = \frac{\lambda_{0,1}}{n_{eff,1}}\Delta n_{eff} \approx \frac{\lambda_{0,1}\Gamma}{n_{eff,1}}\Delta n \tag{8.31}$$

For cases where the modulator material is the waveguide core, the effective index is proportional to the material index shift by a factor of Γ, the fill factor of the waveguide power in the core ($\Delta n_{eff} = \Gamma\Delta n$).

From (8.2) the relation for the line width can be rewritten as:

$$\Delta\lambda^{LW} \approx \frac{\lambda_0}{Q} \tag{8.32}$$

and therefore we find that the FOM for modulation depth is:

$$FOM = \frac{\Delta\lambda_{shift}}{\Delta\lambda^{LW}} = \frac{\Delta n_{eff}\, Q}{n_{eff}} \tag{8.33}$$

Assuming that the minimal acceptable FOM is equivalent to one, this implies that there is a direct tradeoff between the quality factor of the resonator and the effective index shift. For HIC waveguides, the lower bound of Q is lithographically limited and the upper bound is loss limited with a typical range of $10^2 < Q < 10^5$. Therefore, in meeting the FOM, the modulating material must have respective index shift capable of $10^{-5} < \Delta n_{eff} < 10^{-2}$.

If we further breakdown the FOM into variables associated with the waveguide, we find that the FOM is inversely proportional to the coupling between the ring and bus χ^2.

$$FOM = \frac{4\pi^2 R}{\lambda_0} \frac{\Delta n_{eff}}{(\chi^2 + 4\pi R\alpha)} \tag{8.34}$$

In contrast, the modulation speed is directly proportional to χ^2 and therefore a tradeoff exists between a ring modulators speed and contrast ratio. Whether to optimize the speed or extinction ratio is application dependent.

8.3.4 Extinction Ratio Optimization

The extinction ratio is optimized when the off-state output power is zero, corresponding to an extinction ratio of infinity. In a ring resonator the output power is equivalent to zero only when the signal wavelength is resonant with a critically coupled ring. For this case, the quality factor is dependent on the loss (α) in the ring:

$$Q = \frac{\omega_0 \tau}{2} = \frac{\omega_0 \tau_L}{4} = \frac{\omega_0}{4\alpha v_g} \approx \frac{\pi\, n_{eff}}{2\lambda_0\, \alpha} \tag{8.35}$$

where the final term uses the approximation $v_g = c/n_{eff}$. Similarly, the line width of the resonance can be approximated as:

$$\Delta\lambda^{LW} \approx \frac{\lambda_0}{Q} \approx \frac{2\lambda_0^2}{\pi n_{eff}}\alpha \tag{8.36}$$

Yielding the figure of merit for the modulation depth as a function of loss:

$$FOM = \frac{\Delta\lambda_{shift}}{\Delta\lambda^{LW}} = \frac{\pi}{2\lambda_0}\frac{\Delta n_{eff}}{\alpha} \tag{8.37}$$

Here we see that the resonant depth, for a critically coupled ring is maximized when α is small and Δn_{eff} is maximized. To be conservative the on-state loss should be used in (8.37), where the loss sum of the off-state loss and any additional loss that may accompany the index shift ($\alpha = \alpha_{off} + \Delta\alpha = \alpha_{on}$).

Again, the tradeoff between the modulation depth and modulation speed exists, however this time it is with respect to the ring loss α; this is seen by comparing relations (8.29) and (8.37). If we start with a critically coupled ring resonator in the off-state: the speed to switch to the on state is proportional to α, but the modulation depth is inversely proportional to α. Intuitively this makes sense; as the loss increases, the ring dissipates power at an increasingly faster rate, but at the same time the resonant line width increases (as seen in (8.36)), which reduces the modulation depth for a given index shift.

8.3.5 Modulator Material Considerations

There are several design issues to be considered when integrating a ring modulator into a photonic circuit. For most applications, an optical modulator must meet a minimum extinction ratio that corresponds to an acceptable bit error rate in the signal. Let us assume that this occurs when the FOM derived in the previous section is equivalent to unity, which roughly corresponds to a 10 dB extinction ratio. Therefore we find a useful criterion for ring modulator material selection:

$$\Delta n_{eff} \geq \frac{2\lambda_0}{\pi}\alpha \tag{8.38}$$

Accordingly, an ideal ring modulator material must have a large index shift and low loss to meet this extinction loss metric. Since a majority of optical power is guided in the waveguide core, the modulating material should be used as the ring waveguide core to optimize the shift. Using typical HIC waveguide ring loss values ($1 < \alpha < 100$ cm^{-1}) in the telecom spectrum, where the ring loss includes transmission and coupling losses, the respective range of effective index shifts: $10^{-4} < \Delta n_{eff} < 10^{-2}$, are estimated (again) for acceptable ring modulator materials.

For cases where relation (8.38) cannot be met, the insertion loss for the on-state can be appreciable. Low insertion loss is one of the major benefits of using a ring resonator as the modulator device geometry. In some cases, the small index shift can be accommodated by minimizing ring loss, giving incentive for low loss waveguide design and processing. However, if this fails, the modulator may be better suited for applications where modulation speed is more important than extinction ratio. Rather than use a critically coupled ring, the modulator is designed to optimize insertion loss and modulation speed at the expense of the extinction ratio.

8.3.6 CMOS Compatible Integrated Ring Resonators

Compact, HIC ring modulator devices are ideal for Electronic Photonic Integrated Circuits (EPICs) where electronic data streams are encoded on an optical signal. To facilitate electric to photonic signal conversion, it is optimal to use an electro-optic effect as the modulating mechanism. Since the index shift of an electro-optical material is proportional to the applied field, only index shifts corresponding to low voltages compatible with existing CMOS electronics are considered. Under these additional constraints, Si and SiGe alloys are the few materials that exhibit electro-optic index shifts within the range of interest.

Silicon Ring Modulators

Professor Lipson's group at Cornell University developed and fabricated the first Si ring modulator. The device, illustrated in Figure 8.18, utilizes a very deeply etched ridge waveguide structure, which confines the mode like a channel waveguide for all intensive purposes, and facilitates a conduction pathway for charge carriers. In this device, the index is modulated by plasma dispersion effects [49] which occur when charge carriers are injected into the Si ring material. The effect was first studied by inciting carriers via the two photon absorption effect (see Section 4.5) with short pulses of light [107], and later optimized by building a lateral p-i-n junction for carrier injection and carrier sweep-out [117].

The large carrier induced index shift (up to $\Delta n = 10^{-2}$) in combination with low waveguide transmission loss (~ 4 dB/cm) and ring loss ($\alpha < 5$ dB estimated from [123]) result in optimal Si ring modulator performance. Recent results, as seen in Figure 8.18, show the Si ring modulator off-state resonance has a very small line width ($\Delta\lambda^{LW} \approx 0.03$ nm) corresponding to a Q of 50,000, suggesting very low ring losses. The application of a voltage across the pin structure results in carrier injection which 1) shifts the resonance and 2) widens the line width (due to free-carrier absorption). The FOM for this device can be as high as 100.

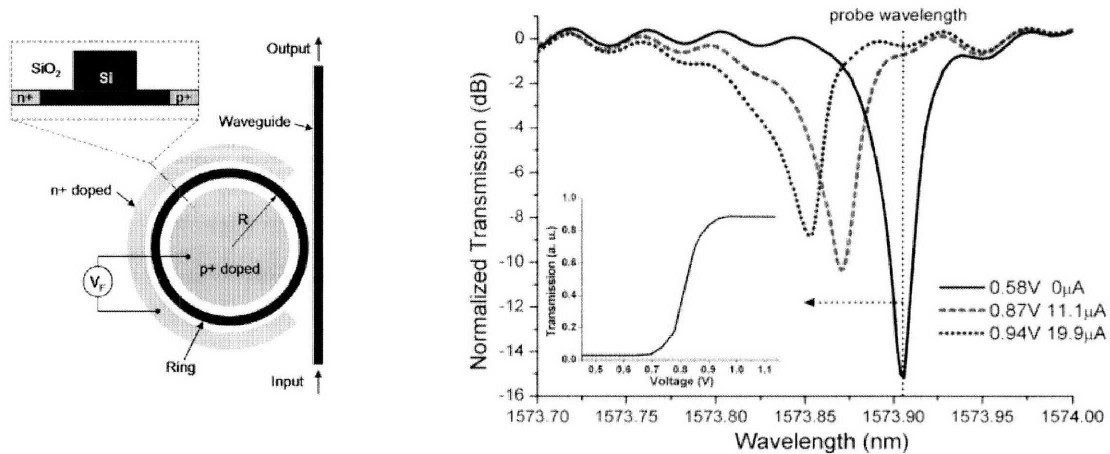

Figure 8.18 – Schematic of pin Si ring modulator (left) and corresponding spectral response for different applied voltages (right) [123]

The speed limiting mechanism for the Si ring resonator approach is the free carrier lifetime of the inserted charge carriers. While the speed by which the carriers are moved in and out of the Si ring can be improved by applying a field to inject and to sweep-out the field (i.e. the voltage is modulated around the open circuit voltage) the incomplete electrode design, as seen in figure 8.18, for the single wafer level configuration limits this effect. Efforts to improve the efficiency of injecting and sweeping away the carriers (increasing the doping concentrations and reducing the junction spacing) are stymied as they increase optical ring loss. In addition, temperature variations that arise during operation from carrier injection result in an altered resonant wavelength, due to the thermo-optic effect, which must be compensated for. However, recent design and fabrication optimization has yielded Si ring modulators that operate at 6 GHz with an 8 dB extinction ratio [119]. Theoretically, the optically-limited modulation frequency can reach tens of GHz in these structures.

Silicon-Germanium Ring Modulators

An alternative CMOS compatible, electro-optic ring material is SiGe. As opposed to modulating the material index by carrier injection at the telecom wavelengths, Ge and Ge-rich SiGe alloys can also modulate their material indices by the Franz-Keldysh (FK) effect [21]. The FK effect is the bulk analog to the Quantum-Stark effect [21], used in ultrafast III-V quantum well electro-absorption modulators. The basic principle behind both effects is that the application of an electric field alters the material (or quantum well) bandgap energy which corresponds to altered material loss and index. The prospect of using an electric field effect as the modulation mechanism for a ring resonator is extremely attractive as the speed is not limited by carrier transport, as it is with Si.

The FK effect is wavelength dependent and strongest for wavelengths near the band edge of the direct band gap (where the electron wavevector or equivalently momentum is zero – E_g^Γ). Hence a semiconductor with a direct bandgap $E_g^\Gamma \sim 0.8$ eV, which corresponds to λ_s=1550 nm, is best suited for FK effect modulation. The FK effect is present in indirect bandgap materials; however the lower energy indirect gap causes significant optical absorption at wavelengths where the FK effect is strongest. Nonetheless, Jongthammanurak et al. recently optimized and measured the FK effect in strained-Ge films deposited on Si where a record Ge electro-optic coefficient of 280 pm/V (larger than that found in $LiNbO_3$) was measured at λ_s = 1647 nm [121]. The strain in the Ge film effectively narrows E_g^Γ and enhances the FK effect. The only drawback is the loss that results from the indirect gap absorption, where the baseline loss (α_0) is of the order 100 dB/cm and the loss that accompanies the applied field ($\Delta\alpha$) can be several times this value. The large losses are deleterious to meeting the FOM for ring modulators.

Two SiGe alloys have been identified as optimal FK effect modulator materials operating at λ_s=1550 nm [122]. Option one is optimized for electro-optic (EO) applications, whereas option two is designed for electro-absorption (EA) applications.

Option 1 – EO optimized SiGe

Option one – an 11% Si, SiGe alloy – is optimized for EO applications, where $\Delta n/\alpha$ is maximized. For this material, the loss is minimized at λ_s=1550 nm ($\alpha_0 \approx 1$ cm^{-1}, $\Delta\alpha$ is negligible) but at the expense of a reduced index shift ($\Delta n = -1.5\times10^{-4}$) for an estimated applied voltage of 4 V. The ring consists of a single mode, SiO_2 clad SiGe ring. The ring loss is estimated to be α = 10 dB, with ring radius R= 5 μm and total coupling of $\chi^2 = 0.063$ chosen to critically couple the ring. As seen in Figure 8.19, the small index shift results in a nearly inconsequential resonant wavelength shift. While the off-state is optimized with zero output power due to critical coupling of the ring, the small $\Delta\lambda_{shift}$, corresponding and proportional to the small Δn, results in a very small modulation depth and an on-state with very high insertion loss. Effectively, the 11% Si, SiGe material is not adequate for ring modulator applications, and is better suited for other modulator devices.

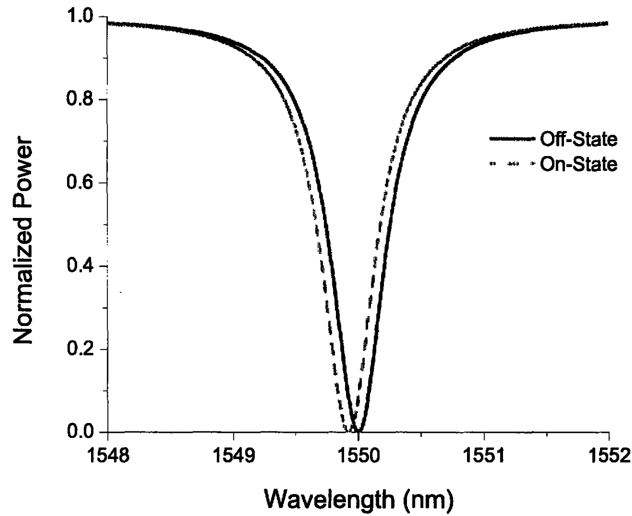

Figure 8.19 – Spectral response of a ring modulator comprised of an EO optimized SiGe waveguide core material for λ_s =1550 nm.

Option 2 – EA optimized

Option two – a 1% Si, SiGe alloy – is designed for electro-absorption (EA) applications where $\Delta\alpha/\alpha$ is optimized (α_0 =160 cm^{-1}, $\Delta\alpha$ = 460 cm^{-1}) with a reasonably large index shift (Δn = $-2x10^{-3}$) at λ_s=1550 nm, for an estimated applied voltage of 3.3 V. In this device, the single mode, SiO_2 clad SiGe ring loss (R= 5 μm) is estimated as identical to the bulk loss in the respective states, as waveguide losses from processing imperfections are negligible in comparison. The enormous material losses, that arise from indirect bandgap absorption, restrict the ring resonators to the under-coupled coupling regime, even when the coupling is pushed to χ^2 = 0.1, as seen in Figure 8.20.

Interestingly, the modulation of optical power by the FK effect is more a result of altering the spectral response shape, a direct consequence of the large $\Delta\alpha$ which increases the line width $\Delta\lambda^{LW}$ (note the scale of the abscissa axis in Figure 8.20), rather than the resonance shift $\Delta\lambda^{shift}$ that causes a shift in the spectral response, as is the case with Si ring modulators. One concern in design is to ensure that the spacing between adjacent resonances is larger than the line width, however the high index of SiGe alloys (n=3.5-4) enables small ring radii that can eliminate this effect (since the FSR is inversely proportional to R). In this configuration, the EA optimized SiGe ring modulator is well suited for applications where modulation speed is valued over extinction ratio. The simulated modulation frequency for this ring resonator is optically limited to f_{mod} ~ 40 GHz; presumably proper electrode configuration can meet this figure to apply the field fast enough to realize this potential modulation speed. The insertion loss for the on-state is 0.09% (0.41 dB), and the extinction ratio is only 1.3 dB.

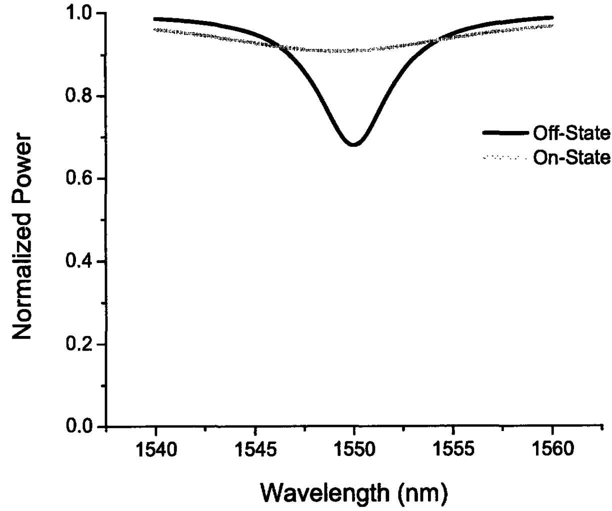

Figure 8.20 – Spectral response of a ring modulator comprised of an EA optimized SiGe waveguide core material for λ_s =1550 nm.

Although the EA optimized SiGe ring modulator is restricted to the under coupled coupling regime, there are tricks which can be played to increase the modulation depth without sacrificing speed. One of which is to place a number of identical modulators in series along the bus waveguide. Assuming that the field is applied to each modulator at the same time, the speed should be unaffected. The resulting output power as a function of frequency, time constants, and input power is given by (8.39) where N is the number of identical rings in series.

$$|s_t|^2 = \left(\frac{(\omega-\omega_0)^2 + \left(\frac{1}{\tau_e} - \frac{1}{\tau_L}\right)^2}{(\omega-\omega_0)^2 + \left(\frac{1}{\tau_e} + \frac{1}{\tau_L}\right)^2} \right)^N |s_i|^2 \tag{8.39}$$

In Figure 8.21, ten EA optimized SiGe ring modulators are used in series to realize the spectral response depicted. In this simulation, the extinction ratio is improved to 12.6 dB; however the insertion loss increases as well to 4.2 dB. For applications where speed is an issue, the added loss is a relatively small tradeoff. The length of this device is less than 150 μm (ten, five micron radius rings, with spacing to prevent ring to ring interactions). In terms of processing, this layout requires precise trimming of each ring to ensure identical resonance conditions. In addition, optimized placement of contacts to apply a field across the modulator material is crucial in reduced loss and high speed.

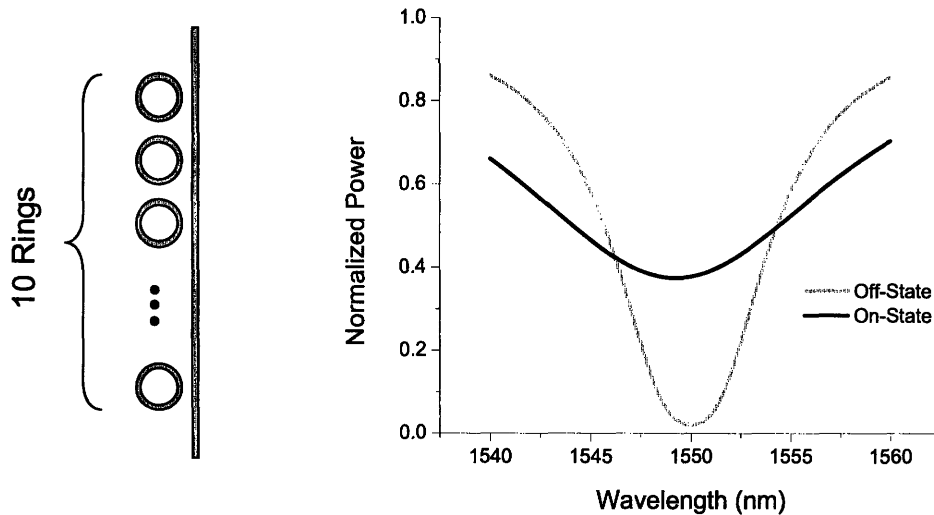

Figure 8.21 – Spectral response of 10 EA optimized SiGe ring modulators operating in series.

The EA optimized SiGe alloy represents an attractive ring modulator material for EPICs. The Franz-Keyldish (FK) index modulating mechanism is electric field based, rather than the carrier dispersion effect used in Si ring modulators, which can theoretically enable modulators that operate at their optically limited speeds of tens of GHz (with proper electrode design). The indirect bandgap of SiGe results in very high absorption at wavelengths where the FK effect is optimized, which in turn prevents optimal coupling to critically couple the resonator. While there are many modulator applications where the modulation speed trumps the modulation depth; placing several SiGe ring modulators in series results is a work-around solution to increasing extinction ratio, with a relatively small insertion loss tradeoff.

Chapter 9 – Waveguide Integration

The integration of low loss photonic interconnects with existing CMOS-based microelectronics holds the key to overcoming performance limitations in many computing applications. Some example applications include board-to-board communication in servers, chip-to-chip communication on motherboards, and intra-chip communication of high speed microprocessors. In each case, the replacement of speed-limited electronic interconnects with photonic interconnects presents a method of avoiding the resistance-capacitance (RC) data communication bottleneck that hinders performance. Outside computation, the development of a low loss, CMOS-compatible photonic interconnect technology benefits communications applications where reduced cost, weight, volume, and power consumption enable increased and enhanced performance. Some example applications include optical network transceivers and routers, disposable high sensitivity bio/chemical sensors, radio frequency (RF) systems, and optical gyroscopes. Ultimately, the high bandwidth capabilities of photonic circuits in combination with the processing capabilities of microelectronics hold the key to enabling many sought after technologies. In this chapter, the challenge of creating a CMOS-compatible electronic-photonic integrated chip (EPIC) is explored in the context of an application specific (AS) design. While the function of this AS-EPIC proprietary, many of the process and design techniques developed in realizing this technology are applicable to all EPICs.

9.1 The EPIC Project

The EPIC project is a DARPA funded research collaboration amongst scientists and engineers from BAE Systems, Columbia University, Cornell University, Lucent Technologies, and MIT. The objective of this research is to create an EPIC that functions as a high resolution, broadband RF channelizer, or what may be thought of as a Fast Fourier Transform (FFT) chip. This work is motivated by improved RF channelizer device size, weight, and performance, as compared to existing electronic RF channelizers which are comprised of many discrete components; a feat that can only be realized by the unique properties of integrated photonics [46]. In addition, the EPIC project represents one of the first attempts at the demonstration of a complete suite of high performance Si nanophotonic devices fabricated in a CMOS-compatible process.

9.1.1 Device Operation

The configuration of the AS-EPIC studied in this chapter is listed in Figure 9.1. In operation, the AS-EPIC RF-channelizer uses an integrated modulator in combination with an external single-wavelength (λ=1.55 μm) mode-locked laser to encode a broadband RF signal input onto an optical carrier signal. The frequency of the optical carrier signal is much greater than the RF signal frequency. The modulated optical signal is then guided and split via optical interconnects (silicon waveguides) into an array of filters that sort the encoded waveform. Each filter is designed to permit a specific portion of the frequency

domain to transmit. Or in other words, the output from each filter is a slice (i.e. channel) of the modulated signal frequency-domain. Post-filter, the optical signal is detected by an integrated photo-detector and converted to an electrical signal with the aid of a trans-impedance amplifier (TIA). Once converted back into an electronic signal, conventional CMOS microelectronic circuits are utilized to process the data.

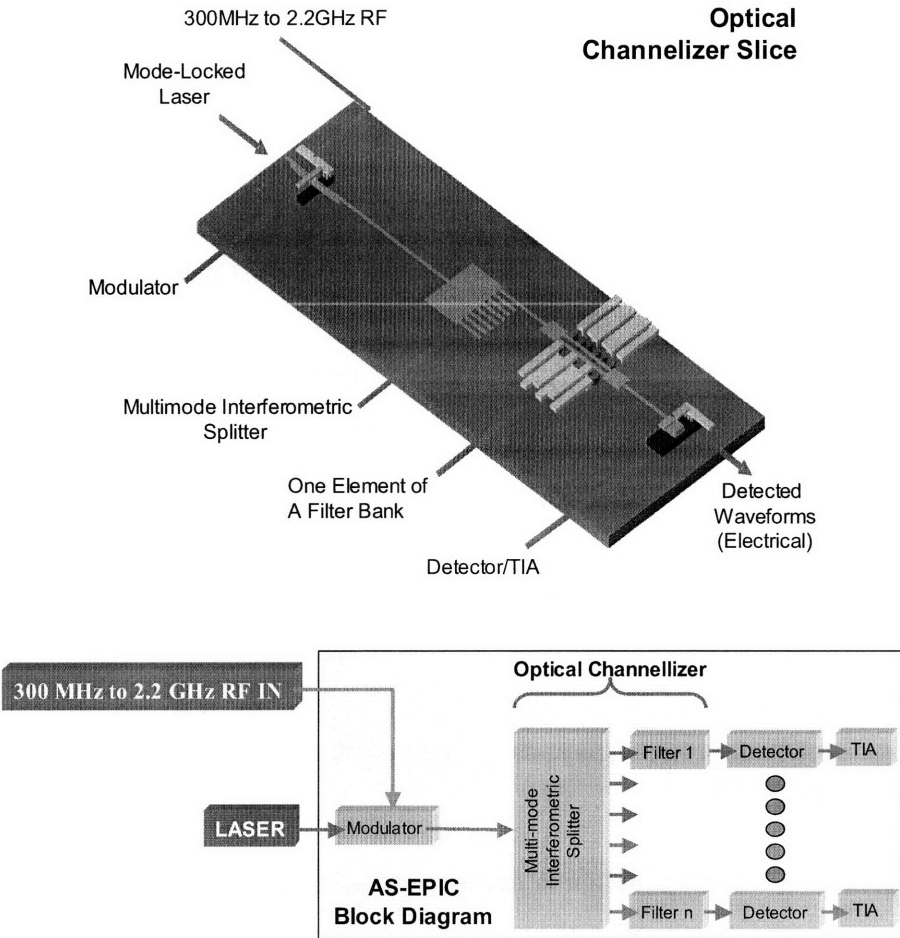

Figure 9.1: Schematic representation of a single-channelizer link on the AS-EPIC (top) and block diagram of the AS-EPIC components (bottom), image taken from [123].

9.1.2 The Need for Low Loss Waveguides

As the fundamental component of photonic circuits, low loss waveguides are critical to the realization of EPIC technology. For the AS-EPIC chip example, the modulator, optical interconnects, multi-mode interferometer (MMI), and filter devices are all comprised of waveguide components.

The principal requirement for low loss waveguides is practical and functional in nature - the transmitted power must be sufficient for detection. Detection requirements vary depending on the input

power, input coupling, detector responsivity, and waveguide transmission loss. Assuming adequate input power and minimal coupling loss, an optical circuit which is several centimeters long, such as that found in an EPIC, should have a maximum transmission loss on the order of dB/cm.

Another loss requirement stems from photonic device performance. For the AS-EPIC studied here, the filter performance is strongly dependent on the waveguide transmission loss and represents a major constraint in realizing ideal device operation. The optical filters are comprised of high Q ring resonators in an all-pass, fourth order pole/zero, Mach-Zehnder configuration, as seen in Figure 9.2. By properly tuning the ring resonators with thermo-optic integrated heaters, ring-induced signal dispersion is utilized to filter the signal [124]. Integrated heaters are used as phase shifters to ensure equal optical power in each arm of the Mach-Zehnder as well as optimal coupling behavior between the ring and the bus waveguide. The ability to dynamically tune each filter component by adjusting the phase shifters enables flexibility in realizing different filter responses (i.e. Butterworth, Chebyshev, etc.).

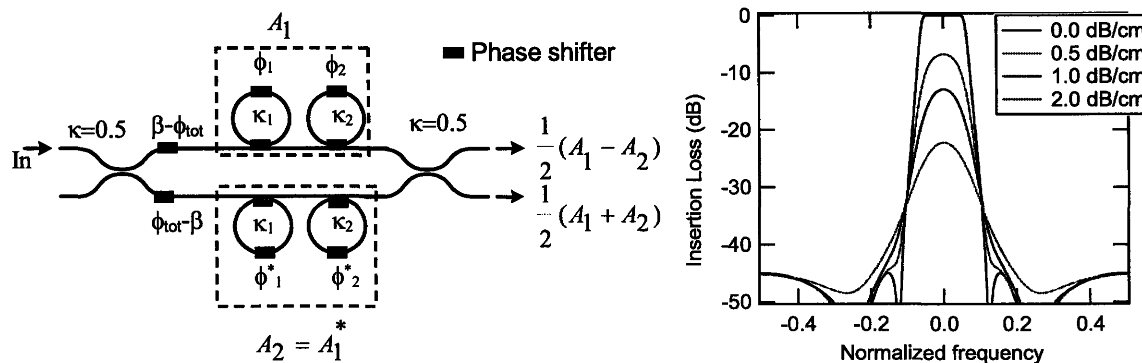

Figure 9.2: Schematic representation the AS-EPIC filter (left) and filter shape as a function of waveguide loss (right), images taken from [123].

The complexity of this filter design is necessary to achieve the narrow band (1 GHz) channel spacing needed for RF-channelizer applications. However, the complexity also results in significant device performance degradation as waveguide transmission loss increases. As seen in Figure 9.2, a slight increase in the waveguide transmission loss drastically affects the overall filter insertion loss and filter shape. For this filter, waveguide losses of less than two dB/cm are required for near-ideal filter performance.

9.2 CMOS-Compatible Process Challenges

There are many challenges in trying to realize a CMOS-compatible electronic-photonic integrated chip. The devices on each wafer level are constrained by available materials, epitaxial compatibilities, thermal-

budget imposed process order, and device communication. In this section, CMOS-compatible process constraints are reviewed in the context of photonic device integration.

9.2.1 Materials

CMOS compatible materials are generally limited to dielectric materials: Silicon (Si), Silicon Dioxide (SiO_2), Silicon Nitride (Si_3N_4), Silicon Oxinitride (SiON); electrical dopants: Boron (B) and Phosphorous (P); and metals for electronic interconnects: Aluminum (Al), Tungsten (W), and Copper (Cu). In addition, there are several CMOS compatible Silicides, Nitrides, and low-k materials used for electrical contact, diffusion barrier, and interconnect insulator materials respectively. More recently, the use of strained silicon (ε-Si) and silicon-germanium (SiGe) in the quest to continually improve CMOS microprocessor performance has arguably and fortuitously promoted germanium (Ge), another semiconductor material well suited for near-infrared detection, to the list of compatible materials.

Interestingly, the introduction of new materials to CMOS process flows is growing at an ever increasing rate. The introduction of new materials requires tremendous effort and capital in ensuring that fabrication compatibility and reliability are not compromised. As seen in Figure 9.3, the rate of new materials introduction has accelerated in recent years. Likewise, in the last five years, the use of SOI substrates, strained-Si, and SiGe materials in microprocessors has become commonplace. Given the difficulty of introducing materials into the CMOS process line, this accelerated trend furthers the notion that continued performance scaling in CMOS microprocessors is reaching its limits. Furthermore, the introduction of new technologies, such as integrated silicon photonics, is likely if this scaling is to continue.

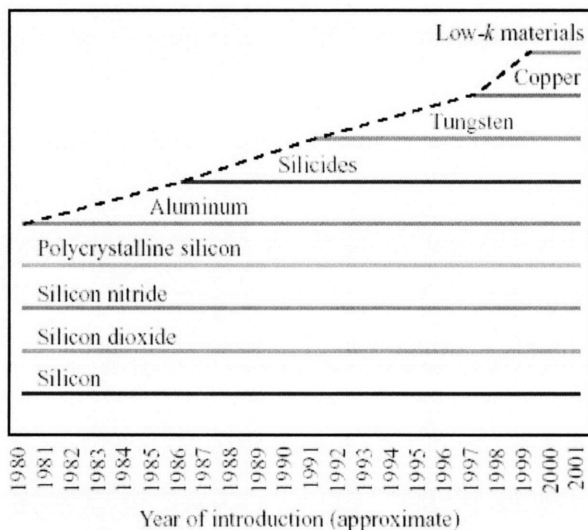

Figure 9.3: The introduction of new materials into CMOS processing [125]

Fortunately, the restrictive CMOS material selection is not a constraint in realizing the AS-EPIC. Si, SiN, SiO_2, Ge, and their respective alloys are sufficient for creating low loss high index contrast waveguides with tight bend radii [13], splitters [14], Si waveguide based tunable optical filters [126], fast Si ring modulators [16], and fast integrated Ge photodetectors [17]. The lack of an integrated light source, not required for the AS-EPIC example, is a major concern for many EPIC applications. As it stands, an adequate light source does not exist using CMOS materials, however the topic is the focus of much research [18, 127]. In addition, flip-chip bonding of III-V light sources to an EPIC has been demonstrated and proposed as a makeshift solution [27].

9.2.2 Epitaxial Constraints

The integration of photonic devices with conventional CMOS electronics affects substrate selection and device placement. The AS-EPIC example operates by encoding an optical signal via a Si ring modulator controlled with an electrical input; the encoded signal is guided, split, and filtered via Si waveguides, and finally the optically encoded signal is detected and converted back to an electrical signal by a Ge detector. In terms of integration, the AS-EPIC devices can be broken down into four categories: electronic devices, active waveguide devices (ring modulator, tunable filter), passive waveguide devices, and Ge-based devices. CMOS-based electronics are comprised of Si transistors, which consign these devices to the first wafer level.

The use of crystalline silicon waveguides is required in meeting the desired performance metrics for the active waveguide devices. Unlike, a-Si, poly-Si, or SiN; crystalline silicon waveguides exhibit superior electro-optic and thermo-optic properties necessary for high performance ring modulator and optical filter devices. Furthermore, the transparency of crystalline silicon is helpful in realizing the tight loss tolerances needed in meeting tolerable optical filter operation. As demonstrated in Section 7.1.1, the use of hybrid waveguide structures can result in losses as low as 0.35 dB/cm. Finally, in maintaining optical confinement with layer thicknesses amenable to CMOS processing effectively renders the employment of silicon on insulator (SOI) substrates as the only feasible course of action. Similar to the EPIC electronic devices, the active waveguide devices are relegated to the SOI level.

The use of an amorphous SiO_2 cladding layer to optically isolate the Si waveguides provides the index contrast sufficient for a highly confined waveguide mode amenable to low loss propagation in an EPIC. However, the use of amorphous cladding layers precludes the growth of crystalline materials on higher chip levels. This is problematic for Ge-based devices which are dependent on the crystalline material properties needed in meeting AS-EPIC performance metrics. The breakthrough development of high quality Ge on Si growth [128], despite a 4% atomic lattice mismatch, has enabled high speed

photodetectors integrated on Si substrates [17]; a perfect candidate for AS-EPIC photonic to electronic signal conversion. However, this growth process constrains Ge-based devices to reside on the surface of the SOI layer.

In terms of integrated waveguide-photo-detector interaction, it is preferential for the coupling to occur on the top surface of the Ge-based device – where the dislocation density is lowest and excited carrier collection is optimized. Therefore it is preferential to couple and absorb optical signals from upper level waveguides which reside on or above the Ge-based device level.

The use of evanescently coupled upper-level passive waveguide devices is also critical in relieving EPIC footprint area constraints. As just discussed, electronic, active waveguide, and Ge-based devices are fabricated from or just above the SOI level due to performance and epitaxial constraints. Thus, the EPIC footprint is simply the sum of the individual device areas for these devices. However, the employment of upper level waveguides relieves this constraint by effectively increasing EPIC real estate. The ability to guide light through multiple chip levels facilitates increased circuit density, complexity, and enhanced functionality for a given EPIC footprint. Ideally, upper-level, passive waveguides can replace all non-active SOI waveguide devices.

Similar to SOI-based waveguides, deposited upper-level waveguide materials must have a high index of refraction and compatibility with SiO_2 to enable a highly confined, optically insulated, sub-micron cross-section, which is compliant with the physical and fabrication tolerances utilized in CMOS processing. The use of amorphous SiO_2 claddings epitaxially restricts the upper-level waveguide materials to amorphous or polycrystalline morphologies. For optimal coupling between the waveguide layers, it is imperative that the respective waveguide layer structures exhibit matching effective indices. For simplicity, it is practical to use an upper level waveguide with a similar core index as crystalline silicon, such as amorphous silicon; otherwise considerable design effort is needed to meet this criterion.

9.2.3 Thermal Budget Limitations

The fabrication process order is dictated by the temperature of each process step. High temperature processes must take place in the beginning of the process order to ensure that temperature sensitive materials are not compromised during fabrication. For example, dopant diffusion, alloying, melting, (re)crystallization, and oxidation are a few of the deleterious consequences that can render electronic and photonic devices inoperable.

The process temperatures used in the fabrication of CMOS-based transistors range from as high as 1050 °C to as low as room temperature. Traditionally, the process flow is divided into front end and back end processes. Front-end processes involve the fabrication of metal-oxide-semiconductor-field-effect-transistors (MOSFETs) which includes a high temperature gate oxidation step, as well as an

annealing step to activate the implanted source and drain dopants. Back-end processes occur later in the process order and involve lower temperature metal and dielectric depositions for electronic interconnects as well as packing steps to hermetically seal the chip.

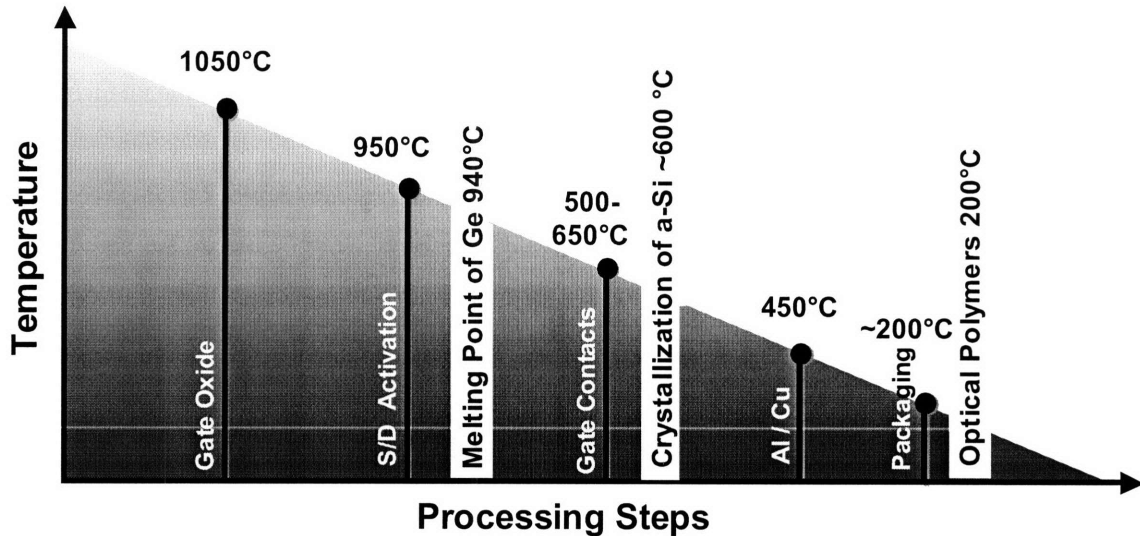

Figure 9.4: Noteworthy CMOS processing temperatures for different steps in microprocessor fabrication [129]

In leveraging the high-volume and low-cost attributes of CMOS processing, it is vital that integrated photonic devices are compatible with microelectronic process temperatures. Figure 9.4 lists the noteworthy CMOS process temperatures for various processing steps, as well as some relevant thermal thresholds for integrated photonic devices, the processing steps are listed in order of descending temperature. In holding to the thermal constraints of CMOS processing, it is clear that electronic device fabrication must occur at the beginning of EPIC fabrication. Similarly, the process order placement of Ge-based devices must occur after MOSFET fabrication. However, in meeting integrated device communication requirements between the electronic and photonic devices, some compromises may be needed.

The Ge growth process involves an initial low temperature (350 °C) growth step, wherein a thin buffer layer (~ 60 nm) is grown on a Si surface, such that surface diffusion during deposition is reduced. Reduced surface diffusion inhibits Ge islanding, enabling crystalline heteroepitaxy. Afterwards, a high temperature (600 °C) growth step is used to grow a low defect, high quality Ge film on the initial seed layer. A short, post-annealing (~ 850 °C) step is required to reduce dislocation defects that are harmful to electrical properties. To accommodate the range of Ge process temperatures, the MOSFET source-drain activation anneal step is shared across several process steps. Instead of one source-drain activation anneal step, the integrated thermal history of the process flow is adjusted and utilized to meet proper device operation for electronic and photonic devices. Prolonged thermal exposure deleteriously affects

the MOSFET electrical properties, such as the threshold voltage. For the AS-EPIC example, the final, high temperature Ge dislocation reduction anneal step is also used to finish dopant activation in the MOSFET and Ge-based devices.

The choice of upper level waveguide material is directly affected by the process step order. As discussed in Chapter 6, the leading low loss deposited waveguide candidates are a-Si and SiN. If the upper level waveguides are deposited prior to Ge-based device fabrication, the annealing temperatures needed to drive out dislocations (~ 850 C) and activate electronic dopants (~ 600 C) in the photo detectors present an obstacle to employing a-Si waveguides. The exposure of a-Si waveguides to Ge device process temperatures results in crystallization of the waveguide core, forming poly-Si, which leads to excessive waveguide loss, also discussed in chapter 6. In contrast, the thermal stability of SiN materials is countered by a lower index contrast with the SiO_2 cladding which necessitates larger optical isolation to maintain low loss propagation. Aside from introducing more process variability, increasing the cladding layer thicknesses reduces device density and adds other process complications, such as film stress and electrical interconnect via depth limitations.

For the AS-EPIC example, optical isolation of the SiN waveguide mode from substrate leakage and metallic interconnect absorption is more of a concern than the poly-Si waveguide transmission loss increase. The poly-Si loss restraint is overcome by restricting the use of the upper level waveguides to regions near the photo detector, thereby limiting the propagation length and total propagation loss. The larger minimum cladding layer thicknesses needed for SiN waveguides (approximately three μm as compared to one μm for respective TE polarized single-mode channel waveguide structures) is not practical, in terms of extra process steps and layer depositions, when utilizing electronic interconnects that transverse the top and bottom cladding film thicknesses. However, the selection of poly-Si over SiN as the upper level waveguide material, limits the utility of the waveguides in the second waveguide layer, thereby limiting the benefits of upper level waveguides. While not needed for the AS-EPIC function, the use of a third a-Si waveguide layer that resides in the highest chip level with a reduced thermal history (i.e. low loss), may be warranted to optically route signals in more complex ways.

9.2.4 AS-EPIC Architecture

Ultimately, the AS-EPIC architecture is shaped by the epitaxial, thermal, and device operation constraints in CMOS processing. All three constraints consign the electronic devices and active Si photonic devices to the SOI level. The integration of Ge photo-detectors, introduces many of the challenges. The low melting temperature of Ge forces the processing of photo detector and other Ge-based devices (such as the ring modulator described in Chapter 8) to take place during electronic device fabrication. Epitaxial constraints also require that the Ge layer is grown on a crystalline silicon surface. Finally, the addition of

upper-level deposited waveguides is needed in routing the optical signal to the Ge film level, where electrical properties are optimal. Limited use of the upper waveguide level permits the use of higher loss waveguides, however at the cost of limiting photonic device complexity.

Figure 9.5 illustrates the chosen AS-EPIC architecture, based on the above arguments. The optical signal is modulated and filtered (devices not shown) and guided in SOI based waveguides. Post-filter the waveguide mode is evanescently coupled to the upper-level deposited waveguide. The optical signal is then absorbed by the Ge photo detector, the architectural interface between electronic and photonic devices. The ensuing electronic signal is routed through metallic interconnects far above the waveguide layers by electronic vias to the electronic devices, so as to maintain optical isolation in the waveguides.

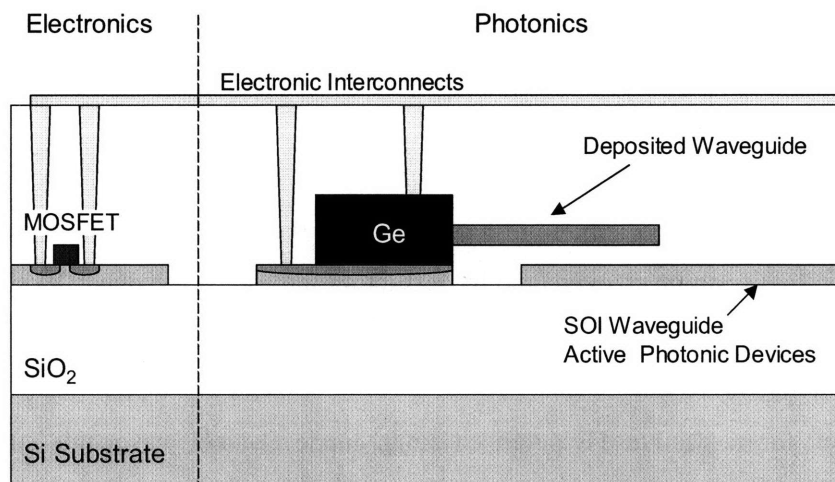

Figure 9.5: Architecture chosen based on CMOS fabrication constraints for the AS-EPIC example

9.3 Waveguide Selection

Optimized waveguide selection is vital to maximizing the density of photonic devices which enables increased photonic circuit complexity and enhanced photonic functionality. For CMOS compatible materials, the Si-SiO_2 material system is well-suited for high density photonic applications due to the high index of refraction difference ($\Delta n=2$). In this section, an investigation into the optimum Si-SiO_2 waveguide geometry for EPIC applications is examined.

9.3.1 Desired Characteristics

An ideal, integrated waveguide highly confines light within a small cross-section, whereby the required cladding layer thickness, needed for optically insulating the waveguide is minimized. For integration with CMOS microelectronics, it is critical to confine light within a sub-micron cross-section, so as to

prevent the waveguide mode evanescent field from overlapping and losing signal power to other device structures. In terms of planar density, it is critical that the waveguide structure support low loss, compact bend radii. Finally and perhaps most importantly, it is crucial to maintain low loss propagation. Of the available planar waveguide geometries (i.e. channel, ridge, etc.) a single-mode, channel waveguide is best suited in meeting these criteria.

9.3.2 Bend Radius

The planar density of a photonic circuit is directly related to the waveguide bend radius. The minimum bend radius for a single mode channel waveguide, defined by a chosen bend loss threshold, is proportional to the Δn of the core and cladding. For CMOS-compatible materials, the Si-SiO_2 system is optimal; it has a very high $\Delta n=2$ (enabling 1 μm bend radii), telecom spectrum transparency, and an extensive material processing knowledge base.

Finding the minimum Si-SiO_2, channel waveguide bend radius is dependent on the waveguide geometry and mode order. Higher order modes exhibit less confinement (larger mode size) and exhibit higher bend losses for a given bend radii. Hence the selection of waveguide geometries is restricted to single-mode dimensions – which are defined by waveguide geometries with dimensions below the second order mode cutoff. However, as discussed in Section 4.9 and demonstrated in section 7.1, the bend radius for single-mode channel waveguides is minimized when the difference between the effective and cladding indices is maximized. The effective index can be viewed as the weighted average of core and cladding indices, with respect to the mode field distribution, and thus the effective index is maximized for waveguides with large dimensions.

Likewise, in terms of the mode field diameter, the mode size is approximately that of the waveguide core for large (with respect to the wavelength) waveguide dimensions. However for single mode waveguides, the mode size scales inversely with waveguide dimension and thus the mode field diameter is largest for reduced waveguide dimensions, as seen in Figure 7.5. Therefore the waveguide dimensions must be maximized to reduce the mode field diameter.

So, in keeping with single-mode transmission, the channel waveguide dimensions are reduced to below the second mode cutoff, but in optimizing the minimum bend radius and mode field diameter within this set of single-mode geometries, the waveguide dimensions should be maximized. By these arguments, Si-SiO_2 channel waveguides are optimized for the set of geometries with second-mode cutoff dimensions.

9.3.3 Aspect Ratio

The aspect ratio of the waveguide geometry has a direct impact on the transmission loss. Waveguides fabricated from thin films exhibit interface roughness on the waveguide sidewalls, as a result of the etch process, which leads to roughness-scattering loss. This is particularly true for Si-SiO_2 waveguides, where highly confined channel waveguide modes exhibit sizeable losses for nm-scale sidewall roughness. As discussed in Section 5.2.4, a comparison of fabricated Si-SiO_2 channel waveguide losses revealed that the transmission loss variation between the various studies is more a function of waveguide geometry than variations in sidewall roughness.

The amount of scattering loss is proportional to the field intensity at the sidewall interface. As discussed in section 4.3.3, the losses for short-wide waveguides are considerable lower than tall-skinny waveguide geometries due to the relative field distributions within these respective geometries. Therefore, the set of Si-SiO_2 waveguide geometries optimal for integrated applications is reduced to those which have height to width aspect ratios of less than unity. Combining these findings with those from the bend radius arguments yields a further curtailed set of optimum Si-SiO_2 channel waveguide geometries. Figure 9.6 depicts the locus of dimensions that meet these criteria. The height and width dimensions were simulated by FIMMWAVE and signify the second TE-mode cutoff for waveguide aspect ratios less than unity.

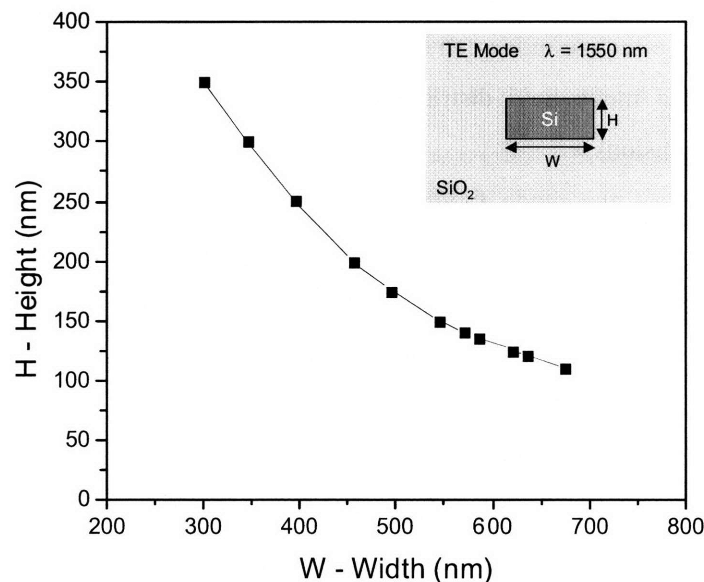

Figure 9.6: Single-mode dimensions, defined by the second TE mode cutoff, for the TE mode in Si-SiO_2 channel waveguides, λ=1550nm, simulated with FIMMWAVE.

9.3.4 Evanescent Field Decay

For single-mode channel waveguides, the mode distribution is concentrated and centered in the waveguide core. Outside the core, the field exponentially decays ($e^{-\gamma x}$) into the cladding and is known as the evanescent field. The evanescent field decay constant (γ_x) is directly proportional to the effective index (n_{eff}) as seen in relation (9.1). Thus, in minimizing the needed optical isolation distance from the waveguide core, the effective index should be maximized.

$$\gamma_x = k_0\sqrt{n_{eff}^2 - n_{clad}^2} \tag{9.1}$$

Incorporating this assumption with our previous findings directly affects the polarization selection. For single mode channel waveguides with a short-wide rectangular cross-section, the electromagnetic boundary conditions that occur at the core-cladding interface, at optical frequencies, results in disparate eigenmode solutions to the wave equation for the TE and TM polarizations (see Section 2.7). In other words, the effective indices are quite different for the TE and TM modes in a short-wide rectangular channel waveguide. Hence, the TE mode is more highly confined in the preferred short-wide waveguides capable compatible with CMOS processing.

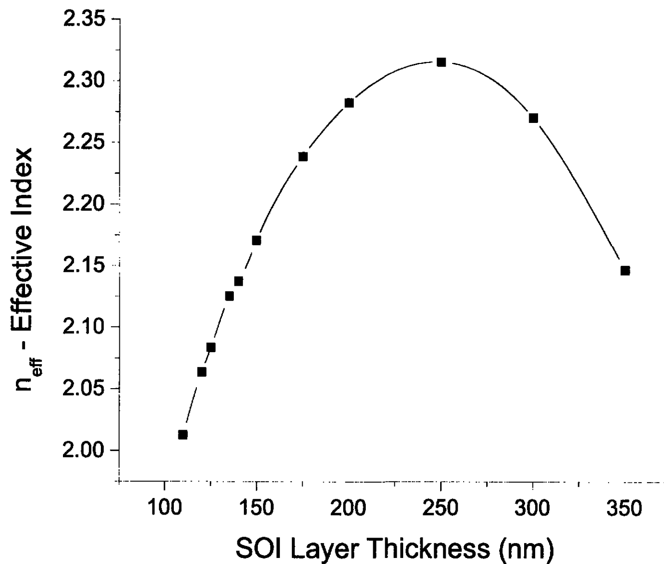

Figure 9.7: Effective index versus SOI layer thickness for single-mode Si-SiO_2 channel waveguides, TE mode, λ=1550nm, simulated with FIMMWAVE.

Amongst the set of TE polarized single-mode geometries considered in our earlier arguments, the 250x400 nm^2 Si-SiO_2 waveguide geometry has the highest effective index. Thus, this geometry

represents the case when the evanescent field decays fastest for TE-polarized, single-mode, short-wide rectangular, Si-SiO_2 waveguides. This was found by simulating the effective index for the geometries in Figure (9.6) with FIMMWAVE. The results of this simulation are plotted in Figure 9.7, where the effective index is plotted versus SOI layer thickness – the waveguide height associated with each geometry. SOI layer thickness is a practical parameter for substrate selection.

For geometries with thinner SOI layer thicknesses, the mode is squeezed out of the core leaving more of the field in the cladding, reducing the effective index. For geometries with a thicker SOI layer thickness, the accompanying reduced waveguide width restricts the confinement of light in the core, due to the field discontinuities at the sidewalls. This latter effect is enhanced because of the high index contrast between Si and SiO_2.

9.3.5 Modal Area

The cross-sectional area needed to optically isolate a waveguide mode from other devices in the out-of-plane direction is another limiting factor in photonic circuit density and integration with CMOS microelectronics. While the effective index argument is an apt approach to finding a minimized modal area, its focus is on the evanescent decay constant. In reality, the total area occupied by the waveguide mode is the sum of the waveguide core area plus contributions from the evanescent field decay. There are several metrics with which to evaluate the effective modal area (A_{eff}); in this analysis relation (9.2) is used, where I is the intensity.

$$A_{eff} = \frac{\left(\int I(x,y)\, dxdy \right)^2}{\int I^2(x,y)\, dxdy} \tag{9.2}$$

Using the same set of TE polarized single-mode geometries considered in our earlier arguments; the 200x470nm^2 waveguide has the smallest effective area. Similar to before, this was found by simulating the effective modal area for the geometries in Figure 9.6 with FIMMWAVE. The results of this simulation are plotted in Figure 9.8, where the effective area is plotted versus SOI layer thickness and a smooth curve is fit to the simulated data.

Not surprisingly, this optimum single-mode Si-SiO_2 waveguide geometry is close to that found by effective index analysis. Interestingly, the modal area is reduced for the 200x470 nm^2 geometry despite having a reduced evanescent field decay constant. This result illustrates the balance between the waveguide core area and the evanescent field decay. While the number of optically insulated single-mode

channel waveguides within a given cross-section is maximized for the 200x470 nm^2 waveguide geometry, the distance between waveguides is minimized for the 250x400 nm^2 waveguide geometry.

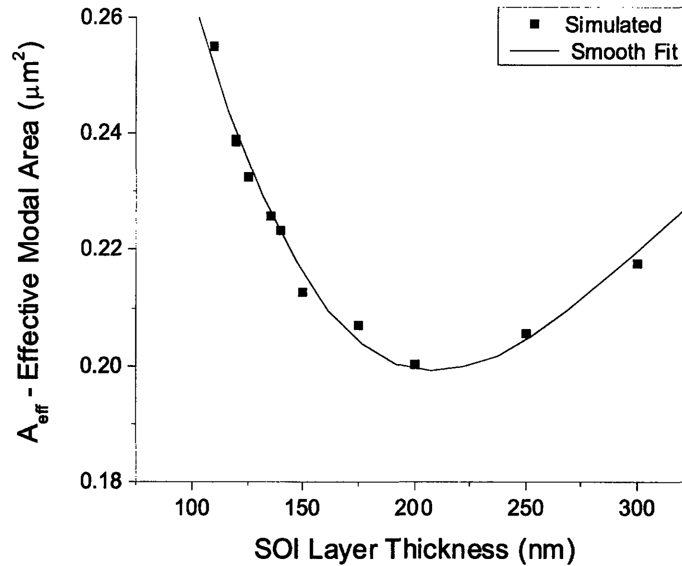

Figure 9.8: Effective Modal Area versus SOI layer thickness for single-mode Si-SiO_2 channel waveguides, TE mode, λ=1550nm, simulated with FIMMWAVE.

In summary, the integration of photonic devices with CMOS microelectronics requires highly confined sub-micron cross-section waveguides. Processing, material, and layer thickness compatibility leaves the use of Si-SiO_2 channel waveguides as one of the few alternatives. The use of single-mode waveguides places an upper limit on waveguide dimensions, while the bend loss (for increased planar circuit density) and lateral confinement places a lower limit on the waveguide dimensions. This tradeoff narrows the waveguide geometry selection to those with dimensions which reside at the second mode cutoff. To minimize sidewall roughness loss, only short-wide single-mode aspect ratios are considered. Within this further reduced set of waveguide geometries, the TE polarization is selected due to its greater confinement. Finally, in calculating the effective index and effective area of the remaining geometries leaves the 250x400 nm^2 and 200x470 nm^2 Si-SiO_2 waveguide geometries as optimal for integrated photonic applications.

9.4 Contributions of this work to the AS-EPIC design

Much of the work from this thesis has focused on realizing low loss waveguides capable of integration with CMOS devices and processes. As a result, many of the process and design techniques developed and demonstrated in this thesis were implemented in the AS-EPIC design. In particular, the integration of

waveguides with CMOS circuitry and improved filter performance by the use of hybrid waveguide structures are two significant contributions to the realization of EPIC technology.

9.4.1 Waveguide Integration

The development of a low loss SOI-based waveguides (Chapter 5) and deposited a-Si waveguides (Chapter 6) enable highly confined, optically insulated, sub-micron cross-section channel waveguides, which are compliant with the physical and fabrication tolerances utilized in CMOS processing. Using optimized waveguide geometries, the mode-field area is minimized to reduce losses from field overlaps with absorptive metallic structures, such as electronic interconnects or heaters used to tune the optical filter. These developments have enabled the fabrication and realization of arguably the first CMOS compatible, multi-level EPIC. As can be seen in figure 9.9, a-Si waveguides were fabricated with working CMOS circuitry below.

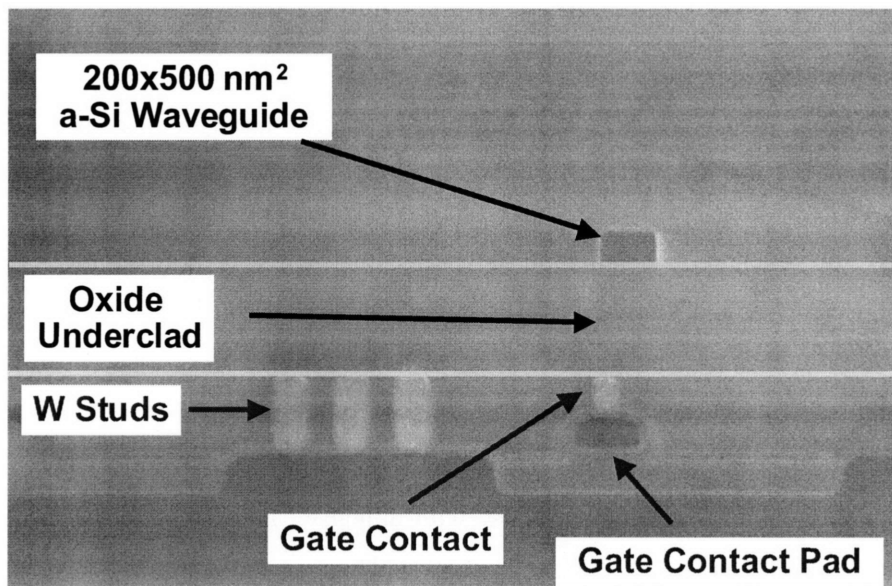

Figure 9.9: Cross-sectional SEM of an integrated amorphous Si waveguide with working CMOS microelectronic devices, courtesy of Andrew Pomerene, BAE Systems.

9.4.2 Improved Filter Response

As discussed earlier, and quantitatively observed in Figure 9.2, the AS-EPIC filter response is extremely sensitive to waveguide transmission loss. The implementation of hybrid SOI waveguides, demonstrated in Section 7.1, dramatically improved the filter response of the AS-EPIC filter. Initial attempts at utilizing single waveguide geometry yielded an average waveguide transmission loss of 12 dB/cm throughout the filter device [130]. However, the incorporation of a hybrid SOI waveguide structure, where the waveguide width is adiabatically increased in wide sections and then decreased for bend or

coupling sections, reduced the average waveguide transmission loss throughout the filter device to 1.6 dB/cm [130].

As seen in Figure 9.10, the hybrid filter architecture is considerably different in appearance than the representation used in Figure 9.2. Rather than use circular rings, the hybrid rings are designed with long straight sections where the waveguide width is increased so as to minimize scattering of the mode field intensity on the rough sidewall. The resulting insertion loss for the fourth order filter using the hybrid approach is less than 6 dB, and a greater than 25 dB stop band rejection [126], meeting the desired AS-EPIC performance metrics.

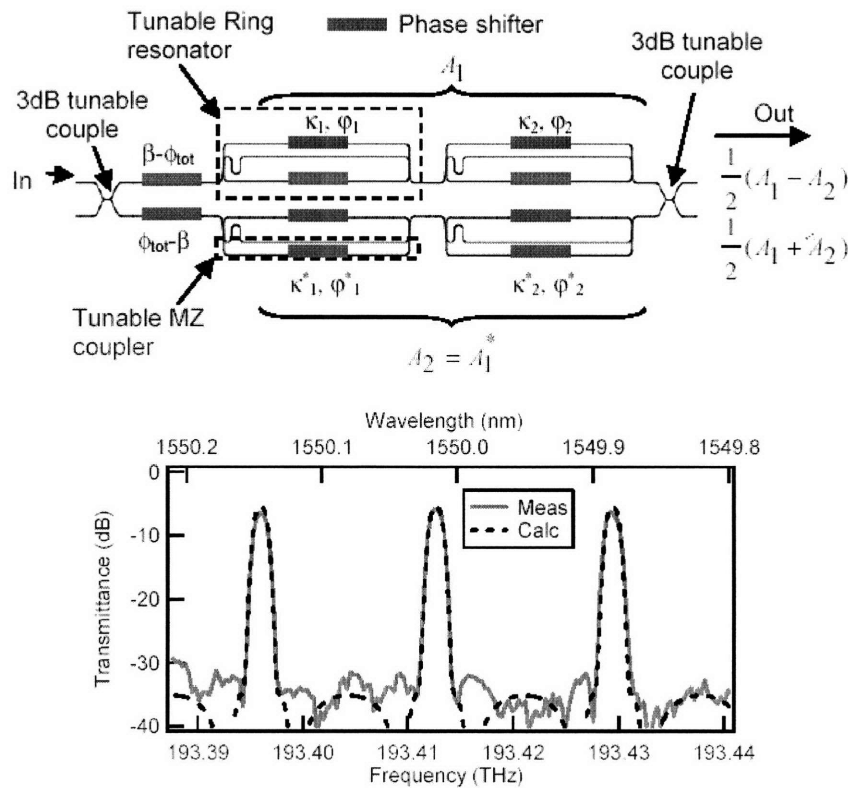

Figure 9.10: Schematic diagram of the AS-EPIC filter architecture (above) and measured filter response, as compared with calculations based on waveguide loss (below), images taken from [126].

Chapter 10 – Conclusions and Future Work

The prospects for integrated, CMOS compatible, photonic circuit technologies are immense. Photonic interconnects offer high data bandwidths with low signal attenuation and virtually zero heat dissipation. Strategic replacement of RC speed-limited electronic interconnects with photonic interconnects is a logical step to improving data processing performance in future microprocessors. Integration of photonic circuits onto electronic chips also enables sought after networking technologies that have higher complexity and unique functionality. Similar to the integrated microchip, the employment of CMOS technology in the fabrication of integrated photonic chips enables high yield, low cost, and increased functionality. In addition, on-chip integration has the benefit of reduced weight, volume, and power consumption, enabling unique technologies such as the AS-EPIC example in Chapter 9 where these savings are crucial and overall functionality is increased. Essentially, the development of an integrated CMOS compatible photonic circuit technology is an enabler of improved communication.

However, there are many challenges in realizing a viable, integrated photonic circuit technology. The constraints associated with fabrication of CMOS compatible, high-index-contrast, planar, thin-film photonic devices add difficulty in realizing the necessary components for a complete photonic circuit. Of these components: light source, waveguide, modulator, splitter, filter, and detector; all are limited in performance and functionality by optical transmission loss. As a result, this thesis has focused on diagnosing and addressing the various loss mechanisms that exist in fabricating CMOS compatible channel waveguides. As the building block of higher order photonic devices, waveguides are useful as diagnostic tools with which one can characterize photonic loss mechanisms. In particular, this work has concentrated on reducing loss in Silicon (amorphous, crystalline, and polycrystalline) and Silicon Nitride, single-mode channel waveguides by developing and optimizing process and design techniques.

10.1 Chapter by Chapter Review

In Chapter 1, the background and motivation for this work is reviewed. The various photonic components which make up a fully functioning integrated circuit are described to fully appreciate the role and constraints that each device plays. In taking account cost, fabrication infrastructure, material compatibility, product yield, and ease of product adoption, the CMOS material platform is deemed optimal for integrating photonic circuits with existing microelectronic devices. Finally, within the CMOS-compatible material system the use of high-index-contrast (HIC) Si-SiO_2 channel waveguides are best suited as the fundamental component of optical interconnects and higher order photonic devices in electronic-photonic integrated chips (EPICs).

In Chapter 2, the relevant physics and calculation methods required for understanding how confined light propagates through a waveguide is reviewed. Unfortunately, many of the common analytical calculation techniques used in determining the eigenvalue solutions to the wave equation are

not accurate for HIC waveguide structures. Hence, the use of numerical mode solving programs is necessary in accurately modeling the mode field distribution. Furthermore, the use of single-mode, HIC, channel waveguides present several unique physical phenomena. First, the asymmetric boundary conditions for the electric and magnetic fields at a dielectric interface, which arise at optical frequencies, result in pronounced differences between the TE and TM mode shape, size, confinement, and effective index. Second, the large difference between the core and cladding indices (Δn), results in a wide range of effective index and therefore propagation constant values. Third, within the single-mode regime, the mode size is indirectly proportional to the channel waveguide dimensions.

In Chapter 3, two methods with which to experimentally measure the transmission loss of waveguides are explored: cutback and Fabry-Perot. Optical measurements of HIC waveguides with standard optical fibers leads to excessive coupling losses, due to the large differences in mode field diameters (MFDs) between the waveguide and fiber modes. High coupling losses impacts the insertion loss measurement of a given waveguide chip, which is the sum of coupling and transmission losses. Ultimately, the goal of measuring waveguides is to obtain transmission loss data, therefore coupling losses should be minimized by using reduced MFD fiber, lens tipped fibers, and or waveguide input couplers. At the end of the chapter, the experimental apparati used for waveguide measurement and effective measurement techniques are discussed.

In Chapter 4, the various loss mechanisms that occur in waveguides: roughness-scattering, absorption, non-linear processes, waveguide coupling, substrate leakage, mode coupling, and bend loss are identified and described in terms of the critical waveguide process and design variables. For each of these loss mechanisms, the distribution and magnitude of optical power in the waveguide structure has a direct effect on the overall loss. For waveguide coupling and substrate leakage, the overlap of the evanescent field overlap with other waveguide structures leads to optical coupling loss. For non-linear and linear absorption, the loss is a function of the optical power distribution and intensity within the waveguide materials. While for roughness scattering, the loss is governed by the interface field intensity. Losses that arise from non-linear processes, waveguide coupling, substrate leakage, mode coupling, and bend loss can be avoided with minimal design effort; although it is worth recognizing that these loss mechanisms do arise when researching new waveguide materials and processing methods. In contrast, the loss mechanisms that are processing based: roughness-scattering and absorption loss, remain the major challenges to realizing low-loss waveguides and are a major focus this work.

In Chapter 5, the processing of crystalline silicon waveguides was investigated. Single-mode SOI channel waveguides are favorable for integration with conventional CMOS microelectronics; however epitaxial limitations limit their use to a single chip level. Transmission losses in SOI waveguides are dominated by light scattering from the rough sidewall interfaces, that arise from the etch process, and

therefore presents a metric with which to gauge the pattern transfer process. SOI channel waveguide losses, measured from chips fabricated in the initial BAE Systems process run, were comparable in magnitude (3.4 dB/cm, TE mode, for the 200 x 570 nm^2 geometry) to the best results reported in the literature, despite the presence of air-voids near the base of the waveguide sidewalls.

Experimental SOI waveguide losses were measured for a variety of waveguide geometries and used to confirm the accuracy of the newly developed Barwicz-Haus theory of roughness-scattering in HIC waveguides. This development is important as it invalidates the widely used Payne-Lacey theory which greatly overestimates loss for a given sidewall roughness. Using the Barwicz-Haus theory, a comparison of SOI channel waveguide loss values was presented. Interestingly, the wide range of losses reported in the literature is more a factor of differing waveguide geometries than sidewall roughness values.

In efforts to reduce SOI waveguide losses, several post-etch smoothing methods to reduce sidewall roughness were explored. Dry thermal oxidation treatments were found to effectively reduce the sidewall roughness; however the accompanying elevated process temperatures and excessive silicon consumption are undesirable for integrated applications. In seeking to improve the sidewall smoothing efficiency, a multiple oxidation smoothing method was devised, where multiple steps of oxidation separated by etch steps, each time the oxidation kinetics transitioned from the reaction-limited regime to the diffusion limited regime, are used to smooth the rough surface. This multi-stepped approach was utilized in developing the wet chemical oxidation smoothing process. Wet chemical oxidation smoothing is a relatively easy, effective method of reducing transmission loss without sacrificing waveguide dimensional integrity or thermal budget; ideal for integrated photonic circuit fabrication. For the case of the air-clad 220x630 nm^2 TE-mode SOI waveguide structure, a 5X RCA wet chemical treatment lowered transmission loss from 10.1 dB/cm to 3.4 dB/cm. These impressive results came from a proof-of-concept study and are bound to improve with further investigation.

In Chapter 6, three CMOS compatible, HIC, deposited waveguide materials were investigated: silicon nitride (SiN), amorphous silicon (a-Si), and polycrystalline silicon (poly-Si). Deposited waveguide materials are vital to routing optical signals in multiple chip-levels, adding versatility and design freedoms which can improve data processing and communication. However, in addition to roughness-scattering losses, deposited waveguide materials suffer from material absorption losses. Interestingly, the presence of hydrogen is desirable for deposited Si waveguide materials and undesirable for SiN waveguide materials.

For SiN, the imperfect dissociation of the SiH_4 and NH_3 precursors results in substantial hydrogen incorporation. This is problematic in that the nitrogen-hydrogen bond (N-H) is resonant within the telecom spectrum, resulting in optical absorption of the signal. For waveguide integration purposes, attention focused on PECVD SiN materials which are deposited at low temperatures. Utilizing improved

(low H-content) precursor recipes, some of the lowest, low temperature deposition, loss results were realized (1.5 dB/cm for a 400x800 nm^2 DCVD-400, TE Mode, SiN-SiO_2 channel waveguide). In addition to PECVD materials, a high temperature LPCVD deposited SiN material, with excess Si-content, was investigated for loss comparison. Unexpectedly, the loss was considerably higher for this SiN material despite its lower H-content. Broad spectral loss measurements reveal that bulk scattering, most likely from silicon nanocrystal formation due to the combination of elevated deposition temperature and excessive Si-content, is the probable loss mechanism.

For a-Si, the imperfect dissociation of the SiH_4 precursors is beneficial to reducing waveguide bulk absorption. The presence of hydrogen satisfies dangling bond states which act as optical absorption centers in the telecom spectrum. By lowering the PECVD deposition power, the hydrogen content within the a-Si film is raised and the bulk absorption loss is reduced. Using a technique (developed here) to estimate bulk loss from waveguide transmission loss data, the a-Si bulk loss was found to decrease from 15.2 ± 2 dB/cm to 0 ± 1 dB/cm when the PECVD deposition power was lowered from 100 W to 25 W. Even with an excessively absorptive SiN nanocladding layer, the TE and TM mode losses for the 25 W, 200x500 nm^2, a-Si-SiO_2 channel waveguides were 6 – 7 dB/cm. These results, which are comparable with SOI waveguide losses, represent the world's best bulk loss and channel waveguide losses for a-Si materials.

Similar to a-Si, the poly-Si waveguide materials benefit from increased H-content. Prior attempts at poly-Si waveguide fabrication utilized an anneal step to crystallize a-Si waveguides post-etch, however in this study, the a-Si layer was annealed and transformed into poly-Si prior to etching. It is believed that this process step alteration is responsible for improved poly-Si waveguide loss. Losses as low as 8 ± 3 dB/cm for a 200x450 nm^2 TM mode poly-Si-SiO_2 waveguide were measured, representing the only (and by default, lowest) single-mode poly-Si waveguide losses ever reported.

In chapter 7, improved waveguide design was utilized to optimize waveguide transmission for a given waveguide material and fabrication process. Using geometric techniques, the loss for a single-mode SOI waveguide was reduced to 0.35 dB/cm by employing a hybrid waveguide structure approach where the waveguide width is adiabatically tapered out (to maintain single-mode operation) to reduce the field intensity at the rough sidewall. Similarly, for absorption limited waveguides, the use of a hybrid waveguide structure, where the waveguide width is tapered in to minimize field overlap with the absorptive core material, was proposed. The use of a thin, conformal nanocladding layer to reduce roughness sensitivity for a given HIC waveguide was demonstrated. Finally the use of {110} SOI substrates was proposed for fabricating ultra-low loss, highly confined, SOI waveguides.

In Chapter 8, ring resonator devices were analyzed in the context of material optimization and HIC waveguide design where the feasibility and limitations of the devices are surmised for CMOS

compatible materials. Particular attention was spent on 1) trimming a ring resonator resonance with a UV-sensitive polymer cladding and 2) modeling and optimizing ring modulator designs for SiGe materials.

Non-deterministic pattern transfer errors limit dimensional precision and preclude the fabrication of identical devices across an entire wafer. Hence, a post-production trimming process to modify the effective index of the ring to precisely define the resonant wavelength λ_0 is essential. In this work, a novel photo-oxidation trimming method, using a UV-sensitive, PECVD polysilane top cladding, deposited on SiN ring resonators and waveguides, was investigated. The UV-induced refractive index decrease (4%) allowed for resonance shifts as large as $\Delta\lambda = 23.5$ nm with Si_3N_4 rings. The experimental trimming results matched well to simulations. As a quick, localized, and controllable technique to produce large and precise resonance shifts, photo-oxidation trimming of PECVD polysilane clad waveguides provides an attractive alternative to conventional trimming techniques.

The sensitivity of ring resonators to variations in cavity length also make them well suited for modulator applications. By employing a mechanism that varies the index of the core or cladding (similar to ring trimming, but faster and reversible), a ring resonator can act as a modulator device. In this work, ring modulator operation was modeled in the context of HIC material properties and waveguide loss. For CMOS compatible materials, the fast Franz-Keyldish effect in SiGe materials is extremely attractive for modulation applications at λ=1550 nm. Interestingly, SiGe alloys optimized for electro-absorption applications exhibited larger modulation depths in device simulations than SiGe alloys optimized for electro-optic applications. While the extinction ratio of SiGe ring modulators is limited due to high absorptive losses, the linking of several SiGe modulators in series can improve the modulation depth with only a slight increase in insertion loss.

Finally, in chapter 9, the challenge of creating a CMOS-compatible electronic-photonic integrated chip (EPIC) is explored in the context of an application specific (AS-EPIC) design. In this study, the CMOS process challenges: material limitations, epitaxial compatibilities, thermal-budget imposed process order, and device communication requirements are discussed and utilized in arriving at an optimal AS-EPIC architecture. An optimal integrated waveguide geometry was also investigated wherein the 200x470 nm^2 Si-SiO_2 channel waveguide, for the TE mode, best met the high confinement, low loss, sub-micron cross-section requirements of EPICs. Lastly, the contributions of this work to the realization of the AS-EPIC are discussed. In particular, the incorporation of low loss a-Si waveguides and extremely low loss SOI hybrid waveguide structures facilitate improved AS-EPIC operation performance.

In conclusion, this thesis has developed process and design techniques to enable CMOS-compatible, low-loss, integrated silicon photonic circuit technology for high-bandwidth communication and computation applications.

10.2 Future Work

While the work in this thesis has added to realizing an integrated photonic circuit technology based on the CMOS platform, there is still much work to be done. Waveguide losses of the order of dB/cm are adequate for many integrated applications, however lower waveguide losses are always desired as they relieve system tolerances and improve device performance. In extending this work, the following future experiments are recommended

10.2.1 Silicon-on-Insulator (SOI) Based Waveguides

- Improve Sidewall Roughness – Sidewall roughness-scattering is the limiting loss mechanism for SOI-based waveguides. As discussed in section 5.2.4, the waveguide sidewall roughness, as estimated by Barwicz-Haus theory, is nearly identical for the top contending SOI waveguide research groups. This makes sense since each group uses approximately the same fabrication tools. The cause of the roughness is still under debate; but most likely arises from photoresist roughness and erosion. However, as process improvements reduce the roughness to the atomic level, the wave-nature of the interface invalidates the traditional description of roughness and the associated modeling of roughness-scattering.
- Optimize Wet Chemical Smoothing Chemistries – The wet chemical smoothing technique developed in this work was a proof-of-concept study which exhibited notable waveguide sidewall smoothing results. In efforts to improve the effectiveness of this technique, a more rigorous and encompassing wet chemical study should be investigated.
- Investigate the Role of SOI waveguide surface contaminants – The presence of water and other contaminants at the core-cladding interface can add considerable loss to waveguides [134], a contaminant free cladding process should be investigated.
- Investigate the Role of Surface Defect States on SOI waveguide sidewalls – Surface defect states that arise from improper bonding at a crystalline interface, similar to the dangling bond defects in a-Si, act as optical absorption centers. Surface states passivation methods should be investigated.
- Investigate the Role of Bulk Defects in SOI – The presence of defects in the Si-bulk, that arise and diffuse from the sidewall interface during the etch process [131], may act as optical absorption centers in SOI waveguides. To understand the extent of this loss mechanism, these defects must be characterized.

- Investigate the SOI interface – The $Si\text{-}SiO_2$ interface on SOI wafers is assumed to be smooth, however recent SOI agglomerations studies have observed nm-scale roughness at this interface [132]. Reduction of interface roughness is critical for realizing low loss waveguides.
- Fabricate (110) SOI waveguides that run along the <211> – As discussed in section 7.3, this waveguide geometry has (111) sidewalls. Therefore, the use of an anisotropic etch can smooth the sidewalls to atomic smoothness, without affecting the waveguide shape, enabling ultra-low loss $Si\text{-}SiO_2$ channel waveguides.

10.2.2 Deposited Waveguide Materials

- Investigate methods of removing H from SiN – The N-H bond resonance is the dominant loss mechanism for SiN materials. The SiN materials studied in this thesis utilized improved precursor chemistries to reduce the H-content in the SiN film, however in keeping with low temperature depositions for integration purposes; these optimized SiN materials exhibited significant absorption of infra-red light. To combat this phenomenon, post-deposition methods of removing H from SiN should be investigated, such as using a high powered laser which is resonant with the N-H bond. Alternatively, deuterium-based precursors could be employed as the N-D resonance is outside the telecom spectrum.
- Fabricate low-loss a-Si waveguides – Low bulk-loss a-Si waveguides were demonstrated in this work, however the presence of an absorptive SiN nanocladding layer dominated the waveguide transmission losses. To fully appreciate the significance of developing a low bulk-loss, high index contrast, deposited waveguide material; single-mode channel waveguides must be fabricated. As an added bonus, the isotropic nature of a-Si waveguides should result in smoother sidewalls. Transmission losses of < 2 dB/cm are expected for $a\text{-}Si\text{-}SiO_2$ channel waveguides.
- Improve poly-Si losses – Poly-Si waveguides have excessive roughness-scattering and material absorption losses. However, the slab anneal approach used in fabricating poly-Si waveguides in this work, which yielded relatively low losses, may work even better if a diffusion barrier (such as SiN) is used to keep the H-content from decreasing during the a-Si to poly-Si transformation. Afterwards, the SiN material (if it happens to induce absorptive loss) can be polished away.

10.2.3 Ring Resonator Devices

- Investigate reversible trimming materials – The ability to trim the resonance of a ring resonator by increasing or decreasing the effective index of the waveguide is useful and forgiving to processing errors. One option is the use of chalcogenide glasses which have an index of $n \sim 2$

and can be used as a waveguide material. For example, the exposure of As_2S_3 to high intensity visible light can shift the index by 10^{-2} and reversed with an annealing step [133].

- Fabricate SiGe ring modulators – The Franz-Keyldish effect in SiGe is one of the few methods of realizing a CMOS compatible modulator that can scale up to 40 GHz and beyond. Other device geometries should be considered.

10.2.4 Integration

- Investigate detector materials with lower process temperatures – The integration of Ge detectors into an EPIC places many constraints on the process flow and architecture. The required elevated process temperatures preclude the fabrication of low loss a-Si waveguides in any process steps prior to Ge deposition. One possibility is to investigate PECVD deposited Ge materials. Alternatively other low process temperature detector materials should be investigated. Another possibility is to use localized laser annealing relieve to thermal budget restrictions.
- Investigate the use of polymer cladding materials for temperature-insensitive waveguide devices. The sensitivity of photonic device performance on operation temperature will almost certainly require the use of thermal compensation, either by the use of a thermal electric cooler (TEC) or individual integrated micro-heaters, to realize optimal operation. However, by properly balancing the thermo-optic coefficients with the relative optical power distribution in the core and cladding materials, such as by using a dielectric core material with a positive thermo-optic coefficient and a polymer cladding with a negative thermo-optic materials, it is possible to create a temperature-insensitive waveguide devices. Thereby eliminating the complications of thermal compensation.

Appendix A – Fabry-Perot Loss Derivation

Fabry-Perot transmission loss is determined by the ratio between the maximum resonant output power and the minimum antiresonant power of the guided light. To understand this relationship, the loss coefficient for a Fabry-Perot cavity is derived using phase notation, see [23] for more details on this notation.

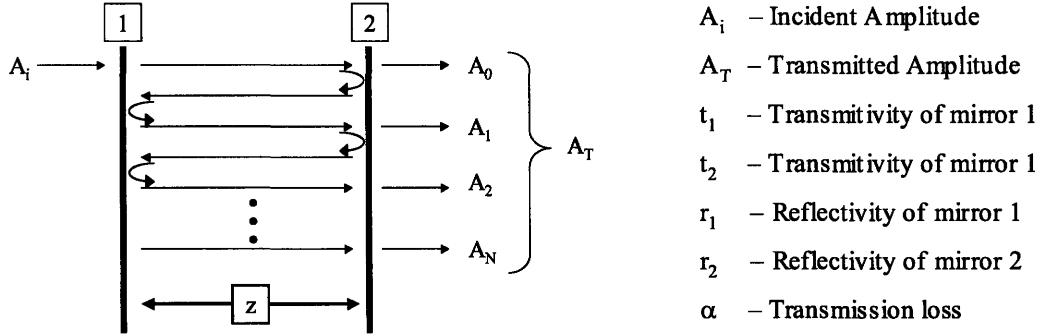

Figure A.1 – Illustration of a Fabry-Perot Cavity

Figure A.1 depicts a typical fabry-perot cavity formed by two mirrors separated by a distance z. For the case of waveguide measurement, mirrors 1 and 2 are the input an output facets and z is the length of the waveguide. The field amplitude of the cavity transmission is the summation of A_0 through A_N.

$$A_T = \sum_{N=0}^{\infty} A_N \tag{A.1}$$

For a given frequency of light, the relations for the field amplitudes A_0, A_1, and A_2 in terms of phase notation are listed below. For example, the field amplitude A_0 is the product of the phase notation for transmitting through mirror 1 ($i\ t_1$), propagating through a length z with loss α ($e^{-\alpha z/2}$), and then transmitting through mirror 2 ($i\ t_2$). Field amplitude A_1 is similar to A_0 with the addition of one round trip or reflections in the cavity, A_2 adds two round trips, and A_N adds N round trips. Each reflection adds a phase shift δ to the reflected light and is realized as $e^{i\delta/2}$. It is important to note that the α used, throughout this derivation, is the loss for a given intensity of the light and not the amplitude; the two differ by a factor of two: $\alpha_{\text{Intensity}} = 2\ \alpha_{\text{Amplitude}}$.

$$\begin{aligned} A_0 &= i\,t_1\, e^{-\frac{\alpha z}{2}}\, i\,t_2\, A_i \\ A_1 &= i\,t_1\, e^{-\frac{\alpha z}{2}}\, r_2\, e^{i\frac{\delta}{2}} e^{-\frac{\alpha z}{2}}\, r_1\, e^{i\frac{\delta}{2}} e^{-\frac{\alpha z}{2}}\, i\,t_2\, A_i \\ A_2 &= i\,t_1\, e^{-\frac{\alpha z}{2}} \left(r_2\, e^{i\frac{\delta}{2}} e^{-\frac{\alpha z}{2}}\, r_1\, e^{i\frac{\delta}{2}} e^{-\frac{\alpha z}{2}} \right)^2 i\,t_2\, A_i \end{aligned} \tag{A.2}$$

As the process continues, we see the trend:

$$A_N = -t_1 t_2 \, e^{-\frac{\alpha z}{2}} \left(r_1 r_2 \, e^{i\delta} e^{-\alpha z} \right)^N A_i \tag{A.3}$$

Assuming that both mirrors have the same reflectivity and transmitivity coefficients r and t, we define the reflection and transmission coefficients R and T and their relation:

$$\begin{array}{lll} t = t_1 = t_2 & T = t^2 & T = 1 - R \\ r = r_1 = r_2 & R = r^2 & \end{array} \tag{A.4}$$

Combining (A.1), (A.3), and (A.4) we find

$$A_T = -\left(1 - R\right) e^{-\frac{\alpha z}{2}} \sum_{N=0}^{\infty} \left(R \, e^{i\delta} e^{-\alpha z} \right)^N A_i \tag{A.5}$$

Recalling the relation

$$\sum_{N=0}^{\infty} x^N = \frac{1}{1 - x} \qquad -1 \leq x \leq 1 \tag{A.6}$$

This allows us to appreciate the relationship between the transmitted and incident amplitudes of a given Fabry-Perot cavity with identical mirrors forming a cavity of length z in a more tractable form.

$$A_T = \frac{-\left(1 - R\right) e^{-\frac{\alpha z}{2}}}{1 - R \, e^{i\delta} e^{-\alpha z}} A_i \tag{A.7}$$

This relation can be rewritten in terms of intensity, rather than amplitude.

$$\frac{I_T}{I_i} = \frac{A_T \, A_T^*}{A_i \, A_i^*} = \frac{\left(1 - R\right)^2 e^{-\alpha z}}{\left(1 - R \, e^{-\alpha z}\right)^2 + 4 \, \mathrm{Re}^{-\alpha z} \sin^2\left(\frac{\delta}{2}\right)} \tag{A.8}$$

As mentioned above, Fabry-Perot Loss measurements use the relative maximum and minimum intensity ratio to determine the loss of the cavity. This occurs in equation (A.8) when:

$$\begin{aligned} \textit{Maximum Intensity} &\rightarrow \sin^2\left(\tfrac{\delta}{2}\right) = 0 \\ \textit{Minimum Intensity} &\rightarrow \sin^2\left(\tfrac{\delta}{2}\right) = 1 \end{aligned} \tag{A.9}$$

Thus a change in the phase shift δ of the cavity will modulate the transmitted intensity of the cavity and from this the loss can be found. In terms of waveguide measurement, a tunable laser wavelength scan of the cavity will create an oscillating intensity output corresponding to the phase shift associated with the wavelength going in and out of resonance. The ratio of maximum to minimum intensity as the phase shift varies is:

$$\frac{I_{\min}}{I_{\max}} = \frac{\left(1 - R\,e^{-\alpha z}\right)^2}{\left(1 - R\,e^{-\alpha z}\right)^2 + 4\mathrm{R}e^{-\alpha z}} \tag{A.10}$$

Solving (A.10) for α, we find the Fabry-Perot Loss relation.

$$\alpha = \frac{1}{z}\ln\left(R\,\frac{1+\sqrt{\frac{I_{\min}}{I_{\max}}}}{1-\sqrt{\frac{I_{\min}}{I_{\max}}}} \right) \tag{A.11}$$

Appendix B – Snell's Law

The angular dependence of reflected and transmitted light at an interface, or what is known as refraction, is governed by the conservation of momentum of the wave vector. As sketched in figure B.1, light incident upon an interface can be reflected and transmitted. Here light in a medium of index n_1 and wave vector $k^{(1)}_+$ encounters an interface with a medium with index n_2 at an angle of θ_i. At the interface, light is reflected at an angle of θ_R with wave vector $k^{(1)}_-$ or transmitted at an angle of θ_T with wave vector $k^{(2)}_+$.

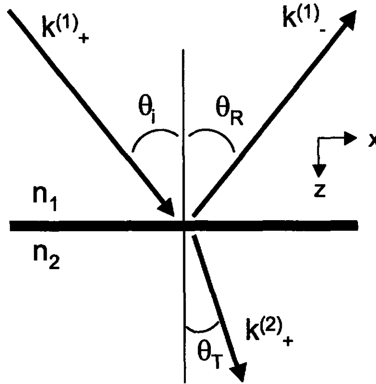

Figure B.1 – Optical interface in the plane of incidence.

Neglecting the amplitudes of the incident, reflected, and transmitted light, the oscillatory nature of these waves in terms of time and space can be respectively written:

$$e^{i\left(\omega_+^{(1)}t-k_+^{(1)}r\right)} \quad e^{i\left(\omega_-^{(1)}t-k_-^{(1)}r\right)} \quad e^{i\left(\omega_+^{(2)}t-k_+^{(2)}r\right)} \tag{B.1}$$

Temporally, the frequency of light remains the same regardless of the medium

$$\omega_+^{(1)} = \omega_-^{(1)} = \omega_+^{(2)} = \omega \tag{B.2}$$

With boundary condition (2.25), we realize that the magnitude of E and H are independent of index and therefore it follows that the wave vectors in the x and y directions, parallel to the interface, are independent as well:

$$\begin{aligned} k_{x+}^{(1)} = k_{x-}^{(1)} = k_{x+}^{(2)} = k_x \\ k_{y+}^{(1)} = k_{y-}^{(1)} = k_{y+}^{(2)} = k_y \end{aligned} \tag{B.3}$$

where $\sqrt{k_x^2+k_y^2+k_z^2}=k$. Recalling relation 2.17, we see that the lengths of the different wave vectors are independent of direction but dependent on the index.

$$\begin{aligned} k_+^{(1)} &= k_-^{(1)} = \frac{\omega}{c}n_1 \\ k_+^{(2)} &= \frac{\omega}{c}n_2 \end{aligned} \tag{B.4}$$

Thus at an interface, the incident and reflected wave vectors are not only equivalent in length (B.4) but have equivalent vector component magnitudes parallel to the interface (B.3). Ultimately, this implies that the angle of incidence is equivalent to the angle of reflection $\theta_i=\theta_R$.

Orthogonal to the interface, the wave vectors can be geometrically related:

$$k_+^{(1)}\sin(\theta_i) = k_+^{(2)}\sin(\theta_T) \tag{B.5}$$

However, by using relations (B.2), and (B.4), equation (B.5) can be rewritten as the more familiar Snell's law:

$$n_1\sin(\theta_1) = n_2\sin(\theta_2) \tag{B.6}$$

where the subscripts have been generalized to represent the two media.

References

1. "Communications Technology Roadmap", The Microphotonics Center, Massachusetts Institute of Technology, 2005
2. Gordon E. Moore, "Cramming More Components onto Integrated Circuits", *Electronics* Magazine, Vol. 38, No. 8 (1965)
3. David A. Muller, "A Sound Barrier for Silicon?", *Nature Materials*, Vol. 4, p. 645-647 (2005)
4. "Amdahl's Law", *Wikipedia,* Retrieved December 19, 2005 from http://en.wikipedia.org/wiki/Amdahl's_law
5. R.M. Ramanathan and V. Thomas, eds., "Platform 2015: Intel® Processor and Platform Evolution for the Next Decade", *Intel Research,* Retrieved December 19, 2005 from ftp://download.intel.com/technology/computing/archinnov/platform2015/download/Platform_2015.pdf
6. Tom Krazit, (October 14, 2004), "Intel Shelves Plans for 4-GHz P4", *PC World*, Retrieved December 19, 2005 from http://www.pcworld.com/news/article/0,aid,118165,pg,1,RSS,RSS,00.asp
7. Alex Salkever, (December 17, 2003), "A G5 Laptop? Maybe Next Year", *Business Week Online*, Retrieved December 19, 2005 from http://www.businessweek.com/technology/content/dec2003/tc20031217_5848_tc056.htm
8. Patrick Schmid, (December 4, 2005), "Top Secret Intel Plans Uncovered", *Toms Hardware*, Retrieved December 19, 2005 from http://www.tomshardware.com/2005/12/04/top_secret_intel_processor_plans_uncovered/index.html
9. "The Cell Architecture", *IBM Research,* Retrieved December 19, 2005 from http://domino.research.ibm.com/comm/research.nsf/pages/r.arch.innovation.html
10. J. Kash and J. Trewhella, "Optical Interconnects: Server Applications," MIT CTR report, 2003
11. "EPIC Electronic & Photonic Integrated Circuits", *Microsystems Technology Office*, Retrieved December 19, 2005 from http://www.darpa.mil/mto/epic/
12. C.V. Thompson, *Massachusetts Institute of Technology*, 3.44 class notes, Fall 2001
13. Y.A. Vlasov, S.J. McNab, "Losses in single-mode silicon-on-insulator strip waveguides and bends" *Optics Express* **12** (8) p.1622-1631 (2004)
14. Victor T. Nguyen "Efficient Coupling to Waveguides in High Index Contrast Systems" *Ph.D. Thesis, Massachusetts Institute of Technology* (2005)
15. T. Barwicz, M.A. Popovic, P.T. Rakich, M.R. Watts, H.A. Haus, E.P. Ippen, and H.I. Smith, "Microring-resonator-based add-drop filters in SiN: fabrication and analysis" *Optics Express* **12** (7) p. 1437-1442 (2004)
16. V.R. Almeida, C.A. Barrios, R.R. Panepucci, and M. Lipson, "All-optical control of light on a silicon chip" *Nature* **431** p.1081-1084 (2004)
17. J. Liu, J. Michel, W. Giziewicz, D. Pan, K. Wada, D.D. Cannon, S. Jongthammanurak, D.T. Danielson, L.C. Kimerling, J. Chen, F.O. Iiday, F.X. Kartner, J. Yasaitis, "High-performance, tensile-strained Ge p-i-n photodetectors on a Si platform" *Applied Physics Letters* **87** (10) p.105501-1-3 (2005)
18. R.J. Walters, G.I. Bourianoff, H.A. Atwater, "Field-effect electroluminesence in silicon nanocrystals" *Nature Materials* **4** p.143-146 (2005)
19. J. S. Shaw, University of Georgia, Department of Physics, 1010 class home page, Retrieved February 28, 2006 from http://hal.physast.uga.edu/~jss/1010/ch6/emwave.jpg
20. B.K. Heffner and P.R. Hernday, "Measurement of Polarization-Mode Dispersion" *hp journal online*, February 1995, Article 4, Retrieved March 1, 2006 from http://www.hpl.hp.com/hpjournal/95feb/feb95a4b.pdf
21. S.L. Chuang, "Physics of Optoelectronic Devices" (John Wiley & Sons, NY, 1995)
22. L.A. Coldren, S.W. Corzine, "Diode Lasers and Photonic Integrated Circuits" (John Wiley & Sons, NY, 1995)
23. H.A Haus "Waves and Fields in Optoelectronics" (Prentice-Hall, Englewood Cliffs, NJ, 1984)
24. Corning® Single Mode Fiber, SMF-28™ Fiber, Retrieved October 25, 2005 from http://www.corning.com
25. G. Roelkens, P. Dumon, W. Bogaerts, D.V. Thourhout, R. Baets, "Efficient Silicon-on-Insulator Fiber Coupler Fabricated Using 248-nm-Deep UV Lithography" *IEEE Photonics Technology Letters* **17** (12) p. 2613 – 2615 (2005)
26. K.K. Lee, D.R. Lim, D. Pan, C. Hoepfner, W-Y Oh, K. Wada, L.C. Kimerling, K.P. Yap, M.T. Doan "Mode transformer for miniaturized optical circuits" *Optics Letters* **30** (5) p.498-500 (2005)
27. C. Gunn "CMOS Photonics™ -- SOI Learns a New Trick" *IEEE International SOI Conference*, (IEEE Cat. No. 05CH37694), p. 7-13 (2005)

28. C.M. Herzinger, C.C. Lu, T.A. DeTemple, W.C. Chew, "The Semiconductor Waveguide Facet Reflectivity Problem" *IEEE Journal of Quantum Electronics* **29** (8) p.2273-2281 (1993)
29. N.N. Feng, W-P Huang, "A Simple Noniterative Solution Scheme for Facet Reflectivity of Optical Waveguides" *IEEE Journal of Lightwave Technology* **22** (2) p.664 – 668 (2004)
30. B.E.A. Saleh, M.C. Teich, "Fundamental of Photonics" (John Wiley & Sons, NY, 1991)
31. A. Liu, R. Jones, L. Liao, D. Samara-Rubio, D. Rubin, O. Cohen, R. Nicolaescu, M. Paniccia, "A high-speed silicon optical modulator based on metal-oxide-semiconductor capacitor" *Nature* **427** (6975) p.615-618 (2004)
32. H. Deng, D.O. Yevick, S.K. Chaudhuri "Bending Characteristics of Asymmetric SOI Polarization Rotators" *IEEE Photonics Technology Letters*, **17** (10) p. 2113-2115 (2005)
33. T. Yoshinobu, A. Iwamoto, K. Sudoh, H. Iwasaki, "Scaling of Si/SiO_2 Interface Roughness" *Journal of Vacuum Science Technology B* **13** (4), p. 1630 – 1634 (1995)
34. D. Marcuse, "Mode Conversion Caused by Surface Imperfections of a Dielectric Slab Waveguide", *The Bell System Technical Journal*, **48**, p.3187-3215 (1969)
35. J.P.R. Lacey and F.P. Payne, "Radiation Loss from Planar Waveguides with Random Wall Imperfections", *IEEE Proc. J. Optoelectronics*, **137**, No.4, p.282-288 (1990)
36. F.P. Payne and J.P.R. Lacey, "A Theoretical Analysis of Scattering Loss from Planar Optical Waveguides", *IEEE Opt. Quantum Electron.*, **26**, p.977-986 (1994)
37. M. Kuznetsov and H.A. Haus, "Radiation Loss in Dielectric Waveguide Structures by the Volume Current Method", *IEEE Journal of Quantum Electronics*, **QE-19**, No.10, p.1505 – 1514 (1983)
38. F. Ladouceur, J.D. Love, T.J. Senden, "Measurement of Surface Roughness in Buried Channel Waveguides", *Electronic Letters*, **28**, No. 14, p.1321-1322 (1992)
39. T. Barwicz, H.I. Smith, "Evolution of line-edge roughness during fabrication of high-index-contrast microphotonic devices", *J. Vac. Sci. Technol. B*, **21**, No. 6, p.2892 – 2896 (2003)
40. T. Barwicz and H.A. Haus "Three-Dimensional Analysis of Scattering Losses Due to Sidewall Roughness in Microphotonic Waveguides", *IEEE Journal of Lightwave Technology*, **23**, No.9, p.2719-2732 (2005)
41. H. Kuribayashi, R. Hiruta, R. Shimizu, " Shape transformation of silicon trenches during hydrogen annealing" *J. Vac. Sci. Technol. A*, **21**, No.4, p.1279 – 1283 (2003)
42. K.K. Lee, D.R. Lim, H-C Luan, A. Agarwal, J. Foresi, and L.C. Kimerling, "Effect of size and roughness on light transmission in a Si/SiO_2 waveguide: Experiments and model" *Applied Physics Letters*, **17**, No.11, p.1617-1619 (2000)
43. S.J. Spector, T.M. Lyszczarz, M.W. Geis, J. Yoon, D.M. Lennon, S. Deneault, "Reflections in Silicon on Insulator (SOI) Waveguides and Ring Resonators" *OSA Integrated Photonics Research and Applications Topical Meeting,* To be presented April 24-26, 2006
44. F. Ay, A. Aydinli "Comparative investigation of hydrogen bonding in silicon based PECVD grown dielectrics for optical waveguides" *Optical Materials*, **26** p.33-46 (2004)
45. F. Iacona, C. Bongiorno, C. Spinella, S. Boninelli and F. Priolo, "Formation and evolution of luminescent Si nanoclusters produced by thermal annealing of SiO_x films," *Journal of Appied Physics*, **95** (7), p. 3723 (2004)
46. L. Pavesi, D.J. Lockwood, *Silicon Photonics,* Springer-Verlag, Berlin (2004).
47. M. Fujii, M. Yoshida, Y. Kanzawa, S. Hayashi, K. Yamamoto, "1.54 μm photoluminescence of Er^{3+} doped into SiO_2 films containing Si nanocrystals: Evidence for energy transfer from Si nanocrystals to Er^{3+}," Applied Physics Letters **71** (9), pp. 1198 (1997)
48. P. Pellegrino, B. Garrido, C. Garcia, J. Arbiol, J. R. Morante, M. Melchiorri, N. Daldosso, L. Pavesi, E. Scheid and G. Sarrabayrouse, "Low-loss rib waveguides containing Si nanocrystals embedded in SiO_2", Journal of Applied Physics, **97** (7), p. 074312 (2005)
49. R.A. Soref, B.R. Bennett "Kramers-Kronig analysis of E-O switching in silicon" *SPIE Integrated Optical Circuit Engineering* **704** , (1986)
50. A. C. Adams, D. P. Schinke, and C. D. Capio, "An Evaluation of the Prism Coupler for Measuring the Thickness and Refractive Index of Dielectric Films on Silicon Substrates", *Journal of the Electrochemical Society*, **126**, 1539 (1979).
51. Neil W. Ashcroft and N. David Mermin, "Solid State Physics" Harcourt Brace College Publishers, New York, 1979
52. R. Claps, D. Dimitropoulos, V. Raghunathan, Y. Han, B. Jalali, "Observation of stimulated Raman amplification in silicon waveguides" *Optics Express*, **11** (5), p. 1731 – 1739 (2003)
53. R.L. Espinosa, J.I. Dadap, R.M. Osgood Jr., S.J. McNab, Y.A. Vlasov, "Raman amplification in ultrasmall silicon-on-insulator wire waveguides" *Optics Express* **12** (16) p.3713 – 3718 (2004)

54. R. Claps, V. Raghunathan, D. Dimitropoulos, B. Jalali, "Influence of nonlinear absorption on Raman amplification in Silicon waveguides" *Optics Express*, **12** (12), p. 2774 – 2779 (2004)
55. M. Dinu, F. Quochi, H. Garcia, "Third-order nonlinearities in silicon at telecom wavelengths" *Applied Physics Letters,* **82** (18), p. 2954 – 2956 (2003)
56. H. Rong, A. Liu, R. Jones, O. Cohen, D. Hak, R. Nicolaescu, A. Fang, M. Paniccia, " An all-silicon Raman laser" *Nature*, **433** (7023), p.292 – 294 (2005)
57. H.K. Tsang, R.V. Penty, I.H. White, R.S. Grant, W.Sibbett, J.B.D. Soole, H.P. LeBlanc, N.C. Andreadakis, R. Bhat, M.A. Koza, "Two-photon absorption and self-phase modulation in InGaAsP/InP multi-quantum-well waveguides" *Journal of Applied Phyics,* **70** (7), p. 3992 – 3994 (1991)
58. H.A. Haus, W.P. Huang, S. Kawakami, N.A. Whitaker "Coupled-Mode Theory of Optical Waveguides" *Journal of Lightwave Technology*, **LT-5** (1), p.16-23 (1987)
59. M.R. Watts, H.A. Haus, "Integrated mode-evolution-based polarization rotator" *Optics Letters*, **30** (2), p.138-140 (2005)
60. H. Deng, D.O. Yevick, S.K. Chaudhuri "Bending Characteristics of Asymmetric SOI Polarization Rotators" *IEEE Photonics Technology Letters*, **17**(10) p. 2113-2115 (2005)
61. E.A.J. Marcatili, "Bends in Optical Dielectric Guides" *The Bell System Technical Journal*, **48** (7) p.2103 – 2132 (1969)
62. D. Marcuse, "Bending Losses of the Asymmetric Slab Waveguide" *The Bell System Technical Journal*, **50** (8) p.2551 – 2563 (1971)
63. M. Heiblum, J. Harris, "Analysis of Curved Optical Waveguides by Conformal Transformation" *IEEE Journal of Quantum Electronics*, **QE-11** (2), p.75-83 (1975)
64. N. Feng, G. Zhou, C. Xu, W. Huang "Computation of Full-Vector Modes for Bending Waveguide Using Cylindrical Perfectly Matched Layers" *Journal of Lightwave Technology*, **20** (11), p. 1976 – 1980 (2002)
65. M. Popovic "Complex-Frequency leaky mode computations using PML boundary layers for dielectric resonant structures" *Integrated Photonics Research (Trends in Optics and Photonics Series)* **91**, p.143-5 (2003)
66. R.A. Soref, "Silicon-Based Optoelectronics" *Proceedings of IEEE* **81** (12), p. 1687-1705 (1993)
67. G. Celler and M. Wolf (July 2003) "Smart Cut™ - A guide to the technology, the process, the products", Soitec, Retrieved March 20, 2006 from http://www.soitec.com/en/pdf/SmartCut_WP.pdf#search='Smart%20Cut%E2%84%A2%20%20SOI'
68. H.H. Li, "Refractive index of silicon and germanium and its wavelength and temperature derivatives," *Journal of Physical and Chemical Reference Data*, **9** (3), p 561 (1980)
69. T. Marshner, A. Lee, S. Fuchs, L. Volkel, C. Stief, "193 nm Resist Roughness Characterization and Process Propagation Investigation Using a CD-SEM" *Proceedings of SPIE*, **5375**, p. 477-487 (2003)
70. S.J. Spector, M.W. Geis, D.M. Lennon, R.C. Williamson, T.M Lyszczarz, "Hybrid multi-mode/single-mode waveguides for low loss", *OSA Topical Meeting: Integrated Photonics Research*, IThE5 (2004)
71. T. Tsuchizawa, K. Yamada, H. Fukuda, T. Wanatabe, J. Takahashi, M. Takahashi, T. Shoji, E. Tamechi, S Itabashi, and H. Morita "Microphotonics Devices Base on Silicon Microfabrication Technology" *IEEE Journal of Selected Topics in Quantum Electronics* **11** (1), p. 232-240 (2005)
72. P. Dumon, W. Bogaerts, V. Wiaux, J. Wouters, S. Beckx, J. Van Campenhout, D. Taillaert, B. Luyssaert, P. Bienstman, D. Van Thourhout, R. Baets "Low-Loss SOI Photonic Wires and Ring Resonators Fabricated with Deep UV Lithography" *IEEE Photons Technology Letters* **16** (5), p. 1328 – 1330 (2004)
73. K.K. Lee, D.R. Lim, and L.C. Kimerling "Fabrication of ultralow-loss Si/SiO_2 waveguide by roughness reduction" *Optics Letters* **26** (23) p.1888 – 1890 (2001)
74. Plummer, Deal, Griffin, "Silicon VLSI Technology" (Prentice Hall, NJ, 2000)
75. H. Nohira, H. Sekikawa, M. Matsuda, T. Hattori, "Effect of chemical preoxidation treatment on the structure of SiO_2/Si interfaces" *Applied Surface Science* **104/105** p.359-363 (1996)
76. Y. Yamashita, K. Namba, Y. Nakato, Y. Nishioka, H. Kobayashi, "Spectroscopic observation of interface states of ultrathin silicon oxide" **79** (9), p.7051-7057 (1996)
77. W. Kearn, "Handbook of Semiconductor Wafer Cleaning Technology" (Noyes Publications, NJ, 1993)
78. G.S. Higashi, Y.J. Chabal, G.W. Trucks, K. Raghavachari, "Ideal hydrogen termination of the Si (111) surface" *Applied Physics Letters* **56** (7) p. 656 – 658 (1990)
79. V. Le Thanh, D. Bouchier, G. Hincelin "Low-temperature formation of Si (001) 2x1 surfaces from wet chemical cleaning in NH_4F solution" *Journal of Applied Physics* **87** (8) p.3700 – 3706 (2000)
80. M. Gotoh, K. Sudoh, H. Iwasaki "Roughening of the Si/SiO_2 interface during SC1-chemical treatment studied by scanning tunneling microscopy", J. Vac. Sci. Technol. B **18**, 4 (2000)

81. M. Miyashita, T. Tusga, K. Makihara, T. Ohmi, "Dependence of Surface Microroughness of CZ, FZ, and EPI Wafers on Wet Chemical Processing", J. Electrochem. Soc. **139**, 8 (1992)
82. L. Lai, E.A. Irene "Limiting Si/SiO_2 interface roughness resulting from thermal oxidation" J. Appl. Phys. **86,** 1729-1735 (1999)
83. H. Kuribayashi, R. Hiruta, R. Shimizu, " Shape transformation of silicon trenches during hydrogen annealing" *J. Vac. Sci. Technol. A*, **21**, No.4, p.1279 – 1283 (2003)
84. M-C. M. Lee, J Yao, M.C. Wu, "Silicon Profile Transformation and Sidewall Roughness Reduction Using Hydrogen Annealing" *IEEE Conference on MEMS* **18th** p.596-599 (2005)
85. Shoji Akiyama "High Index Platform for Silicon Photonics" *Ph.D. Thesis, Massachusetts Institute of Technology* (2004)
86. R. Germann, H.W.M. Salemink, R. Beyeler, G.L. Bona, F. Horst, I. Massrek, B.J. Offerein, "Silicon Oxinitride Layers for Optical Waveguide Applications" *Journal of The Electrochemical Society* **147** (6) p.2237 – 2241 (2000)
87. O.P. Agnihotri, S.C. Jain, J. Poortmans, J. Szlufcik, G. Beaucarne, J.Nijs, R. Mertens "Advances in low temperature processing of silicon nitride based dielectrics and their applications in surface passivation and integrated optical devices" *Semiconductor Science and Technology* **15,** p.R29 – R40 (2000)
88. R.M. Ridder, K. Worhoff, A. Driessen, P.V. Lambeck, H. Albers " Silicon Oxynitride Planar Waveguide Structures for Application in Optical Communication" *IEEE Journal of Selected Topics in Quantum Electronics* **4** (6) p. 930 – 937 (1998)
89. R. Henda, L. Laanab, E. Scheid, R. Formeaux "Characterization of Chemically Vapor Deposited Silicon Nitride Films from Disilane and Ammonia" *Japanese Journal of Applied Physics* **34** (4A) p.L437 -L439 (1995)
90. ZX-J Liu, J-J Zhang, X-W Sun, Y-B Pan, L-P Huang, C-Y Jin, "Growth and properties of silicon nitride films prepares by low pressure chemical vapor deposition using trichlorosiliane and ammonia" *Thin Solid Films* **460** p.72 – 77 (2004)
91. F. Ay, A. Aydinli "Comparative investigation of hydrogen bonding in silicon based PECVD grown dielectrics for optical waveguides" *Optical Materials*, **26** p.33-46 (2004)
92. W.A. Lanford, M.J. Rand "The hydrogen content of plasma-deposited silicon nitride" *Journal of Applied Physics* **49** (4) p. 2473 – 2477 (1978)
93. M.J. Shaw, J. Guo, G.A. Vawter, S. Habermehl, C.T. Sullivan, "Fabrication techniques for low loss silicon nitride waveguides" *Proceedings of the SPIE - Photonics West,* **5720** (15), (2005)
94. L. Dal Negro, J. H. Yi, L. C. Kimerling, S. Hamel, A. Williamson, G. Galli, "Light emission from silicon-rich nitride nanostructures" *Applied Physics Letters* **88** (1), (2006)
95. N-M Park, C-J Choi, T-Y Seong, S-J Park, "Quantum Confinement in Amorphous Silicon Quantum Dots Embedded in Silicon Nitride" *Physical Review Letters* **86** (7) p.1355-1357 (2001)
96. Retrieved March 29, 2006 from http://www.library.uu.nl/digiarchief/dip/diss/2003-1015-151807/c1.pdf
97. S.M. Sze, "Physics of Semiconductor Devices" (John Wiley & Sons, NY, 1981)
98. R.A. Street, "Hydrogenated amorphous silicon" (Cambridge University Press, Cambridge, 1991).
99. M.J.A. de Dood, A. Polman, T. Zijlstra, E.W.J.M. van der Drift, "Amorphous silicon waveguides for microphotonics" *Journal of Applied Physics* **92** (2), p. 649 – 653 (2002)
100. J.S. Foresi, M.R. Black, A.M. Agarwal, L.C. Kimerling "Losses in polycrystalline silicon waveguides" *Applies Physics Letters* **68** *(15),* p.2052 – 2054 (1996)
101. A.M. Agarwal, L. Liao, J.S. Foresi, M. Black, X. Duan, L.C. Kimerling "Low-loss polycrystalline wavetguides for silicon photonics" *Journal of Applied Physics* **80** (11), p. 6120 – 6123 (1996)
102. S.M. Sze, "VLSI Technology" (McGraw Hill, NY, 1988)
103. A. Harke, M. Krause, J. Mueller, "Low-loss singlemode amorphous silicon waveguides" *Electronic Letters* **41** (25), (2005)
104. B. E. Little, S. T. Chu, H. A. Haus, J. Foresi, and J.-P. Laine, "Microring resonator channel dropping filters" J. *IEEE Journal of Lightwave Technolgy*, **15**, p.998–1005 (1997)
105. C.K. Madsen, G. Lenz, A.J. Bruce, M.A. Capuzzo, L.T. Gomez, T.N. Nielsen, and I. Brener, "Multistage Dispersion Compensator Using Ring Resonators" *Optics Letters*, **24**, No.22, 1555-1557 (1999)
106. S.J. Choi, Z. Peng, Q. Yang, S.J. Choi, P.D. Dapkus "Eight-Channel Microdisk CW Laser Arrays Vertically Coupled to Common Output Bus Waveguides" IEEE Photonics Technology Letters, **16** (2), p.356-358 (2004)
107. V.R. Almeida, C.A. Barrios, R.R. Panepucci, M. Lipson "All-Optical Control of Light on a Silicon Chip" Nature, **43**, 1081-1084 (2004)

108. P. Heimala, P. Katila, J. Aarnio, and A. Heinamaki, "Thermally Tunable Integrated Optical Ring Resonator with Poly-Si Thermistor" *IEEE Journal of Lightwave Technology*, **14**, No.10, 2260-2261 (1996)
109. P. Rabiei, W.H. Steier, "Tunable Polymer Double Micro-Ring Filters" *IEEE Photonic Technology Letters*, **15**, No.9, 1255-1257 (2003)
110. S.T. Chu, W. Pan, S. Sato, T. Kaneko, B.E. Little, and Y. Kokubun "Wavelength Trimming of a Microring Resonator Filter by Means of a UV Sensitive Polymer Overlay *IEEE Photonic Technology Letters*, **11**, No.6, 688-690 (1999)
111. L. A. Hornak, T. W. Wedman, and E. W. Kwock, "Polyalkylsilyne photodefined thin-film optical waveguides," *Journal of Applied Physics*, 67, (5) 2235-2239 (1990).
112. P. K. Tien, G. Smolinsky, and R. J. Martin, "Thin organosilicon films for integrated optics," *Applied Optics* 11, (3) 637-642 (1972).
113. L. Eldada, "Polymer microphotonics," in *Nano- and Micro-Optics for Information Systems*, L. Eldada, ed., Proc SPIE 5225, 49-60 (2003).
114. J.P. Lock and K.K. Gleason, "Tunable Waveguides via Photo-Oxidation of Plasma-Polymerized Organosilicon Films," *Applied Optics* **44**, p.1691 (2005).
115. H.G. Tomkins and W.A. McGahan, *Spectroscopic Ellipsometry and Reflectometry*, Wiley-Interscience, New York (1999).
116. R.D. Miller and J. Michl, "Polysilane high polymers," *Chemical Review* **89**, (6) 1359-1410 (1989).
117. S. Pradhan, B. Schmidt, L. Martinez, Q. Xu, V.R. Almeida, C. Barrios, M. Lipson, "Electro-Optic Modulator on Silicon-on-Insulator Substrates Using Ring Resonators" *Conference of Lasers & Electro-Optics (CLEO)*, **CMG2,** p.107-109 (2005)
118. A. Liu, R. Jones, L. Liao, D. Samara-Rubio, D. Rubin, O. Cohen, R. Nicolaescu, M. Paniccia, "A high-speed silicon optical modulator based on metal-oxide-semiconductor capacitor" *Nature* **427** (6975) p.615-618 (2004)
119. Private communication from Michal Lipson to EPIC design team
120. Shun Lien Chuang "Physics of Optoelectronics Devices", (John Wiley & Sons, Inc., New York, 1995)
121. S. Jongthammanurak, J. Liu, K.Wada, D.D. Cannon , D.T. Danielson, D. Pan, J. Michel, L.C. Kimerling, "Strain-enhanced Electro-optic effect in Tensile Strained Ge films on Si at Weakly Absorbing Regime" To be submitted to *Applied Physics Letters*
122. Calculated by Samerkhae Jongthammanuruk and Jifeng Liu, MIT
123. L. C. Kimerling, D. Ahn, A. B. Apsel, M. Beals, D. Carothers, Y.-K. Chen, T. Conway, D. M. Gill, M. Grove, C.-Y. Hong, M. Lipson, J. Liu, J. Michel, D. Pan, S. S. Patel, A. T. Pomerene, M. Rasras, D. K. Sparacin, K.-Y. Tu, A. E. White, and C. W. Wong "Electronic-Photonic Integrated Circuits on the CMOS Platform", *Proceedings of SPIE - CLEO* **6125**, 612502 (March 2006)
124. C. K. Madsen," Efficient Architectures for Exactly Realizing Optical Filters with Optimum Bandpass Designs", *IEEE Photonics Technology Letters*, **10** (8), p.1136-1138, (1998)
125. E. J. Nowak "Maintaining the benefits of CMOS scaling when scaling bogs down" *IBM Journal fo Research and Development* **46** (2/3) p.169-180 (2002)
126. M.S. Rasras, D.M. Gill, S.S. Patel, A.E. White, K-Y. Tu, Y-K. Chen, D. N. Carothers, A.T. Pomerene, M.J. Grove, D. Sparacin, J. Michel, M.A. Beals, and L.C. Kimerling, "Tunable Narrowband Optical Filter in CMOS", Presented at the *OFC/NFOEC Conference*, PDP13, (March 2006)
127. S. Saini, J. Michel, L.C. Kimerling "Index Contrast Scaling for Optical Amplifiers", *IEEE Journal of Lightwave Technology*, **21** (10), p.2368-2376 (2003)
128. H-C Luan, D.R. Lim, K.K. Lee, K.M. Chen, J.G. Sandland, K. Wada, L.C. Kimerling "High-quality Ge epilayers with low threading-dislocation densities" *Applied Physics Letters* **75** (19) p.2909-2911 (1999)
129. Figure courtesy of Dr. Michael Morse, Intel.
130. Private correspondence from Lucent to EPIC design team January 3, 2006.
131. J.L. Benton, B.E. Weir, D.J. Eaglesham, R.A. Gottoscho, J. Michel, L.C. Kimerling "Measurement of defect profiles in reactive ion etched silicon" *Journal of Vacuum Science and Technology B* **10** (1) p. 540 – 543 (1992)
132. D.T. Danielson, MIT, unpublished work
133. A. Zoubir, M. Richardson, C. Rivero, A. Schulte, C. Lopez, K. Richardson, N. Ho, R. Vallee, "Direct femtosecond laser writing of waveguides in As_8S_3 thin films" *Optics Letters* **29** (7) p.748-750 (2004)
134. M.W. Geis, S.J. Spector, D.M. Lennon, J.U. Yoon, M.E. Grein, T.M. Lyszczarz, "Intensity and Polarization Modulation by Electrical Biasing of a Conductive Optical Wavguide" *OSA Integrated Photonics Research and Applications Conference* **IWA4** (April 2006).